AN AUTOMATED APPROACH TO ASTROGEODETIC LEVELLING

MARK BREACH

A thesis submitted in partial fulfilment of the requirements of The Nottingham Trent University for the degree of Doctor of Philosophy

April 2002

Abstract

An Automated Approach To Astrogeodetic Levelling

Mark Breach

Height determined using the Global Positioning System (GPS) is height above the World Geodetic System 1984 ellipsoid, a mathematical model of the earth. Surveyors and engineers require orthometric height, normally realised as height above sea level. Therefore knowledge of "*separation*" between height systems is essential when using GPS for the precise determination of orthometric height. One method of finding separation is by "*Astrogeodetic Levelling*"

Astronomic position may be determined by "Position Line" observations to stars and geodetic position by GPS. The difference between astronomic and geodetic positions, "*deviation of the vertical*", is the same as the rate of change of separation.

In this research a least squares approach to Position Lines was developed, in which refraction, vertical collimation and their rates of change are modelled as unknowns. Equations to correct for the effect on the observed vertical angle of an error in horizontal pointing were developed. Observing and computing strategies were considered. Star catalogues were constructed and tested. The effect of lunar gravitation and barycentric centrifugal force on deviation of the vertical was examined and new theory was developed to correct for this source of error. Several possible solutions to the evaluation of a personal equation were examined. A simple method to determine the topographic-isostatic effect using wedges across a longitudinal section on the line of greatest slope through a point was developed.

Video-based methods for detecting the instant of passage of a star across theodolite crosshairs and for linking GPS and video time by exposure of a GPS timed flash were developed. Analysis of the Astrogeodetic Geoid Model using ideas based on Kaula's "rule of thumb" was made and the geoid was modelled by polynomial coefficients and by interpolation of deviations. This leads to the application of "progressive nodes" as a means of avoiding a full least squares solution.

A practical determination of astronomical position was made giving position to about 0".15 (5 metres) with less than an hour's worth of observations. This suggests that astronomically derived deviation is an economical data source for the determination of a local precise geoid model. The process may find a practical application where precise height is required from GPS, such as in large engineering projects, especially where a precise relative local geoid model is only required in the area of the works. In this case, an astrogeodetic geoid will be much easier to construct than a gravimetrically derived one because it will require fewer observations.

Keywords. Astrogeodetic. Barycentric Centrifugal Force. Deviation of the Vertical. Geoid. GPS. Lunar Gravitation. Position Line. Topographic-Isostatic. Video.

Acknowledgements

The author wishes to acknowledge the following for their practical support.

Dr Ihsan Sholji and John Abbiss, the project supervisors, for their encouragement and down-to-earth guidance.

The Department of Civil and Structural Engineering for the use of survey and computing facilities.

His family for their tolerance and understanding.

I haven't a clue as to how my story will end. But that's all right. When you set out on a journey and night covers the road, you don't conclude that the road has vanished. And how else could we discover the stars?

Anon

Contents

List of Figures

List of Tables

Chapter 1

Introduction

1.1 Background

The Global Positioning System (GPS) is a real time navigation system developed by the United States Department of Defense (DoD) and is used primarily for military purposes. GPS consists of a constellation of earth orbiting satellites that enable navigators on or near the surface of the earth to determine, **in real time**, their absolute positions and velocities to a few metres and decimetres per second respectively. The system is known both as NAVSTAR (for NAVigation System using Timing And Ranging) and more simply as GPS.

The system is funded and controlled by the US DoD but is partially available for civilian and foreign users. The accuracy that may be obtained from the system depends on the degree of access available to the user, the sophistication of the receiver hardware and data processing software, and the degree of mobility during signal reception.

Originally, the system was designed for twenty-four satellites, now more, placed four in each of six orbital planes, which in turn are evenly spaced around the equator. Each orbital plane is inclined to the equator by an angle of 55° and within each orbital plane, the four satellites were to be evenly spaced in almost circular orbits. The nominal radius of the orbit is to be 26,000 km or about 4 times the radius of the earth.

GPS is also used by surveyors to find position on the surface of the earth and can be used to find height. See, for example, Wells (1986), Leick (1990), Hofmann-Wellenhof et al (1992), Ackrody & Lorimer (1989). The height determined by GPS is height above the World Geodetic System 1984 (WGS84) ellipsoid, a mathematical model of the earth. Surveyors and engineers require orthometric height, which is height above the geoid, an equipotential surface very close to mean sea level. Defense Mapping Agency (1991) and, more recently, NIMA (2001) give details of the WGS84. The difference between these two height datums is termed *separation* and, although substantially constant in time, varies with location. Further data is required if separation is to be computed.

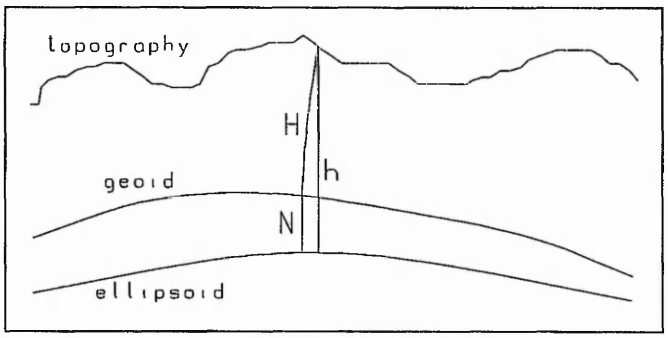

Figure 1.1 Orthometric height (H), Ellipsoidal height (h) and separation (N).

Knowledge of separation is essential for using GPS for the precise determination of orthometric height. The precise determination of separation over the area of a large project is a complex and costly operation. Technical solutions to this problem include:

Precise levelling coupled with GPS. Levelling is a very slow, land-based and labour-intensive operation, even with modern precise levels. The accuracy of such an approach is limited by the combined inaccuracies of GPS and levelling. Therefore such an approach is unlikely to ever be able to provide a geoid model of sufficient precision to be able to be used with GPS observations when precise orthometric height is required

Gravity observations. This requires theoretically world-wide, but practically nation-wide, gravity observations for the determination of separation at a single point. This has been done by the Ordnance Survey / Nottingham University. The theoretical basis for this work may be found in several texts such as Heiskanen & Moritz (1979), Vanicek & Krakiwsky (1982), Bomford (1980), Cross et al (1981), in order of theoretical rigor. The product is available from the Ordnance Survey, on a point-by-point basis, through their web site at Ordnance Survey (2001). A relative 2-5 cm geoid model, for distances up to 30 km is understood to be available for the whole of UK. However, GPS height differences, derived from baseline measurements may have standard errors in the order of 1 cm.

Gravity Satellite Missions. There have been a number of recent gravity satellite missions and more are planned. The GRACE mission with satellites launched in March 2002 consists of a pair of satellites about 220 km apart with nominal altitudes of 500 km. The satellite absolute and relative positions are found using on board GPS receivers and inter-satellite ranging. As the satellites pass through irregularities in the earth's gravity field. The distance between the satellites will vary and so by studying the changes in distance the form of the potential field and

hence the geoid may be found. A gravity model will be generated every 30 days. A 180 degree and order spherical harmonic expansion of the earth's potential field smoothed to 160 degree and order will be computed. More details are at the GRACE website (GRACE, 2002)

The GOCE programme (GOCE, 2002) with a launch programmed in 2005 is planned to determine the rate of change of gravity between pairs of accelerometers with a sensitivity of about 4 milliEötvös in each of three axes. The unit of the Eötvös is the rate of change of gravity with distance. One Eötvös is defined as $10^{-5}(m/s^2)/10km$ which is $=10^{-9}s^{-2}$ (Units, 2002). It is hoped to determine the geoid to an accuracy of one centimetre.

Astrogeodetic levelling. Astronomic position is defined by the local gravity vector and may be determined by "Position Line" observations to the stars. Details of the method and the theoretical basis may be found in most geodesy textbooks such as Vanicek & Krakiwsky (1982), Bomford (1980), but in greatest detail in Robbins (1976). Geodetic position in WGS84, or more precisely in Europe, in ETRS89, may be found from GPS. The European Terrestrial Reference Frame 1989, ETRF89, is a reference frame that moves with the tectonic plate that Europe is on. ETRF89 is realised as the European Terrestrial Reference System 1989, ETRS89, through specific stations with defined co-ordinates. As such, the co-ordinates of all stations in ETRS89 do not change substantially. The difference between astronomic and geodetic position is termed the "deviation of the vertical" and is the same as the rate of change of separation in the direction in which deviation is stated. If the separation can be determined at a single point, such as by using GPS at a bench mark of known height, then the change in separation between the known point and the next point can be found by astrogeodetic levelling and so give the separation at the next point. In principle then, an astrogeodetic geoid model can be formed from the known separation at one point and deviation of the vertical at the same point and many others.

A relative astrogeodetic geoid may be produced at any chosen level of precision by increasing the number of points at which astronomic observations are carried out within a given area and by increasing the number of stars observed at each point. In short, to meet a range of specifications in terms of precision, relative astrogeodetic geoid models could be created. It is unlikely that the precision of the Ordnance Survey's gravimetric geoid can be improved without extensive further gravity observations and computations using height and density models.

A gravimetric geoid requires, theoretically, world-wide gravity data but practically, countrywide gravity data. Alternative, less extensive date will be required if a global spherical harmonic model of the earth's potential field is used to create a smoothed gravity model. The remove-restore technique can then be used to provide the fine detail in the local area for the geoid model. A relative astrogeodetic geoid only requires data within the area of interest and so is much easier and cheaper to develop if the astronomical observations can be reasonably cheaply obtained. At present that is doubtful and therefore it is a challenge for this research to find a more cost-effective way of doing so.

The UK's Ordnance Survey has recently stated new policy with respect to its use of reference frames and surfaces (Ordnance Survey, 2002). The Ordnance Datum Newlyn (ODN) is a height system realised by tidal observations at the South Pier at Newlyn in Cornwall and a Terrestrial Reference Frame (TRF) created by precise levelling between about 200 fundamental bench marks over mainland Britain and densified by over half a million lower-order bench marks.

The Ordnance Survey (OS) has a national GPS network that is designed to provide a three dimensional TRF to bring together ODN and the horizontal datum, OSGB36 by a transformation model. By using the National GPS Network points, GPS users will get co-ordinates of new points in the European Terrestrial Reference System 1989 (ETRS89) which can then be converted into OSGB36 co-ordinates and ODN heights

The Principal Triangulation of Britain was carried out between 1783 and 1853. Only one distance measure, the Houndslow baseline, was observed. The resulting network of primary control stations therefore had significant distortions, especially in scale at points some distant from the Houndslow baseline. The retriangulation associated with OSGB36 used the average of 11 of the original Principal Triangulation control stations in the definition of the new datum.

In the new definition of the OSGB36 TRF, the primary triangulation stations were taken as error free but the real distortions of OSGB36 are recognised in the ETRS89-OSGB36 transformation model. Within OSGB36, the standard error of horizontal position varies from nothing, by definition, for Primary control stations to 0.05m at 7km for "third order" control stations.

Height data published by the OS is orthometric height relative to ODN. A network of precise levelling lines was used to find orthometric height at other points across Britain. The OS states (Ordnance Survey, 2002) that "the accuracy of the precise levelling technique is rivalled by the combination of GPS ellipsoid heighting with a precise gravimetric Geoid model, which allows the ellipsoid height difference between two points to be easily converted to an orthometric height difference".

There is a vast resource of height data in Britain, about half a million bench marks. However many have not been levelled since the 1950s and especially in areas where mining has caused subsidence, such as around Nottingham, errors of several metres are known to exist.

In the ODN TRF, as with horizontal control, the "first order height control points" the fundamental bench marks, are considered error free. ODN orthometric heights are related to the to the GPS ellipsoid GRS80 through the OS National Geoid Model. Within the ODN TRF the standard error of height varies from nothing, by definition, for Fundamental bench marks to ±12mm for "third order" bench marks.

The OS plans to retain OSGB36 and ODN for mapping purposes but these will be available through co-ordinate transformations from ETRS89 to OSGB36 and ODN provided by the OS. The transformations are the National Grid Transformation OSTN97 and the National Geoid Model OSGM91. An advantage of this process is that height relative to ODN will be continuously accessible rather than just at discrete OS benchmarks.

The system of benchmarks in Britain has now been largely abandoned. In practice, surveyors will get height in the local area of interest by using GPS to transfer height from one or more of the OS active of passive GPS stations. For this to be successful the heights of those stations, especially the passive stations must be maintained with more rigour than was applied to the former system of benchmark. If not then the same kinds of subsidence and disturbance errors could affect the new system of passive GPS stations.

Soon, by definition the National Grid will become a transformation of ETRS89 and so can be directly related to the International Reference System, ITRS, and therefore to many other national geodetic datums. The OS state that "a real-time precise positioning service offering five-centimetre accuracy in ETRS89, OSGB36 and ODN co-ordinate systems is likely to become available from Ordnance Survey in the next few years".

It must be hoped that height solutions will be rather better than the "five-centimetre accuracy" suggested in the previous paragraph. It is understood that OSGM91 has relative uncertainty of 0.01m up to 30km and rather more beyond. Clearly, error in height computed from GPS and the OSGM91 will reflect the errors in both the GPS derived co-ordinates and the geoid model used. The precision of height solutions from GPS will improve with advances in technology, software and the availability of future signals, especially the new L2C code and the third frequency, L5, due for implementation

on new GPS satellites from 2003 and 2005 respectively. The approval and funding for the development phase Galileo (Galileo 2002) given on 26 March 2002 indicates that by 2008 there will be about 60 satellites, not counting Space Based Augmentation Systems or the Russian GLONASS, available for positioning. Receivers that can maximise the use of all available signals are likely to be able to compute position and height faster and more accurately than is available today. A geoid model capable of enabling height determination by satellite means, with the accuracy that may soon be achieved, will be required to support high precision engineering and scientific projects.

1.2 Aims of the investigation

The original aims of this investigation were:

a. To develop a method for the rapid determination of astronomical latitude and longitude including investigation of methods for optimising the selection of observational data and development of field procedures to minimise the time for the collection of observational data.

b. To investigate the application of rigorous statistical techniques to the precise determination of astronomical latitude and longitude.

c. To investigate the deviation of the vertical by astronomical observations at a chosen site.

d. To develop the application of mathematical techniques for the determination of a geoid model from astronomical deviation of the vertical data of a chosen area.

1.3 Structure of the Thesis

In Chapter 2 the context of the proposed work is reviewed and the methodology is stated in Chapter 3. Existing " Position Lines" theory is reviewed and developed in Chapter 4 in a "least squares" context to take account of several previously un-modelled small errors. Observing and computing strategies are considered. Original contributions are made in terms of the development of the least squares approach to position lines in which refraction, vertical collimation and their rates of change are modelled as unknowns. Several possible solutions to the evaluation of a personal equation are examined and equations to correct for the effect on the observed vertical angle of an error in horizontal pointing are developed.

Chapter 5 concerns the construction and testing of suitable catalogues of stars and updating of co-ordinates to the time of observation.

In Chapter 6 observing and computing processes are examined in some detail to find a method that will give a good solution under the specific conditions of a particular set of astronomical observations. There is analysis of a method for detecting the instant of passage of a star across theodolite crosshairs using a photodiode. A method for linking GPS and video time by exposure of a GPS timed flash was developed and this lead to a video based method for detecting the instant of passage of a star across theodolite crosshairs.

The effect of lunar gravitation and barycentric centrifugal force on deviation of the vertical is examined in Chapter 7 and original formulae for the correction of observations of the vertical are derived.

The usual method of determining the topographic-isostatic effect is reviewed and a new simpler method that does not require a local terrain model is developed in Chapter 8. The model uses wedges across a longitudinal section on the line of greatest slope through the point under investigation.

Some theoretical and practical aspects are considered in Chapter 9. There is analysis of the Astrogeodetic Geoid Model using ideas based on Kaula's rule of thumb and modelling the geoid by polynomial coefficients and by the interpolation of deviations. This leads to the application of "progressive nodes" as a means of avoiding the need for a full least squares solution.

A practical determination astronomical position is described in Chapter 10.

In the next Chapter, the relationship between the geoid and an ellipsoid is reviewed. Methods for the determination of the shape of the geoid are stated and compared. Historical progress in the determination of the geoid is reviewed, suggestions as to the future utility of the astrogeodetic geoid are made, and the place of astronomy in the determination of the geoid is reviewed.

Chapter 2

Contextual Review

2.1 Introduction

In this chapter, the relationship between the geoid and an ellipsoid is reviewed and methods for the determination of the shape of the geoid are stated and compared. Historical progress in the determination of the geoid is reviewed and suggestions are made as to the future utility of the astrogeodetic geoid.

2.2 Geoid Determination

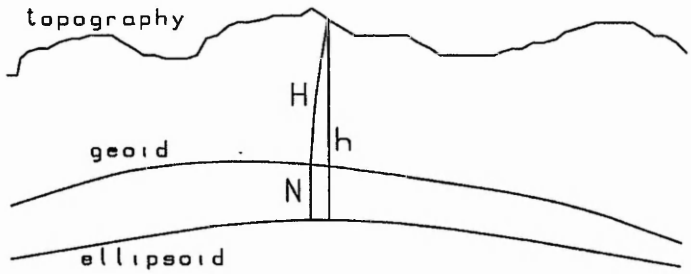

Figure 2.1 Relationship between geoid and ellipsoid.

The surveyor and engineer usually require height to be the height above the geoid or height above Mean Sea Level. Heights from GPS are found with respect to the ellipsoid. To be able to convert heights above the ellipsoid (h) to heights above the geoid (H) it is necessary to know the separation (N) between the ellipsoid and the geoid. See Figure 2.1, above. The height above the ellipsoid is measured along the normal to the ellipsoid. The height above the geoid, orthometric height, is measured along the plumb line from the point in question to the geoid. The two lines are not coincident but are very close to one another such that the approximation:

$$h \approx H + N$$

is normally without significant error.

The geoid and an ellipsoid may be considered as reference surfaces. An ellipsoid is defined mathematically. Placing it with respect to the real earth is a problem of datum definition. The geoid is a physical surface and may be defined as that equipotential surface that most closely approximates to mean sea level in the open oceans.

To find the form of the geoid using measurements of gravity it is necessary to make assumptions about the density of the earth between the topography and the geoid. Density does vary but is very difficult to measure. To avoid the problem Molodensky suggested an alternative approach. In Molodensky's model, the distance between the ellipsoid and the topography, h, is made up of two parts, the normal height from the ellipsoid to the telluroid, H^N, and the height anomaly from the telluroid to the topography, ζ. See Figure 2.2, below.

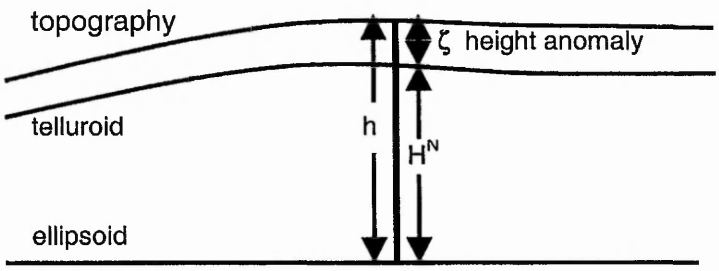

Figure 2.2 Relationship between telluroid and ellipsoid.

Therefore the relationship is:

$$h = H^N + \zeta$$

where H^N the normal height from the ellipsoid to the telluroid,

Compare this with the relationship of the geoid to the orthometric height on the previous page.

A new surface may now be plotted that is the distance of the height anomaly above the ellipsoid. This surface, the quasigeoid, is identical with the geoid in the open oceans and very close to it elsewhere, see Figure 2.3, below.

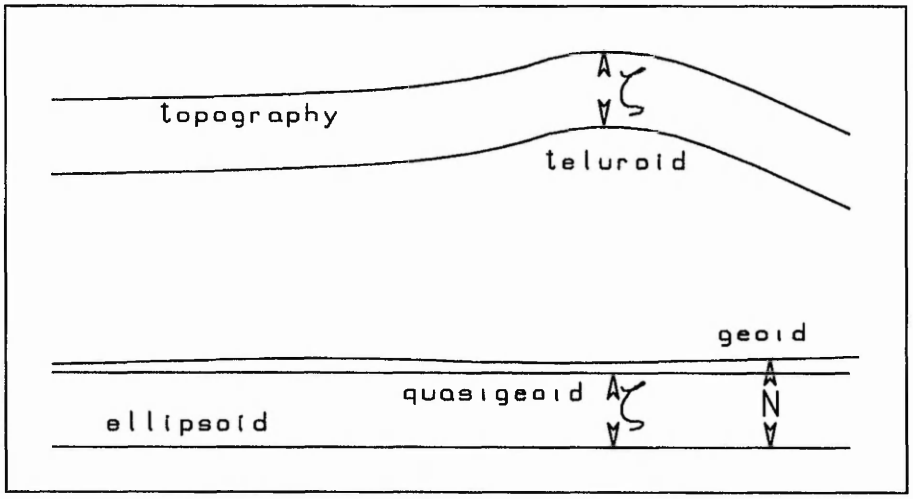

Figure 2.3 Relationship between geoid and quasigeoid.

However, it is not a level surface and so has neither geometrical nor physical meaning. It is merely a convenient surface that is relatively easy to define and to compute and is close to the geoid. However, the quasigeoid and normal heights are used extensively in Eastern Europe and are becoming more used in Western Europe as well.

2.3 Geoid Methods

There are four general methods using terrestrial observations by which a geoid may be determined. They are GPS with levelling, classical gravity methods, remove-restore gravity methods and astrogeodetic levelling. The methods involve quite different observational techniques, data processing routines, theoretical approximations, compromises and quality of output. A fifth method involves the study of satellite orbits to determine the potential field of the earth from which a smoothed, world best fitting, geoid may be derived. Such studies lead to best absolute geoids, but because of excessive smoothing, relative precision is less good.

2.4 GPS and levelling

The use of GPS with precise levelling is probably the easiest way to establish a local relative geoid. As with many observations in surveying and geodesy, it is much easier to be precise, relatively, than absolutely. If height above the ellipsoid, h, can be found from GPS and height above Mean Sea Level or the geoid, H, (or the

quasigeoid) can be found from levelling and gravity observations, through geopotential numbers, then the separation is simply given by

$$N = h - H$$

If the separation is found at a suitable number of points in the area of interest, then a model of the separation may be formed. However, from GPS what we really get is relative height above the ellipsoid, and from levelling difference in orthometric height. Therefore, the following equation better reflects the situation:

$$N_1 - N_2 = h_1 - h_2 - (H_1 - H_2)$$

where the subscripts refer to the points at the end of the GPS baseline. $h_1 - h_2$ comes from GPS, $H_1 - H_2$ comes from levelling and therefore to find N_2 we must first know or assume a value for N_1, that is, at the origin of the survey the separation must be defined. Therefore, all subsequent values for separation are relative to the origin. Similarly, all values of orthometric height, derived from GPS observations and geoid model heights, will lead to orthometric heights relative to the assumed orthometric height of the origin.

If GPS is to be used to find orthometric (or normal) heights to the best available precision then a GPS and levelling derived geoid is unlikely to be sufficiently precise. A numerical example illustrates the problem. If difference in height between two points by levelling/gravity may be found to ± 0.01m and difference in height above the ellipsoid may be found by GPS to ± 0.015m then the difference in separation may be found to

$$\sigma_{\Delta N} = (0.01^2 + 0.015^2)^{½}\,m = 0.018m$$

If this value is now used to find the orthometric height of a point with a different set of GPS observations then the formula becomes

$$H_1 - H_2 = h_1 - h_2 - (N_1 - N_2)$$

and the precision of the orthometric height difference is

$$\sigma_{\Delta H} = (0.015^2 + 0.018^2)^{½}\,m = 0.023m$$

Thus the orthometric height solution using GPS and a derived geoid model, in this example, is worse by a factor of 2.3 compared with a straightforward levelling solution, and by a factor of $^{0.023}/_{0.015} = 1.5$ compared with the difference of ellipsoidal height found from GPS.

To avoid the problem of an orthometric difference height solution which is significantly worse than the quality of the GPS value for ellipsoidal difference in height, it is necessary to use a relative geoid model that is significantly better than the quality of the observed/computed GPS difference heights. This of course cannot be obtained from GPS and levelling.

2.5 Classical Gravity Methods

There are two approaches to the problem of creating a geoid from observed gravity data, those of Stokes (Stokes, 1849) and Molodensky (Molodensky et al, 1962). The derivation of the formulae for the Stokes solution is complex and may be found in Heiskanen & Moritz (1979) and Vanicek & Krakiwsky (1982) among others. Stokes' Formula leads to the determination of the geoid, while that of Molodensky leads to the quasigeoid.

2.6 Stokes' Formula

Stokes Formula is derived from a consideration of a solution to the *geodetic boundary value problem*, that is, the determination of the figure of the earth. From gravity measured on the surface of the earth the separation of the geoid and the ellipsoid can be derived, if a number of quite significant assumptions can be accepted. Simply stated, Stokes' Formula is:

$$N' = \frac{R}{4\pi\gamma_m} \iint_\sigma S(\psi)\, \Delta g\, d\sigma$$

where

$R = (a^2.b)^{1/3}$ = radius of sphere of equal volume to the ellipsoid. a and b are the semi-major and semi-minor axes of ellipsoid.

γ_m = mean gravity of the ellipsoid

Δg = free air anomaly at angular distance ψ

$S(\psi) = \operatorname{cosec}(\tfrac{1}{2}\psi) - 6\sin(\tfrac{1}{2}\psi) + 1 - 5\cos\psi - 3\cos\psi \log_e(\sin(\tfrac{1}{2}\psi) + \sin^2(\tfrac{1}{2}\psi))$ (Stokes' Function)

ψ = the angular separation of the observation and computation points at the centre of the erath

$d\sigma = \cos\phi\, d\lambda\, d\phi$, a surface element

The free air anomaly is defined as:

$$\Delta g = g + F - \gamma$$

where g, the magnitude of the gravity vector, is measured on the surface; γ is computed on the ellipsoid; and the free air reduction, F, is

$$F = -\frac{\delta g}{\delta h} h \approx -\frac{\delta \gamma}{\delta h} h \approx 0.3086\ h \text{ mGal} \quad (h \text{ is in metres})$$

The free air reduction assumes that there are no masses external to the geoid. The masses to be removed are assumed to be all below the observation point. In practice, there will be nearby mountains or hills higher than the observation point and valleys below the observation point. Both reduce the magnitude of the local gravity vector. The correction for this terrain or "orological" effect is further described in Bomford (1980) and Heiskanen and Moritz (1979). World-wide gravity therefore requires a world-wide terrain model. In fact, if all external masses were removed to infinity that would change the mass of the earth and move the geoid.

As a result Stokes' Formula does not find the geoid but more strictly the separation of the co-geoid, N', from the earth mass centred ellipsoid used in the computation of the normal gravity, γ.

The Stokes' Formula above requires integration over the surface of the earth. Gravity observations are made at discrete points and so the formula needs to be adapted for a practical solution, as a summation rather than integration process. The practical application of formula is:

$$N' = \frac{R}{4\pi\gamma_m} \sum_{-\pi/2}^{\pi/2} \sum_{0}^{2\pi} \Delta g\, S(\psi) \cos\phi\, d\lambda\, d\phi$$

In practice, the earth is divided into a number of blocks. The nearer the block is to the computation point for N', the smaller it is made because errors in the computed value of N' are more sensitive to errors in gravity anomalies nearest to the point of computation. The values of N' are with respect to the earth mass centred reference ellipsoid as used in the standard gravity formula which was used to calculate the gravity anomalies. The reference ellipsoid must have the same rate of rotation and same mass as the earth or a "zero-order" undulation will occur.

Global gravity observations are required. Global gravity data of sufficient precision does not exist and therefore there will be systematic errors in any gravimetric geoid. However, the absence of a complete block of data on one side of the world will have a near constant effect over a block on the other side. In practice, dense gravity data is required over the area (country) of interest and some distance beyond. For the UK, this will require significant amounts of marine gravity.

Systematic errors in the block mean anomaly can occur at higher altitudes. The free air reduction is 0.3086 mGal/m. This means that it is necessary to measure height each time gravity is measured. If levelling data of sufficient accuracy already exists then there should not be a problem. If height data does not exist and height transfer is made with GPS over long ranges, of say 100km, then an error of up to 4m in the relative assumed orthometric height could occur. This would lead to an error of over 1 mGal in the computed block mean anomaly.

The method is based upon a "spherical earth", therefore there are approximations relating to the earth's flattening, i.e. of the order of 0.0033. This is systematic over a small area and will not exceed 0.3m.

One point requires global gravity coverage, in theory at least. Once global gravity coverage has been obtained then it can be used to create a global geoid.

Stokes' Formula can give the detailed shape of the geoid in a local area but will contain major systematic errors. Astronomy, see Section 2.9, below, can give precise values of the slope of the geoid without significant systematic error. Therefore a combination of astronomical and gravity data can lead to a precise local relative geoid.

2.7 Molodensky's Solution

For the reduction of measured gravity on the surface, it is necessary to assume the density of the masses below the point, as in the free air reduction in Stokes Formula. Molodensky's solution for "geoid" determination avoids this problem. The geometric height is expressed as

$$h_P = H^N_P + \zeta_P$$

so

$$\zeta_P = h_P - H^N_P$$

$$= h_P - h_Q$$

where P and Q are as defined in Figure 2.4. The gravity anomaly is now defined as

$$\Delta g = g_P - \gamma_Q$$

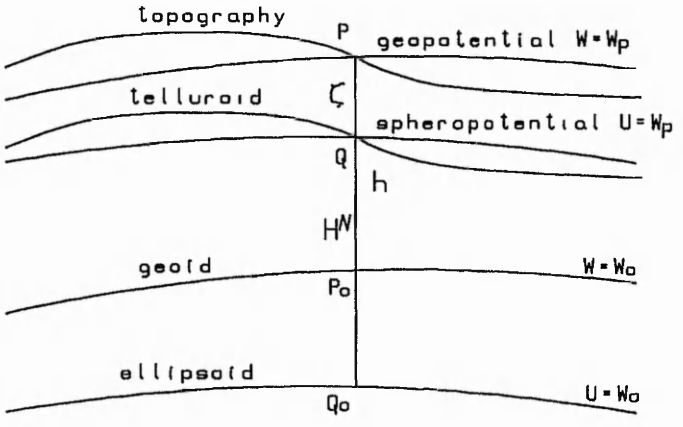

Figure 2.4 The relationship between geopotential at ground surface and spheropotential at telluroid.

This is quite a difference in definition. Note in particular that there is no assumption about density involved in this. The gravity anomaly is now the difference between observed gravity on the ground and computed normal gravity on the telluroid. This can be found from a free air reduction applied upwards to normal gravity on the ellipsoid. A direct formula for computing γ_Q is given in Heiskanen & Moritz (1979):

$$\gamma_Q = \gamma_o \{ 1 - 2(1 + f + m - 2f\sin^2\phi)\frac{H^N}{a} + 3\frac{H^{N2}}{a^2} \}$$

The solution for ζ_P is similar to that of Stokes; in fact, the Stokes' Formula forms the first part of the Molodensky solution. Bomford (1980) quotes the following as the Molodensky Formula.

$$\zeta_P = \zeta_0 + \zeta_1 = \frac{R}{4\pi\gamma_m}\iint_\sigma S(\psi)\,\Delta g\,d\sigma + \frac{R}{4\pi\gamma_m}\iint_\sigma S(\psi)\,G_1\,d\sigma$$

where Δg has been defined on the previous page and G_1 is given by

$$G_1 = \frac{R^2}{2\pi}\iint_\sigma \frac{(h_A - h_P)}{r^3}\left(\Delta g + \frac{3\gamma_m\zeta_0}{2R}\right)d\sigma$$

where

h_A is the height of the observed anomaly point or, more practically, the block centre.

h_P is the height of the point where the height anomaly is to be computed.

r is the distance between the observation and computation points.

The full Molodensky Formula has further terms but they are very small and have been neglected.

Both the geoid from Stokes and the quasigeoid from Molodensky are correlated with the topography but the numerical value of the quasigeoid is in general greater than that of the geoid. At sea, of course, the geoid is coincident with the quasigeoid. The difference between the geoid and the quasigeoid may be expressed as

$$\zeta - N = H - H^N$$

$$= \frac{C}{g} - \frac{C}{\gamma}$$

$$= \frac{\gamma - g}{\gamma} H$$

where g and γ take their mean values along their respective lines. An approximate formula from Heiskanen & Moritz (1979) is:

$$\zeta - N \approx 10^{-7} \bar{H} H \text{ metres}$$

where

$\bar{H}$ is the mean height of the area in metres

H is the height of the point in metres

Some examples of approximate values are in Table 2.1, below.

Table 2.1 The difference between ζ and N at four sample points.

Feature	height of point	mean height of area	ζ - N
Mt. Everest, Nepal	8848 m	5000 m	4.4 m
Mt. Blanc, Switzerland	4807 m	3000 m	1.4 m
Ben Nevis, Scotland	1344 m	800 m	0.11 m
Brown Willy, Cornwall, England	419 m	100 m	0.004 m

2.8 The Astrogeodetic Geoid

The slope of the geoid is the same as the deviation of the vertical at a given point in a given direction. The deviation of the vertical may be found from a comparison of

astronomical and geodetic latitude and longitude. There are a number of ways in which astronomical position may be found; of these "Position Lines", as described by Robbins (Robbins, 1976), is the most efficient field survey method because both astronomical latitude and longitude are found at the same time. Geodetic position may be found by conventional survey means or by GPS.

The astrogeodetic geoid may be found by observing deviations at a series of stations. Deviation is the slope of the geoid and, if separation is known at least at one point, then it may be estimated at all other points within the area of the observing stations. It can take most of a single night to complete the astronomical observations for a precise determination of deviation of the vertical by conventional means at one point.

There are methods other than Position Lines, but no single other method determines both components of position simultaneously. The minimum necessary observations for Position Lines are those of precise zenith angle, and precise time. The determination of the astrogeodetic geoid is described in detail in Chapter 9.

2.9 Remove-Restore Gravity Methods

A more recent approach to the problem involves using the "remove-restore" technique with least squares collocation. The basis of the approach is to use Stokes' integral applied to gravity data but as it may not be practical to use apply the integration over the whole of the earth the long and short wavelength components of the geoid are computed separately using a "remove-restore" approach.

Gravity anomalies are computed from the long wavelength component from a global geopotential model such as EGM96 (EGM96, 1996). The gravity anomalies are then subtracted from the raw gravity data. The remaining gravity anomalies are then used to compute the short wavelength component of the geoid height. The long wavelength component of the geoid height computed from the global geopotential model is then restored and finally the total geoid height is computed as the sum of the short and long wavelength components.

In computing the short wavelength component of the geoid from local gravity data least squares collocation may be used. The quality of local solution is highly dependant upon the quality of the local gravity data used which is why a good digital elevation model (DEM) for the computation of the terrain correction is important.

2.10 Space Based Methods

There have been a number of campaigns to determine the geoid using satellite-derived data.

Direct measurements of the lake and sea surface may be made by satellite altimetry. If the position of the satellite is known, e.g. from onboard GPS then a comparison of the satellite height above the ellipsoid, derived indirectly from GPS, coupled with altimetry data can, in principle, lead to a measure of the height of the sea surface. With knowledge of the disturbances of the sea surface such as wind, tides currents, temperature and density sea surface height can be related to the geoid. Such methods do not work well over land where knowledge of the geoid is more often needed. Programmes have included ERS-1, launched by the European Space Agency in July 1991 and the current TOPEX/Poseidon satellite being replaced now by Jason-1 (JPL, 2002).

Alternatively, the study of satellite orbital perturbations leads to knowledge of the gravity field. For the best results, the satellite needs to be close orbiting to be subject to the greatest effect of the irregularities in the earth's gravity field. However any satellite with an altitude of less than about 300km will suffer excessive atmospheric drag and its orbit will soon decay. A number of other disturbing forces such as Electromagnetic force perturbation, solar radiation, tidal perturbations and relativistic effects will also need to be taken into account (Vanicek and Krakiwsky, 1982). An analysis of orbital perturbations leads to the determination of spherical harmonic coefficients of the earth's gravitational potential field. Satellite laser ranging is a method of direct measurement to a space vehicle. It has been used with a number of satellites with corner cube prisms such as Lageos, the laser geodynamic satellite launched by NASA in 1976, the French satellite, Starlette the Japanese satellite Ajisai and the Russian satellites Etalon I and II. (SLR, 2002).

A third approach is to measure the motion of one space vehicle relative to another. With two space vehicles in the same orbit, but with different arguments of perigee, the distance between then will be affected by local gravity variations. Again, the same difficulties with minimum desirable and minimum practical altitude will apply. The new GRACE mission (GRACE, 2002) uses this approach.

A further development will be to use a gravity gradiometer and this is the main component of the future GOCE mission (GOCE, 2002).

2.11 Comparison of methods

The methods described above have their advantages and disadvantages and therefore their specific applications.

Space based methods are able to give global data and therefor a global geoid model. In all cases, except satellite altimetry the geoid model lacks short wavelength resolution because the satellites must orbit the earth at several hundred kilometres, any less and their orbits will decay rapidly. With satellite laser ranging the limitation is that the technique works well over water but less well over land. In all cases, there are enormous amounts of data to manage especially where the measurements are to be used to compute spherical harmonic coefficients.

GPS with levelling is the simplest method but does rely upon good existing orthometric height information. If there are significant errors in the height data then the geoid model will reflect those errors. Even with good height data, the geoid model will reflect the combined errors of GPS and height data.

The application of GPS with levelling for geoid model determination will be where:

- Significant orthometric height data already exists.
- A geoid of limited accuracy is acceptable.

A gravimetric geoid model requires, theoretically, worldwide gravity and height observations. In practice, gravity measured over a limited area but in extent well beyond the area of the proposed geoid model is required. For islands, this will involve the observation of significant amounts of marine gravity. Gravity observations require specialist equipment, i.e. gravimeters. Gravity magnitude values on land are easy to observe and require no more than a short stay at each point with a gravimeter. The height information does not have to be as precise as that for GPS with levelling but interpolation of map contours is unlikely to be acceptable. Although data capture is simple, processing the data to derive a gravimetric geoid is rather more complex, especially where the data is sparse. A gravimetric geoid derived with limited gravity data, especially near or in the area of the gravimetric geoid model, will contain significant biases and systematic errors.

The application of gravity for geoid model determination will be where:

- The geoid model is required for a large area, eg 100s of km square.
- A national or world geoid model is required.

- Significant amounts of gravity data already exist and computing facilities are available.

An astrogeodetic geoid model requires time-consuming astronomical observations, which can only be carried out on relatively cloud-free nights. Geodetic position is required, ideally to better precision than that obtained by astronomy and this may easily be found with GPS. The computing process to derive deviation from astronomical observations is moderately tedious. Deviation is the same as geoid slope and therefore needs further processing to derive geoid height. Precise orthometric height information is not required. The only requirements for height are for the reduction of latitude for plumb line curvature for which contour interpolation will normally be acceptable and for topographic-isostatic reductions for which a local elevation model would normally be required.

The application of astronomy for geoid model determination will be where:

- The geoid model is required for a limited area and,
- Significant systematic errors in the model are not acceptable and,
- Astronomical observations for position already exist or may be observed and,
- A precise solution is required.

In practice, geoid models of large areas are obtained using a combination of all available data, including satellite orbit and altimetry data.

2.12 Progress in the determination of the geoid

The quality of geoid and related solutions has improved significantly over the past 20 years.

Torge & Denker (1998) reviewed that Wolf in 1948 calculated an astrogeodetic geoid for Central Europe based upon 100 deflections of the vertical and achieved an accuracy of several metres. Tani in 1949 achieved a similar precision with 100 gravity anomalies. In both cases, the quality of solution reflects the sparseness of the data.

An unpublished Polish astrogeodetic geoid of 1961 is reported by Lyszkowicz (1991) as having a contour interval of 0.5 m and an estimated relative accuracy of ±0.15 m over 100 km.

In Australia, an early, 1967, astrogeodetic geoid using 600 astrogeodetic observations probably had an accuracy of ±6 m, Kearsley & Govind (1991). Subsequently an astrogravimetric geoid with contour interval of 1 m, Fryer (1972), with 1200 astrogeodetic and some gravity observations had an uncertainty of ±3 m.

Monka et al (1978) contains three short papers on, (1) a gravimetric geoid for the North Sea, (2) a GEOS-3 altimeter geoid of the German Bay and (3) an astrogeodetic geoid around the North Sea. (1) is on land and sea, (2) is at sea and (3) on land. Agreement between (1) and (2) is ±0.2 m RMS. Agreement between (1) and (3) varies from ±0.5 m RMS to ±1.4 m RMS. Astrogeodetic data is limited, in (3) but data is very dense in parts, in particular 2 groups of sites in Germany where stations are less than 5km apart. Stations in Norway are up to 120 km apart. There is little more than a single line of stations in UK.

Torge & Denker (1998) review that Levallois & Monge in 1978 had improved the Central European Astrogeodetic geoid to an accuracy of 1 to 3 metres with about 1000 deflections of the vertical.

In Poland (Lyszkowicz 1991) the 1983 situation, based upon astrogravimetric data, is little improved at ±0.10 to ±0.15 m per 100 km. However, Torge & Denker (1998) report that The European Astrogravimetric geoid EAGG1 (Brenecke et al 1983) with about 5000 vertical deflections had an absolute accuracy of ±0.9 m and relative accuracies ranging from ±0.3 m per 100 km to ±1.1 m per 1000 km.

Tziavos & Arabelos (1991) show that surface gravity with the OSU86F geopotential model gives absolute geoid heights at ±0.5 m and 2-3 ppm for relative heights in North America. Agreement with deviation data in Greece is better than ±2". After removal of geopotential model and terrain model effects, the standard deviation of a gravity anomaly set is ±32 mGal with point accuracy of 2 to 5 mGal. Astronomical deflections ($\Delta\xi$, $\Delta\eta$) after removal of geopotential model effects are ±5".5.

The local quasigeoid for Hungary, based on OSU86F geopotential coefficients and gravity anomaly data, Ádám & Denker (1991), has 0.2 m contour intervals.

Rapp & Nikolaos (1991) report that the OSU89A/B potential coefficient models of degree 360 have absolute agreement of ±0.59 m with the GEOSAT implied undulation and ±1.60 m with Doppler results. Relative agreement with a precise European traverse is 0.25 m ±3.5 ppm.

A gravimetric quasigeoid of Scandinavia and Finland, (Forsberg, 1991), uses a DTM with 0.5 km to 1 km resolution for terrain corrections and the OSU89B geopotential

model. Agreement with a 2000 km GPS levelling traverse is ±0.10 m RMS with local relative agreement at ±0.03 m to ±0.05 m RMS over approximately 20 km (≈ 1.5 to 2.5 ppm).

Comparison of the German 1989 quasigeoid, derived from 440000 blocks of gravity data, with GPS levelling (Denker, 1991) shows RMS differences of ±0.01 m to ±0.06 m at distances of 10 to 800 km.

Fukuda & Segawa (1991) report on a Japanese geoid based on satellite altimeter and surface land and ship gravity data, with 0.2 m contour intervals.

A geoid for Italy derived from surface gravity and the IfE88E2 geopotential model, Benciolini et al (1991), has agreement of ±0.1 m to ±0.3 m with GPS and levelling.

The UNB '90 geoid uses 266000 land and 323000 sea gravity values with the GEM-T1 geopotential model up to degree 20. Accuracy is estimated by Vanicek et al (1991) to be ±1 ppm.

Bürki and Marti (1991) report on three geoid models for a Swiss geoid, which agree to ±0.1 m to ±0.3 m. They are gravimetric, astrogeodetic and astrogravimetric. The Ivrea zone of Switzerland shows anomalies of the order of 170 mGal and deviations of 35". A plot of an astrogeodetic geoid has 0.2 contour intervals but geoid height accuracy is claimed to be ±0.03 m. GPS results, with the Bernese software, show agreement to ±0.1 m to ±0.15 m over all of Switzerland.

Kearsley & Govind (1991), report on an Australian gravimetric geoid constructed from 430000 land and offshore gravity points for which limited tests show a comparison with GPS/levelling of ±1.7 ppm.

Torge & Denker (1991) suggest possible improvements in the existing European geoid/quasigeoid. All the methods involve improved geopotential models, global topographic-isostatic models, regional DTMs, satellite altimetry, sea surface topography models, GPS and levelling. There is no mention of astronomy presumably because of the assumed slow rate of data capture.

By 1996, astronomy as a data source appears to have been abandoned. In the whole of Segawa et al (1997) there appears to be not one mention of it. All efforts for geoid determination are based on world geopotential models, gravity, altimetry and GPS with levelling, in spite of the respective limitations of the individual methods.

Jiang (1997) reports on the geoid for France. A gravimetric geoid was adjusted to fit 1081 GPS/levelling points. The accuracy of the geoid is estimated to be 2-3cm in plane areas and 4-7 cm in mountainous areas with a relative accuracy of 2ppm over

20km, 0.2ppm over 300 km and 0.06ppm over 1000km. This latter statistic suggests a relative accuracy of 6cm over 1000km. In Belgium, Pâquet (1997) reports that the BG96 Belgian geoid has an absolute accuracy of 3-4cm and a relative accuracy of 1-2ppm up to 50km and 0.3-0.5ppm up to 300km. Similar levels of accuracy are also claimed by Denker et al (1997) for the whole of Europe for the European Gravimetric Quasigeoid EGG96. The accuracies are ±1-5cm over 10 to a few 100km and ±5-20cm over a few 1000km when compared with independent GPS/levelling data. In the Nordic and Baltic region of Europe, Forsberg et al (1997) report a fit of their geoid to ±10cm across the region but with a fit at the 1cm level in Denmark where the topography is relatively flat and the gravity coverage is particularly good. In Latvia, Kaminskis (1997) reports that there is an ±8cm agreement between the gravimetric geoid and GPS/levelling. In all the cases in this paragraph, terrain models, altimetry, tide-gauge readings, geopotential models and GPS/levelling have been taken into account.

The need for high-resolution terrain models is emphasised by Kühtreiber (1997) if geoid accuracy is to be obtained at the ±1cm level in mountainous regions.

In Australia, Zhang & Featherstone (1997) investigate the effect of the terrain correction as it affects the AUSGEIOD93 free air co-geoid. They conclude that the application of the terrain correction only reduces the RMS discrepancy from ±0.428m to ±0.410m even though the terrain effects affect the geoid by up to 0.69m. It is clear that there must be other sources of systematic error yet to be accounted for. Featherstone et al (1997) discuss the tasks for improving the Australian geoid, including considerations with respect to terrestrial gravity and terrain data, geodetic datums, geopotential models and GPS/levelling on the Australian Height Datum.

In Canada, the gravimetric geoid GSD95, as reported by Véronneau (1997), has a precision of ±5-10cm over 10s of kilometres when compared with GPS/levelling. A geoid with a precision of ±2.5cm is planned for the year 2000.

The Japanese Geoid, JGEOID 93, as reported by Fukada et al (1997) shows an RMS difference between the gravimetric and GPS/levelling geoid of ±7cm. Takana (1997) determines a local geoid with GPS and conventional but unspecified survey in the region of a volcano in Japan but only to ± 10 cm.

Marson et al (1997), working in the Ross Sea Antarctica, show a relative geoid plot with 0.25m contours based upon marine gravity, a topographic model and the remove-restore technique applied to the OSU91 geopotential model.

By contrast, in South America, Blitzkow et al (1997), report that the gravimetric geoid of South America when compared with Doppler and GPS/levelling points shows a mismatch with geoids derived from OSU91 and WGS84 of the order of ±2m. Similarly, there is a poor absolute geoid in Indonesia, a country of 16000 islands. There is a shortage of marine gravity and the uncertainty is still at the 0.7m level.

With the exception of the centre of the Western Europe, there is as yet, in 1998, no geoid that can match the relative accuracy of GPS ellipsoidal heighting.

By 1998, the EGG97 quasi-geoid model for Europe (EGG97, 1997) had been published and much of Vermeer and Ádám (1998) is concerned with its evaluation. The EGG97 was computed from 2.7 10^6 gravity measurements and 7 10^8 heights. Even so there are areas of insufficient data at sea, Torge & Denker (1998). Several of the papers are concerned with testing the EGG97 with GPS and levelling. Some incompatibility in terms of significant amounts of bias and tilt are reported. Bias is of no consequence when the geoid model is used for relative GPS heighting, but tilt is of concern. Denker (1998) reports an RMS discrepancy in Lower Saxony of ±0.038m with bias and ±0.013m with bias and tilt over 300 km, an RMS discrepancy in France of ±0.128m with bias and ±0.080m with bias and tilt over 1000 km and an RMS discrepancy through Europe of ±0.294m with bias and ±0.175m with bias and tilt over 3000 km. Since most GPS work is undertaken over short ranges this is approaching acceptable values. However, when GPS height differences can be routinely computed at the ±0.005 m level then this quasi-geoid will need to be improved.

In Hungary, Kenyeres & Virág (1998) find, after bias and tilt is removed, a fit of ±0.063 m between GPS and levelling and the EGG97.

In Denmark, a relatively flat country, a 1-cm geoid for most of the country is reported by Forsberg (1998). In Finland, also relatively flat, Ollikainen (1998) reports a fit of the FIN95 geoid to GPS/levelling of ±0.060 m, but a worse fit with other geoid models.

In Australia AUSGEOID93 is reported by Zhang et al (1998) to achieve a national fit of ±0.33m and a local fit of ±0.04 m to ±0.18 m with GPS/levelling. The national fit is a significant improvement upon that reported by Zhang & Featherstone (1997) for the AUSGEOID93 co-geoid.

In Israel, Sharni (1998) reports on a pilot project for a geoid model of a small area of 570 km^2. When compared with GPS/levelling the result has a standard error of

±0.040 m. The project has been hampered by insufficient gravity coverage, especially off the western coast of the project area.

Overall, in Torge & Denker (1998) astronomy has a higher profile than in Segawa et al (1997). "The Recomputation of the Austrian Astrogeodetic Geoid", Heiland et al (1998), is a refinement of previous work and incorporates a denser DTM of 50 x 50 m compared with the previous 350 x 350 m. The improved DTM model leads to changes of over 0".5 in some vertical deflections. The Austrian astrogeodetic geoid is seen not as a product in its own right but as a by-product of the process to produce the "Austrian Geoid 2000" which will use the 50 x 50 m DTM, 30 000 gravity observations and 700 deflections of the vertical. The accuracy of the Austrian astrogeodetic geoid is not stated.

In describing a 1-centimetre local geoid in Croatia, Colic et al (1998) used 18 vertical deflections observed with a Zeiss Ni2 astrolabe, with GPS and precise levelling. The Airy-Heiskanen model for isostasy (p135 of Heiskanen & Moritz (1979)) has been used with fixed values for $\Delta\rho$ and the depth of the Mohorovicic discontinuity. The quality of vertical deflections is ±0".5 to ±0".75 and ±0.020 m for GPS/levelling and it is claimed that this leads to a geoid model of ±0.015 m but over a limited area of less than 1000 km^2. The limitation of the knowledge of variation in surface density is acknowledged.

For Switzerland, Marti (1998) describes the CHGEO97 geoid model that has been derived from 600 vertical deflections, 70 GPS/levelling stations and a 25 m DTM. 20000 available gravity observations were not used because they did not improve the quality of the solution, probably because of insufficient rock density data. The result has uncertainty of ±0.03 m to ±0.05 m depending upon the flatness of the terrain. The CHGEO97 quasigeoid was compared with the EGG96 quasigeoid and the fit varied from ±0.05 m to ±0.15 m for flat and extreme mountainous areas respectively. Updated figures for the CHGEO98 geoid model are given in Marti (2000).

Ming (1999) reported on recent advances in the geoid determination by airborne gravimetry but current technology is limited to 5 cm local geoids.

Blitzkow et al (1999) describe the current state of progress towards a South American geoid that currently is at the decimetre level. Clearly, development across the entire world is not consistent and there are areas where considerable work is still required.

In South East Asia a regional gravimetric co-geoid is reported by Majid et al (1999) where limited sets of gravity data are used to produce a co-geoid of 0.4 metre RMS fit to GPS/levelling. The solution is claimed to be better than the Earth Gravity Model 1996 (EGM96) and OSU91A geoids in the 40º latitude by 50º longitude window under investigation.

In the UK (Iliffe 2000), evaluation of the OSGM91 geoid in a limited area suggests that relative geoid model heights are of the order of 0.013 to 0.026 m for distances between 1 and 10 km. This is now approaching the level of precision that is desirable for use with GPS.

It was recognised by Featherstone in Western Australia that a gravimetric geoid model does not allow the accurate transformation of Global Positioning System (GPS) ellipsoidal heights to Australian Height Datum (AHD) because of the effect of local geological structures, the availability and quality of gravimetric data, and the possibility of distortions in the AHD (Featherstone 2000). A solution combining GPS and AHD heights was used to adjust the gravimetric geoid so that it provided a model of the separation between the AHD and the GRS80 reference ellipsoid. An improved model of the AHD–GRS80 separation was found at the ±8 mm level in comparison to the gravimetric geoid fit of ±128 mm.

Smith (Smith et al 2000) describe problems associated with the determination of a geoid for Florida USA. They find airborne gravity data unreliable and marine gravity introduces tilts and biases to the gravimetric geoid. The test of the geoid is against GPS/levelling data but there is no overall quality statement relating to the Florida geoid model.

In the determination of a gravimetric geoid for Hong Kong, Yang and Chen (Yang and Chen 2001) use the EGM96 geopotential model with the remove-restore technique, a limited data set of 600 gravity points and a 500 metre DTM to create a gravimetric geoid. 31 checkpoints from GPS/levelling show agreement to ±20 mm.

The US National Imagary and Mapping Ageny (NIMA) and NASA's EGM96 is now considered by many as the current definitive model for practical applications. It is available as a spherical harmonic coefficient file and a correction coefficient file to calculate point geoid undulations (EGM96, 1996). The Geoid Height File consists of a 15 minute grid of point values. The EGM96 Geopotential Model to degree and order 360 has been used. The WGS 84 defined constants of ellipsoid semi-major axis and eccentricity were used to define the reference ellipsoid. In constructing the EGM96, surface gravity data was used to give detail where satellite information was

insensitive, that is where degree is greater than 40. Satellite to satellite tracking data from Topex/Poseidon, EP/EUVE, and GPS/MET was used. Altimeter data from GEOSAT, TOPEX/POSEIDON, and ERS1 was used to provide detail where degree is greater than 70. Conventional tracking data included observations by SLR to Lageos2, Stella and GFZ-1 and from TRANET (Doppler) HILAT and RADCAL tracked satellites (EGM96, 2001).

The UCL Geomatics Engineering Research page states the absolute value of the WGS84 geoid height computation using EGM96 as better than metre world-wide (UCL, 2002). Relative values will of course be better.

As the area over which the geoid is to be determined decreases, problems associated with a lack of gravity data become more apparent. Although local precision becomes greater, tilts and biases in the model, due to an absence of gravity outside the immediate area of interest, become more problematic.

By way of illustration, Figure 2.5 shows a part of the geoid model currently available for UK. It is associated with the ETRS89. Figure 2.5, below, was constructed on a 10km by 10km grid at 100 metre intervals, 10000 points, using the "co-ordinate converter" at Ordnance Survey (2001) which in turn uses OSGM91. The area is centred on the village of Ravenshead in Nottinghamshire. The "contour interval" is 0.05 metres. The smooth contours probably reflect a lack of resolution in the original data set used to construct the geoid model.

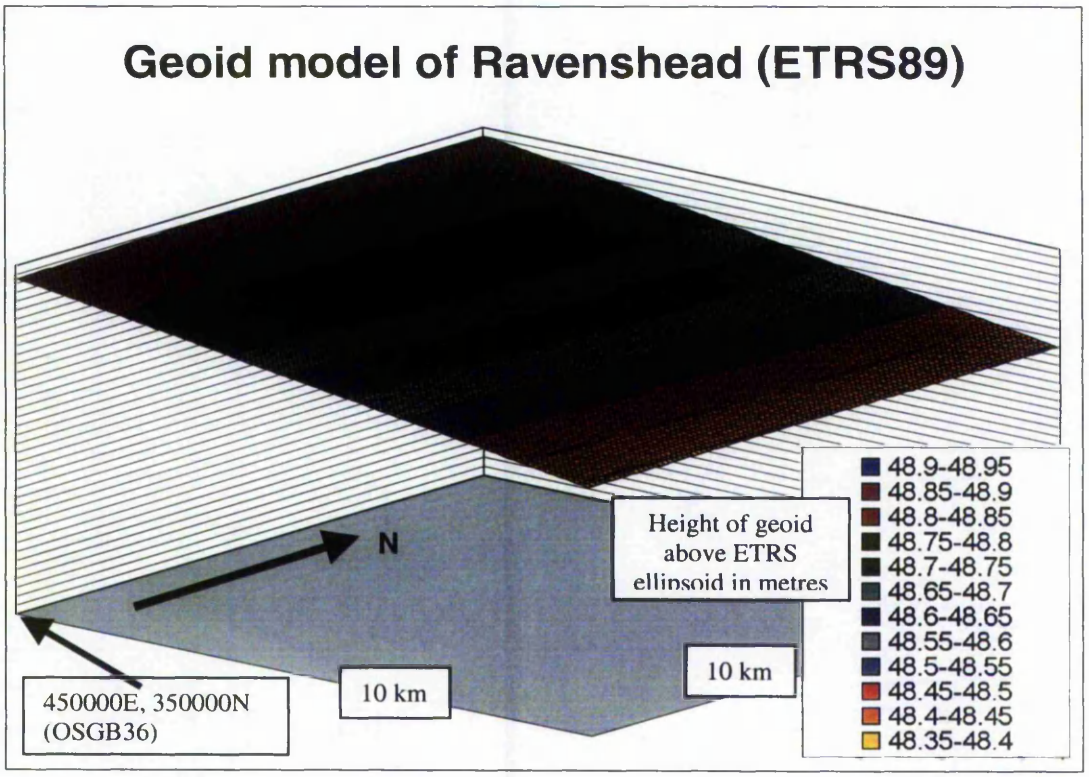

Figure 2.5 A geoid model for Ravenshead

2.13 Data Compression

Barthelmes & Dietrich (1991) describe the use of point masses for the approximation of a gravity field. This is a form of data compression where 3568 Bouguer anomalies are represented by 200 "buried masses". The quality of the gravity model reduces from an RMS of ±2 mGal to ±2.6 mGal. The compression is of 3568, 3D points (2D position plus Bouguer value), to 200, 4D points (3D position plus mass size), and so represents a data compression ratio of 1:13.4 with quality loss ratio of 1:1.7 (≈ 1:2.62/2.2). The overall gain is therefore 1:7.9.

2.14 Astrogeodetic data capture

Rowe et al (1985) describe a star sensor developed by the US Defense Mapping Agency and Ball Aerospace Systems in 1984 that uses a temperature controlled, 256 x 256 pixel, charge injection device (CID). A substantial amount of observational

data is required because each pixel has a 7".7 field of view. Observing time is 2 to 3 hours and position solutions for φ and λ of $\pm$0".15 and $\pm$0".15secφ are claimed.

Bürki and Marti (Bürki and Marti 1991) report on Swiss geoid models, including an astrogeodetic one. The astronomy was observed with a "Hannover-type" zenith camera. Verticality was controlled with 2 Talyvel III levels; there is no statement of the quality of the astronomic positions.

Eissfeller & Hein (1994) report another study of the potential use of a charge-coupled device (CCD) camera system. The theoretical study considers the use of a 2048 pixel square chip mounted in a zenithal Cassegrain reflecting telescope with a focal length of 1.5 m and a 0.14 m aperture. As with all CCD approaches, there is a problem of relating the azimuth and altitude of the principal axis of the telescope to the azimuth and altitude corresponding to an individual pixel. Their system appears to need a cooling system to ensure electronic stability of the sensor chip. In spite of the size and complexity of the technology, for portable field use their expected accuracy is still no more than $\pm$ 0".3 in position, a result achievable by manual means.

Buerki (1998) in a private communication describes work over a 15-year period leading towards an automated position line capture system using a transportable zenith camera system. He believes that the resulting accuracy of the geoid over the Alps is within 1 to 3 cm for most of Switzerland. He asserts that the results clearly indicate that deflections of the vertical are very well suited to determination of the geoid in mountainous regions. In the Geodesy and Geodynamics Laboratory at the Institute of Geodesy and Photogrammetry in the Swiss Federal Institute of Technology, they operate a zenith camera and electronic theodolites with a software package that enables on-line observation and computation of position. The hardware includes a time digitising unit, 1 pps input from a time signal or GPS-receiver, providing epochs defined by a manual stop switch with a resolution of a few milliseconds and a "steering Notebook-PC". The software uses precise computations of apparent places of stars in the FK5. The estimation of position does not appear to use least squares but the method is claimed to produce results within one hour, although the precision is not stated.

Wei (1999) describes the adjustment of an astrogeodetic and GPS network of China that includes 48519 astrogeodetic points. This indicates that there is an extraordinary amount of astronomical data in existence in China. Whether that is just from Laplace stations, or whether there is a similar amount of positional data, is

unknown but, if there is, then it could be used for the computation of a Chinese astrogeodetic geoid.

Hui et al (1999) describe how an earthquake affected the local plumbline in Yunnan, China in 1995.

2.15 Data quality comparison

Comparing the utility of gravity and astronomic data is not a simple task. The quality of a geoid derived from a single data type will depend upon:

- Quality of the observations.
- Available observation density or cost of new data capture.
- Reduction of the observations.
- Theoretical assumptions in the use of the reduced observations to create the geoid.

2.14.1 Quality of the observations

Gravity and astronomy use measurements of the magnitude and direction of the gravity vector respectively. The full range of possible gravity measurements at sea level is approximately 5000 mGals. A semi-circle above the horizon is 64800". If the two can be compared, then 1 ppm of the full observational range is both 5 μGals and 0".65. Current instrumentation is of the order of both precisions, though single observations in the field are unlikely to be this good.

2.14.2 Available observation density or cost of new data capture

There is currently much more gravity data available than astronomical data. New gravity data is observed in traverses and several points per operator may be observed in a day. The previous limitation on astronomical data capture has been the observing time required at a point, which has been of the order of several hours. With an electronic theodolite and the method described in Chapter 6 of this thesis the point data capture time could approach that of gravity.

As a questioner at the IUGG99 conference at Birmingham in July 1999 noted, deflections of the vertical are sensitive to local gravity variations but these can

be filtered by terrain modelling to reduce the sensitive astronomic determinations to smoothed gravity based determinations. Gerstbach (1999) supports the view that fewer plumb line deflections than gravity observations are required to compute a geoid of equal precision. He quotes the need for astronomical points every 5-10 km or gravity observations every 1-3 km to obtain a 1-cm geoid in Austria. He does not state the basis for these figures. If correct, they imply that over a given area between 11 and 25 times more gravity than astronomical observations are required. The time taken to collect data consists of travel time to and from site and observation time on site. This indicates that even with longer on-site data collection time, astronomy could be significantly more economical.

2.14.3 Reduction of the observations

Correction of gravity observations requires position for earth tide corrections, correction for drift, and a one-dimensional network adjustment for best internal fit. Reduction of gravity observations to gravity anomalies requires precise knowledge or observations of height. The approximate reduction of 0.3086 mGal/m means that a height uncertainty of ±0.01 m leads to a further ±3 μGal uncertainty. For large or national networks, this can be very demanding. The factor 0.3086 mGal/m depends upon the assumed value of density of the underlying masses being known to the same precision as the height. Height data will be required for the calculation of the terrain model used for the orological correction.

Correction of astronomical observations requires knowledge of earth rotation parameters for polar motion and approximate height for the downward continuation of the vertical for the correction for latitude. A DTM of the surrounding area will be required for a topographic-isostatic reduction where there is significant altitude variation in the surrounding area. Systematic errors in the star almanac can lead to systematic errors in astronomical position. A zenith instrument observes a limited range of stars for which the declinations are approximately the same as the latitude of the point under investigation. An instrument/system that observes stars away from the zenith will be less vulnerable to star almanac systematic errors but must properly account for the effects of zenith distance related refraction. Both systems will be vulnerable to the small amounts of systematic refraction that may exist in the zenith at the time of the observations, especially if the observations are taken over a short period.

2.14.4 Theoretical assumptions in the use of the reduced observations to create the geoid

Stokes' and Molodensky's Formulae are integrals and are replaced in practical work by summations over meaned blocks of gravity anomalies. As free air anomalies are correlated with height, then a representative anomaly at the mean block height must be found. Block sizes must be small near the computation point or there will smoothing of the computed geoid. If any theoretically worldwide data is missing, there will be errors in the computed geoid especially in points near the missing data. These effects are reduced, but not eliminated, by using geopotential models and "remove and restore" techniques such as were used in the construction of many of the geoid models reported in Rapp and Sansò (1991) and Vermeer and Ádám (1998).

Astronomical deviations give the slope of the geoid, not the geoid height itself. The geoid must either be modelled as a series expansion or by conventional astrogeodetic levelling carried out to determine the geoid height at points other than at the origin of the network.

Astronomy gives a much more direct measure of the geoid than gravity. For a relative geoid over a moderately flat and limited area of interest, for example the UK, an astrogeodetic geoid will be much easier to determine than a gravimetric one.

2.15 Plumb Line Variations

It is generally believed that there are significant and detectable non-tidal variations in the plumb line. Barlik et al (1999) report that non-tidal variations of up to 0".1 have been detected by astrometric and gravimetric means at sites in Poland and China. In one Chinese case, the variation has been associated with an earthquake where variations of up 0".1 were detected before the event. This suggests that the detection of non-tidal plumb line variations might be used as a tool for earthquake prediction. In such a case, the non-tidal variation in the plumb line could be because there has been some form of change in the earth, as suggested by Barlik et al (1999). In that case, the astrometric and gravimetric results should agree. If however the surface has moved without significant changes below the surface, then astrometry would show a difference before and after the event but gravimetry would not. In the Chinese case mentioned above, there was significant, but not complete, correlation.

2.17 The Problem with Astronomy

Astrogeodetic levelling has been used in the past for the geodetic control of national mapping. It is little used today because the astronomy part is labour intensive. The collection of papers edited by Rapp and Sanso (1991) which, although entitled "Determination of the Geoid Present and Future", is concerned only with gravity and GPS, and makes no mention at all of astrogeodetic techniques. The author of this thesis notes that the problems associated with practical astrogeodetic levelling are many. For example, with a Wild T2000 theodolite and tripod, short wave radio, stop watch, thermometer and barometer and an appropriate almanac such as the Star Almanac for Land Surveyors (SALS), (HMSO 1995), or Apparent Places of Fundamental Stars (APFS), Astronomisches Rechen-Institute (1995) and a calculator, a solution with a standard error of 3" of latitude and the equivalent in longitude (100 m) can be found. The method is very slow: it may involve two full nights' observations with a party of two per station. The author notes from his experience of astronomy that it has the following drawbacks:

- There is a danger of accidentally stopping the stopwatch by pressing the wrong button in the dark.
- Nights are cold and antisocial when standing still in the same place all night.
- The stopwatch must be calibrated against a time signal such as RWM Moscow.
- Each observer will have a different personal equation, i.e. un-calibrated individual reaction time between observing the star and pressing the stopwatch.
- The precision of operating the stopwatch is limited to about 0.2 - 0.4 seconds.
- The time taken to find suitable stars is long.
- Stars must be balanced in azimuth and altitude.
- There is no guarantee that the star seen will be in the SALS or APFS.
- Computations for one night's observations will take one day (***if*** they work out!)
- Final solution is a graphical one, so expert interpretation is required to identify the correct solution. There is no statistical determination of the quality of the solution and therefore it is difficult to estimate the precision of the computed position.

In summary, there may be two nights of observations and one day of computations per station, leading to a position solution of ±3" (Robbins, 1976). Therefore, with so much effort for so little result, there is now little use for the process. Time was not a significant consideration before computers were readily available because other surveying and geodetic operations also took significant amounts of time.

The solution to the problem is to automate the data capture and the data processing.

Recent preliminary work in this area has been completed in the form of several BEng (Hons) Engineering Surveying final year projects at Nottingham Trent University, based upon ideas by, and under the supervision of, the author. The students' understanding and the time available have limited the projects. The approach by Brookes (1994) and Greenfield (1994) was to make observations without preparation, discover which stars had been observed and use a simplified least squares solution, that is by observation equations, to find position. This represented a first attempt at Nottingham Trent to bring positional astronomy into the computer age. Davidson (1995) and Hayward (1995) took the project a little further in that they collected observations at several sites and, with a revised version of Brooks and Greenfield's suite of spreadsheets, made some (now shown to be erroneous) determinations of the deviation of the vertical. However, they managed to improve productivity to 3 hours of observations and 2 hours of computation per station. The solution would still only have been good, theoretically, to ±3" if the errors in the suite of spreadsheets had been corrected.

In the summer of 1995, the author conducted feasibility trials with a Wild T2000 electronic theodolite and his own Hi8 video camera for recording the image of a moving star against the theodolite graticule. The RWM Moscow radio time signal was recorded on the sound track with voice recording of the theodolite readings. RWM Moscow was used because it codes the difference between earth rotation time and Universal Time (DUT1) to 0.02s.

Internal camera time code was recorded on the picture. The time was correct to 1 video frame, that is 0.04 of a second. There was no "personal equation", that is systematic human bias in timing, because the observer was not recording the time. A spreadsheet with limited data was used to predict star positions and therefore there was no requirement to search for stars. The achieved data capture rate was five minutes per star with a single observer. Most of the five minutes was taken up with manually lining-up the camera with the theodolite telescope since both instruments were on different tripods. It is probable that this data rate could be improved to four

minutes per star with an assistant, and therefore 80 minutes per station for 20 stars should be achievable.

2.18 The "Position Lines" Method

"Position Lines" is an astronomical method for simultaneously determining latitude and longitude. The method is documented in published literature such as Robbins (1976) and in Breach (1997) from which the early sections of Chapter 4 have been adapted. Other astronomical methods for determining latitude require knowledge of longitude and, likewise, other methods for determining astronomical longitude require knowledge of latitude. There is also the requirement, that stars must be well balanced to mitigate against imperfect knowledge of latitude or longitude, as appropriate. The observations for position lines are those of precise altitude, time and an approximate azimuth to the star if the computation is to include a graphical plot. Approximate values of latitude and longitude are also required, as provisional values. Observations are usually made to balanced pairs of stars at opposite azimuths and at altitudes normally greater than 35°.

Correct star co-ordinates are required for the time of observation. The positions of stars are published in various astronomical catalogues each at a specific epoch, usually "J2000". J2000 is defined as the 12 hours (midday) on 1 January 2000 in Barycentric Dynamical Time (TDB) (Seidelmann, 1992). The star's positions are required at the time of observation.

For an observing programme to be efficient, stars need to be selected so that they are balanced to minimise the effect of errors in the computed value of the refraction coefficient, collimation, latitude and longitude. See Robbins (1976).

Some small corrections need to be made to compute astronomical position. Two need further development for this thesis. One relates to the gravitational attraction of the moon as the earth and moon orbit around their own barycentre. The other relates to the determination of the topographic-isostatic effect. Although theory and formulae have been developed for this effect, the formulae are cumbersome in the extreme and a more "user-friendly" approach is required.

By 1996, astronomy as a data source was in significant decline (Segawa et al, 1997) and most efforts for geoid determination were based on world geopotential models, gravity, altimetry and GPS with levelling. One exception was in Austria, (Heiland et al, 1998) where the topography limited the availability of gravity data.

For geoid models of centimetre or less accuracy, both high-resolution terrain models (Kühtreiber, 1997) and a detailed knowledge of subsurface density (Colic et al, 1998 and Featherstone, 2000) are required.

Although centimetre level geoid models are now becoming available we appear to be some way from millimetre level geoid models. If relative geoid models are to be used in conjunction with relative heights from GPS to find relative orthometric height, then it is desirable that the errors in the geoid models do not add significantly to the overall error budget. If relative heighting from GPS or its successors improves beyond current levels then a near millimetre relative geoid will become an urgent goal of geodesy. The rest of this thesis suggests one possible way forward.

2.19 Summary

In this chapter on geoid determination, the available methods of Space based systems, GPS and levelling, gravity and astronomy were compared. Historical progress in the determination of the geoid was reviewed and it was noted that astronomy had largely gone out of fashion because of the difficulty of original data capture. However if local high precision models are required then astronomy, using a method such as that described in Chapter 6, may be the best answer. Astrogeodetic data capture techniques were reviewed and an attempt to compare the differing quality of different data types was made. In the next chapter, the methodology of such an approach is detailed.

Chapter 3

Methodology

3.1 Introduction

In the previous chapter the "Position Lines" method for the determination of astronomical position and progress in the determination of the geoid were briefly described. The overall methodology of this thesis is to develop appropriate theory relating to various aspects of the determination of astronomical position, to develop practical procedures to enable the determination of astronomical position and to investigate methods for using astronomical position to create an astrogeodetic geoid model.

3.2 Theory of various aspects of the determination of astronomical position

The theory relating to the determination of position by the technique of "Position Lines" needs to be developed. The classical graphical approach is to be reviewed and least squares based solutions considered. The least squares solutions may include: refraction effects and their rates of change; theodolite vertical collimation and its rate of change also latitude and longitude as unknowns to be solved for. Equations are derived.

Investigations of the direction of balance based on error in computed refraction coefficient and on error in computed collimation are required.

The nature, effect and evaluation of non-random errors in time are to be considered. An equation for the effect on the observed vertical angle of an error in horizontal pointing must be found. Observing and computing strategies are to be considered including; consideration of the observing parameters of star elevation and azimuth limits; start time of observations; the number of stars to be observed; the overall balance of stars in azimuth and altitude and the number of observations per star against number of stars. A simple formula to model refraction will be required.

The earth and moon orbit around their own barycentre. The barycentre is within the earth. Because of this orbit, there is a centrifugal effect that varies with time and

place. It is anticipated that it will have a variable effect upon the local direction of the vertical.

The effect of the moon's gravitational attraction, and the effect of centrifugal acceleration of the observation point around the barycentric rotation axis, upon the deviation of the vertical need to be evaluated. To achieve this the relationship between the Geocentric, Orbital and Topocentric Co-ordinate systems must be established.

The variations of Lunar Right Ascension and Declination must be reviewed so that lunar co-ordinates may be used to determine the magnitude and direction of the lunar deviation of the vertical.

Variations in the Earth's mass distribution will have an effect upon the direction of the local vertical. If observations could be made at the geoid then deviation of the vertical measured at the geoid would truly represent the slope of the geoid. However observations are made on the surface and must be reduced to the geoid by the application of a correction for curvature of the plumb line in the meridian (Robbins, 1976) and for the topographic-isostatic effect (Nagy, 1966). In the latter case it is necessary to compute the difference between the sideways attraction at the point of observation on the ground and at the point of computation at the geoid. For a fully rigorous correction to be applied then variations in the density of the topography must also be taken into account. Since the topographic-isostatic effect can be of the order of several arc seconds in mountainous terrain then variations in overall density with direction may also be significant. Since the practical approach to computing the topographic-isostatic effect involves dividing the terrain into blocks and computing the sideways force then it will be necessary to find the mean density for each block by other means. Such data may not always be available.

Earth tides, due to the attraction of the sun and moon will have a small effect upon measured astronomical position. Vanicek and Krakiwsky (Vanicek, Krakiwsky 1982) state that the effect is less than 0".05, and is therefore negligible.

Ocean loading might also have a small effect in some places. It is understood that the West of Cornwall rises and falls by about 5cm with the tide. If the West Country may be considered as hinged about a meridian through Bristol then the 2½cm variation from the mid tide value over the distance from Bristol to Land's End, 220km gives a maximum discrepancy of 0".024 and therefore probably negligible.

3.3 Practical procedures to enable the determination of astronomical position

The productivity associated with a number of possible observing strategies is to be investigated. Methods of automating the observing process need to be examined and a practical process developed. Applicable methods worthy of investigation include using a photodiode for precise timing of star observations, detection of star passage over the theodolite crosshair and the determination of time of star passage over the theodolite crosshair.

Alternatively a method using a video camera may be appropriate and this will require consideration of issues relating to precise linkage of time to a video frame, the determination of the motion of the image of the star, the determination of the theodolite horizontal crosshair in the video image and the determination of the time of star image passing the horizontal crosshair image to be considered.

A practical method for the determination of precise observing time is essential. Time may be obtained from radio time signals or from GPS. With GPS and video recording of the star passage across the crosshairs, the problem to be solved is that of linking the video frames to the GPS time signal.

Updated values of star co-ordinates must be found before an observing programme or computations to find position can be made. The process necessary is to create a suitable catalogue of star data at a reference date, J2000, and to compute updated values of the co-ordinates at the epoch of interest. J2000 is the reference date for all modern catalogues.

Observing and computing processes need to be examined in some detail to find a method that will give a good solution under the specific conditions of observation. Stars must be selected in an observing programme so that they are balanced to minimise the effect of errors in the computed value of the refraction coefficient, collimation, latitude and longitude. The "productivity" of various technology combinations needs to be considered to find a process that delivers economical solutions. Automation of the observing process using a photodiode or a video camera, with or without a video capture board must be considered. Relating time to the observation will be a major issue. Theory, formulae and computational method must be considered for each case.

Astronomical position is observed on the ground surface but the slope of the geoid is computed at the geoid. The reduction of observed astronomical position includes a

component to account for the different attractions of the surrounding topography on the ground surface compared with that at the geoid. The usual method of determining this topographic-isostatic effect on the ***magnitude*** of gravity observations needs to be adapted and developed for the effect on the ***direction*** of gravity observations. If a simpler method that does not require a local terrain model could be developed it would reduce the computational effort required to compute the topographic-isostatic effect.

To demonstrate the application of theory and processes developed, a practical determination of astronomical position, and hence slope of the geoid, will be required.

3.4 From astronomical position to astrogeodetic geoid model

The relationship between the geoid and an ellipsoid was reviewed in Chapter 2. Methods for the determination of the shape of the geoid by GPS with precise levelling, by gravity observations and by astrogeodetic methods were compared. Historical progress in the determination of the geoid is reviewed and suggestions as to the future utility of the astrogeodetic geoid are put forward. Previous methods of astrogeodetic data capture were reviewed and an attempt was made to compare the usefulness of gravity and astronomical data.

In Chapter 9 the classical method for the determination of the Astrogeodetic Geoid is reviewed. The density of observations needed for an astrogeodetic geoid model is considered in terms of Kaula's rule of thumb. An alternative consideration is developed by finding the effect of a hemispherical mountain on the deviation of the vertical and using this to create three test models of simulated topography of "Mountains", "Hills", "Lowlands" and a "Plain". Geoid models are then developed and examined using "Polynomial Coefficients" deduced from observations by least squares. A similar investigation is made using "Interpolation of Deviations". Finally a scheme for the development of a geoid model by "Progressive Nodes" is proposed.

The first stage, now, is to develop "Position Lines" theory to make it applicable for practical applications using least squares methods and this is the subject of the next chapter.

Chapter 4

Position Lines Theory

4.1 Introduction

In the last chapter it was established that practical procedures to enable the determination of astronomical position were required and that the theory relating to the determination of position by the technique of "Position Lines" needed to be developed for application by least squares methods. To achieve this the classical graphical approach will be reviewed and least squares based solutions considered. A least squares solution may include: the refraction effect and its rate of change; theodolite vertical collimation and its rate of change as well as latitude and longitude as unknowns to be solved for. The nature, effect and evaluation of non-random errors in time must also be considered, as must the effect on the observed vertical angle of an error in horizontal pointing.

To optimise the process observing and computing strategies need to be considered including; consideration of the observing parameters of star elevation and azimuth limits; start time of observations; the number of stars to be observed; the overall balance of stars in azimuth and altitude and the number of observations per star against number of stars.

4.2 The Theory of Position Lines

The sub-stellar point of a star (Figure 4.1) is defined as the point where the star is at the observer's zenith. In other words:

$\phi = \delta$ and

LST $= \alpha$

Where ϕ is the latitude of the point

δ is the Declination of the star

LST is Local Sidereal Time

α is the Right Ascension of the star

Therefore, the observer's longitude can be given by the formula:

$$\lambda = LST - GST$$
$$= \alpha - GST$$
$$= \alpha - UT_1 - R \pm 12^h$$

where λ is the longitude of the point

GST is Greenwich Sidereal Time

UT_1 is Universal Time corrected for earth rotation

R is the Right Ascension of the Mean Sun

In all the above, the units must consistently be those of angle or time.

If the observer observes another star, then it will be in the zenith of a sub-stellar point, point B, where:

$$\phi_B = \delta_2 \text{ and}$$
$$\lambda_B = \alpha_2 - UT_1 - R$$

z is the zenith distance to a star, so

$$z = 90° - h$$

where h is the vertical angle to the star.

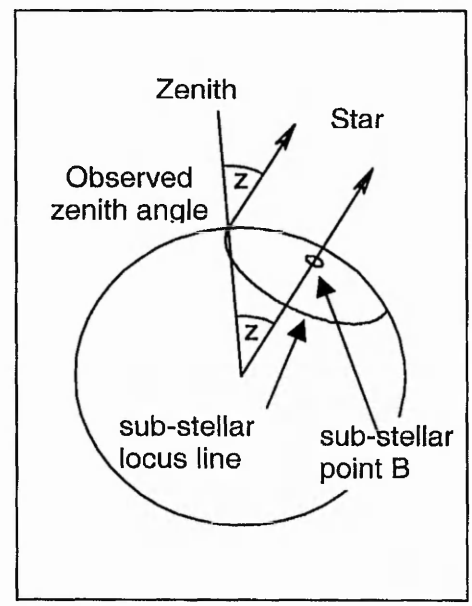

Figure 4.1 The Position Circle.

If an observer observes the star, then the observer's zenith will be on a small circle of the celestial sphere, centred on the star and with an angular radius of z. The observer's position on the earth will be somewhere on the sub-stellar locus line of that small circle (see Figure 4.1). With a second star at a different azimuth, there is a second sub-stellar locus line, crossing the first at the observer's position (see Figure 4.2).

4.2.1 Position line

In the region of the observer, the sub-stellar locus lines will be almost straight, unless z is very small. Each straight line will have a direction at right angles to the azimuth to the star. The observed zenith distance to the second star represents the spherical angular distance from the sub-stellar point of the second star to the observer's position.

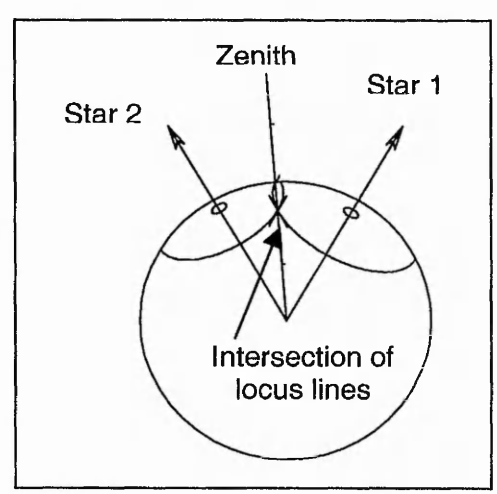

Figure 4.2 Two Position Circles.

If the observer moves towards the sub-stellar point of the second star, the observed zenith distance will decrease. If the observer moves away from the sub-stellar point of the second star, the observed zenith distance will increase.

The observer observes the zenith distance from his or her actual position. The observer can also calculate the zenith distance at any other point to the same star, at the same time. The difference between the observed zenith distance and the computed zenith distance therefore represents the angular distance (at the centre of a spherical earth) of the component of the angular separation between the actual and assumed positions, in the direction of the star.

The position solution may be derived either graphically or by least squares:

4.2.2 Computations

In the graphical method it is necessary to define a provisional value for computation of the observed position in terms of latitude and longitude ϕ_p and λ_p. The hour angle of the star at the provisional position at the observed time is given by:

$$t_p = LST_p - \alpha$$
$$= UT_1 + R + \lambda_p - \alpha$$

The computed altitude from the provisional position is given by:

$$\sin h_p = \sin \phi_p \sin \delta + \cos \phi_p \cos \delta \cos t_p$$

where

For plotting purposes, the azimuth to the star may be taken as the observed azimuth to a sufficient level of precision.

4.2.3 Plotting

The observer must be nearer the star from his provisional position, by an angular amount $(h_o - h_p)$ where h_o is the observed altitude and h_p is the altitude computed from the provisional position (see Figures 4.3 and 4.4, below).

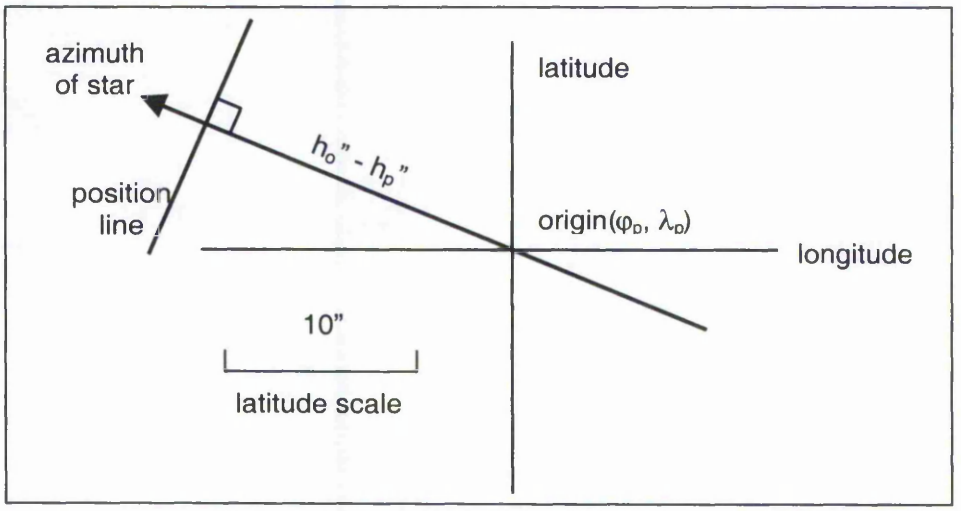

Figure 4.3 Plotting a Position Line.

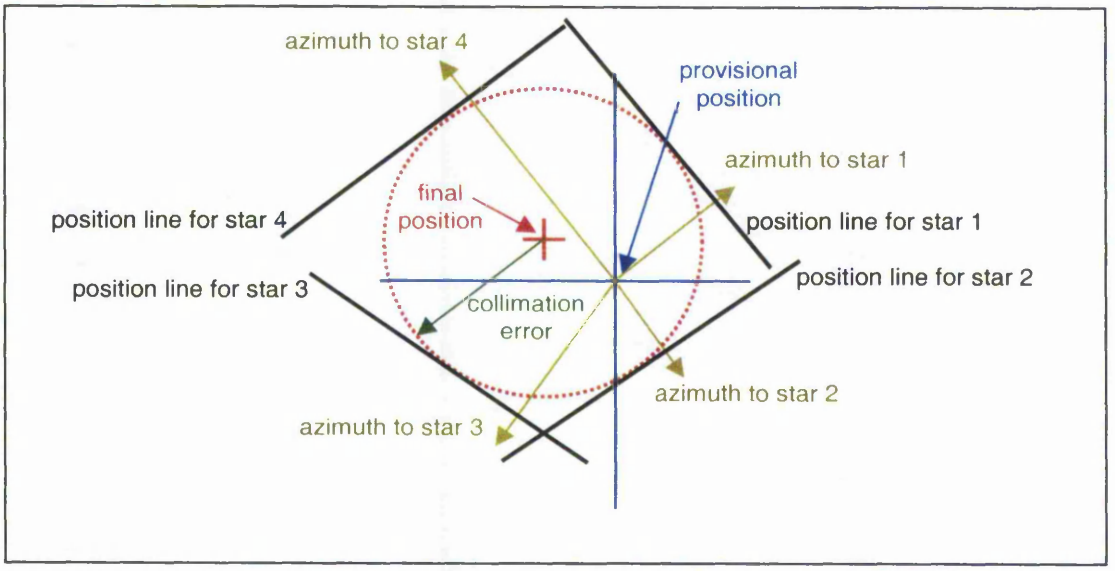

Figure 4.4 Four Position Lines surrounding the final position.

4.2.4 Accuracy

Systematic refraction and collimation errors are eliminated with four balanced stars. A systematic error in timing will give an equal error in longitude, but will give no error in latitude. With the following specification, the precision of computed position should have a standard error in the order of 3″ in latitude and 3″sec ϕ in longitude (Robbins 1976).

4.2.5 Specification

For a conventional solution, 3 sets of 6 stars may be observed. Altitudes should be greater than 40°. A one-second theodolite or better should be used. There should be 6 pointings to each star. The stars in each set should be approximately at azimuths of 45°, 135°, 225°, 315°, 90°, and 270°, each to ±10°. Altitudes should be balanced to ±5°. All observations of one set should be on the same face. The next set should be observed on the other face.

An observing programme is not necessary. In the northern hemisphere the northern star of a balanced pair should be observed first because there will usually be a star in the south, which may easily be found to balance the northern one. Because of the slower apparent movement of stars near the elevated pole, the opposite will not normally be the case.

4.2.6 Observations

The horizontal circle may be set to 0° at north by observations to Polaris. Six timed altitudes may be taken, on one face, to each star. All the readings should be made close to the centre of the horizontal cross-hair. A horizontal circle reading to the star should be made after the last vertical angle has been observed. This is for plotting and misidentification purposes. Temperature and pressure readings should be taken to enable computation of a refraction correction to the observed altitude. One set of observations may be defined as observations to 6 stars with the specification above. For the second set, the face should be changed. The stars should be observed set-by-set and not grouped by azimuth. This will ensure that all the stars of one set are more likely to be subject to the same refraction conditions.

The conventional graphical solution to position lines, described above, is suited to a solution based upon few observations. When many stars are observed, the solution can become confused if there are gross errors in the observations. Figure 4.5, below, shows a solution based on the observation of approximately 45 stars and with no gross errors in the observations. Note how the plot forms a circle around the best estimate of the solution. The circle's radius is approximately the vertical collimation of the instrument plus the average error in the refraction model. In this case, it is about 20", which is 600 m on the ground. The least squares solution described below, with the same data, leads to an error ellipse of semi-major axis of 10 metres. It is unlikely that it would not have been possible to identify a solution by graphical means with such precision. The graphical solution, of a position computed by Position Lines, shown in Figure 4.5, below, has had all information, other than the position lines, removed.

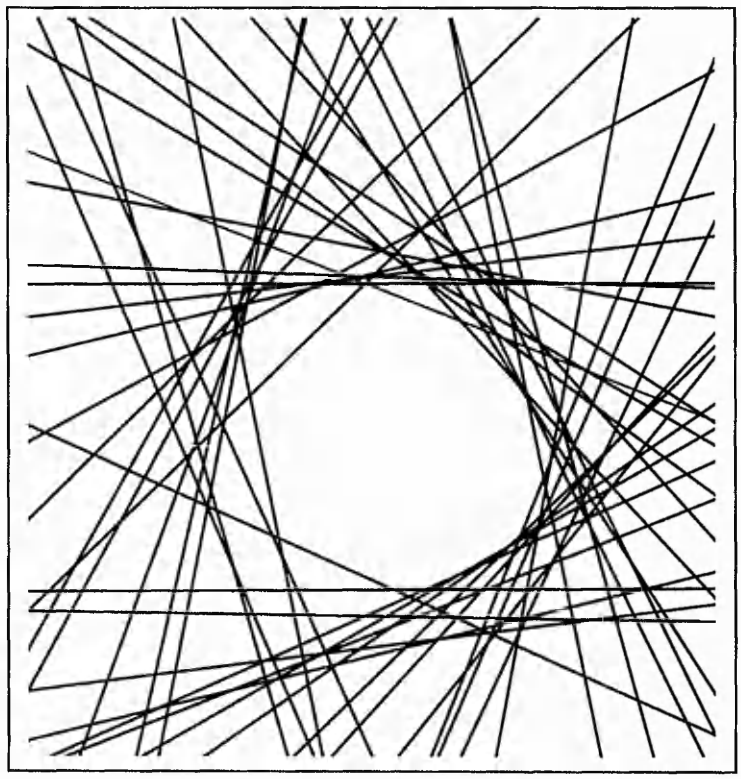

Figure 4.5 Position Line solution based on observations to 45 stars.

4.3 Least squares approach to position lines

By applying the spherical cosine formula to the astronomical triangle and taking account of the formulae in section 4.2 the observation equation may be written as:

$$\sin(h - k \cot h + c) = \sin\phi \sin\delta + \cos\phi \cos\delta \cos(UT_1 + R + \lambda - \alpha)$$

where

k is a refraction constant to be solved for and assumes that the effect of refraction is proportional to cot h

c is the vertical collimation of the instrument

The solution to the generalised least squares problem

$$\mathbf{Ax + Bv = b}$$

is

$$\mathbf{x} = \mathbf{(A^T(BW^{-1}B^T)^{-1}A)^{-1}A^T(BW^{-1}B^T)^{-1}b}$$

and

$$\sigma_{(x)} = \mathbf{(A^T(BW^{-1}B^T)^{-1}A)^{-1}}$$

In this problem:

$$\mathbf{x} = \begin{bmatrix} \delta k \\ \delta c \\ \delta \phi \\ \delta \lambda \end{bmatrix}$$

and the units of all angular quantities are most easily expressed as radians. The equation at the beginning of this section may be rearranged as:

$$f = \sin(h - k \cot h + c) - [\sin\phi \sin\delta + \cos\phi \cos\delta \cos(U + R + \lambda - \alpha)]$$
$$= 0$$

Note the change of notation where U is the observed value of time UT_1.

$$\mathbf{A} = \begin{bmatrix} \frac{\partial f_1}{\partial k} & \frac{\partial f_1}{\partial c} & \frac{\partial f_1}{\partial \phi} & \frac{\partial f_1}{\partial \lambda} \\ \frac{\partial f_2}{\partial k} & \frac{\partial f_2}{\partial c} & \frac{\partial f_2}{\partial \phi} & \frac{\partial f_2}{\partial \lambda} \\ .. & .. & .. & .. \end{bmatrix}$$

The observations are those of vertical angle and of time, so:

$$\mathbf{B} = \begin{bmatrix} \frac{\partial f_1}{\partial h} & 0 & 0 & .. & \frac{\partial f_1}{\partial U} & 0 & 0 & .. \\ 0 & \frac{\partial f_2}{\partial h} & 0 & .. & 0 & \frac{\partial f_2}{\partial U} & 0 & .. \\ .. & .. & .. & .. & .. & .. & .. & .. \end{bmatrix}$$

which may be partitioned into two diagonal matrices:

$$\mathbf{B} = \begin{bmatrix} \mathbf{B_1} & \mathbf{B_2} \end{bmatrix}$$

The weight matrix may be divided as follows:

$$\mathbf{W} = \begin{bmatrix} \mathbf{W_1} & \mathbf{0} \\ \mathbf{0} & \mathbf{W_2} \end{bmatrix}$$

where $\mathbf{W_1}$ refers to the observations of vertical angle (h) and

$\mathbf{W_2}$ refers to the observations of time (U)

Provided that all the observations and the corrected model are uncorrelated with each other then $\mathbf{W_1}$ and $\mathbf{W_2}$ will both be diagonal matrices.

$$\mathbf{b} = \sin(h_o - k_p \cot h_o + c_p) - [\sin\phi_p \sin\delta + \cos\phi_p \cos\delta \cos(U + R + \lambda_p - \alpha)]$$

The partial differentials are:

$$\frac{\partial f}{\partial h} = + \cos(h - k \cot h + c)\left(1 + \frac{k}{\sin^2 h}\right)$$

$$\frac{\partial f}{\partial U} = + \cos\phi \cos\delta \sin(U + R + \lambda - \alpha)$$

$$\frac{\partial f}{\partial k} = - \cot h \cos(h - k \cot h + c)$$

$$\frac{\partial f}{\partial c} = + \cos(h - k \cot h + c)$$

$$\frac{\partial f}{\partial \phi} = - \cos\phi \sin\delta + \sin\phi \cos\delta \cos(U + R + \lambda - \alpha)$$

$$\frac{\partial f}{\partial \lambda} = + \cos\phi \cos\delta \sin(U + R + \lambda - \alpha)$$

$\mathbf{B_1}$, $\mathbf{B_2}$ and $\mathbf{W}$ are diagonal matrices.

$$\mathbf{BW^{-1}B^T} = \begin{bmatrix} \mathbf{B_1} & \mathbf{B_2} \end{bmatrix} \begin{bmatrix} \mathbf{W_1^{-1}} & \mathbf{0} \\ \mathbf{0} & \mathbf{W_2^{-1}} \end{bmatrix} \begin{bmatrix} \mathbf{B_1} \\ \mathbf{B_2} \end{bmatrix}$$

$$\mathbf{BW^{-1}B^T} = \begin{bmatrix} \mathbf{B_1W_1^{-1}B_1 + B_2W_2^{-1}B_2} \end{bmatrix}$$

and so the i*th* element on the leading diagonal of $(\mathbf{BW^{-1}B^T})^{-1}$ is:

$$(B_{1ii}^2\, 206265^{-2}\, \sigma_h^2 + B_{2ii}^2\, 13751^{-2}\, \sigma_U^2)^{-1}$$

where σ_h is in seconds of arc and

σ_U is in seconds of time

and all the non-diagonal elements are 0.

The only matrix inversion is now that of $\mathbf{(A^T(BW^{-1}B^T)^{-1}A)}$ which has 4 rows and columns. Provisional values of ϕ and λ should be as good as possible (and will be in radians, given the units above). The provisional values of c and k may be taken as 0° and 0°.016

respectively. Note that in the computation of the error ellipse of the computed position, the scales of ϕ and λ are not the same. It would first be best to convert the units of σ_ϕ^2, σ_λ^2 and $\sigma_{\phi\lambda}$ all to metres before computing the error ellipse.

If observations are taken over a protracted period there is likely to be a change in meteorological conditions. A change of temperature may affect the theodolite vertical compensation mechanism. The change of refraction conditions may also affect the value of k in the observation equation. To accommodate linear changes of these parameters with time, and so avoid taking meteorological observations, the observation equation could be modified to:

$$\sin(h - (k + t\,p)\cot h + c + t\,q) = \sin\phi \sin\delta + \cos\phi \cos\delta \cos(UT_1 + R + \lambda - \alpha)$$

where p and q are coefficients and t is the time from the first observation. c and k therefore are now the refraction and collimation values at the first observation. There are now two further parameters to solve for and the **x** vector becomes:

$$\mathbf{x} = \begin{bmatrix} \delta k \\ \delta c \\ \delta p \\ \delta q \\ \delta\phi \\ \delta\lambda \end{bmatrix}$$

$$f = \sin(h - (k + t\,p)\cot h + c + t\,q) - [\sin\phi \sin\delta + \cos\phi \cos\delta \cos(U + R + \lambda - \alpha)] = 0$$

The **A** matrix becomes:

$$\mathbf{A} = \begin{bmatrix} \frac{\partial f_1}{\partial k} & \frac{\partial f_1}{\partial c} & \frac{\partial f_1}{\partial p} & \frac{\partial f_1}{\partial q} & \frac{\partial f_1}{\partial \phi} & \frac{\partial f_1}{\partial \lambda} \\ \frac{\partial f_2}{\partial k} & \frac{\partial f_2}{\partial c} & \frac{\partial f_2}{\partial p} & \frac{\partial f_2}{\partial q} & \frac{\partial f_2}{\partial \phi} & \frac{\partial f_2}{\partial \lambda} \\ .. & .. & .. & .. & .. & .. \end{bmatrix}$$

The $\mathbf{B_2}$ sub-matrix and **W** matrix are unchanged. The **b** vector becomes:

$$\mathbf{b} = \sin(h_o - (k_p + t\,p_p)\cot h_o + c_p + t\,q_p) - [\sin\phi_p \sin\delta + \cos\phi_p \cos\delta \cos(U + R + \lambda_p - \alpha)]$$

The partial differentials are:

$$\frac{\partial f}{\partial h} = + \cos(h - (k + t\,p)\cot h + c + t\,q)\,(1 + \frac{(k + t\,p)}{\sin^2 h})$$

$$\frac{\partial f}{\partial U} = + \cos\phi \cos\delta \sin(U + R + \lambda - \alpha)$$

$$\frac{\partial f}{\partial k} = - \cot h \cos(h - (k + t\,p)\cot h + c + t\,q)$$

$$\frac{\partial f}{\partial c} = + \cos(h - (k + t\,p)\cot h + c + t\,q)$$

$$\frac{\partial f}{\partial p} = - t \cot h \cos(h - (k + t\,p)\cot h + c + t\,q)$$

$$\frac{\partial f}{\partial q} = + t \cos(h - (k + t\,p)\cot h + c + t\,q)$$

$$\frac{\partial f}{\partial \phi} = - \cos\phi \sin\delta + \sin\phi \cos\delta \cos(U + R + \lambda - \alpha)$$

$$\frac{\partial f}{\partial \lambda} = + \cos\phi \cos\delta \sin(U + R + \lambda - \alpha)$$

The provisional values of p and q may both be taken as 0°/hour.

The observations are those of time and vertical angle. Observations are imperfect and subject to random and systematic errors. Systematic errors due to error in the time signal and error due to the personal equation will need to be corrected for.

4.4 Non-random errors in time

Non-random errors in time include error in the time signal and errors due to the personal equation.

4.4.1 Error in the time signal

Error in the time signal will have a systematic effect on the determination of astronomic longitude at a site because all time observations will be affected by the same amount. RWM Moscow broadcasts DUT1 to $0^s.02$. On the assumption that this is correct, then UT1 can be determined to not worse than $0^s.01$, and the average error is therefore $0^s.005$. The longitude equivalent to this is 0".075, or at UK latitudes, 1.5 m. Alternatively, DUT1 can be found on the Internet in the International Earth Rotation Service's Bulletins at IERS (1998).

4.4.2 Errors due to the personal equation

The personal equation relates to the systematic error in all time observations and at all sites for an individual observer. It is caused by human interaction with the timing process. In conventional observations, the stopwatch is calibrated against a radio time signal, but real observations are of time as the stars cross the theodolite horizontal cross hair. The personal equation is therefore the difference in reaction time to the auditory stimulus of a radio time signal compared with that of the visual stimulus of a star crossing a theodolite crosshair. Such a relationship is hard to determine with any degree of certainty although experiments have been devised.

One such experiment undertaken by this author was to compare the calibration of a stopwatch using time from RWM Moscow with a calibration using time from the display of a Leica System 200 GPS receiver. If the DUT1 and dUT1 corrections are not applied to the RWM Moscow signal then both signals should give UTC. RWM broadcasts from 10 to 20 minutes past each hour and from 10 to 20 minutes to each hour. To avoid any possibility of stopwatch drift corrupting the results, the following observations were taken:

Table 4.1 Radio and GPS observations for stopwatch calibration.

Calibration with	Date 26/4/96 Period	Number of observations
RWM Moscow	$13^h\ 40^m$ - $13^h\ 50^m$	54
GPS	$13^h\ 50^m$ - $14^h\ 10^m$	108
RWM Moscow	$14^h\ 10^m$ - $14^h\ 20^m$	55

Ignoring the minutes and integer seconds, which were the same, the results were:

Table 4.2 The difference between Radio and GPS stopwatch calibrations.

	RWM Moscow	GPS	Difference
mean	$0^s.2308$	$0^s.4784$	
difference of the means			**$0^s.2476$**
standard error of the sample	$0^s.0375$	$0^s.0542$	
standard error of the mean	$0^s.0035$	$0^s.0051$	
standard error of the difference of the means			**$0^s.0062$**

There is a difference of $0^s.25$. Part of this could be explained as the difference in personal equations relating to auditory and visual stimuli but it seems excessive. From a conversation with the manufacturer's representative it is now understood that the difference is a function of the GPS processing time, which in turn is a function of the number of satellites, and will therefore vary with time. If the experiment were to be repeated using the "GPS flasher", described below, then it is likely that the results from GPS and the RWM Moscow would be more compatible.

The solution to the personal equation problem depends upon the method by which time is observed. The best solution is one where the observations do not depend upon human reaction or interpretation, that is, both time signal and star passage across the cross hair are recorded in the same medium, such as on the same videotape. Where human interaction with the observations cannot be avoided then systematic error will occur. There are several possible solutions to the evaluation of a personal equation.

4.4.2.1 Evaluation of the systematic error in the east-west component of the deviation of the vertical by astronomical and GPS observations.

Error in the computation of east-west deviation of the vertical relates to error in astronomical longitude which in turn relates to error in time. The east-west deviation of the vertical may be found from consideration of the Laplace equation:

$$A_G = A_A - (\lambda_A - \lambda_G)\sin\varphi$$

where

A_G and A_A are geodetic and astronomical azimuth respectively

λ_A and λ_G are geodetic and astronomical longitude respectively

Which, when rearranged, becomes:

$$\lambda_A = (A_A - A_G)/\sin\varphi + \lambda_G$$

If the astronomical azimuth, A_A, is found by the "azimuth by altitude" method then there are no observations of time and therefore there is no personal equation. The geodetic quantities, azimuth and longitude, are found by GPS.

The relationship between the uncertainties of the above parameters is:

$$\sigma^2_{\lambda A} = \frac{\partial f}{\partial A_A}^2\sigma^2_{AA} + \frac{\partial f}{\partial A_G}^2\sigma^2_{AG} + \frac{\partial f}{\partial \lambda_G}^2\sigma^2_{\lambda G}$$

$$= (\sin\varphi)^{-2}\sigma^2_{AA} + (\sin\varphi)^{-2}\sigma^2_{AG} + \sigma^2_{\lambda G}$$

If λ_G is found by GPS the uncertainty will be negligibly small. A_G is found from GPS and, with a relative GPS positional uncertainty of 0.005m and 1ppm of baseline length, the geodetic azimuth's uncertainty will be approximately:

$(0.005\text{m} \pm d10^{-6})/d$ radians

where d is the length of the line in metres.

The uncertainty of A_A will depend upon the number of observations that are taken to determine it. If the latitude is 53°, as it is in Nottingham, and A_A and A_G are each to make an equal contribution to $\sigma_{\lambda A}$, which is to be 0".5 say, then σ_{AA} and σ_{AG} must each be 0".28. This implies that the length of the GPS base line will be 14 km.

Although sufficient azimuth by altitude observations could be taken to meet a similar criterion for the astronomic azimuth, there is always the real danger of systematic horizontal refraction putting significant systematic error back into the final determination of the personal equation.

The personal equation will be the difference between the λ_A found from the position lines solution and the λ_A found from above. If both are found with uncertainty of 0".5 then the personal equation still has an uncertainty of $0^s.05$ and this is considerably greater than the uncertainty of the time signal from RWM Moscow.

4.4.2.2 Evaluation of the systematic error in the east-west component of the deviation of the vertical by precise levelling and GPS observations.

If the personal equation is ignored then a geoid model formed by astrogeodetic levelling will have a systematic east-west slope with a gradient equal to the personal equation. If

points on the east and west sides of the area, for which an astrogeodetic geoid with systematic east-west slope has been determined, are connected by GPS heighting and also by precise levelling then, in principle, the systematic slope error of the geoid can be found. If the east-west distance is 20 km and if a GPS reference station is set up at the centre of the area of interest and roving receivers are at the east and west extremities of the area, then from consideration of propagation of error formulae, the ellipsoidal height difference may be found with a precision of:

$$\sqrt{2}\,(0.01\text{m} \pm 10^{-6}\,10000\text{m}) \quad = \quad 0.02\text{ m.}$$

Likewise, 20 km of double-run precise levelling may give an orthometric height difference of:

$$\sigma_h \quad = \quad 0.002\sqrt{20}\text{ m}$$
$$= \quad 0.009\text{ m}$$

These statistics combine to give an uncertainty of a difference in the geoid model of 0.022 m. Over the 20 km east-west distance across the area, this is equivalent to an uncertainty of 0".23 in the slope of the astrogeodetic geoid model.

4.4.2.3 Evaluation of personal equation by misclosure of an astrogeodetic levelling loop.

Imagine an astrogeodetic levelling loop that started at a point on the equator and continued eastwards until the loop closed back at the start point, i.e. the loop went around the earth at the equator. Then in the absence of error, there would be no misclosure. If there were an error in the personal equation then the misclosure would be the personal equation times the circumference of the earth. Such a method would produce a precise solution for the personal equation but the experiment is clearly impractical.

An alternative, which reduces the length of the astrogeodetic levelling loop but still involves a full 360° circumnavigation of the globe, would be to make the levelling loop follow a high parallel of latitude, say 89° 50'. Although the route would be on land and only 120 km long, the location would be difficult to get to. At the poles, each star is at a near constant altitude. Therefore, the uncertainty of the times of the vertical angles would be such that the derived east-west deviation of the vertical would be almost meaningless.

A rather more practical approach to the problem would be to examine the misclosure of an astrogeodetic levelling loop at mid-latitudes.

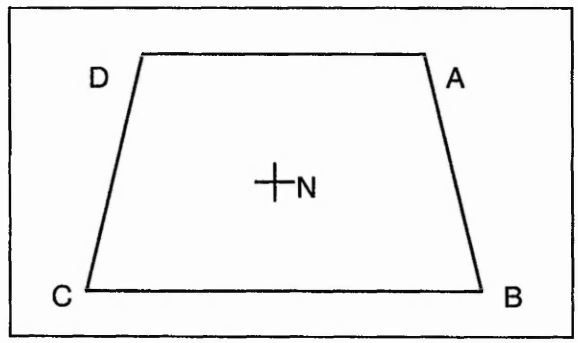

Figure 4.6 An astrogeodetic levelling loop at mid-latitudes.

In Figure 4.6, above, A and D are at the same latitude, and so are C and B. A and B are on the same meridian, and so are C and D. N is at the centre of the figure and has latitude φ_N. The latitudes of A and B are, respectively, $(\varphi_N + \delta\varphi)$ and $(\varphi_N - \delta\varphi)$. The longitude difference between A and D is λ. If R is the radius of the earth, assumed spherical for computational simplicity, with all angular terms in radians, the lengths of the sides of the figure are:

$$AB = 2\,\delta\varphi\,R$$

$$BC = \lambda\cos(\varphi_N - \delta\varphi)\,R$$

$$CD = 2\,\delta\varphi\,R$$

$$DA = \lambda\cos(\varphi_N + \delta\varphi)\,R$$

The distance, L, around the figure is the sum of the lengths of the sides:

$$L = R\,(4\,\delta\varphi + 2\,\lambda\cos\varphi_N\cos\delta\varphi)$$

which can be rearranged as

$$\lambda = (L - 4\,R\,\delta\varphi)(2\,R\cos\varphi_N\cos\delta\varphi)^{-1}$$

The distance difference west and east, over which the personal equation will have effect is:

$$d = BC - DA$$

$$= 2\,\lambda\,R\sin\varphi_N\sin\delta\varphi$$

If the misclosure is solely due to the personal equation, p, then the misclosure will be

$$m = 2\,p\,\lambda\,R\sin\varphi_N\sin\delta\varphi$$

$$= 2\,p\,(L - 4\,R\,\delta\varphi)(2\,R\cos\varphi_N\cos\delta\varphi)^{-1}R\sin\varphi_N\sin\delta\varphi$$

$$= p\,(L - 4\,R\,\delta\varphi)\tan\varphi_N\tan\delta\varphi$$

To ensure that the personal equation is found with greatest precision the figure must be optimised to maximise m for a given L. This will be achieved when:

$$\frac{\partial m}{\partial \delta\varphi} = 0$$

$$\frac{\partial m}{\partial \delta\varphi} = p\,(-4\,R\,\tan\varphi_N\,\tan\delta\varphi + (L - 4\,R\,\delta\varphi)\tan\varphi_N\,\cos^{-2}\delta\varphi)$$

Therefore:

$$L - 4\,R\,\delta\varphi = 4\,R\,\sin\delta\varphi\,\cos\delta\varphi$$

This equation requires an iterative solution. However, an approximate solution will suffice so, if $\delta\varphi$ is small, the above may be rewritten as

$$L - 4\,R\,\delta\varphi = 4\,R\,\delta\varphi$$

Therefore:

$$\delta\varphi = \frac{L}{8R}$$

and from substitution:

$$\lambda = L\,(4\,R\,\cos\varphi_N)^{-1}$$

$$m = \frac{p\,L^2\,\tan\varphi_N}{16\,R}$$

It is next necessary to find a value for L such that the personal equation can be significantly detected. To be at least 95% certain that p exists,

$$m > 1.96\,\sigma_m$$

If a deviation of the vertical with a standard error of 0".5 is determined every 500 m then:

$$\sigma_m = \frac{500\;0.5\;\pi\;\sqrt{(L/500)}}{648000}$$

$$= \sqrt{L}\;5.4\;10^{-5}$$

Therefore from above:

$$\frac{p\,L^2\,\tan\varphi_N}{16\,R} > 1.96\,\sqrt{L}\;5.4\;10^{-5}$$

So, to be significant:

$$p > 1.96\,L^{-3/2}\;5.4\;10^{-5}\;16\,R\,(\tan\varphi_N)^{-1}$$

$$> 10800\,L^{-3/2}\,(\tan\varphi_N)^{-1}$$

At the latitude of 53° this becomes:

$$p > 8138\ L^{-3/2}$$

Minimum significantly detectable values of p for various values of L are listed in Table 4.3, below.

Table 4.3 Lengths of astrogeodetic levelling loops required to find the magnitude of a personal equation.

p	L
$1^s.0$	232 km
$0^s.1$	1078 km
$0^s.01$	5003 km

The conclusion must be that for the value of p to be meaningfully determined and applied, the length of the astrogeodetic levelling loop would have to be of such a size that it would not fit in England.

There might possibly be an application for this method if a large number of independent routes similar to the one described in Figure 4.6 could be found. For example, 100 routes each of 1078 km could lead to the determination of p to $0^s.01$.

4.4.2.4 Evaluation of personal equation by video means

If the simultaneous sounds and sights of events are recorded on videotape then timed reaction to a series of sounds followed by timed reaction to a series of sights, and vice versa, could be used as the basis of an experiment. For example, a regular short sound, like the normal second time signal from RWM Moscow, is synchronised with a video recording of a star crossing the graticule. If there is no personal equation then the mean time of a number of consecutive audio events will be an integer number of seconds different from the mean time of the same number of consecutive visual events.

A suitable videotape might contain two minutes of audible signals and 30 simulated star crossings. Four seconds between simulated star crossings should be enough to ensure that the rhythm of visual repetition could not be used. In such an experiment, the observer times the audible signals every four seconds for the first minute and times the visual signals for the second minute. The personal equation is then the difference of the

mean time of the audible events and the mean time of the visual events less the nearest integer number of seconds. In such an experiment, the observer must have the sound switched off when observing visual signals and face away from the screen when timing the audible observations.

The last solution is probably the most practical because it could be conducted in a laboratory.

4.5 The effect on the observed vertical angle of an error in horizontal pointing

In Figure 4.7, below:

O	is the observer
C	is the projection of the theodolite cross hairs onto the celestial sphere
S	star
OAB	local horizon plane
dA	angular departure of the star from the cross hairs along the horizontal hair
h	true vertical angle to the star
h_o	observed vertical angle to the star

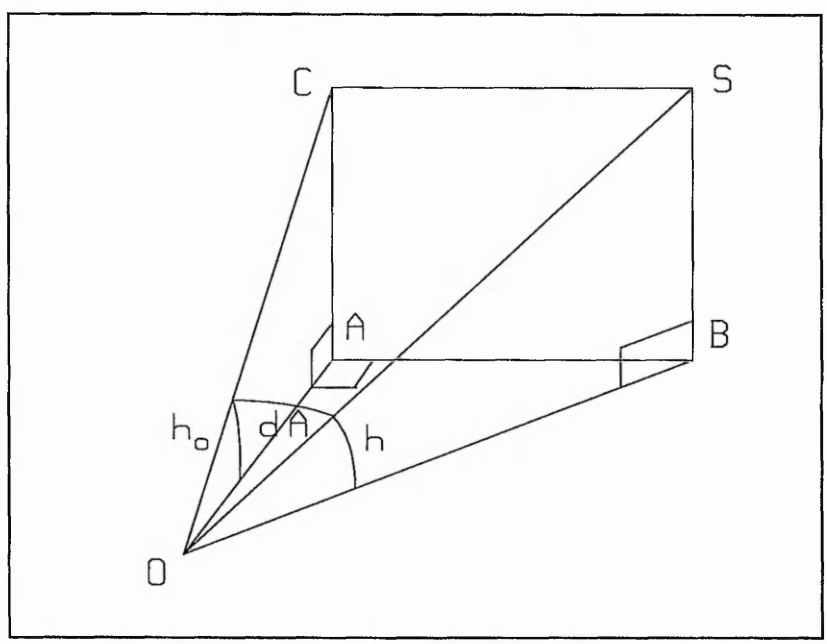

Figure 4.7 The effect on the observed vertical angle of an error in horizontal pointing.

If OB has unit length then:

$$SB = \tan h$$
$$OS = \sec h$$
$$OC = \sec h \cos dA$$
$$AC = \sec h \cos dA \sin h_o$$

Therefore since AC = SB:

$$\sec h \cos dA \sin h_o = \tan h$$
$$\cos dA \sin h_o = \sin h$$

If $h = h_o - \delta h$

where δh is the error in the observation

$$\delta h = h_o - \sin^{-1}(\cos dA \sin h_o)$$

dA may be taken as 2' 30", because it is a sensible minimum for the Wild T2000 theodolite. 2' 30" it is 2½ times the distance from the centre of the crosshairs to the main part of the horizontal hair. Table 4.4, below lists δh against h_o.

Table 4.4 The error in the observation of vertical angle at various vertical angles when the pointing is 2' 30" from the crosshairs.

h_o	δh
45°	0".05
60°	0".09
70°	0".15
80°	0".31
85°	0".62
88°	1".56
89°	3".12
89° 30'	6".24
89° 50'	18".47

If the altitude is greater than about 80°, it is apparent that there will be a significant systematic error in all observed vertical angles. The correction:

$$\delta h = h_o - \sin^{-1}(\cos dA \sin h_o)$$

will need to be subtracted from all observed vertical angles. However, if it is difficult to be consistent about the 2' 30" offset, then it will be best to avoid altitudes greater than 85°.

4.6 Investigation of a "Position Lines by Least Squares" observing and computing strategy

Before any field observations were undertaken, a computer-based study was carried out to confirm that a proposed observing and computing strategy would be workable. A prediction spreadsheet was used to create simulated observations where the observations were at the regular rate of one star every two minutes. Two minutes were chosen as that is the rate at which most observers, including the author, can observe. Changing the rate will have no significant effect upon the quality of any result, except for the amount of simulated time that is needed to achieve the result. Stars were selected so that they progressively increased in azimuth. In the field this would speed the observing process. A set of 50 stars may take about three circuits of the horizontal circle. All data sets were based upon a site near Nottingham. The maximum zenith angle was 52° with lesser values up to a zenith angle of 8°. 50 observations led to an error ellipse with a major axis of 14.5 m. The standard errors of the simulated observations were:

vertical angle	0".5 and
time	$0^s.15 \cos h / (\cos \delta \cos \varphi \sin (UT1 + R + \lambda - \alpha))$

The later is a fixed value, $0^s.15$, times an expression that describes the vertical velocity of the star. The value of $0^s.15$ relates to the author's precision of reaction to a visual stimulus, a personal statistic evaluated during an investigation of alternative methods of gyrotheodolite measurements (Breach, 1985). The assumption is that a fast rising star, e.g. a star at elongation near the prime vertical, will be easier to time precisely than a star near the pole at transit which will not appear to move much in elevation.

There are two observations associated with the Position Lines method, zenith angle and time. The numerical values stated above are based upon The Wild T2000 and a hand held stopwatch. Improvement in the quality of the observations will lead to a smaller error ellipse for position, however improvement of only one observation type may have

limited effect. Table 4.5 shows the relationship between the un-scaled error ellipse semi-major axis in metres, that is the figures in the shaded area, and observation quality for the particular data set. It is reasonable to suppose that a similar pattern of results would be obtained for any data set.

Table 4.5 The relationship between the un-scaled error ellipse semi-major axis in metres (figures in the shaded area), and zenith angle and time observation quality.

		Zenith angle standard error in arc seconds						
		5	2	1	0.5	0.2	0.1	0.05
Time	1	99.5	95.2	94.6	94.4	94.4	94.4	94.4
	0.5	56.7	48.3	47.6	47.3	47.2	47.2	47.2
standard	0.2	36.7	22.7	19.9	19.1	19.1	18.9	18.9
error in	0.1	32.9	15.7	11.3	9.9	9.5	9.5	9.4
arc	0.05	31.8	13.4	7.9	5.7	4.9	4.8	4.7
seconds	0.02	31.5	12.6	6.6	3.7	2.3	1.9	1.9
	0.01	31.5	12.6	6.4	3.3	1.5	1.1	1.0

Table 4.5, above, suggests that if time and zenith angle precision fall in the lighter shaded area then improvement in time quality will have more effect than improvement in zenith angle quality. If time and zenith angle precision fall in the darker shaded area then improvement in zenith angle quality will have more effect than improvement in time quality. The border between the light and dark shaded areas lies approximately where the ratio of zenith angle to time is 1 : 15, which is the numerical ratio of time and angle as circular measure i.e. $24^h : 360°$.

4.7 Options for Programmed Observations

Given a chosen site, latitude and longitude, there are a number of parameters that need to be specified to create an observing programme. They are:

Star elevation and azimuth limits

Start time

Number of stars to be observed

Overall balance of stars in azimuth and altitude

Observations per star against number of stars

A programme could be devised so that stars are observed at regular intervals. The observing process could be speeded up if the changes in altitude and azimuth between stars are minimised. A continuous clockwise rotation, i.e., successively increasing azimuth, would at least minimise horizontal circle movements. An example of part of such a programme, based upon stars of magnitude 3.5 or greater for observation with stopwatch and T2000 theodolite, is shown in tables 4.6 and 4.7, below.

Table 4.6 Parameters for a specimen observing programme.

Position line programme	
Approx latitude	51° 01' 30"
Approx longitude	-1° 10' 50"
Date	16 April 1996

In Table 4.7, below, the zenith angle has been corrected for standard temperature and pressure. The azimuth is such that the star will appear 2' 30" from the central cross of the crosshairs.

Table 4.7 A specimen observing programme.

SALS		Right Ascension	Declination	Time GMT	Zenith	Az
No	Mag	hh.mmss	dd.mmss	hh.mm	dd.mmss	dd.mmss
Polaris		2.2651	89.1450	0.00	39.4140	359.4730
440	2.9	16.2359	61.3120	0.02	25.0730	49.0710
494	2.4	17.5629	51.2922	0.04	39.1310	63.0640
449	3.0	16.4107	31.3637	0.06	38.2850	102.3020
442	2.8	16.2959	21.3005	0.08	44.0510	116.0220
410	2.3	15.3430	26.4339	0.10	32.1120	128.2750
416	2.7	15.4360	6.2634	0.12	50.5630	140.3820
344	2.9	12.5546	38.2053	0.14	15.3310	220.3250
316	2.2	11.4847	14.3610	0.16	43.4140	224.3530
301	2.6	11.1349	20.3314	0.18	43.1220	240.0260
280	2.6	10.1946	19.5129	0.20	51.5030	253.3350
280	2.6	10.1946	19.5129	0.22	52.0840	254.0120
300	3.1	11.0921	44.3142	0.24	28.2910	273.3150
281	3.2	10.2200	41.3138	0.26	37.4520	277.1720
257	3.3	9.2043	34.2458	0.28	51.5620	280.0400
318	2.5	11.5333	53.4331	0.30	19.4540	290.3850
245	3.1	8.5850	48.0349	0.32	47.2640	298.0920
263	3.3	9.3229	51.4210	0.34	41.1240	298.5540
297	2.4	11.0131	56.2443	0.36	27.4100	299.4510
342	1.7	12.5347	55.5923	0.38	12.2720	301.0930
352	2.4	13.2342	54.5714	0.40	8.2300	303.0010
298	1.9	11.0324	61.4651	0.42	27.4910	311.2050

The formulae associated with such a programme are stated below.

Given the following parameters:

The site in terms of latitude, and longitude

The star, in terms of its right ascension and declination

The date and time

Find: the azimuth and altitude of the star

UT1 leads to R (by computation or from tables such as SALS)

$t = UT1 + R + \lambda - \alpha$

$h = \sin^{-1}(\cos t \cos \delta \cos \varphi + \sin \delta \sin \varphi)$

$z = 90° - h - r_o$

$A = \tan^{-1}(\sin t (\sin \varphi \cos t - \cos \varphi \tan \delta)^{-1})$

where r_o is the effect of refraction.

If the altitude were to be kept constant, and therefore movement were only in azimuth, then the programme would predict when and where stars would enter or leave the small circle on the celestial sphere of given angular radius about the observer's zenith. In this case the refraction correction would be the same for all stars and could not be separated from the collimation error in the least squares solution. Therefore there could only be three unknowns to solve for at a given time and site. Observations would be irregular in time and appear randomly in azimuth.

Since stars move approximately east to west near the observer's zenith then the azimuths of the stars as they cut the small circle on the celestial sphere tend to group towards the east and the west and therefore away from the north and the south. Since error in the determined longitude is sensitive to error in time, then an east and west predominance of stars is desirable. The major decision required would be to allocate a value to the radius of the small circle. If the radius is small then the refraction and collimation factor will be small and can be well determined. However, there will only be a small number of stars that pass in and out of the small circle. In addition, the correctness of the horizontal pointing would become more important. An example of such a programme for observation with stopwatch and T2000 theodolite is in Tables 4.8 and 4.9, below.

Table 4.8 Parameters for a specimen observing programme for equal altitude observations.

Position line programme	
Approx latitude	51° 01' 30"
Approx longitude	-1° 10' 50"
Date	16 April 1996

Once again, in Table 4.9, the zenith angle has been corrected for standard temperature and pressure. The azimuth is such that the star will appear 2' 30" from the central cross of the crosshairs.

Table 4.9 A specimen observing programme for equal altitude observations.

SALS		Right Ascension	Declination	Time GMT	Zenith	Azimuth
No	Mag	hh.mmss	dd.mmss	hh.mmss	dd.mmss	dd.mmss
298	1.9	11.0324	61.4651	19.0313	19.5939	45.4111
300	3.1	11.0921	44.3142	19.2000	19.5939	97.5634
318	2.5	11.5333	53.4331	19.4636	19.5939	69.3156
257	3.3	9.2043	34.2458	20.2614	19.5939	219.5347
342	1.7	12.5347	55.5923	20.4557	19.5939	62.5405
245	3.1	8.5850	48.0349	21.0534	19.5939	273.4048
352	2.4	13.2342	54.5714	21.1555	19.5939	65.5550
344	2.9	12.5546	38.2053	21.3133	19.5939	120.5419
263	3.3	9.3229	51.4210	21.4522	19.5939	284.4402
358	1.9	13.4719	49.2026	21.4538	19.5939	82.3737
281	3.2	10.2200	41.3138	22.0831	19.5939	251.4905
300	3.1	11.0921	44.3142	23.0625	19.5939	262.1802
377	3.0	14.3151	38.1956	23.0728	19.5939	120.5821
298	1.9	11.0324	61.4651	23.1119	19.5939	314.3325
297	2.4	11.0131	56.2443	23.1644	19.5939	298.3437
318	2.5	11.5333	53.4331	24.0758	19.5939	290.4241
440	2.9	16.2359	61.3120	24.2214	19.5939	46.2850
344	2.9	12.5546	38.2053	24.2706	19.5939	239.2018
342	1.7	12.5347	55.5923	25.0845	19.5939	297.2032
352	2.4	13.2342	54.5714	25.3828	19.5939	294.1847
494	2.4	17.5629	51.2922	25.5044	19.5939	76.0843
358	1.9	13.4719	49.2026	25.5551	19.5939	277.3659
377	3.0	14.3151	38.1956	26.0250	19.5939	239.1616

The formulae associated with such a programme are below.

Given the following parameters:

The site in terms of latitude, and longitude

The star, in terms of its right ascension and declination

The date

The altitude

Find: The azimuth of the star and

East and west cross times of the small circle

$$h = 90° - z - r_o$$

$$A = \cos^{-1}((\sin\delta - \sin\varphi \sin h)(\cos\varphi \cos h)^{-1})$$

$$t = \cos^{-1}((\sin h - \sin\varphi \sin\delta)(\cos\varphi \cos\delta)^{-1})$$

$$GST = t - \lambda + \alpha$$

$$UT1 = GST - R$$

Problems with the computation of this programme will occur when the star path does not cross the small circle because the declination is too great or too small. The problem can be avoided if the declination range for a given altitude and latitude are first computed.

The range will be:

$$\text{Maximum } \delta = 90° + \varphi - h$$

$$\text{Minimum } \delta = h + \varphi - 90°$$

If the above computation gives a value of greater than 90° for the maximum δ in the northern hemisphere, or less than -90° in the southern hemisphere, then that implies that some stars may be at lower transit. Therefore, the numerical values of maximum and minimum δ should be taken as +90° and -90° respectively.

4.8 Polar Motion

The earth's spin axis is not fixed with respect to the earth's surface and wanders in an approximately circular motion. The movement of this axis of maximum moment of inertia cannot be predicted precisely but values of the change of the instantaneous pole with respect to the Conventional International Origin (CIO) are made available on the Internet at IERS (1998). The corrections, x and y, are in arc seconds and are, respectively, x in the direction of 0° longitude and y in the direction of 90° west longitude. Robbins (1976) quotes the corrections as:

$$\Delta\phi = y \sin\lambda - x \cos\lambda$$

$$\Delta\lambda = -(x \sin\lambda + y \cos\lambda) \tan\phi$$

The values of x and y do not normally exceed 0".3.

4.9 The effect of height above the geoid upon latitude

The downward vertical at a point curves slightly away from the equator because the equipotential surfaces are divergent towards the equator. Details are given in Robbins (1976), where a correction to the observed latitude is quoted:

$$\Delta\phi = - 0".00017\ H \sin 2\phi$$

where H is the orthometric height

The correction is small as it amounts to only 0".17 at 45° latitude and 1000 m height.

4.10 Vertical refraction

A widely accepted model for atmospheric refraction is that of Saastamionen (1973a and 1973b). His formula is:

$$\Delta z_o" = 16".271 \tan z \left[1 + 0.0000394 \tan^2 z \left(\frac{p - 0.156e}{T}\right) \right] \left(\frac{p - 0.156e}{T}\right) - 0".0000749\ p\ (\tan^3 z - \tan z)$$

Where $\Delta z_o"$ vertical angle correction

z apparent zenith distance

p total pressure (in mb)

e partial pressure of water vapour (in mb)

T temperature (°K)

With arbitrary but realistic values for p, e and T the formula could be approximated to:

$$\Delta z_o" \approx k \tan z - 0".075\ c \tan^3 z$$

where k is a function of p, e and T and is approximately 58" and c, also a function of p, e and T and is very close to 1.

The contribution of the second term can be seen in table 4.10, below.

Table 4.10 The contribution of 0".075 c $\tan^3 z$ to vertical refraction.

Zenith angle	2nd term
0°	0".0
10°	0".0004
20°	0".004
30°	0".014
35°	0".026
40°	0".044

If the theodolite is direct reading to 0".1 then there is no significant systematic error created by ignoring the second term for zenith angles less than 35°. Therefore a refraction correction model of:

$$\Delta z_o'' \approx k \tan z$$

may safely be used for zenith angles of less than 35°.

4.11 Summary

In this chapter the theory of the determination of astronomical position by the technique of "Position Lines" was adapted and developed for least squares. Within the least squares solution, the effect of refraction and theodolite vertical collimation and their rates of change as well as latitude and longitude were solved for. A simple formula to model refraction has been found. Non-random errors in time were considered. The effect of an error in horizontal pointing on the observed vertical angle has been corrected for. The observing parameters of star elevation, azimuth limits, start time of observations, the number of stars to be observed, the overall balance of stars in azimuth have been considered. This influences the practical observing strategies to be discussed in Chapter 6 but any practical process will require accurate star data for the time of observation, and this is the subject of the next chapter.

Chapter 5

Star Positions

5.1 Introduction

For the theory developed in Chapter 4 to be applied, it is necessary to find updated values of star co-ordinates so that an observing programme and later computations to find position, can be made. The process is to create a suitable catalogue of star data at a reference date, J2000, and to compute updated values of the co-ordinates to the epoch of interest.

5.2 J2000 Catalogue Construction

Several different catalogues were investigated for their usefulness. The Fifth Fundamental Catalogue (Fricke, 1988) was downloaded via the Internet from the US Naval Observatory at USNO (1997a). The advantage of using the Internet version of the FK5 over the printed FK5 was that there was no human error during data entry and the Internet file contains more stars with values for parallax and radial velocity. Parallax is the apparent movement of a star because of the motion of the earth around the sun and radial velocity is the rate of change of distance of the star from the earth and sun barycentre. However, the introduction to the printed FK5 contains useful formulae for the determination of precession and incorporating the effects of parallax and radial velocity.

Precession is the angular motion of the earth's polar axis around the ecliptic pole plus the absolute motion of the ecliptic pole. General precession is the combined motion and its effect on the position of the vernal equinox. Nutation is the predictable short-term deviation of the earth's axis from its long-term precession.

The Internet file contains the full FK5 whereas the printed version is in 2 publications, Pt I and Pt II. Pt II contains mostly the less bright stars.

The Internet FK5 file was edited in an Excel spreadsheet to remove all data except J2000 Right Ascension, Declination, their rates of change, star number, parallax and radial velocity. All stars less bright than those with a magnitude of 4, at J2000, were also removed. The resulting file contained 429 stars.

The FK5 is not a "bright star" catalogue. The contents of the resulting spreadsheet were compared with the Star Almanac for Land Surveyors (SALS) 1996 (HMSO, 1995) to identify which stars brighter than magnitude 4 were missing. The US Navy Observatory has several other much larger catalogues, but none of these could be downloaded because of the excessively slow load times, on readily available computers in the Department of Civil and Structural Engineering at the time of investigation (1996).

The missing stars identified in SALS 1996 were found in the printed (Yale) Bright Star Catalogue (YBSC) (Hoffleit, 1982) and for these the J2000 Right Ascensions, Declinations, their rates of change, parallax and radial velocity were manually abstracted. The rates of change of Right Ascension and Declination in the FK5 are in time seconds and arc seconds per century respectively. In the YBSC they are both in arc seconds per year. The YBSC values of rates of change were made compatible with the FK5 equivalents by transforming as follows:

$$\alpha'_{FK5} = 0.15\ \alpha'_{YBSC}\ \sec\delta$$

$$\delta'_{FK5} = 0.01\ \delta'_{YBSC}$$

where α is Right Ascension

δ is Declination

Since large catalogues from the US Naval Observatory could not be downloaded and edited, Right Ascensions and Declinations with more significant figures were found, one star at a time from VizieR (1997). The data set is the Smithsonian Astrophysical Observatory (SAO) catalogue. Values from the YBSC and use of the "minimum search area" setting ensured that on most occasions only the target star was found. The final result was that all stars were listed in the spreadsheet to at least $0^s.01$ in Right Ascension and 0".1 in Declination.

The distribution of stars by magnitude and catalogue is shown in Table 5.1 below.

Table 5.1 Star Magnitudes in the FK5 catalogue with additional stars from the YBSC/SAO catalogue.

Magnitude	Catalogue		
	FK5	YBSC/SAO	Total
≥ 0	4	0	4
≥ 0.5	10	0	10

≥ 1.0	16	0	16
≥ 1.5	23	0	23
≥ 2.0	48	2	50
≥ 2.5	86	5	91
≥ 3.0	157	14	171
≥ 3.5	258	27	285
≥ 3.99	429	51	480

A second larger catalogue was created to give more flexibility in the selection of stars for different investigations. This catalogue only used data from sets available on the Internet. The two selected data sets were the Bright Star Catalogue (BSC), (NASA, 1997a) and the Positions and Proper Motions Catalogue (PPM), (NASA, 1997b) which between them contain α, δ, α', δ', parallax and radial velocity at J2000 to respective places of decimal of $0^s.001$, 0".01, $0^s.0001$/yr, 0".001/yr, 0".001 and 1km/s. However, neither catalogue contains all the data to the required level. Before selecting data from the two catalogues, it was first necessary to select only those stars that were unambiguously common to both catalogues. The selection routine was as follows:

1. Remove all stars with a magnitude less bright than 7.1 from both catalogues. This reduced both catalogues to a size that could be handled in an Excel spreadsheet.
2. Remove all stars within 5 arc minutes of each other. This was to avoid ambiguous solutions in future work.
3. Remove all stars from the BSC that did not appear in the PPM, based upon agreement in α and δ, at the $0^s.1\sec\delta$ and 1" levels respectively.
4. Remove all stars from the PPM that did not appear in the BSC, based upon agreement in α and δ, at the $0^s.1\sec\delta$ and 1" levels respectively.
5. Remove all stars from the BSC that did not appear in the PPM, based upon agreement in SAO number.
6. Remove all stars from the PPM that did not appear in the BSC, based upon agreement in SAO number.
7. Remove all stars from both catalogues where the SAO and HD (Henry Draper) numbers were not the same in both catalogues.

8. Select the star number as the SAO number. Select α, δ, α' and δ' from the PPM. Select parallax and radial velocity from the BSC.

This composite catalogue was termed MCBJ2000. The distribution of stars by magnitude is in Table 5.2, below.

Table 5.2 Star Magnitudes in the MCBJ2000 catalogue.

Magnitude	No of stars
≥0	5
≥0.5	10
≥1.0	16
≥1.5	22
≥2.0	42
≥2.5	85
≥3.0	170
≥3.5	286
≥4.0	478
≥4.5	844
≥5.0	1419
≥5.5	2386
≥6.0	3886
≥6.5	6053
≥6.6	6694

In 1998 a single catalogue containing all the necessary parameters, i.e. α, δ, α', δ', parallax and radial velocity was published at NASA (1997c and 1997d). The former is in 24 files, one for each hour of Right Ascension and the latter as a single 32Mb zip file that expands to a text file of 152Mb. The SKY2000 Master Star Catalog is reported on by Myers et al (1997).

SKY2000 contains 299,485 stars, some with as faint a magnitude as 11.5. SKY2000 contains α, δ, α', δ', parallax and radial velocity at J2000 to respective places of decimal of $0^s.0001$, 0".001, $0^s.00001$/yr, 0".0001/yr, 0".00001 and 0.1km/s. This represents an order of improvement in all statistics, and 2 orders for parallax, compared with the composite catalogue, MCBJ2000, described above.

Compared with the PPM catalogue, where position uncertainties were globally quoted as 0".22, there are individual uncertainties for α and δ at J2000. The first 31000 stars in SKY2000 were investigated to see if there was a relationship between magnitude and position uncertainty. The results expressed graphically are in Figure 5.1, below.

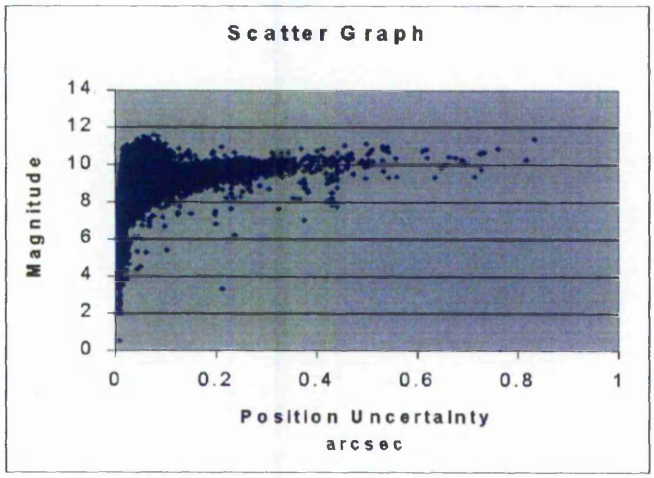

Figure 5.1 Star Magnitude and Position uncertainty for SKY2000 Master Star Catalog.

The graph gives an impression of a greater spread of uncertainties than actually exists. A better indication of the relationship between magnitude and position uncertainty can be shown from Figures 5.2, below, where the star set is divided into magnitude bands, 2.0 to 2.4999, 2.5 to 3.999 etc. A graph of the number of stars in each band against the mean magnitude of the band is on the left. The relationship between RMS position uncertainty and mean magnitude of the band is on the right. The large "spike" in Figure 5.2b for the 3.0 to 3.499 magnitude band is due to a single star with a very large position uncertainty. If that star is removed from the set then the graph becomes very much smoother. The offending star has been removed from the final sub-set of SKY2000 that is to be used for practical observations. The graphs do indicate that the RMS of position uncertainty of all stars brighter than magnitude 7.0 is better than 0".02.

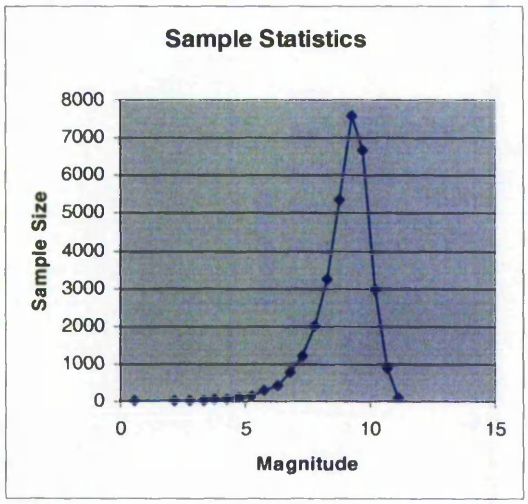

Figure 5.2a Star Magnitude and sample size for the SKY2000 catalogue.

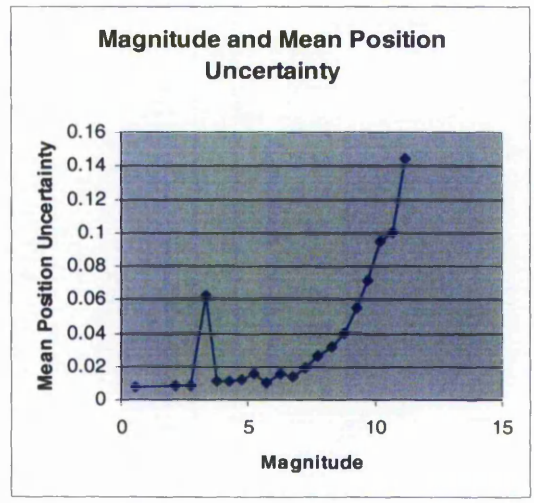

Figure 5.2b Star Magnitude and Mean Position Uncertainty for the SKY2000 catalogue.

A useful set of suitable stars from the SKY2000 catalogue was required for practical observations. The criteria for acceptance of a star were that:

There is no "distance to the nearest neighboring master catalog star no more than two magnitudes fainter than this star" listed, i.e. no close stars of similar brightness, OR

There is no "magnitude difference of brightest and second brightest components" listed, i.e. no bright double stars, OR

The magnitude of the duller component is numerically greater than 7, i.e. a double star can be accepted if the duller star is very faint, OR

The magnitude difference between the brightest and second brightest component is greater than 3, i.e. close stars can be accepted provided that there is a big difference in magnitude between them, OR

The distance to the nearest star more than 2 magnitudes fainter is less than 0º.00011 away, i.e. a pair of stars of sufficiently unequal magnitudes are so close that the visual centre of gravity of the pair will be negligibly far from the brighter star of the pair, OR

The distance to the nearest star greater than 2 magnitudes fainter is greater than 6', i.e. a pair of stars of sufficiently unequal magnitudes are so far apart there will be no ambiguity as to which star is being observed.

Since the SKY2000 catalogue appears to be at least an order of magnitude better than the composite MCBJ2000 catalogue compiled earlier, then it might be expected that the RMS difference between star positions in SKY2000 and MCBJ2000 would be of the order of the uncertainties of the MCBJ2000 catalogue, i.e. 0".2.

An arbitrary set of 1700 stars that appear in both SKY2000 and MCBJ2000 were selected and the differences in α and δ and their RMS at J2000 were found. The results are in Table 5.3, below.

Table 5.3 Co-ordinate differences between the SKY2000 and MCBJ2000 catalogues.

	Mean Difference Arc seconds	**RMS difference Arc seconds**
Right Ascension * cos(Declination), α*cos(δ)	-0.00404	0.026836
Declination, δ	0.002063	0.027242

The results indicate that the worst mean difference, i.e. in Right Ascension would lead to an East-West tilt of any computed geoid of less than 2mm in 100km (1.8mm subtends 0".004 at 100km). The RMS differences are well below the precision of any theodolite currently on the market. Therefore, it can be concluded that it will make no practical difference whether the SKY2000 or the MCBJ2000 catalogue is used. The above also shows that either the MCBJ2000 catalogue was more precise than the 0".22 suggested by the PPM catalogue or that SKY2000 is not as precise as its authors' claim.

5.3 Ephemeris Update

J2000 Right Ascension and Declination values for stars need to be updated to the epoch of interest. Since a set observations with a T2000 theodolite takes about 1½ hours then the Right Ascensions and Declinations in the middle of the set of observations will still be precise enough for the beginning and the end of the observations. The systematic errors associated with such an assumption will be largely a function of the change in short-term nutation. An estimate of the maximum systematic effect upon Right Ascension and Declination can be found as follows.

5.3.1 *Error in Right Ascension*

If $\delta = 0$

$\Delta\alpha = \cos 23°.5\ \Delta\psi$

where $\Delta\psi$ is the nutation component in longitude

From Table I of APFS 1996 (Astronomisches Rechen-Institute, 1995) the maximum one day change in $\Delta\psi$ appears to be 0".127 (18-19 January) and therefore the maximum error in Right Ascension in ½ of 1½ hours is:

$$\Delta\alpha = \cos 23°.5\ \ 0".127\ \ 0.75/24$$
$$= 0".004$$

An error in Right Ascension translates directly as an error in longitude and when δ = 0 the error in longitude will be 0.12 m.

5.3.2 *Error in Declination*

If $\alpha = 6^h$

$\Delta\delta = \Delta\varepsilon$

where $\Delta\varepsilon$ is the nutation component in obliquity.

In Table I of APFS 1996 the maximum one day change in $\Delta\varepsilon$ appears to be 0".045 (21-22 January) and therefore the maximum error in Declination in ½ of 1½ hours is:

$$\Delta\delta = 0".045\ \ 0.75/24$$
$$= 0".001$$

Both systematic errors are negligible.

In converting J2000 values to the epoch of interest, account needs to be taken of precession, long and short periods and planetary elements of nutation, proper motion, radial velocity, annual parallax, annual aberration, diurnal aberration, polar motion and gravitational light deflection.

5.3.3 *Diurnal Aberration*

Diurnal aberration depends, among other things, upon latitude and hour angle and is therefore best applied as a final correction to Right Ascension and Declination in the "position line" computation.

5.3.4 *Gravitational light deflection*

Gravitational light deflection by the sun is small but significant only if the star is near the sun. In practical terms, a worst case might be that if the star and sun are on the same observer's azimuth with the star at a zenith angle of 50° and the sun is 10° below the horizon. In this case the gravitational light deflection is less than 0".01. This can be verified by applying formula 3.261-1 of Seidelmann (1992).

5.3.5 *Polar motion*

Although polar motion is unpredictable and can only be included in computations processed after the observations have been taken, estimates of its value for a recent epoch can be found on the Internet. Alternatively, it can be ignored, and if all observations are taken within a period of a few days its effects upon position and hence geoid slope will be constant.

With the last three corrections omitted, at least at this stage, the remaining corrections listed above are applied as follows:

5.3.6 *Precession and Space Motion*

A description of precession is given in Section 3.21 of Seidelmann (1992). The precession angles ζ, z and Θ are quoted from Lieske (1979) in both Seidelmann (1992) and Fricke (1988). The formulae can be simplified as follows:

$$\zeta = 2306".2181t + 0".30188t^2 + 0".017998t^3$$
$$z = 2306".2181t + 1".09468t^2 + 0".018203t^3$$
$$\Theta = 2004".3109t - 0".42665t^2 - 0".041833t^3$$

where t is the period in Julian centuries since J2000. In the above simplification, it is assumed that the "initial equinox" and J2000 are the same. The determination of the updated Right Ascension and Declination can be computed by means of a unit vector of direction cosines, **u**, and a precession matrix, **P**.

$$\mathbf{P} = \mathbf{R}_z(-z)\,\mathbf{R}_Y(\Theta)\,\mathbf{R}_z(-\zeta)$$

and from formula 3.21-8 of Seidelmann (1992)

$$\mathbf{P} = \begin{bmatrix} \cos z \cos\Theta \cos\zeta - \sin z \sin\zeta & -\cos z \cos\Theta \sin\zeta - \sin z \cos\zeta & -\cos z \sin\Theta \\ \sin z \cos\Theta \cos\zeta + \cos z \sin\zeta & -\sin z \cos\Theta \sin\zeta + \cos z \cos\zeta & -\sin z \sin\Theta \\ \sin\Theta \cos\zeta & -\sin\Theta \sin\zeta & \cos\Theta \end{bmatrix}$$

In Fricke (1988), **u** and its derivatives are:

$$\mathbf{u} = \begin{bmatrix} \cos\delta \cos\alpha \\ \cos\delta \sin\alpha \\ \sin\delta \end{bmatrix}$$

$$\frac{d\mathbf{u}}{d\alpha} = \begin{bmatrix} -\cos\delta \sin\alpha \\ \cos\delta \cos\alpha \\ 0 \end{bmatrix}$$

$$\frac{d\mathbf{u}}{d\delta} = \begin{bmatrix} -\sin\delta \cos\alpha \\ -\sin\delta \sin\alpha \\ \cos\delta \end{bmatrix}$$

At the epoch of interest

$$\mathbf{r} = \mathbf{P}(\mathbf{u}_0 + \frac{d\mathbf{u}_0}{dt} \Delta t)$$

where $$\frac{d\mathbf{u}_0}{dt} = 4.8481368\ 10^{-6} \left(\mu_0 \frac{d\mathbf{u}_0}{d\alpha} + \mu_0' \frac{d\mathbf{u}_0}{d\delta} + 21.094953\ \pi_0 V_0 \mathbf{u}_0 \right)$$

where μ_0 is the rate of change of Right Ascension in units of "/century

μ'_0 is the rate of change of Declination in units of "/century

π_0 is the parallax is in arc seconds

V_0 is the radial velocity is in km/s.

Right Ascension and Declination are then formed from:

$$\alpha = \tan^{-1}\left(\frac{r_2}{r_1} \right)$$

$$\delta = \tan^{-1}\left(\frac{r_3}{(r_1^2 + r_2^2)^{1/2}} \right)$$

5.3.7 Nutation

A description of nutation is given in Section 3.22 of Seidelmann (1992) where the International Astronomical Union (IAU) nutation series and set of fundamental arguments (Van Flandern 1981) are used with updates to some terms from Herring

(1987). Planetary effects upon nutation have been included even though they are very small, in the order of 0".0001 to 0".00001. The contents of the main nutation table of 530 argument multiples and 106 coefficients, each for longitude and obliquity have all been included (Table 3.222.1 from Seidelmann (1992)). The coefficients and arguments of multiples were confirmed by comparing with those on Internet page at USNO (1997b). The planetary terms are listed on pages 117-119, equations 3.224-3 and Table 3.224-2 of Seidelmann (1992).

The fundamental arguments listed at Table 3.222.2 in Seidelmann (1992), have also been used in this research. Initial computations produced Right Ascensions and Declinations that were significantly at variance with APFS 1996 (Wielen, 1994). Some "trial and error" and deductive reasoning led to the conclusion that there was an error in the formula for Ω, "the longitude of the mean ascending node of lunar orbit on the ecliptic measured from the mean equinox of date". The formula quoted in Seidelmann (1992), can be condensed to:

$$\Omega = 135° 2' 40".280 - 1934° 8' 10".539t + 7".455t^2 + 0".0008t^3$$

where t is the time since J2000 in Julian centuries.

If the first term is revised to **125**° 2' 40".280 then there is agreement between the output of this author's spreadsheet and Table II of APFS 1996 (Wielen, 1994) in the determination of $\Delta\psi$ and hence in the computation of both the long and short period terms of the equation of the equinox. The value of 125º was verified by comparing with the value of Ω computed from 1900 to J2000 using the formulae on page 544 of Anon (1976) and is also implicit in the Fortran code at IERS (2001) which is a published sub-routine of the International Earth Rotation Service (IERS), Central Bureau (IERS/CB).

The mean obliquity from equation 3.222-1 on page 114 of Seidelmann (1992) is given by:

$$\varepsilon_0 = 23° 26' 21".448 - 46".8150t - 0".00059t^2 + 0".001813t^3$$

and the obliquity of date is

$$\varepsilon = \varepsilon_0 + \Delta\varepsilon$$

and so the nutation matrix is

$$\mathbf{N} = \mathbf{R}_x(-\varepsilon)\,\mathbf{R}_z(-\Delta\psi)\,\mathbf{R}_x(\varepsilon_0)$$

which is:

$$\mathbf{N} = \begin{bmatrix} \cos\Delta\psi & -\sin\Delta\psi\cos\varepsilon_0 & -\sin\Delta\psi\sin\varepsilon_0 \\ \sin\Delta\psi\cos\varepsilon & \cos\Delta\psi\cos\varepsilon\cos\varepsilon_0 + \sin\varepsilon\sin\varepsilon_0 & \cos\Delta\psi\cos\varepsilon\sin\varepsilon_0 - \sin\varepsilon\cos\varepsilon_0 \\ \sin\Delta\psi\sin\varepsilon & \cos\Delta\psi\sin\varepsilon\cos\varepsilon_0 - \cos\varepsilon\sin\varepsilon_0 & \cos\Delta\psi\sin\varepsilon\sin\varepsilon_0 + \cos\varepsilon\cos\varepsilon_0 \end{bmatrix}$$

The terms $\Delta\psi$ and $\Delta\varepsilon$, the nutation components in longitude and obliquity, are derived from:

$$\Delta\psi = \sum_{i=1}^{n} S_i \sin A_i \qquad \Delta\varepsilon = \sum_{i=1}^{n} C_i \cos A_i$$

where S_i and C_i are coefficients and A_i are the sums of the arguments and multiples.

The nutation matrix is applied as:

$$\mathbf{r} = \mathbf{N}\mathbf{r}_0$$

where $\mathbf{r}_0$ is the **r** vector corrected for precession above and therefore precession and nutation corrections are applied in the new **r**.

5.3.8 Parallax

Diurnal parallax is negligibly small. Annual parallax for closer stars is significant. Seidelmann (1992) quotes as the corrections from barycentric to geocentric place as:

$$\Delta\alpha = \pi_0 (X\sin\alpha - Y\cos\alpha)/(15\cos\delta)$$

$$\Delta\delta = \pi_0 (X\cos\alpha\sin\delta + Y\sin\alpha\sin\delta - Z\cos\delta)$$

where π_0 is the parallax in arc seconds and X, Y and Z are the earth's barycentric co-ordinates in astronomic units.

If the earth's orbit around the sun is assumed to be circular and the effect of the obliquity of the ecliptic is assumed to be negligible, then:

$$X = -\cos\odot$$

$$Y = -\sin\odot$$

$$Z = 0$$

where $\odot$ is the longitude of the sun.

Robbins (1976) gives more useable and precise formulae for parallax. They may be reduced to:

$$\Delta\alpha = \pi_0 (\sin\odot \cos\alpha \cos\varepsilon - \cos\odot \sin\alpha) \sec\delta$$

$$\Delta\delta = \pi_0 (\sin\odot (\sin\varepsilon \cos\delta - \cos\varepsilon \sin\alpha \sin\delta) - \cos\odot \cos\alpha \sin\delta)$$

5.3.9 Application of Gravitational Light Deflection

Although the effect of gravitational light deflection is small, a correction has been applied for completeness. The formulae used are those quoted or adapted from pages 484-5 of Seidelmann (1992) and Breach (1997) for approximate Right Ascension and Declination of the sun.

$$L = 280°.460 + 36000°.77\ t$$

$$G = 357°.528 + 35999°.050\ t$$

$$\lambda = L + 1°.915 \sin G + 0°.020 \sin 2G$$

$$\varepsilon = 23°.4393 - 0°.01300\ t$$

$$E = -1°.915 \sin G - 0°.020 \sin 2G + 2°.466 \sin 2\lambda - 0°.053 \sin 4\lambda$$

$$\alpha_\odot = GAST - UT_1 - E + 12^h$$

$$\delta_\odot = \sin^{-1}(\sin\varepsilon \sin\lambda)$$

where L is the mean longitude corrected for aberration

G is the mean anomaly

λ is the ecliptic longitude

ε is the obliquity of the ecliptic

E is the equation of time

$\alpha_\odot$ and $\delta_\odot$ refer to the sun

Although the formulae are approximate, they are more than good enough for the purpose of determining $\alpha_\odot$ and $\delta_\odot$ for the correction for the gravitational light deflection.

Anon (1983), on page S20, gives formulae for the determination of corrections to α and δ for gravitational light deflection from which the following are derived.

$$\cos D = \sin\delta_\odot \sin\delta - \cos\delta_\odot \cos\delta \cos(\alpha - \alpha_\odot)$$

$$\Delta\alpha = \frac{0".00407 \cos\delta_\odot \cos(\alpha - \alpha_\odot)}{(1 - \cos D) \cos\delta}$$

$$\Delta\delta = \frac{0".00407 (\sin\delta \cos\delta_\odot \cos(\alpha - \alpha_\odot) - \sin\delta_\odot \cos\delta)}{(1 - \cos D)}$$

where:

D is the geocentric angular separation of the star from the sun.

The above formulae lead to small corrections for α and δ. Values for α and δ for a selection of FK5 stars on various dates in 1996 were computed using a spreadsheet. The results were compared with the values listed in Wielen (1994). Short term and planetary nutation terms were not applied. The results are given in Table 5.4 below. Only seconds of time or arc are shown.

Table 5.4 Comparison of star co-ordinates between the FK5 catalogue and this author's spreadsheet.

At date and time – Upper Transit on	FK5 Star No	α from APFS time s	δ from APFS arc s	α from spread-sheet time s	δ from spread -sheet arc secs	δ dd.mm	15 $\Delta\alpha$ cosδ arc secs	$\Delta\delta$ arc secs
8-Jan-96	1	11.282	16.66	11.2819	16.662	29.04	0.001	-0.002
28-Mar-96	20	6.770	19.49	6.7701	19.469	30.50	-0.001	0.021
17-May-96	42	31.122	52.42	31.1225	52.412	35.35	-0.006	0.008
25-Aug-96	99	28.716	38.77	28.7155	38.747	55.52	0.004	0.023
3-Dec-96	1134	41.814	15.26	41.8139	15.259	6.57	0.001	0.001
23-Dec-96	215	34.044	-43.64	34.0437	-43.634	-34.04	0.004	-0.006
19-Jan-96	263	52.761	-50.88	52.7587	-50.883	-50.36	0.022	0.003
8-Mar-96	294	14.275	16.79	14.2742	16.797	24.24	0.011	-0.007
27-Apr-96	336	58.866	-17.19	58.8664	-17.205	-60.37	-0.003	0.015
6-Jun-96	365	57.266	25.85	57.2651	25.850	9.54	0.013	0.000
5-Aug-96	423	2.744	58.41	2.7426	58.409	15.26	0.020	0.001
24-Sep-96	481	30.345	-12.85	30.3433	-12.849	-59.39	0.013	-0.001
3-Nov-96	545	52.372	-28.50	52.3713	-28.470	-5.38	0.010	-0.030
23-Dec-96	585	26.690	-7.61	26.6890	-7.602	-3.24	0.015	-0.008
9-Jan-96	633	28.010	55.14	28.0106	55.137	9.22	-0.009	0.003
28-Feb-96	674	36.675	46.27	36.6747	46.272	29.14	0.004	-0.002
8-Apr-96	720	32.832	-39.20	32.8335	-39.194	-7.56	-0.022	-0.006
17-Jun-96	780	5.698	24.49	5.6986	24.493	33.57	-0.007	-0.003
5-Sep-96	859	24.068	4.44	24.0685	4.442	23.32	-0.007	-0.002
23-Nov-96	890	26.047	46.43	26.0478	46.435	46.26	-0.008	-0.005
						RMS	0.011	0.011

The RMS values indicate that star positions are in agreement with Wielen (1994) to 0".013. Better agreement could probably have been achieved with more precise formulae for ⊙, the true geometric longitude of the sun. However, since the precision of the spreadsheet will lead to systematic errors of astronomic position in the order of only 0.3 m, then there is no need to pursue the matter further.

The output of this author's spreadsheet with short term and planetary nutation terms applied was tested against the output of MICA (1998). The FK5 catalogue in MICA was computed for 5 separate dates, 200 days apart and starting at 0^h 1 January 1999. The apparent co-ordinates of 547 arbitrarily chosen stars that were common to this author's spreadsheet and the FK5 in MICA for each of the 5 epochs were compared. The RMS of $\Delta\alpha \cos\delta$ and $\Delta\delta$ were respectively, 0".012 and 0".009 with an overall RMS of 0".010. These values are indication of the correctness of the formulae applied in this author's spreadsheet. A similar test was applied using selected stars from the SKY2000 Master Star Catalog (NASA, 1997d). The RMS of $\Delta\alpha \cos\delta$ and $\Delta\delta$ were respectively, 0".102 and 0".126 with an overall RMS of 0".115.

These values indicate the changes that have taken place in the J2000 values of the star co-ordinates and other parameters, from the various catalogues used in the construction of the MCBJ2000 catalogue, to those of the SKY2000 Master Star Catalog. It appears to indicate that, although MICA was published in 1998, it does not use the most precise data available at the date of its own publication.

5.3.10 Aberration

The movements of the observer and of the star through space cause an apparent displacement of the star as seen by the observer. This aberration has three components, secular, annual and diurnal aberration. Secular aberration is caused by the proper motion of the earth and of the star. It is very small, different for each star and therefore ignored. Annual aberration is caused by the earth's orbit around the sun.

Annual Aberration

Seidelmann (1992) quotes the following formulae for corrections to be applied to the geometric Right Ascension and Declination to get the apparent Right Ascension and Declination.

$$\Delta\alpha = -(\kappa \sin\odot + \kappa\, e \sin\Pi) \sin\alpha \sec\delta$$
$$- (\kappa \cos\odot \cos\varepsilon + \kappa\, e \cos\Pi \cos\varepsilon) \cos\alpha \sec\delta$$

$$\Delta\delta = -(\kappa \sin\odot + \kappa\, e \sin\Pi)\cos\alpha \sin\delta$$
$$- (\kappa \cos\odot \cos\varepsilon + \kappa\, e \cos\Pi \cos\varepsilon)(\tan\varepsilon \cos\delta - \sin\alpha \sin\delta)$$

where κ is the constant of aberration

$\odot$ is the true geometric longitude of the sun

e is the eccentricity of the solar orbit

Π is the longitude of perigee of the solar orbit

ε is the mean obliquity of the ecliptic

κ, the constant of aberration for the standard epoch, is given in Seidelmann (1992) as 20".49552. e, the eccentricity of the solar orbit, is 0.016708617. Π is given as:

$$\Pi = 282° 4' 49".951 + 6190".67(t-t_0) + 1".65(t-t_0)^2 + 0".012(t-t_0)^3$$

No formulae are quoted for $\odot$ in the part of Seidelmann (1992) that deals with aberration. However, Yallop and Hohenkerk in a later chapter (p484) of Seidelmann (1992) give the following formulae that lead to the "ecliptic longitude".

$$L = 280°.460 + 36000°.770t$$
$$G = 357°.528 + 35999°.050t$$
$$\lambda = L + 1°.915 \sin G + 0°.020 \sin 2G$$

where t is the number of centuries since J2000

L is the mean longitude corrected for aberration

G is the mean anomaly

λ is the ecliptic longitude

It is assumed that, at least to an acceptable approximation, $\odot$, the true geometric longitude of the sun may be replaced by λ. The other terms have already been described.

Diurnal aberration

Diurnal aberration results from the observer being on a rotating earth. Seidelmann (1992) quotes the following formulae for corrections to be applied to the mean Right Ascension and Declination to get the apparent Right Ascension and Declination.

$$\Delta\alpha = 0^s.02133\, \rho/_a \cos\phi' \cos t \sec\delta$$

$$\Delta\delta = 0".3200\, \rho/_a \cos\phi' \sin t \sin\delta$$

where ρ is the geocentric distance

ϕ' is the geocentric latitude

t hour angle

a equatorial radius

t may be found from:

$$t = \alpha - GMT - R - \lambda$$

Since $\rho\cos\phi'$ is the distance of the station from the earth's rotation axis, that is the radius of the small circle of latitude, then the equations may be rewritten as:

$$\Delta\alpha = 0^s.02133\ \nu/a\ \cos\phi\ \cos t\ \sec\delta$$

$$\Delta\delta = 0''3200\ \nu/a\ \cos\phi\ \sin t\ \sin\delta$$

where ν, the radius of curvature in the transverse, plane is given by:

$$\nu = a(1 - e^2\sin^2\phi)^{-½}$$

and e in this formula is the eccentricity of the earth ellipsoid model. With negligible loss of accuracy geodetic values may be used in place of astronomic values for this purpose.

5.4 Star Catalogues

In the Table below is a summary of the star catalogues used during this investigation.

Table 5.5 Star catalogues used during this investigation.

Catalogue	Source or Publisher	Format	Useful data	Significant figures	Remarks
Star Almanac for Land Surveyors (SALS)	HMSO	Book	α at 12 epochs δ at 12 epochs magnitude	$0^s.1$ 1" 0.1	α and δ insufficiently precise. This is a bright star catalogue so it can be used to identify all bright stars in other catalogues. 695 stars
Fifth Fundamental Catalogue Part 1 (FK5 Pt1)	Astronomisc hes Rechen-Institut	Book	α J2000 δ J2000 α' J2000 δ' J2000 magnitude * parallax * radial velocity	$0^s.001$ 0".01 $0^s.001$/cy 0".01/cy 0.01 0".001 0.1km/sec	Precise catalogue. This is an astronomical catalogue with an even spread of stars but does not contain all the bright stars. 1535 stars.

Fifth Fundamental Catalogue Parts 1 and 2 (FK5)	Internet USNO, (1997a)	electronic	α J2000 δ J2000 α' J2000 δ' J2000 magnitude	$0^s.001$ 0".01 $0^s.001$/cy 0".01/cy 0.01	Precise catalogue. This is an astronomical catalogue with an even spread of stars but does not contain all bright stars.
Apparent Places of Fundamental Stars (APFS)	Astronomisc hes Rechen-Institut	Book	α 36 epoch/year δ 36 epoch/year magnitude	$0^s.001$ 0".01	Precise catalogue based upon FK5 Pt1. This is an astronomical catalogue with an even spread of stars but does not contain all bright stars. Long period nutation is included. Corrections for short period nutation calculated. Tables for Apparent and Mean Sidereal Time to $0^s.001$ and short period terms of nutation to 0".001. Useful to verify stars reduced from J2000 to epoch of date. 1535 stars.
(Yale) Bright Star Catalogue, 5th revised edition (BSC)	Internet NASA, (1997a)	electronic	α J2000 δ J2000 α' J2000 δ' J2000 magnitude parallax radial velocity SAO number Henry Draper (HD) number	$0^s.1$ 1" $0^s.1$/cy 0".1/cy 0.01 0".001 1km/sec	α and δ insufficiently precise. This is a bright star catalogue so it can be used to complete parallax and radial velocity data. Contains about 9000 stars
(Yale) Bright Star Catalogue	Yale University Observatory	Book	α J2000 δ J2000 α' J2000 δ' J2000 magnitude parallax radial velocity	$0^s.1$ 1" $0^s.1$/cy 0".1/cy 0.01 0".001 1km/sec	α and δ insufficiently precise. This is a bright star catalogue so it can be used to complete parallax and radial velocity data. Less easy to use than SALS to identify brightest stars.
Smithsonian Astrophysical Observatory (SAO)	Internet VizieR, (1997)	electronic	α J2000 δ J2000	$0^s.01$ 0.1"	α and δ found 1 at a time through internet address.

Positions and Proper Motions (PPM)	Internet NASA, (1997b) for PPM north	electronic	α J2000 δ J2000 α' J2000 δ' J2000 magnitude SAO number Henry Draper (HD) number	$0^s.001$ 0".01 $0^s.0001$/yr 0".001/yr 0.1	Comes in 3 parts PPM North, South and Supplementary, containing approximately 180000, 180000 and 90000 stars respectively with magnitudes to less than 10 though PPM Supplementary contains no stars of magnitude brighter than 7.4. Data used in conjunction with BSC.

* some stars only

5.5 Summary

In this chapter the process of creating a suitable catalogue of star data at the reference date, J2000, was reviewed. The star data needs to be updated to the epoch of interest taking account of Aberration, Gravitational light deflection, Polar motion, Precession and Space Motion, Nutation and Parallax. Spreadsheets have been created to produce updated values of Right Ascension and Declination for stars. These updated values then form a database that can be used to create star observing programmes and to compute position as described in Chapters 6 and 10.

Chapter 6

Observing and Computing Processes

6.1 Introduction

A suitable observing and computing process is required. Such a process must lead to precise and reliable results delivered in an economical manner. Precision is a measure of the numerical uncertainty of the solution assessed with reference to the internal quality of the observations and reliability is a measure of the degree of redundancy in the computation of the solution. The key to making observations efficiently is preparation, and that in turn requires that observing programmes are prepared.

6.2 Optimising the observing programme for balanced stars

Many parameters can be varied when creating an observing programme. Location is fixed by the needs of the task. Stars are selected for brightness and availability near the zenith of the observer. The observing programme, described elsewhere, was constructed to minimise the theodolite telescope movement from star to star to speed the observing process. The observing rate is dictated by the ability of the observer and the time of start of observations depends upon the time of arrival on site. Choice of azimuth of the first star is therefore arbitrary.

The traditional approach to Position Lines determination requires that the stars be balanced about the zenith to mitigate against the effects of uncertain refraction and collimation. Although the solution for position in this programme of work is by least squares, it is apparent that if the stars are balanced then the effect of errors in the computed values of vertical collimation and in the refraction coefficient will have less effect upon the solution. Star balance can be viewed in a number of ways. In the following, a specific star set, is used for illustrative purposes. It was prepared for a site near Nottingham for early evening on 28 December 1997 using this author's prediction programme spreadsheet.

6.2.1 *Investigate direction of balance based on error in computed refraction coefficient*

The effect of refraction is a function of zenith angle and the prevailing meteorological conditions. Imbalance of stars in a given azimuth, β, can be given by:

$$I_{R\beta} = \tan^{-1}(\Sigma(\tan z \cos(\alpha - \beta))/n)$$

where z zenith angle

α azimuth of each star

n number of stars

$I_{R\beta}$ is therefore an angular measure of the "centre of gravity" of the star set in the direction of β relative to the zenith. This statistic can be computed for a full circle range of β. The value of β that gives the lowest value of $I_{R\beta}$ indicates the best balance. An example of the variation of $I_{R\beta}$ with azimuth is in Figure 6.1, below.

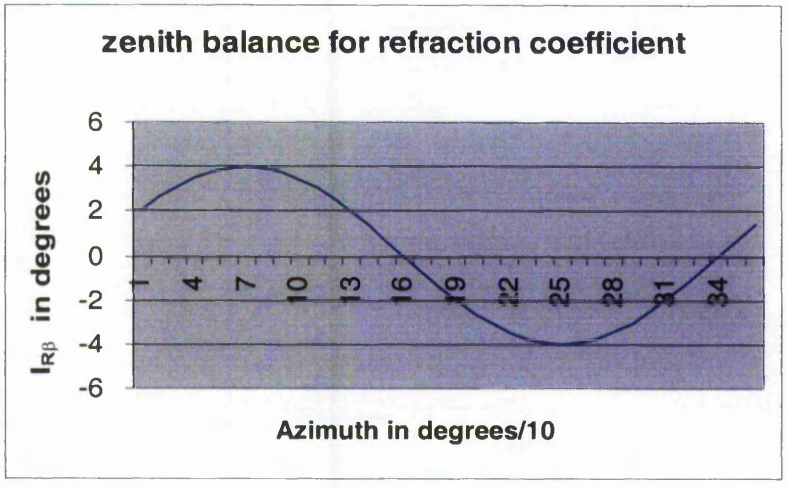

Figure 6.1 Zenith balance for refraction coefficient.

6.2.2 *Investigate direction of balance based on error in computed collimation*

The effect of collimation in a given azimuth, β, is a function of the error in the computed value of collimation and the numerical imbalance of stars in that azimuth. Imbalance of stars in a given azimuth, β, can therefore be given by:

$$I_{C\beta} = \Sigma(\cos(\alpha - \beta))/n$$

where α and n are as above. $I_{C\beta}$ is therefore a unitless measure of the "centre of gravity" of the star set in the direction of β relative to the zenith. For perfect balance, $I_{C\beta}$ should be zero. For the worst imbalance, i.e. where all the stars are at an azimuth of β from the observer, $I_{C\beta} = 1$. Again, this statistic can be computed for a full circle range of β. The

value of β that gives the lowest value of $I_{C\beta}$ indicates the best balance. See Figure 6.2, below.

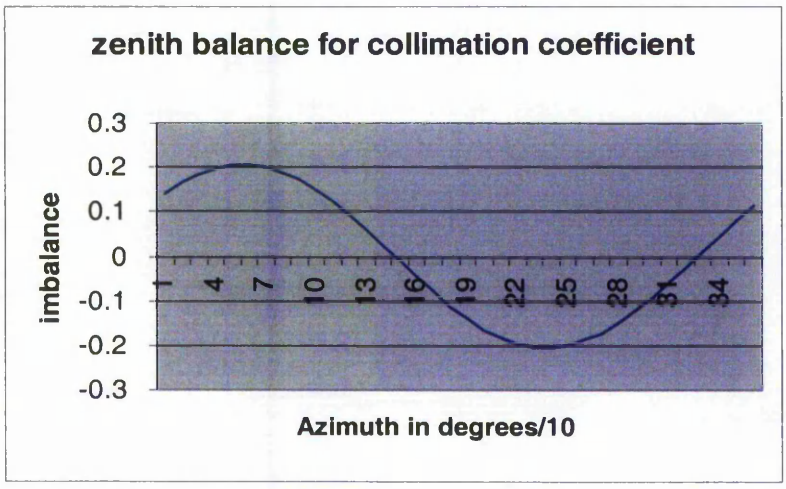

Figure 6.2 Zenith balance for collimation coefficient.

For a given star set, location, start time, etc the maximum values of $I_{R\beta}$ and $I_{C\beta}$ can be investigated for different first azimuths. This author's prediction spreadsheet creates an observing programme based upon selecting a convenient series of stars. The series will depend upon the time and azimuth for the first star to be selected. Therefore, the maximum values of $I_{R\beta}$ and $I_{C\beta}$ will not follow a sine wave, as in the Figures 6.1 and 6.2, above. The following shows maximum values of $I_{R\beta}$ and $I_{C\beta}$ for different first star azimuths of a specimen star programme prediction.

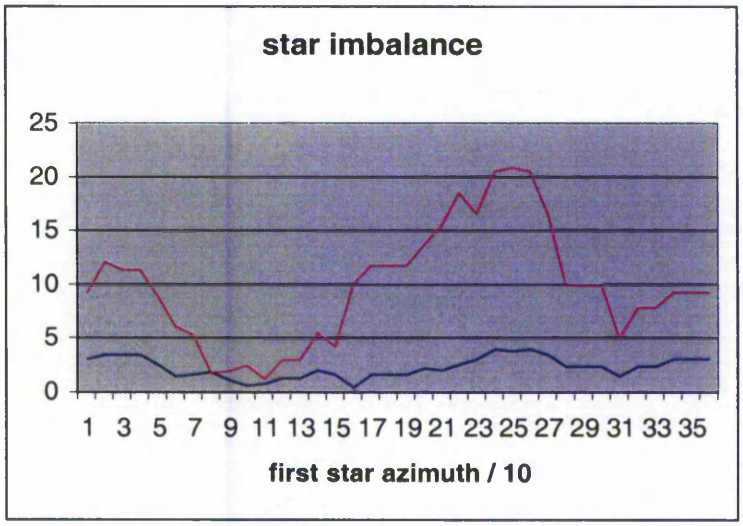

Figure 6.3 Zenith balance for maximum values of $I_{R\beta}$ and $I_{C\beta}$ for different first star azimuths.

In Figure 6.3, the upper, purple, line relates to $I_{C\beta}$ and the lower, blue, line to $I_{R\beta}$. The y-axis is % for $I_{C\beta}$ and degrees (°) for $I_{R\beta}$.

The distribution of stars for a given prediction is shown on a scatter graph in Figure 6.4, below.

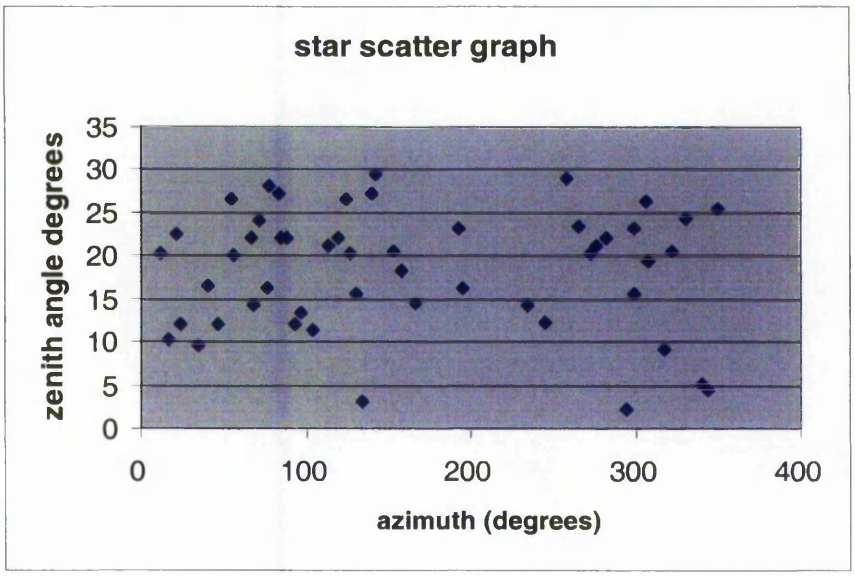

Figure 6.4 Star Scatter Graph for a specimen prediction programme.

This may be examined for any obvious anomalies, in this case a lack of stars in the range 180° to 260°. The star imbalance in latitude, N/S and longitude, E/W may be calculated as:

$$I_{N/S} = \Sigma(z \cos\alpha)/n$$

$$I_{E/W} = \Sigma(z \sin\alpha)/n$$

The units of $I_{N/S}$ and $I_{E/W}$ will be those of z. A value of 0 indicates perfect balance. The other variable of significant interest is the semi-major axis, σ_{max}, of the positional error ellipse. A minimum value is desired. A graph of N/S and E/W imbalance is at Figure 6.5, below.

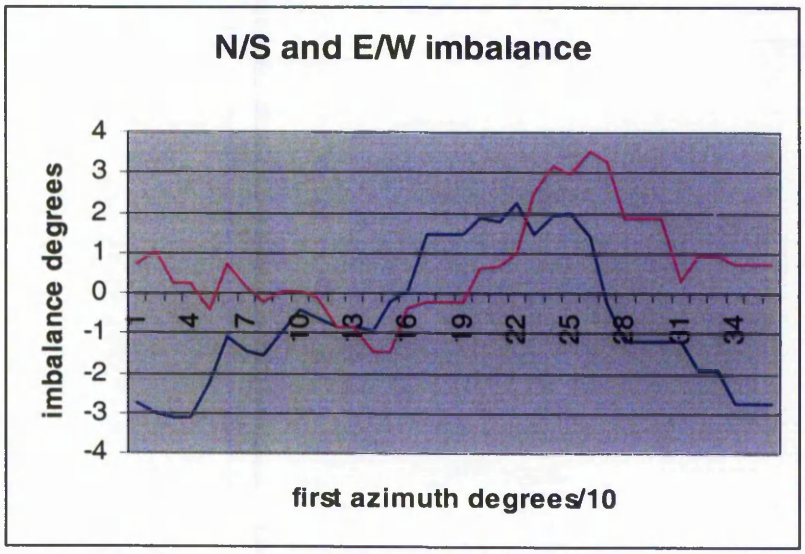

Figure 6.5 Zenith balance in the North-South and East-West directions for a specimen prediction programme.

In Figure 6.5 $I_{N/S}$ is the blue line and $I_{E/W}$ is the purple line.
A summary of all the quality statistics is at Figure 6.6, below.

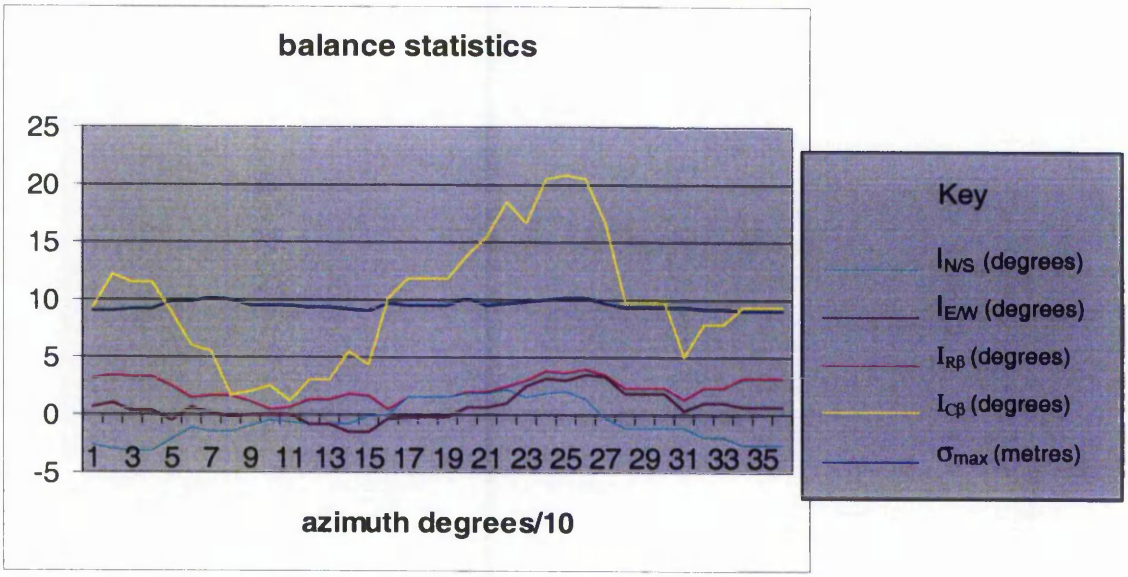

Figure 6.6 Summary of Zenith balance statistics for a specimen prediction programme.

The minimum value of all the quality statistics is most unlikely to fall at the same "first azimuth" as can be seen above. A decision criterion for selecting the best first azimuth must be made taking all the quality statistics, $I_{R\beta}$, $I_{C\beta}$, $I_{N/S}$, $I_{E/W}$, σ_{max} into account. If

absolute values of the statistics are used then their weights will depend upon their units unless some scaling is applied. It was noted that changing the "first azimuth" has little effect upon σ_{max}. The range of σ_{max} is usually less than 10% of its absolute value. Therefore, a single decision statistic that is insensitive to σ_{max} will have little effect upon the absolute value of σ_{max}. The chosen "first azimuth" was the one associated with the minimum value of:

$$\frac{I_{R\beta}}{I_{R\beta(max)}} + \frac{I_{C\beta}}{I_{C\beta(max)}} + \frac{abs(I_{N/S})}{abs(I_{N/S})(max)} + \frac{abs(I_{E/W})}{abs(I_{E/W})(max)} + \frac{\sigma max}{\sigma max(max)}$$

A graph showing the decision statistic to find the optimal "first azimuth" is at Figure 6.7, below.

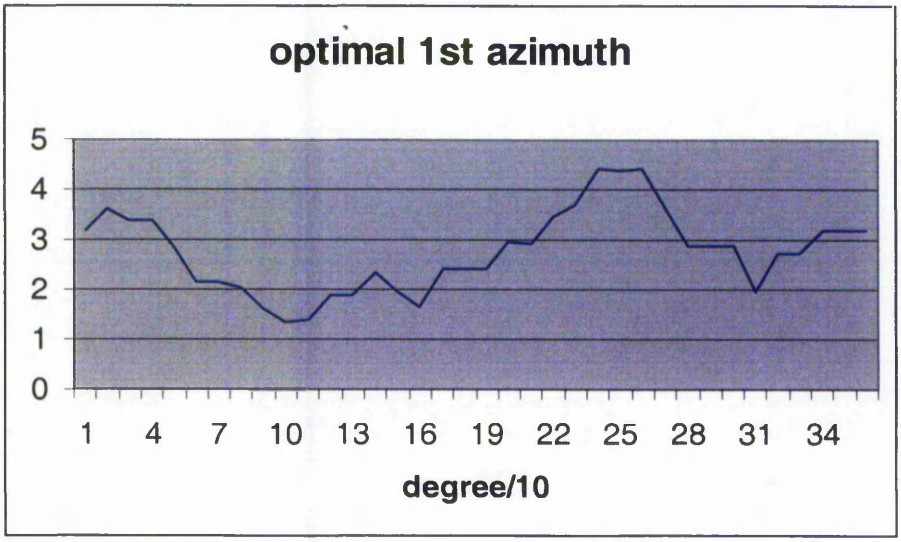

Figure 6.7 Optimal first azimuth for a specimen prediction programme.

In this case, the minimum value is at a first azimuth of 100°.

6.3 Productivity

The productivity associated with a number of possible combinations of technology is summarised below. The statistics are based upon the following assumptions concerned with the time for the various activities.

Set horizontal and vertical pointing to find a star, manual	80 secs
Set horizontal and vertical pointing to find a star, motorised	5 secs
Adjust for a subsequent observation of the same star, manual	15 secs
Adjust for a subsequent observation of the same star, motorised	5 secs
Manually record time	15 secs

Manually record vertical angle	15 secs
Automatically record time	3 secs
Automatically record vertical angle	3 secs
Set up theodolite and orient with Polaris	20 mins
Set up vertical angle data logger	5 mins
Set up time data logger	5 mins
Download automatically recorded time	5 mins
Download automatically recorded vertical angles	5 mins
Download manually recorded time	15 mins
Download manually recorded vertical angles	15 mins
Compute astronomical position	5 mins

Vertical angles are not recorded with a motorised theodolite: they are "set out". Table 6.1, below shows the "productivity" based upon estimated output, that is size of position error ellipse, and time taken on site for a number of different instruments and data recording scenarios.

Table 6.1 Productivity for different instruments and data recording scenarios.

Instrument	time recording	angle recording	No of stars, obs. per star		Error ellipse major axis σ_{max} metres	Observing, set up and processing time t mins	Productivity factor $= \frac{10000}{t\,\sigma^2_{max}}$
TM3000	data log	motorised	50	1	10	32	3.13
TM3000	data log	motorised	10	5	10	32	3.13
TM3000	manual	motorised	50	1	10	47	2.13
TM3000	manual	motorised	10	5	10	47	2.13
T2000	data log	data log	10	5	10	63	1.59
T2000	manual	data log	10	5	10	78	1.28
T2000	data log	manual	10	5	10	78	1.28
T2000	manual	manual	10	5	10	93	1.08
T2000	data log	data log	50	1	10	107	0.93
T2000	manual	data log	50	1	10	122	0.82
T2000	data log	manual	50	1	10	122	0.82
TM1800	data log	motorised	50	1	20	32	0.78
TM1800	data log	motorised	10	5	20	32	0.78
T2000	manual	manual	50	1	10	137	0.73
TM1800	manual	motorised	50	1	20	47	0.53
TM1800	manual	motorised	10	5	20	47	0.53
T1600	data log	data log	10	5	30	63	0.18
T1600	manual	data log	10	5	30	78	0.14
T1600	data log	data log	50	1	30	107	0.1
T1600	manual	data log	50	1	30	122	0.09

As would be expected, the greater the degree of automation, the greater the productivity, but only to a point. A TM3000 theodolite with automated time data logging, is only about four times better than a T2000 theodolite with automatic time, data logging and manual vertical angle recording, the technology available to the author.

6.4 Automating the observing and computing process

The observations may be automated in two ways, digital data capture and servo-driven theodolite pointings. Two separate processes for time data capture were considered. One involved a sensitive photodiode and the other, a video camera.

6.5 Photodiode method

In the photodiode method the passage of a star is to be detected by a single sensitive photodiode. The issues associated with the photodiode method are:

- Precise timing of star observations
- Detection of star passage over the theodolite crosshair
- Determination of time of star passage over the theodolite crosshair

6.5.1 Precise timing of star observations

A one-millisecond systematic error in absolute time is equivalent to an error of approximately 0.3 metres in longitude at mid-latitudes, e.g. Nottingham. The level of acceptable systematic error in position and time will depend upon the specification for the determination of the geoid model.

A number of time transfer software packages for PCs are listed at Uber (2001). Most of the products are designed to update a PC clock through the Internet or with a modem. As a result, the accuracies that can be achieved are limited. This is especially true with a modem because of the uncertain time delays in the telephone networks. For example BBC (2001) can give a 500ms solution with a 25 second telephone call. Better results are claimed with longer, and therefore more expensive calls. None of the PC solutions could work with a laptop in the field unless a modem and mobile phone were also available.

The most accessible sources of absolute time are the Global Positioning System (GPS) and radio time signals. The most precise solution would come from GPS where time transfer can be achieved in theory to a few nanoseconds and in practice to much better than 1 microsecond. The disadvantage of GPS is that additional hardware would be required.

Radio time signals can be received on a simple short-wave radio. HMSO (1995) lists a number of time signals that can be received worldwide. This investigation concentrates on the time signals from RWM Moscow. This station has been chosen because the signals can be received throughout much of Europe, Asia and North Africa although the signal quality can be poor at times. Therefore, if absolute time of acceptable quality can be achieved with this station other stations with better more reliable signal quality could also be used with results at least equally as good. The signals are broadcast on the 4.996, 9.996 and 14.996 MHz frequencies from 10^m - 20^m and 40^m - 50^m past each hour.

Second markers are 100ms long and minute markers are 500ms long. Some second markers are doubled to encode DUT1.

Initial investigations used a Roberts 801 short-wave radio and an oscilloscope to display the signal output. It was found that even with a noisy audible signal the presence of the second markers was identifiable on the oscilloscope as a faint DC voltage pulse. DC voltage output at the earphone socket was recorded on a Schlumberger data logger. The mean DC voltage at $^1/_{80}$ second epochs gave little clue as to the location of the one second pulse. A graph of typical vales is at Figure 6.8, below.

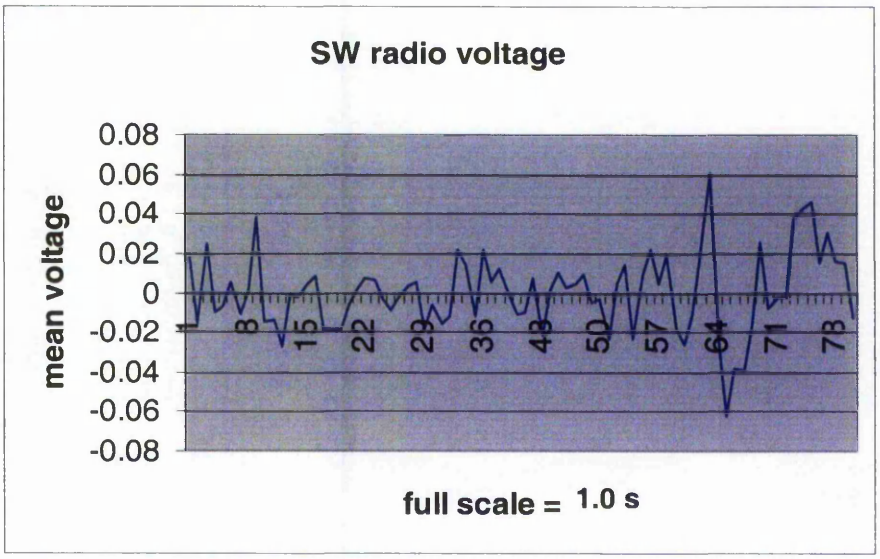

Figure 6.8 Short-wave radio mean voltage at the earphone socket for 80 successive 1/80-second periods. Time and date 0811-0820 on 27/1/98 at frequency 14.995MHz.

In Figure 6.8, the means of the same segment of each 1-second period over the interval 08:11 to 08:20 on 27 January 1998 are shown. The time signal is from RWM Moscow on 14.995 MHz.

However, the one-second pulse could be extracted from the data by investigating the mean squared DC voltage at $^1/_{80}$-second epochs. A graph of typical values is in Figure 6.9, below.

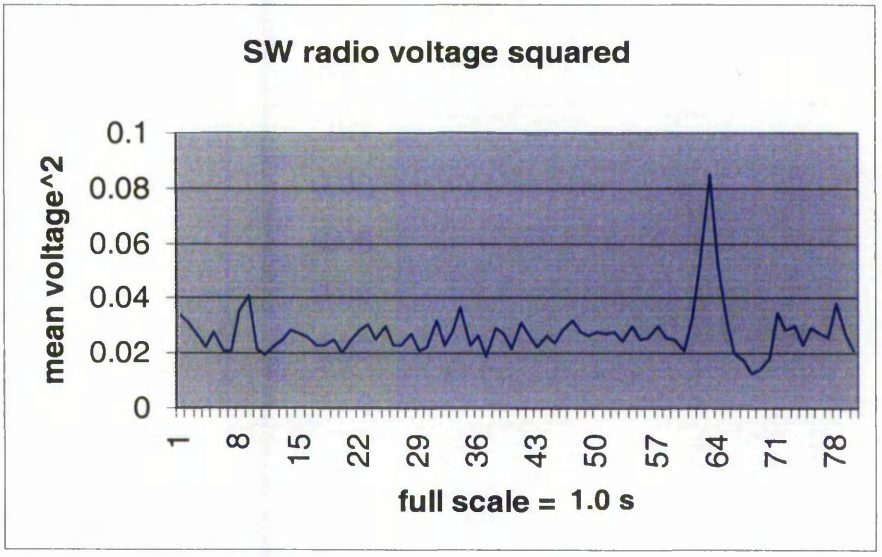

Figure 6.9 Short-wave radio mean voltage at the earphone socket, squared, for 80 successive 1/80-second periods. Time and date 0811-0820 on 27/1/98 at frequency 14.995MHz.

The proof that the peak at $^{64}/_{80}$ of a second, in Figure 6.9, represents the second marker may be seen from the results of repetitions of the experiment carried out several times during the same day. The results are in Figure 6.10, below.

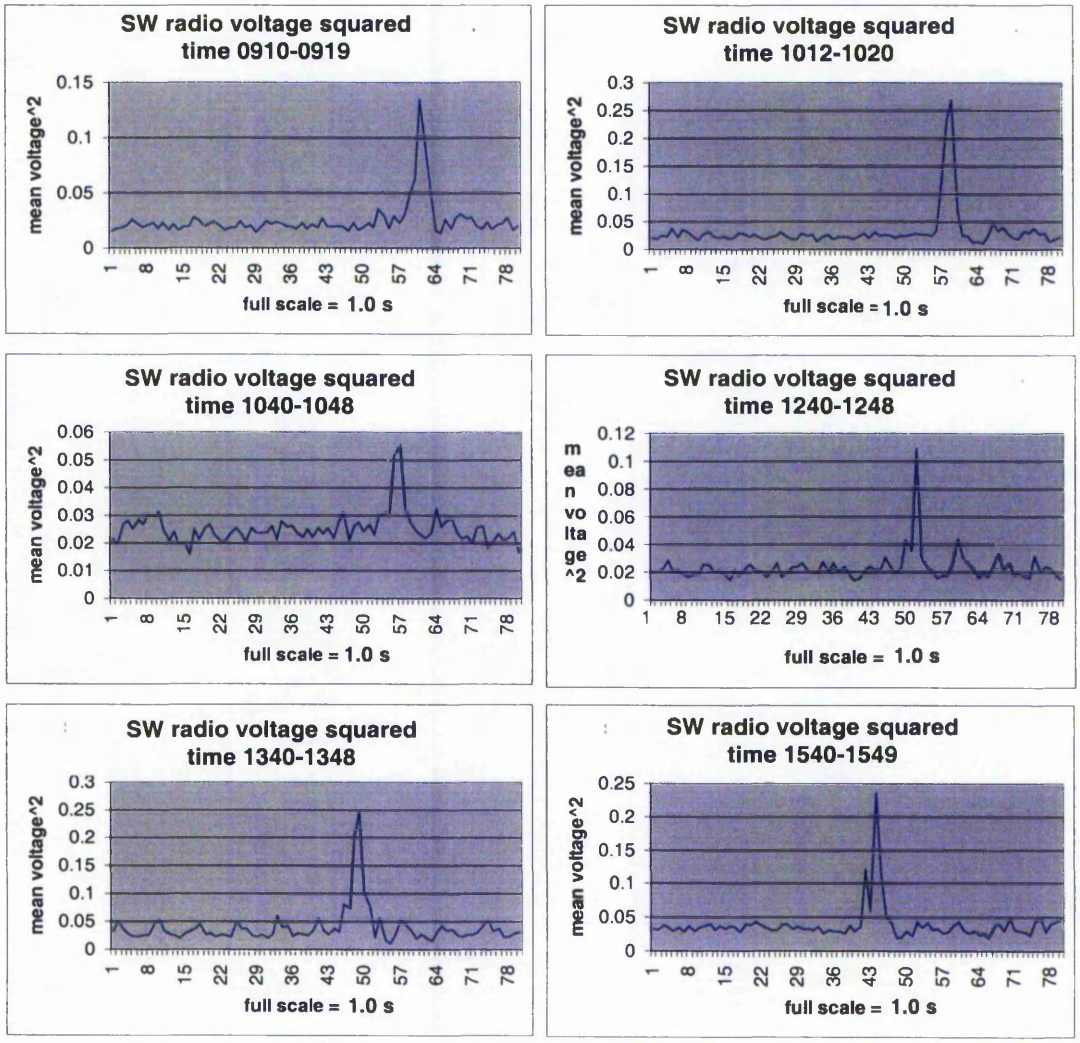

Figure 6.10 Short-wave radio mean voltage at the earphone socket, squared, for 80 successive 1/80-second periods at six different times on the same day. Time as shown, date 27/1/98, frequency 14.995MHz.

The graph of the times of the peaks, within the second, against time during the day, in Figure 6.11 below, shows that there is a near linear drift in the data logger clock.

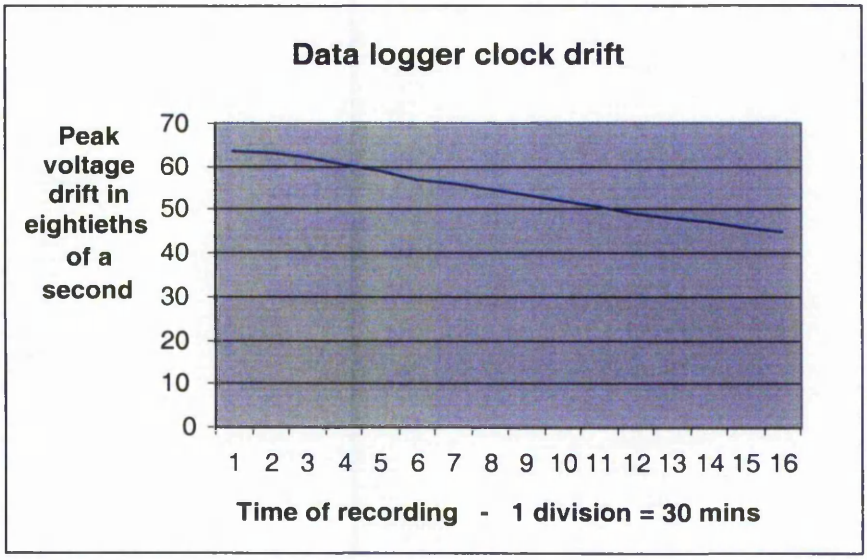

Figure 6.11 Variation of peak voltage during a day.

6.5.1.1 Radio time signal delays

There is a time delay between transmission of the time signal and receipt at the data logger. The delay is made up of 2 parts. The radio waves travel at a finite speed from transmitter to receiver. The receiving radio takes time to process the signals. The time delay from transmitter to receiver, assuming a spherical earth, is given by:

$$\text{delay} = R \cos^{-1}(\sin\phi_t \sin\phi_r + \cos\phi_t \cos\phi_r \cos\Delta\lambda)\, c^{-1}$$

where c is the speed of radio waves (speed of light)

R is the radius of the earth

ϕ_t is the latitude of transmitter

ϕ_r is the latitude of receiver

$\Delta\lambda$ is the difference in longitude between transmitter and receiver.

The propagation delay for time signals from RWM Moscow, received at Nottingham, for example, is 0.0083 seconds.

To investigate the delay in a short wave radio an RF signal generator producing signals on a frequency near that of one of the RWM Moscow signals was connected to the aerial of a Roberts 801 radio. A storage oscilloscope was connected to both aerial and earphone socket. The signal delay was scaled off the display and estimated to be 0.0002 seconds with an uncertainty of 0.00002 seconds. Therefore, it was concluded that the electronic delays in the short-wave radio could be considered as negligible.

6.5.2 Detection of star passage over the theodolite crosshair

The chosen mechanism for detecting the passage of a star over the theodolite crosshair was continuously to measure the total amount of light collected by the telescope. When a star goes behind a crosshair, the total amount of light will be reduced because the star is obscured. Therefore, a momentary minimum light level will indicate the instant that the star is fully hidden by the crosshair or that the crosshair straddles the star. However, it may be that another star appears or disappears from the field of view or that cloud cover interferes with the light levels. In that case, there may be errors in the detection of the time of star transit.

The total amount of light collected by the telescope was to be measured by a single, very sensitive photodiode. The light was to be focused on the crosshair in the normal way. The sensitivity of the required photodiode is computed as follows.

Total power emitted by the sun (Rees, 1994) $= 4\pi R^2 \sigma T_S^4$

where R is the radius of the sun (m)

σ is the Stefan-Boltzman constant, ($5.671\ 10^{-8}$ W m^{-2} K^{-4})

T_S is the sun's effective temperature, (5800 °K)

At distance D from the sun the power per unit area is:

$$\frac{4\pi R^2 \sigma T_S^4}{4\pi D^2} = \frac{R^2 \sigma T_S^4}{D^2}$$

If the radius of the theodolite objective lens is r then the total power entering the lens is given by:

$$\text{Total power} = \frac{2\pi r^2 R^2 \sigma T_S^4}{D^2}$$

A mean value for R/D is 16' (HMSO 1995), or 0.0046 radians. Therefore the total power entering the lens is $8500r^2$ W. If the objective lens has a radius of 2 cm, the total power is 3.4 W. The magnitude of the sun, in astronomical terms, is -26. A star with a magnitude of 4 is 2.51^{-30} ($\approx 10^{-12}$) less bright than the sun and therefore will radiate 10^{-12} as much power onto the objective lens. For an objective lens with a radius of 2 cm that will be $3.4\ 10^{-12}$ W. This assumes that all radiant flux leaving the sun is detected by the photodiode: in particular that all radiant flux impacting upon the objective lens finds its way to the photodiode. Clearly there will be losses within the telescope optics and therefore a more realistic amount of light arriving on the photodiode for a star of magnitude 4 will be *very* approximately $2\ 10^{-12}$ W. A table of magnitudes and radiant flux has been constructed using this assumption, Table 6.2.

Table 6.2 The radiant flux, in watts, through a 2 cm theodolite telescope from stars of different magnitudes.

Star magnitude	Radiant flux W
0	$5\ 10^{-11}$
1	$2.5\ 10^{-11}$
2	$1\ 10^{-11}$
3	$5\ 10^{-12}$
4	$2\ 10^{-12}$
5	$8\ 10^{-13}$
6	$3.2\ 10^{-13}$
7	$1.3\ 10^{-13}$

A catalogue of photodiodes, Hamamatsu (1996), indicated that most photodiodes had an undefined response to a radiant flux of less than 10^{-12}W. Advice received by the author, from the company, was to use a S5590 Si photodiode with preamp integrated with feedback resistance and capacitance. This photodiode has a photosensitivity of 0.5 V/nW for light of wavelength 960 nm and of 0.1 V/nW for light of wavelength 200 nm. Therefore, the anticipated output voltage for a star of magnitude 4 would be of the order of 100-1000 μV.

A photodiode holder to replace the eyepiece of a number of Leica and Geodimeter theodolites was constructed, partly from a dismantled Wild T2 theodolite eyepiece. A sketch of the inner part of the eyepiece with mountings for the photodiode is at Figure 6.12, below.

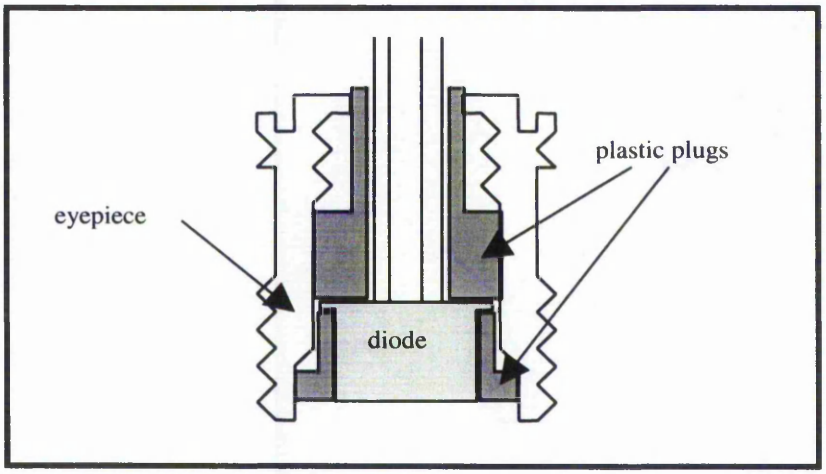

Figure 6.12 Theodolite eyepiece modified for a photodiode.

6.5.3 Determination of time of star passage over the theodolite crosshair

In the absence of atmospheric scintillation, the passage of star over a crosshair could be represented diagrammatically as in Figure 6.13, below.

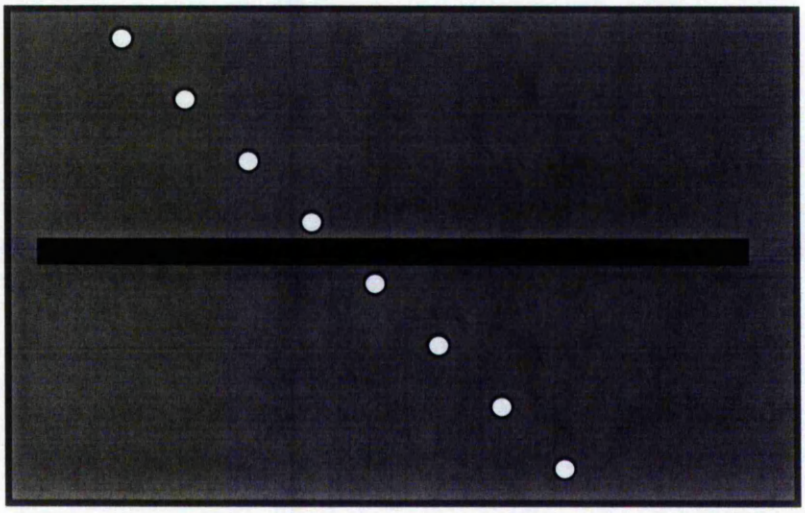

Figure 6.13 Diagrammatic representation of the passage of star over a crosshair.

The radiant flux would then be of the form of Figure 6.14, below.

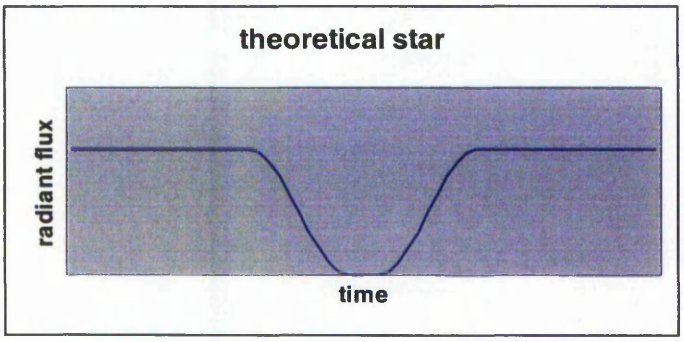

Figure 6.14 The form of the radiant flux as a star passes over a crosshair.

With atmospheric scintillation and other background fainter stars, the real situation is more like that in the diagram in Figure 6.15, below. Therefore the true form of the radiant flux as a star passes over a crosshair is more likely to be as shown in Figure 6.16.

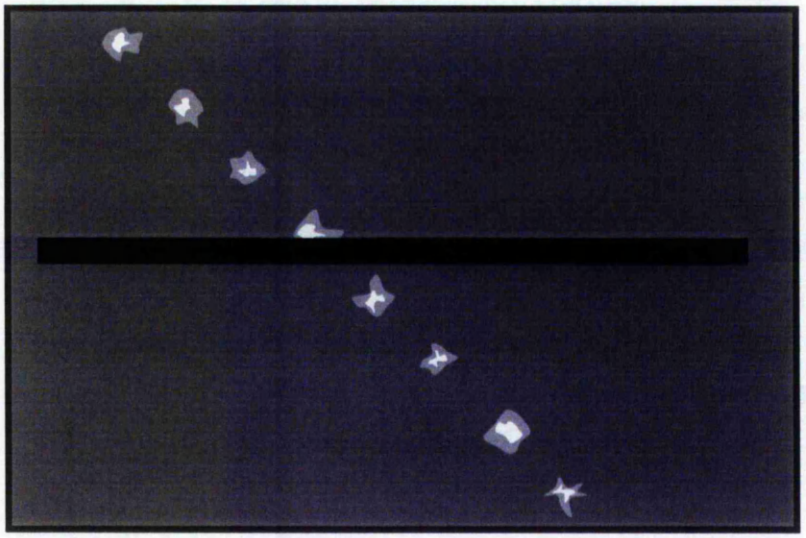

Figure 6.15 Diagrammatic representation of the passage of a star over a crosshair, with scintillation.

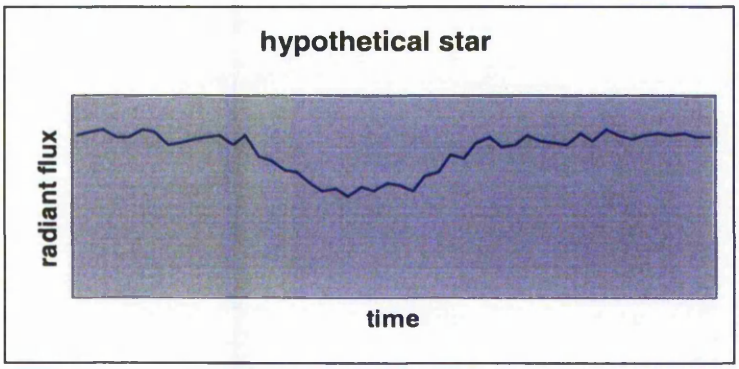

Figure 6.16 The form of the radiant flux as a star passes over a crosshair, with scintillation.

The time of the passage of the star is determined by application of a form of auto-correlation function combined with a least squares fit of a "theoretical star". Figure 6.17, below, shows two stars passing a horizontal crosshair. Star A is smaller than the width of the crosshair. Star B is larger. The stars are descending in line with a positive rate of change of zenith angle.

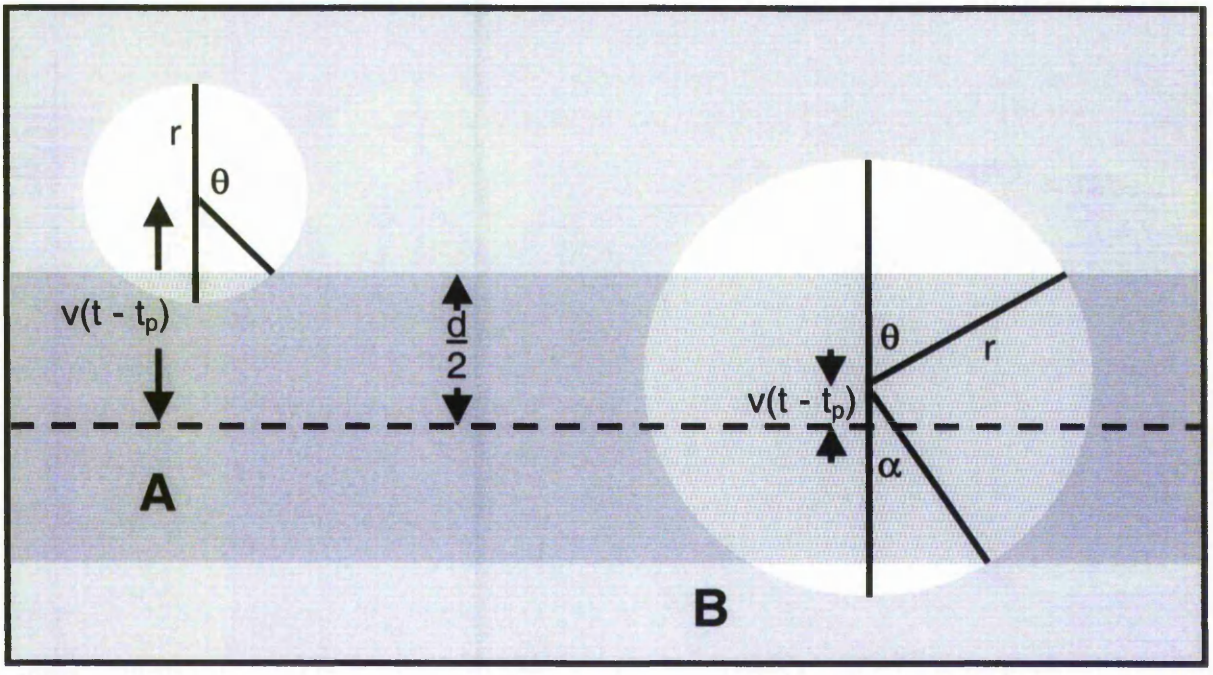

Figure 6.17 The geometry of two stars passing a crosshair.

In the following:

t_p	is the time of passage of the star
r	is the radius of the star
d	is thickness of the crosshair
v	is the velocity of the star perpendicular to the crosshair
F	is the radiant flux of the star when the star is not obscured

The radiant flux, f, will be as follows:

with respect to a star in position A in Figure 6.17

$f = F$ if $v(t - t_p) < -(r + \frac{1}{2}d)$

$f = F(2\theta - \frac{1}{2}\sin 2\theta)\pi^{-1}$ if $-(r + \frac{1}{2}d) < v(t - t_p) < (r - \frac{1}{2}d)$

with respect to a star in position B in Figure 6.17

$f = 0$ if $(\frac{1}{2}d - r) > v(t - t_p) > -(\frac{1}{2}d - r)$ and if $r < \frac{1}{2}d$

$f = F(2\theta + 2\alpha - \frac{1}{2}\sin 2\theta - \frac{1}{2}\sin 2\alpha)\pi^{-1}$ if $-(\frac{1}{2}d - r) > v(t - t_p) > (\frac{1}{2}d - r)$ and if $r > \frac{1}{2}d$

and when a star emerges below the crosshair

$f = F(2\theta - \frac{1}{2}\sin 2\theta)\pi^{-1}$ if $-(r + \frac{1}{2}d) > v(t - t_p) > (r - \frac{1}{2}d)$

$f = F$ if $v(t - t_p) > -(r + \frac{1}{2}d)$

and θ and α are given by:

$\theta = \cos^{-1}((\frac{1}{2}d + v(t - t_p))r^{-1})$ if $(t - t_p) > 0$

$= \cos^{-1}((\frac{1}{2}d - v(t - t_p))r^{-1})$ if $(t - t_p) < 0$

$\alpha = \cos^{-1}((\frac{1}{2}d - v(t - t_p))r^{-1})$ if $(t - t_p) > 0$

$= \cos^{-1}((\frac{1}{2}d + v(t - t_p))r^{-1})$ if $(t - t_p) < 0$

In the above, the scale of the distance units of r, d and v are undefined. They can be defined in terms of d, where for simplicity, d takes the value of 2. The above equations therefore simplify as in Table 6.3, below.

Table 6.3 Summary of radiant flux equations as a star passes a crosshair.

No	Equation	Conditions for application
1	$0 = f_o - F - B$	all r $v(t-t_p) < -(r+1)$
2a	$0 = f_o - F(2\theta - \frac{1}{2}\sin 2\theta)\pi^{-1} - B$	$r < 1$ $-(r+1) < v(t-t_p) < r-1$
2b	$0 = f_o - F(2\theta - \frac{1}{2}\sin 2\theta)\pi^{-1} - B$	$r > 1$ $-(r+1) < v(t-t_p) < 1-r$
3a	$0 = f_o - B$	$r < 1$ $r-1 < v(t-t_p) < 1-r$
3b	$0 = f_o - F(2\theta + 2\alpha - \frac{1}{2}\sin 2\theta - \frac{1}{2}\sin 2\alpha)\pi^{-1} - B$	$r > 1$ $1-r < v(t-t_p) < r-1$
4a	$0 = f_o - F(2\theta - \frac{1}{2}\sin 2\theta)\pi^{-1} - B$	$r < 1$ $1-r < v(t-t_p) < -(1+r)$
4b	$0 = f_o - F(2\theta - \frac{1}{2}\sin 2\theta)\pi^{-1} - B$	$r > 1$ $r-1 < v(t-t_p) < -(1+r)$
5	$0 = f_o - F - B$	all r $v(t-t_p) < -(1+r)$

$$\theta = \cos^{-1}((1 + v(t - t_p))r^{-1}) \quad \text{if } (t - t_p) > 0$$
$$= \cos^{-1}((1 - v(t - t_p))r^{-1}) \quad \text{if } (t - t_p) < 0$$

$$\alpha = \cos^{-1}((1 - v(t - t_p))r^{-1}) \quad \text{if } (t - t_p) > 0$$
$$= \cos^{-1}((1 + v(t - t_p))r^{-1}) \quad \text{if } (t - t_p) < 0$$

where f_o is the observed radiant flux

B is the background radiant flux

If $r < 1$, then for a star crossing the crosshairs, equations 1, 2a, 3a, 4a and 5, in order will apply. If $r > 1$ then for a star crossing the crosshairs, equations 1, 2b, 3b, 4b and 5, in order will apply. Each observation must be examined, based on provisional values of r, v and t_p, to determine which of the above observation equations applies.

The photodiode is very sensitive to temperature changes and therefore a term, $A(t - t_p)$, will also be required to account for a constant rate of change of voltage with time in the absence of signal. A describes the slope and t_0 is an arbitrary start time such as the time of the first observation. For each of the above observation equations the linearised form of each observation equations is below.

$$\mathbf{x} = \begin{bmatrix} \delta r \\ \delta v \\ \delta t_p \\ \delta F \\ \delta B \\ \delta A \end{bmatrix}$$

and the units are

r	2d
v	2d second^{-1}
t	second
F, B and A	arbitrary units of data logger output

$$\mathbf{A} = \begin{bmatrix} \frac{\partial f_o}{\partial r} & \frac{\partial f_o}{\partial v} & \frac{\partial f_o}{\partial t_p} & \frac{\partial f_o}{\partial F} & \frac{\partial f_o}{\partial B} & \frac{\partial f_o}{\partial A} \\ .. & .. & .. & .. & .. & .. \end{bmatrix}$$

A template for **A** is as follows:

1	0	0	0	-1	-1	$(t-t_0)$
2a & 2b	$-2F(1-v(t-t_p))(1-((1-v(t-t_p))r^{-1})^2)^{½}\pi^{-1}r^{-2}$	$-2F(t-t_p)(1-((1-v(t-t_p))r^{-1})^2)^{½}\pi^{-1}r^{-1}$	$2Fv(1-((1-v(t-t_p))r^{-1})^2)^{½}\pi^{-1}r^{-1}$	$-(\theta-½\sin 2\theta)\pi^{-1}$	-1	$(t-t_p)$
2a & 2b	$-2F(1+v(t-t_p))(1-((1+v(t-t_p))r^{-1})^2)^{½}\pi^{-1}r^{-2}$	$2F(t-t_p)(1-((1+v(t-t_p))r^{-1})^2)^{½}\pi^{-1}r^{-1}$	$-2Fv(1-((1+v(t-t_p))r^{-1})^2)^{½}\pi^{-1}r^{-1}$	$-(\theta-½\sin 2\theta)\pi^{-1}$	-1	$(t-t_p)$
3a	0	0	0	0	-1	$(t-t_p)$
3b	$-2F\{(1-v(t-t_p))(1-((1-v(t-t_p))r^{-1})^2)^{½} + (1+v(t-t_p))(1-((1+v(t-t_p))r^{-1})^2)^{½}\}\pi^{-1}r^{-2}$	$-2F(t-t_p)\{(1-((1-v(t-t_p))r^{-1})^2)^{½} - (1-((1+v(t-t_p))r^{-1})^2)^{½}\}\pi^{-1}r^{-1}$	$2Fv\{(1-((1-v(t-t_p))r^{-1})^2)^{½} - (1-((1+v(t-t_p))r^{-1})^2)^{½}\}\pi^{-1}r^{-1}$	$-(\theta+\alpha-½\sin 2\theta - ½\sin 2\alpha)\pi^{-1}$	-1	$(t-t_p)$
4a & 4b	$-2F(1-v(t-t_p))(1-((1-v(t-t_p))r^{-1})^2)^{½}\pi^{-1}r^{-2}$	$-2F(t-t_p)(1-((1-v(t-t_p))r^{-1})^2)^{½}\pi^{-1}r^{-1}$	$2Fv(1-((1-v(t-t_p))r^{-1})^2)^{½}\pi^{-1}r^{-1}$	$-(\theta-½\sin 2\theta)\pi^{-1}$	-1	$(t-t_p)$
4a & 4b	$-2F(1+v(t-t_p))(1-((1+v(t-t_p))r^{-1})^2)^{½}\pi^{-1}r^{-2}$	$2F(t-t_p)(1-((1+v(t-t_p))r^{-1})^2)^{½}\pi^{-1}r^{-1}$	$-2Fv(1-((1+v(t-t_p))r^{-1})^2)^{½}\pi^{-1}r^{-1}$	$-(\theta-½\sin 2\theta)\pi^{-1}$	-1	$(t-t_p)$
5	0	0	0	-1	-1	$(t-t_p)$

where *2a & 2b* and *4a & 4b* apply if $(t - t_p) < 0$

2a & 2b and *4a & 4b* apply if $(t - t_p) > 0$

Much effort was expended into trying to get this method to work. Although the photodiode was capable of detecting the light from distant street lamps, no recognisable signals were received from stars. It seems that thermal noise in the photodiode may the have been well in excess of the signal from the star. The only solution would have been

to employ some form of cooling around the diode. Although liquid nitrogen may have achieved the desired effect, there would have been significant danger to personnel if it had been used in the field. This approach was abandoned.

6.6 Video camera method

In the video camera method, the passage of the star is to be detected using a video camera. A Pulnix black and white camera was mounted on the telescope of a Wild T2000 electronic theodolite as in Figure 6.18 below.

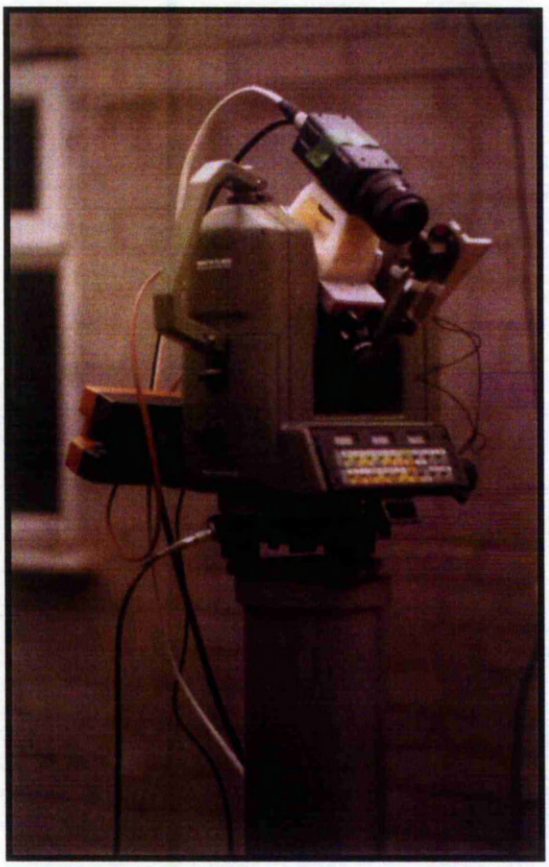

Figure 6.18 T2000 with video camera.

The camera sees exactly what the conventional observer would see except that the video image is only of the central portion of the theodolite crosshairs. The video camera is set to maximum aperture and focused at infinity. Theodolite crosshairs, and then theodolite telescope, are focused in the normal way except that the observer's view is on a TV screen. Data is captured using a video capture board controlled by a LABVIEW "virtual instrument". The data is then analysed in a spreadsheet.

The issues associated with the use of a video camera method are:

- Precise linkage of time to a video frame
- Determination of the motion of the image of the star
- Determination of the theodolite horizontal crosshair in the video image
- Determination of the time of star image passing the horizontal crosshair image

6.6.1 Precise linkage of time to a video frame

For this method, time was taken from GPS because that was the most precise and practical solution available. Impersonal absolute timing has always been an issue with geodetic positional astronomy. Where the observational data is recorded on videotape or analysed electronically the element of personal judgement is, at least, largely removed. The method of determining absolute time chosen for this project was to create a small light flash every 10 seconds of GPS time. A small electronic circuit was designed and manufactured for this author. The input trigger was taken from the timing output, a negative spike, of a Leica System 300 GPS receiver. The circuit was designed so that the flash of an LED started at the spike and could be set to last for 10ms to 100ms in increments of 10ms, i.e. 10 possible settings.

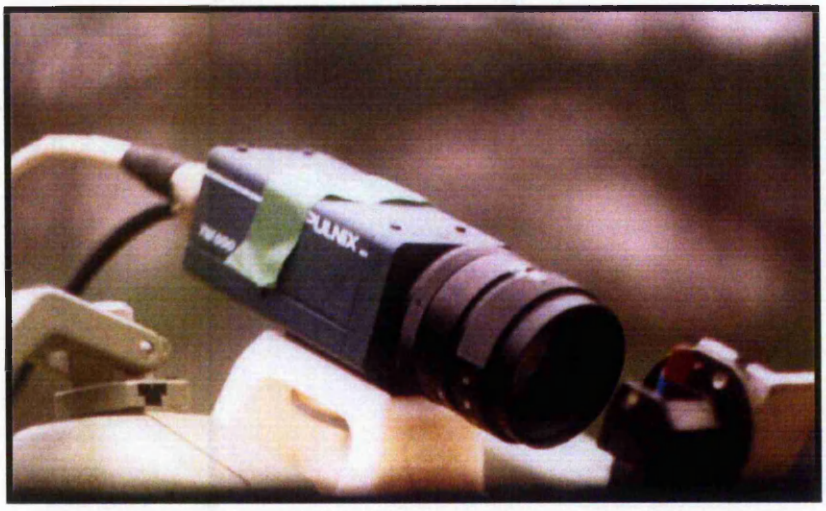

Figure 6.19 The LED (red object at bottom right of photo) connected to the "GPS flasher" circuit.

If a flash of 40ms were chosen, then either part of two video frames or one whole video frame would be exposed. In the former case, timing could be determined exactly but in the latter, the general case, there would be some ambiguity.

Within each 40ms cycle of the video camera there is a period of exposure and a period of non-exposure. A flash, depending upon its length could fall:

- Entirely within the period of non-exposure
- Entirely within a single period of exposure
- Partly in a period of exposure, in the whole of the following period of non-exposure and partly in the following period of exposure
- Partly in a period of non-exposure, in the whole of the following period of exposure and partly in the following period of non-exposure.

The time of interest is the epoch at the mid-point of exposure of a frame. A theoretical solution for finding this epoch is described. See Figure 6.20, below.

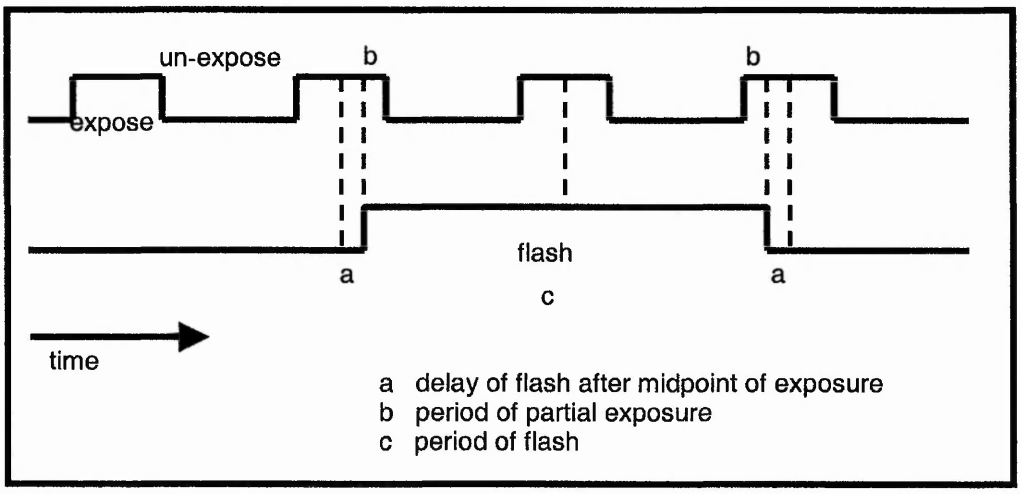

Figure 6.20 Diagrammatic relationship of video frame exposure and GPS flash.

The period of flash is adjusted until there is equal exposure of two frames separated by a frame of equal or greater exposure. In this situation, the middle of the flash is at the middle of the second exposure. In this case:

$$a = 40ms - {}^{c}/_{2}$$

If the exposure of the first two frames is equal then it indicates that the start of the flash lies somewhere in the unexposed part of the video cycle and the above method will not work. In this case, the maximum flash period for no exposure and minimum period for full exposure are found, as in Figure 6.21, below.

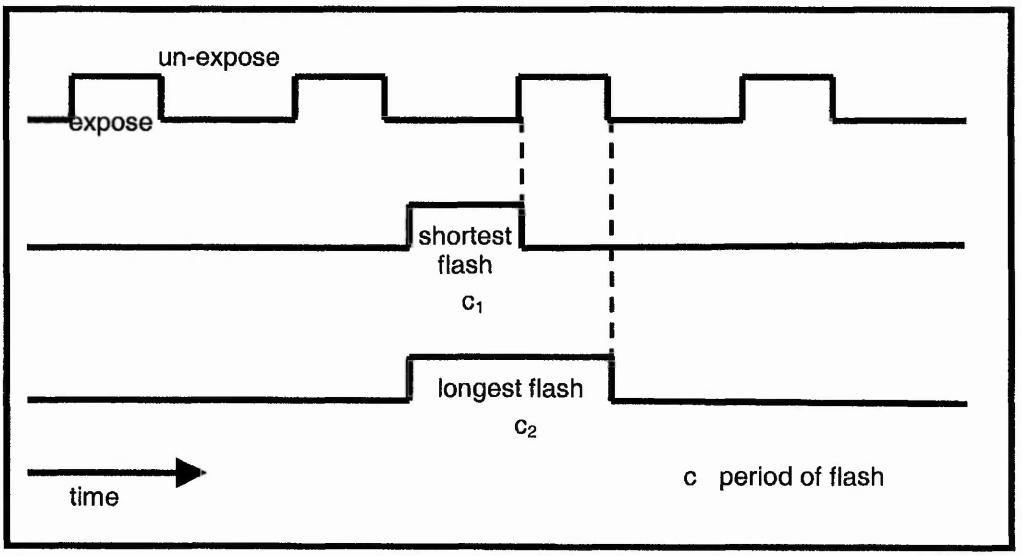

Figure 6.21 Diagrammatic relationship of video frame exposure and GPS flash to find maximum flash period for no exposure and minimum period for full exposure.

In this case the delay of the midpoint of exposure is given by:

$$\text{delay} = \tfrac{1}{2}(c_1 + c_2)$$

A flash rate of once every 10 seconds was chosen as a comfortable rate at which the resolution of integer ambiguity could be assured. If there was an error of identification of the correct 10 second epoch it would reflect as a 150" error in computed longitude and hence in deviation in the prime vertical. Therefore, there is no need to record which 10-second epoch the system is calibrated with; only the right epoch will give a sensible answer.

6.6.2 Determination of the motion of the image of the star

A LABVIEW "virtual instrument" programme was written to collect suitable data via a video capture board and output to a file that could be read into a spreadsheet. For each video frame, the row average of the pixel values for each row is read to file. The average is more sensitive to the presence of a star if the row is short. The file size is proportional to the number of rows and the number of frames. The image size also affects the maximum possible frame rate. The chosen frame size was reduced to 60 pixels square. That represents, approximately a 60 arc second square. The wiring diagram of the "virtual instrument" (.vi file) and the control interface are shown in Figure 6.22, below.

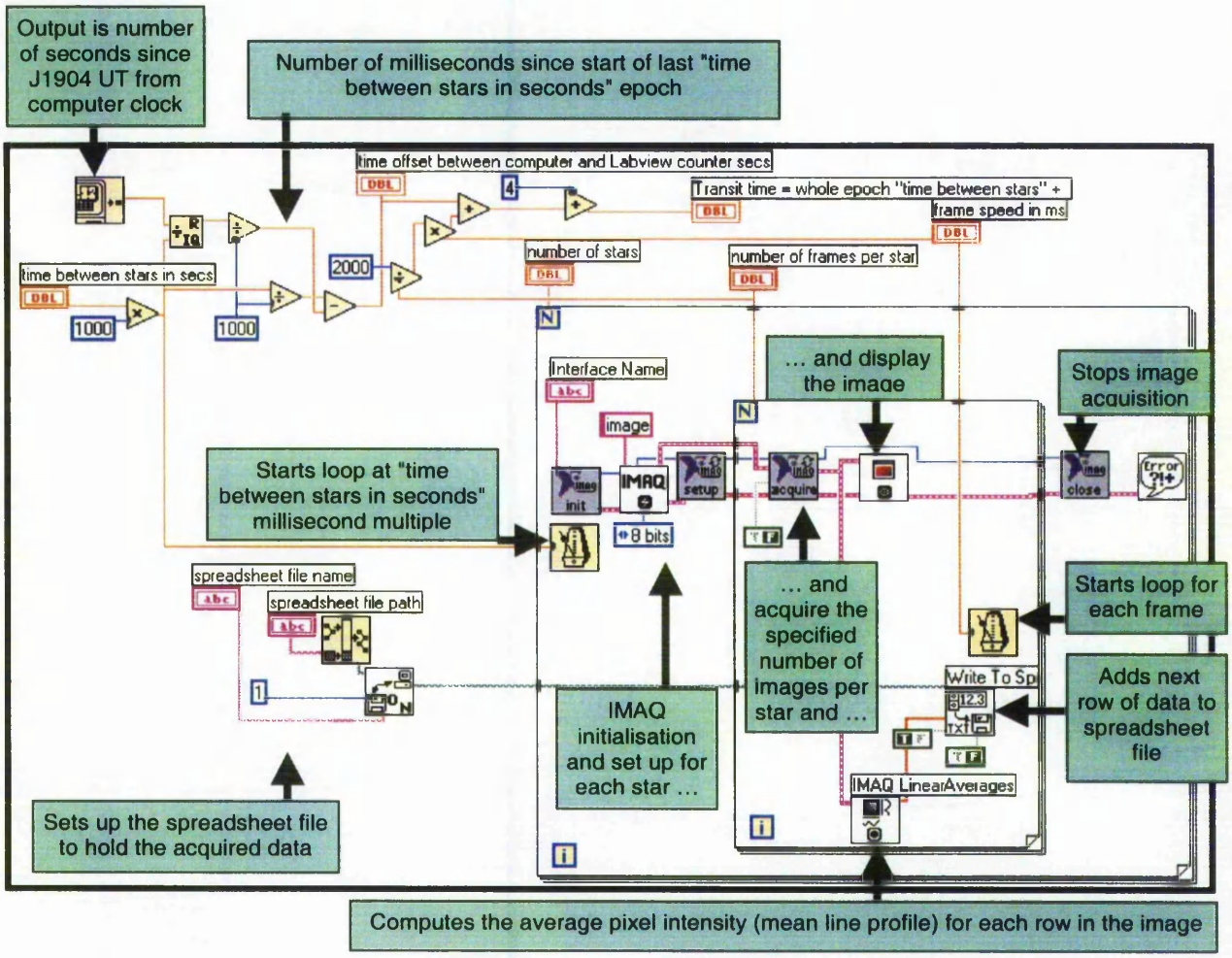

Figure 6.22 Annotated wiring diagram of the LABVIEW "virtual instrument" (.vi file) used for video frame data capture.

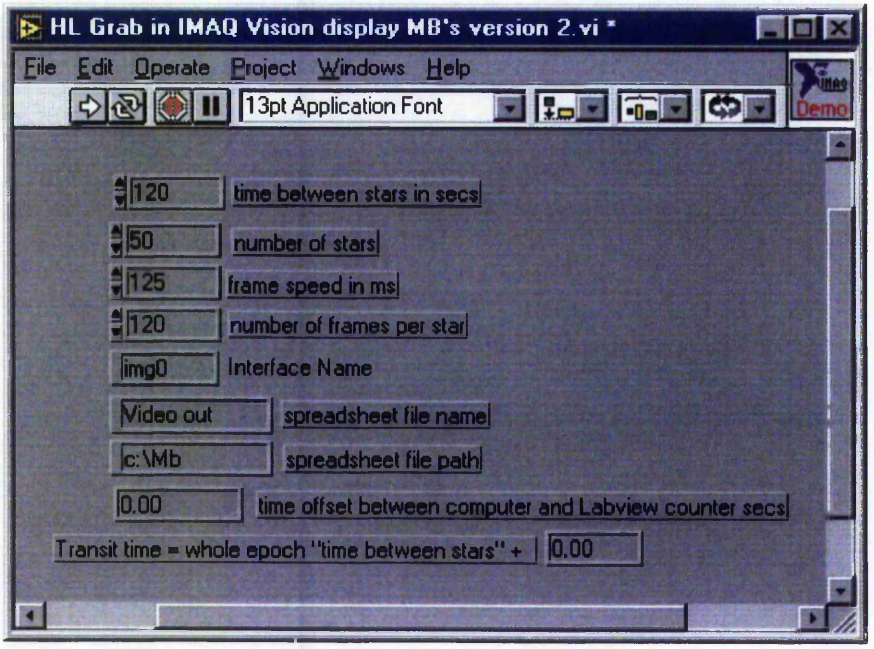

Figure 6.23 User interface for the "virtual instrument" (.vi file) used for video data capture.

In Figure 6.23, above, the interface is set to collect data for 50 stars at 2-minute intervals at 8 frames/second (a limitation of the computer used) for 15 seconds for each star.

The 60 pixel square window is centred on a gap in the horizontal crosshairs as in Figure 6.24, below.

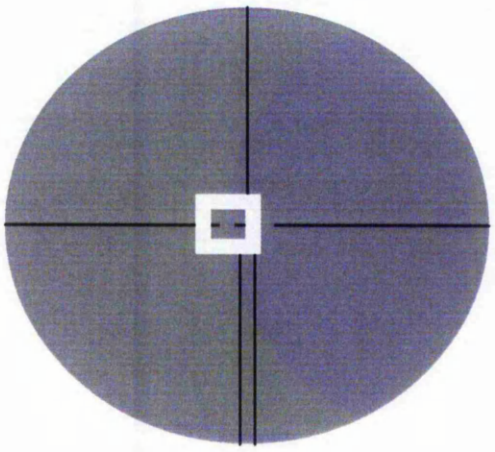

Figure 6.24 The 60 pixel square window is centred on a gap in the horizontal crosshairs.

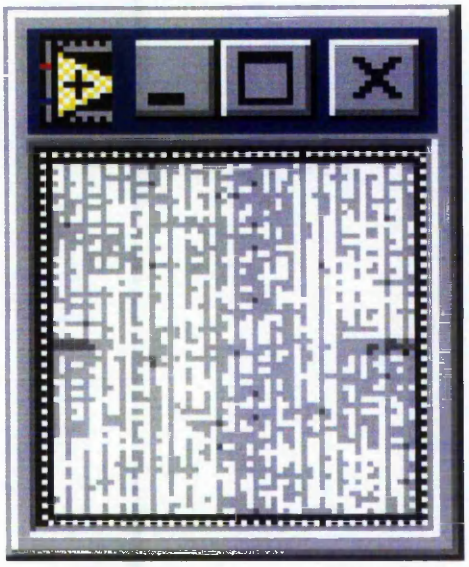

Figure 6.25 Screen shot of 60 pixel square window.

In Figure 6.25, above, the ends of the horizontal crosshair on either side of the gap can be seen. The background is light because the crosshairs are being illuminated. When waiting for a star to appear the whole image is black.

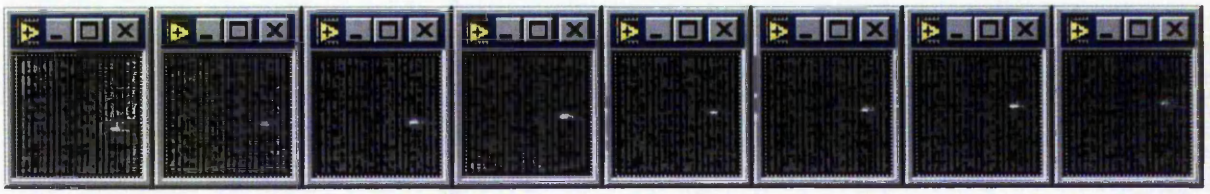

Figure 6.26 Screen shots of Polaris.

Figure 6.26, above, shows eight screen shots of Polaris. The shots are about 10 seconds of time apart, although the time intervals between shots are not equal. Figure 6.27 shows a blow-up of the star from each shot in Figure 6.26. The blow-ups show the variable effects of scintillation on the received image of the star. Note that the stars look flat. This is because the video is "non-interlaced". Interlacing is a technique of scanning alternate odd numbered lines followed by a scan of even numbered lines. When the video is "non-interlaced" only alternate lines are scanned.

Figure 6.27 Blow-up of Screen shots of Polaris.

As one would expect, brighter stars have bigger images. Figure 6.28, below, shows screen shots for stars of variable magnitude. Although the 3.4 magnitude barely appears on the screen, it is still detectable in the processing.

Figure 6.28 Screen shots for stars of magnitude, in order, 0.1, 1.2, 1.9, 2.1, 2.7 and 3.4.

The file created by this data capture process is copied into a spreadsheet and the parameters of the motion of the star are determined by least squares. An example of a set of data for one star is in Figure 6.29, below.

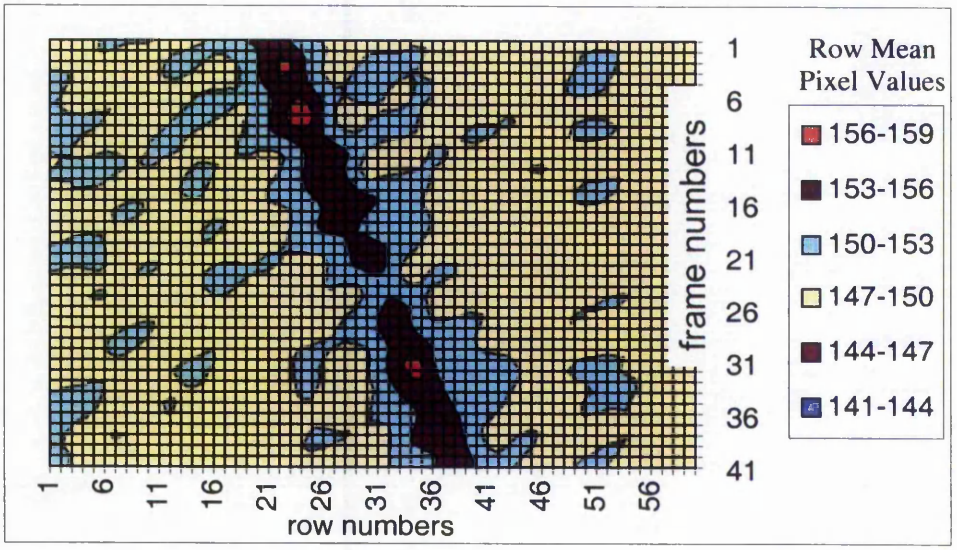

Figure 6.29 Graphical representation of data from the passage of one star.

The row mean pixel values from top row to bottom row of one 60 by 60 pixel frame are shown from left to right in a row of Figure 6.29, above. There are eight rows per second so Figure 6.29 represents just over 5 seconds worth of data. Time progresses down the page, i.e. the top row appears first. The path of the star is clearly visible as the higher valued squares in Figure 6.29.

Two 3D representations of the same data are in Figure 6.30, below.

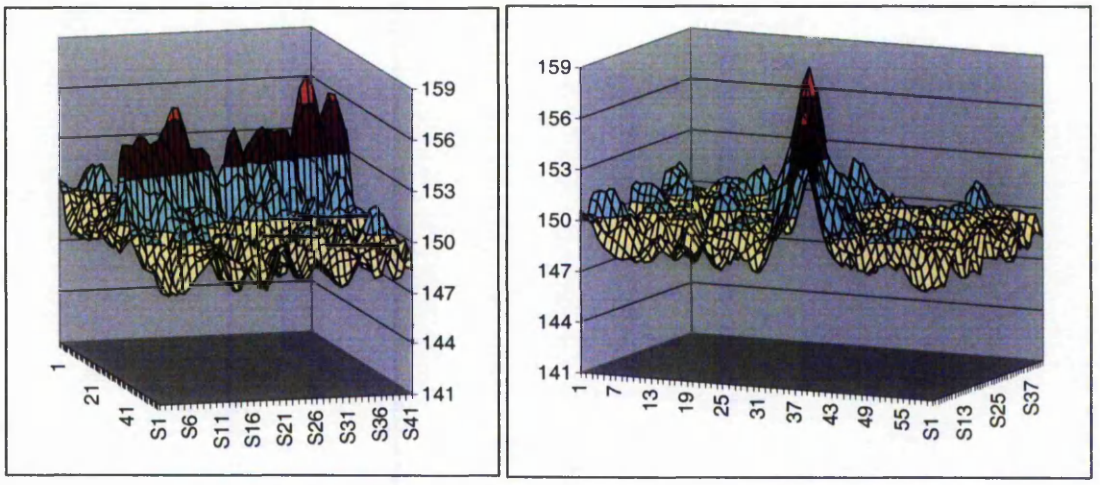

Figure 6.30 3D Graphical representation of data from the passage of one star

Initially an "equation of motion" of the star was assumed to be:

$$y = Ae^{(-(x-B-Ct)^2/D)} + Ee^{(-(x-B-Ct)^4/D)} + F$$

In the above equation y is the height of the point on column x, the row number, at time t in frame numbers, in Figure 6.29.

A and E give the magnitude of the ridge,
F is the height of the floor and
D describes the spread of the ridge.
B is the column value of the centre of the ridge at time t = 0 and
C is proportional to the rate of change of zenith angle.

This is purely a convenient formula, which gives a reasonable representation of the data. It is used because it fits the data and the function contains few variables. There is no theoretical basis for the equation. The ridge in the Figure 6.30 is assumed to have a normal distribution form of cross-section. However, it is accepted that this may not be fully representative so a kurtosis-like element is also introduced.

Partial differentials for the **A** matrix in the least squares solution are:

$$\frac{\partial y}{\partial A} = e^{(-(x-B-Ct)^2/D)}$$

$$\frac{\partial y}{} = 2Ae^{(-(x-B-Ct)^2/D)}(x-B-Ct)/D + 4Ee^{(-(x-B-Ct)^4/D)}(x-B-Ct)^3/D^2$$

$$\frac{\partial y}{\partial B} = 2Ate^{(-(x-B-Ct)^2/D)}(x-B-Ct)/D + 4Ete^{(-(x-B-Ct)^4/D)}(x-B-Ct)^3/D^2$$

$$\frac{\partial y}{\partial C} = Ae^{(-(x-B-Ct)^2/D)}(x-B-Ct)^2/D^2 + 2Ee^{(-(x-B-Ct)^4/D)}(x-B-Ct)^4/D^3$$

$$\frac{\partial y}{\partial D} = e^{(-(x-B-Ct)^4/D^2)}$$

$$\frac{\partial y}{\partial E} = 1$$

$$\frac{\partial y}{\partial F}$$

If the signal from the star is weak then the least squares adjustment is unstable and is divergent. To achieve convergence in these conditions it is necessary to have good initial estimates for the parameters and heavily damp the iterative process. The initial estimates used were:

F = average of all row pixel averages (2400 values)

A = $^2/_3$ of maximum row pixel average - F

C = $\frac{15 f \cos\phi \cos\delta \sin(UT+R+\lambda-RA)}{1000 \sin z}$

where f is the camera frame rate in milliseconds

z is the zenith angle of the star

B = 30 - Ct/2

where 30 is half the row length

t is the number of frames in the data set

D = 8

E = 0

The damping function (k) used in the parameter solution

$$\mathbf{x_1} = \mathbf{x_0} + k\,\delta\mathbf{x}$$

was:

$$k = \text{minimum of } 1 \text{ or } \frac{a}{(\Sigma\ \delta x^2/(x_0^2 + 0.1))^{0.5}}$$

where a is the minimum of (1 - maximum (r)) and (1 + minimum (r))

and r is the coefficient of correlation between and two parameters and is derived from the covariance matrix of parameters.

In practice, it was found that the "equation of motion" above was unstable and, in spite of the damping process described above, the adjustment either failed to converge or took an excessive amount of time. In the final version of the spreadsheet it was simplified to:

$$y = Ae^{(-(x-B-Ct)^2/D)} + F$$

In spite of earlier reservations this converged successfully.

6.6.3 Determination of the theodolite horizontal crosshair in the video image

When the instrument and camera are set up, great care is taken to ensure that the image of the horizontal crosshairs is truly horizontal in the video frame. Before, during and after each set of star observations the crosshairs are illuminated with a light emitting diode placed in front of the telescope objective lens on the telescope axis. The image is then analysed in a similar way to that described above. In this case, C should be zero and B should be unchanged during the star observations.

6.6.4 Determination of the time of star image passing the horizontal crosshair image

The row of the horizontal crosshairs is found from Section 6.6.3 above. Once B and C have been determined, as in Section 6.6.2 above, the time may be found when the star is at a particular row, that is the row equivalent of the theodolite crosshairs.

6.7 Practical determination of precise observing time

To link the video frames to GPS time, the "GPS flasher" was set "on" for 60 ms every 1 second and the video frame period set to a nominal 124 ms. 124 ms was chosen because it was a rate that the computer could accommodate without apparent error and was a period close to a simple fraction of 1 second, i.e. $^1/_8$ of a second. If 125 ms had been chosen then it would not have been possible to find "video time" to better than $^1/_8$ of a second. However, with a slightly different rate the following will apply.

Figure 6.31, below, shows the exposure of a series of video frames and the state of the GPS flasher.

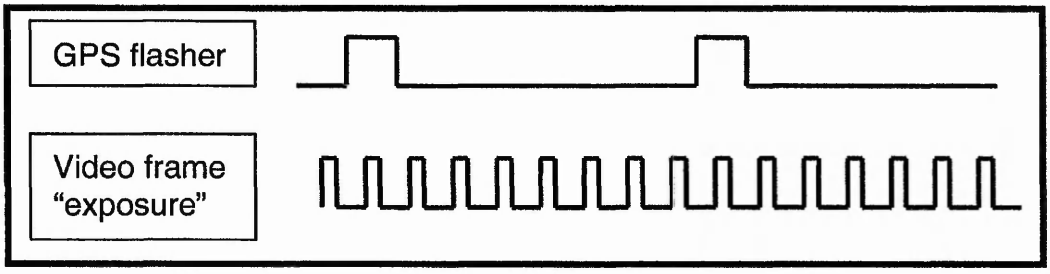

Figure 6.31 Exposure of a series of video frames and state of the GPS flasher.

In Figure 6.31, a video exposure takes place during a GPS flash, but it is not possible to say precisely when, as the pattern repeats exactly every second. However, if the frame rate is changed very slightly, then the GPS flash will occur at different times relative to the video exposure. There will be occasions when the GPS flash will start or stop during a video exposure. This will be reflected by reduced average frame pixel values compared with a full exposure. The figure below shows frame average pixel values, scaled 0 - 1, with a 60 ms GPS flash for a 40 ms video exposure every 124.75 ms. Figure 6.32, below, has been constructed with theoretically perfect data.

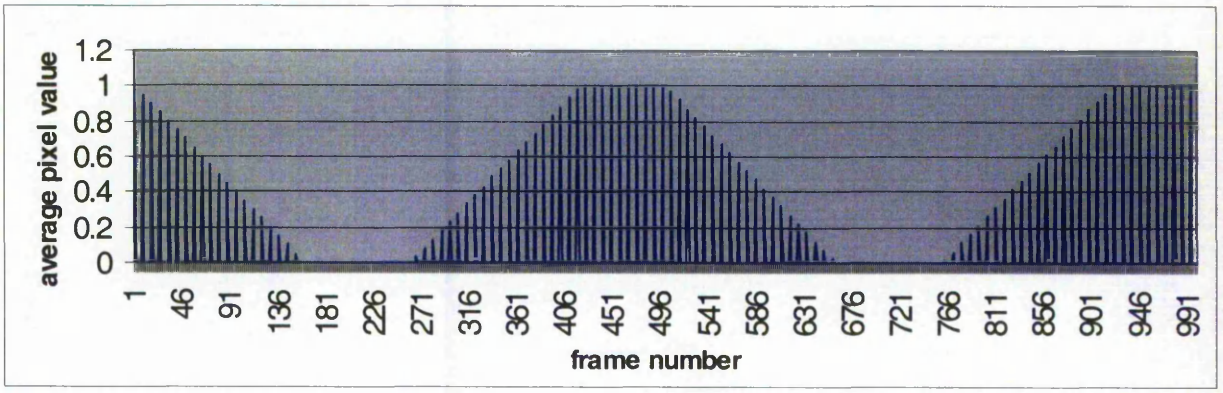

Figure 6.32 Expected frame average pixel values with a 60 ms GPS flash for a 40 ms video exposure every 124.75 ms.

The outline of the waveform shows four distinct parts in every cycle.

A floor where the average pixel value is 0
A ramp up
A ceiling where the average pixel value is 1
A ramp down of equal length to the ramp up

The floor and ceiling are not the same length. If the time between video exposures is just less than a simple fraction of a second then the end of the ceiling is where the start of a GPS flash is coincident with the start of a video exposure.

If the video exposure time is less than the GPS flash time, the video exposure time is given by:

$$v_e = f_p (1 - r/c)$$

If the video exposure time is greater than the GPS flash time, the GPS flash time is given by:

$$G_f = f_p (1 - r/c)$$

where v_e is the video exposure time

G_f is the GPS flash time

f_p is the frame period (124.75 ms in the example above)

r is the length of one ramp

c is the length of a cycle

Therefore, it will be necessary to ensure that the video exposure time is less than the GPS flash time. This is easily done as a normal camera, capable of 25 frames per second, could not have an exposure of greater than 40 ms and the GPS flasher can be set for flashes up to 100 ms.

The cycle length and period is given by:

$$c = 125\,(125 - f_p)^{-1} \text{ frames}$$

and therefore:

$$f_p = 125(1 - c^{-1}) \text{ ms}$$

The length of a cycle can be found by observing frame exposures for a long period and fitting a square wave to the output so that the square wave includes all full and partial exposures and excludes all non-exposures. In an experiment under semi-laboratory conditions, over an hour of data was captured with a nominal video frame period of 124 ms and GPS flash of nominal 60 ms.

The frame average pixel values followed the format predicted above with approximate floor values at about 150 and ceiling values of 250. The length of a cycle was determined by manually fitting a square wave to a set of frame average pixel values to minimise the number of outliers. Three sample graphs for frame numbers 5000 – 6000, 15000 – 16000 and 25000 – 26000 respectively are shown in Figures 6.33 to 6.35.

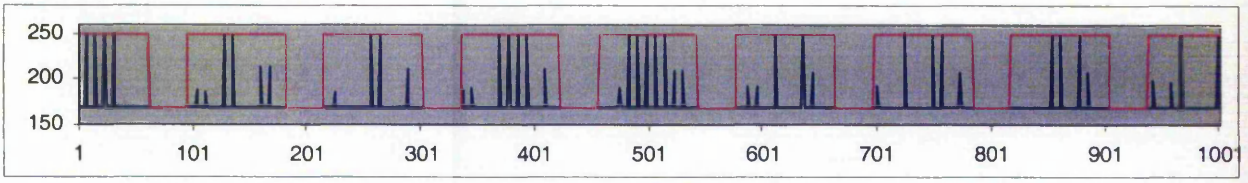

Figure 6.33 Fit of a square wave to frames numbered 5000 – 6000 in a set of frame average pixel values.

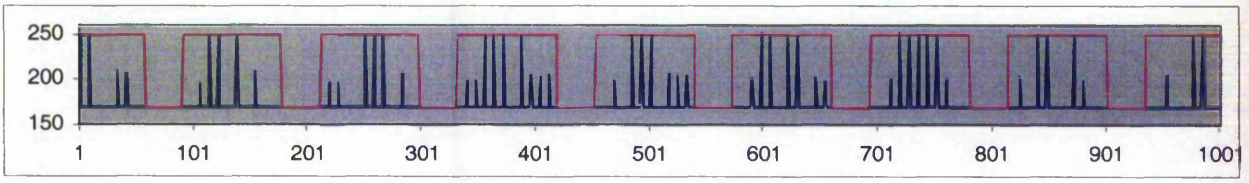

Figure 6.34 Fit of a square wave to frames numbered 15000 – 16000 in a set of frame average pixel values.

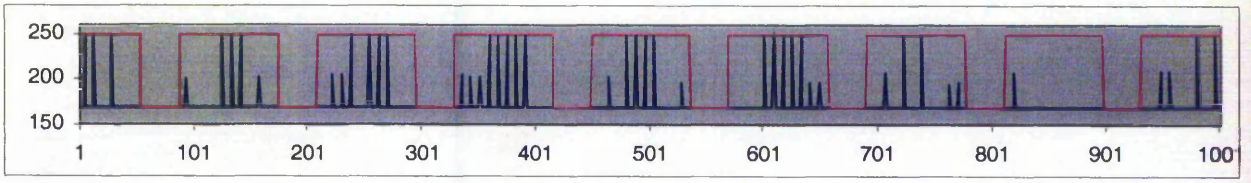

Figure 6.35 Fit of a square wave to frames numbered 25000 – 26000 in a set of frame average pixel values.

It will be noted that the square wave contains all the GPS 1-second flashes but also contains many blanks when a signal would have been expected. The GPS flasher will flash only at the desired multiples of one second as set into the Leica 399 GPS controller but does not always flash. A cut-off of a pixel row average of 170 was set to remove noise in the floor data. The best fit for a cycle length was 120.453 video frames with an estimated variation of ± 0.002 video frames. Note that there is no suggestion of standard error as the fit was not by rigorous means. Using the formula above, this leads to an actual frame period of 123.9623 ms with an estimated variation of ± 0.00002 ms.

Examination of the row average pixel values for a frame shows that there is occasionally a jump in the row averages during a frame. This occurs only in the region of a ramp and is taken to reflect the situation when the GPS flash starts or stops during a video frame exposure. For example, a new flash will only affect that part of a video frame exposure not already captured. The graph in Figure 6.36 shows the average row pixel values for such an occasion.

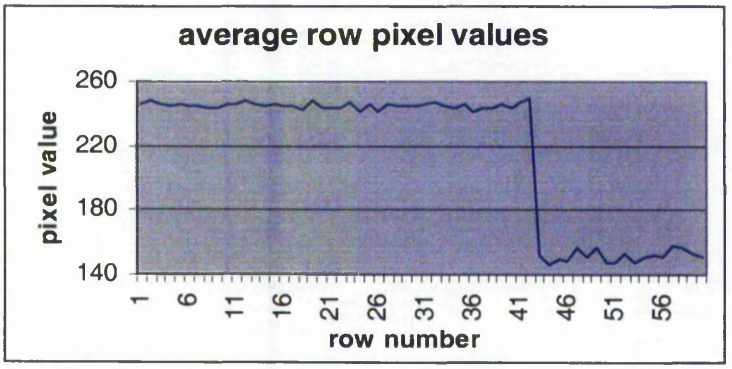

Figure 6.36 The jump in row pixel values when a GPS flash starts during a video frame exposure.

In one frame exposure, the number of pixel rows that have full value will depend upon the degree of overlap between the video exposure and the GPS flash. Figure 6.37 illustrates the situation.

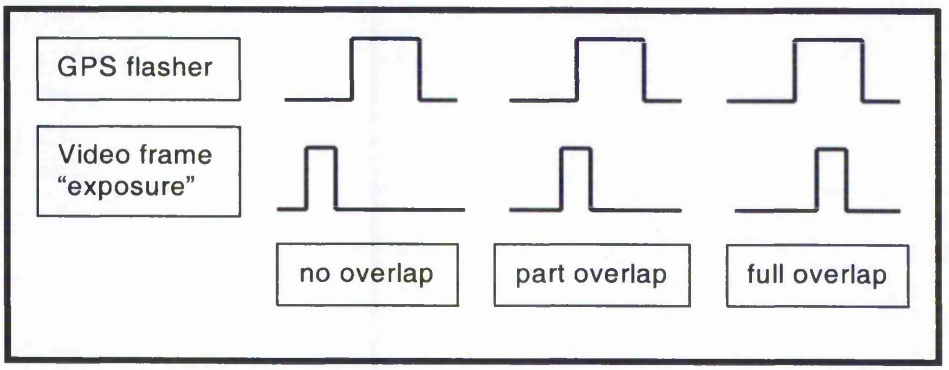

Figure 6.37 Overlap between GPS flash and video frame exposure.

The jump in average row pixel values can only take place during a part overlap of GPS flash and video frame exposure. Such an event is identified by counting the number of average row values in a frame that are above a threshold value, such as 200 in the example in Figure 6.36. The element of a frame used for observational purposes has been chosen as a 60-pixel square so the number of average row values in a frame above the threshold value must take an integer value from 0 to 60. If the period of a video frame exposure can be determined then precise timing of the start of a video frame can be achieved.

To find the period of a video frame exposure the following experiment was carried out. A vertical line was created on the display of an oscilloscope. The vertical line was made to move horizontally across the oscilloscope's display at a suitable rate and the video camera was pointed at the display. Since the camera's scanning process takes a finite time then it would be expected that the video image of the oscilloscope's vertical line would have a slope and the degree of slope would indicate the delay between top and bottom line scans.

The oscilloscope's horizontal rate was set to be 5 ms/division and the camera window was 100 pixels square. Some sample screen outputs are shown in Figure 6.38, below.

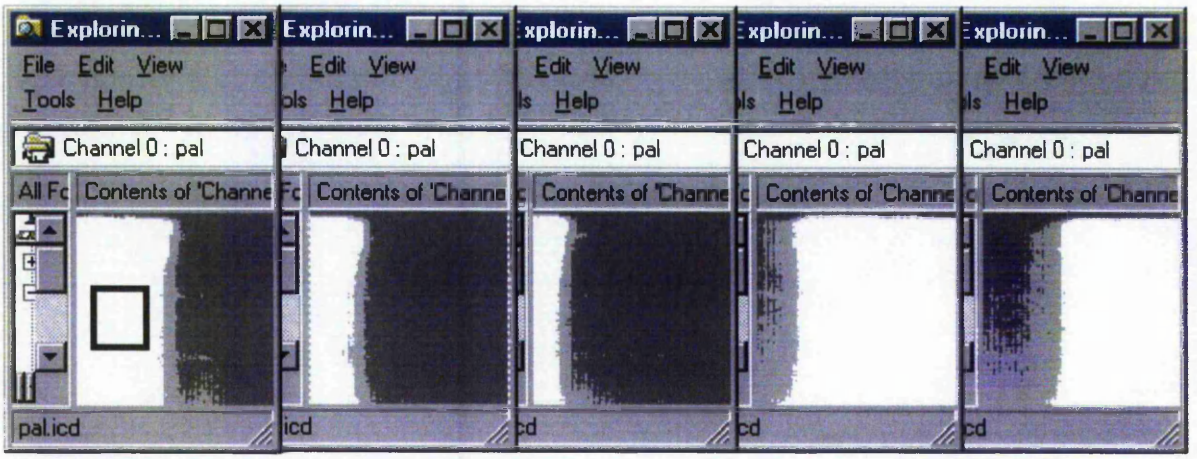

Figure 6.38 Five sample video screen outputs for a vertical line moving horizontally across an oscilloscope display.

The white parts of the separate displays are part of the vertical line. The square superimposed over the first display is approximately the size of a division on the oscilloscope. Although the edges of the vertical lines in the display are not precisely defined, it appears that the time for 60 lines of scan is significantly less than 1 ms. Assuming this to be the case, it implies that the time for the start/end of a video exposure which overlaps the start of a GPS flash can be determined at the sub-millisecond level.

Using the computed frame period above, the video times of all occurrences of a jump in the row averages during a frame were found. The scatter plot in Figure 6.39, below, shows the results. The lower band represents the start of a GPS flash in video time and the upper band the end of a GPS flash. The mean start and stop times have population standard deviations of 0.0064 and 0.0061 s respectively.

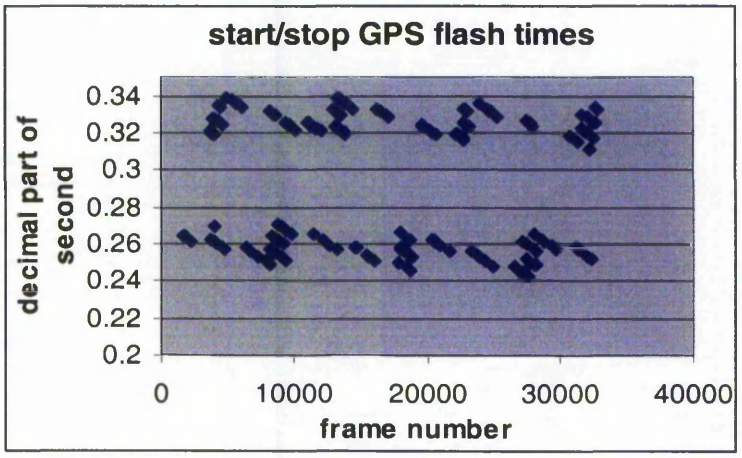

Figure 6.39 Video times of occurrences of a jump in the row averages during a frame.

Several different hypothetical scan rates were applied to the data to see if a significant improvement could be made to the population standard deviations for the start and end of a GPS flash in video time. The results in the graph of Figure 6.40, below suggest that the optimum scan rate is between 0.05 and 0.1 ms/row.

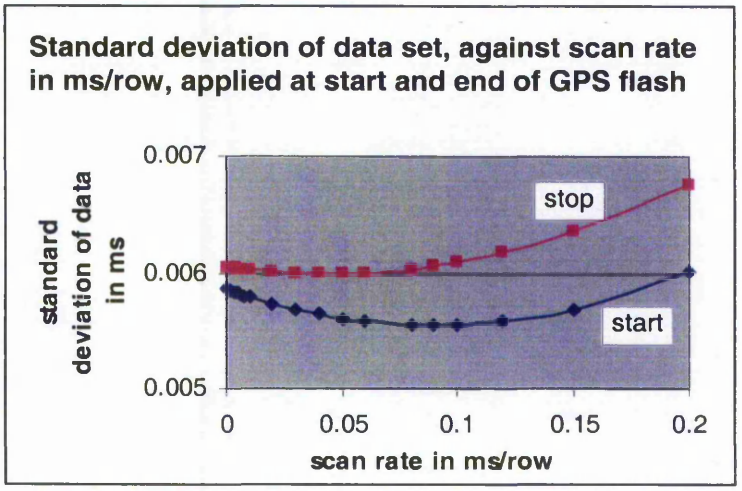

Figure 6.40 Standard deviation of data set, against assumed scan rate in ms/row, applied at the start and the end of a GPS flash

An alternative view is to consider the number frames with a jump in row averages as a proportion of the total number of frames.

During a 1-second period there will be one GPS flash, provided that is the rate that has been set. Each flash will have 2 ends, a start and a stop. The proportion (p) of individual frames that overlap with an end of a GPS flash will be:

$$p = 0.002\, s_c\, r\, f^{-1}$$

where s_c is the scan rate in ms/row

r is the number of rows to be scanned

f is the number of seconds between GPS flashes

and therefore

$$s_c = 500\, p\, f\, r^{-1}$$

In this experiment, p was 0.0063, f was 1, and r was 60. However only about half of the GPS flashes were successful, so a more realistic value for f would be 2. In that case $s_c \approx 0.1$ ms/row. This result is compatible with the above graph relating to starts of GPS flashes. On this basis, 60 rows will take about 6 ms to scan.

The above study leads to the following method for the determination of the mid-time of a video frame exposure.

- Data is to be collected at a nominal frame period of 124 ms. The GPS flasher may be set to 5 seconds and the flash period to a nominal 60 ms. The standard video frame is set at 60 pixels square.
- Open the video data, row average pixel values for each video frame, in a spreadsheet. The number of columns in the spreadsheet equals the number of pixel rows in the video frame (60). The number of rows in the spreadsheet equals the number of video frames. 2 hours of data gives approximately 58000 rows. Add a frame count column to the spreadsheet
- In the Excel spreadsheet, identify the rows where there is a jump in values in the row as in the "average row pixel values" graph above where the value in cell "A_n" is greater than the value in "BH_n" by at least half the difference between the floor and ceiling values. n is the row number.
- Count the number of cells after the jump. The time at the middle of the exposure of that frame is given by:

$$t_e = t_{GPS} - 0.0001\ (c + 30)$$

where t_e is the time at the middle of the frame exposure

t_{GPS} is the GPS time of the start of the GPS flash

0.0001 is the rate of scan in seconds per row

c is the number of cells after the jump

30 is half the number of rows

6.8 System Architecture

Below, in Figure 6.41, is a graphic showing the configuration of the field equipment for a low cost practical application.

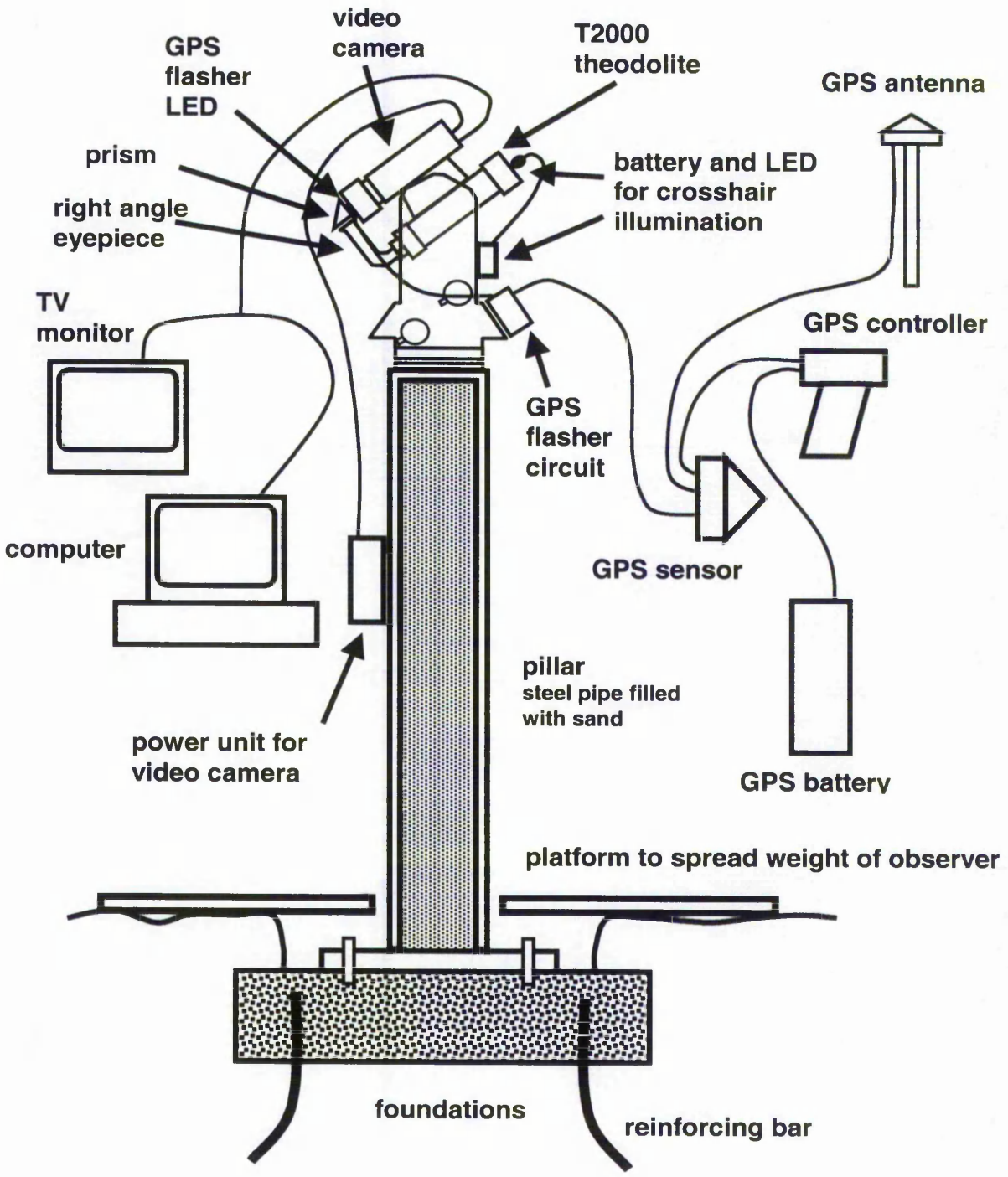

Figure 6.41 Field system architecture

6.9 Practical preparation, observing and processing routines

This section outlines the preparation, observing and processing routines for collection and processing of astronomical data leading to position lines solutions using a T2000 electronic theodolite with video camera and GPS. This section was used as an on-site checklist.

T2000 and camera/GPS time recording

a. *Predictions*

- Estimate WGS84 position with handheld GPS.
- In UK only, find slope of the geoid from Grid InQuest, (2001)
- Apply slope to WGS84 position to find an estimate of the astronomical position.
- Select start date and time for observations.
- Use spreadsheets:

  "MCBJ2000.xls" to update star data and find a suitable star set.

  "PREDICT.xls" to identify Polaris, orient horizontal circle, prepare and print observing programme.

b. *Prepare T2000 and data recording system*

- Set up Leica System 300 GPS receiver. Set T2000 on tripod, connect battery, attach video camera, right angle eyepiece, GPS flasher, external crosshair illumination and level instrument. (The position of the GPS flasher is critical. If it is pointing into the camera lens there is too much light and the .vi fails. Set at right angles to the camera axis but close to the prism).
- Connect video camera output to computer with video capture board.
- Adjust the right angle eyepiece and video camera for a good picture on the TV monitor.
- Set the IMAQ video capture board:
- Obtain a good picture of the apparent left gap in the horizontal hair with the ends of the horizontal hair equally visible at the centre of the left and right edges of the captured picture, Figure 6.26.
- On the video capture board select "Channel 0 : Pal". Set:

Camera Description	Generic PAL
Camera Type	PAL
Interlace	Non-Interlaced
Acquisition Window	
Width 60	Height 60

Left and Right	as required
Chroma Filter	PAL
Scale	None
Reference Level(Volt)	
White 0.15 Black 0.10	

- Set LABVIEW "virtual instrument" "HL Grab in IMAQ Vision display MB's version 2.vi" to ensure continuous recording as follows:

Time between stars in seconds	10000
Number of stars	1
Frame speed in ms	124
Number of frames per star	65000

- Switch on external cross hair illumination
- Point to Polaris and set horizontal circle [SET] [Hzo] *1.2345* [RUN]
- Ensure GPS flasher is flashing (5 s rate at 60 ms flash)

c. *Collect data*

- Start LABVIEW "virtual instrument" at GPS flash. Record GPS time.
- After 20 seconds switch off external cross hair illumination.
- Point to first star. Record actual vertical circle reading.
- After passage point to next star etc.
- After 10 stars switch on external cross hair illumination for 20 seconds.
- Point to next star. Record actual vertical circle reading.
- After passage point to next star etc.
- After 10 stars switch on external cross hair illumination for 20 seconds.
- Etc.
- Stop LABVIEW "virtual instrument" and save data.

d. *Compute data*

- Open saved file as a spreadsheet in Excel
- Copy data to spreadsheet "Convert video time to GPS time". Follow on screen instructions. Output is a set of parameters to convert frame number to GPS time.
- Select data when external cross hair illumination is "on" and import to spreadsheet "equation of motion of star on screen 5 parameter.xls". Output is picture row value for the crosshair. Compute for all similar data sets.

- Select data for star crossing and import to spreadsheet "equation of motion of star on screen 5 parameter.xls". Output is time, as frame number, for star crossing of horizontal hair.
- Use computed parameters to find GPS time for each star crossing.
- Input star co-ordinates (copy from prediction spreadsheet), observed zenith angles & GPS time for all stars into spreadsheet "POSNSOLN with changing refraction and collimation.xls"
- Set "S/W correction" as offset between UT and GPS (currently 13 s) + 5n* secs + (UT1R-UTC)**
- Input polar motion** and station height.

  * This assumes that the GPS flash rate is 5 seconds. n is the integer that leads to the only realistic solution for the computed longitude of the station.

  ** (UT1R-UTC) & polar motion from GIBS (2001)

- Find and remove gross errors. Iterate to convergence for astronomical position.
- Open spreadsheets "POSNSOLN.xls" and "PREDICT.xls - Predict ".
- Copy star co-ordinates from "PREDICT.xls" to "POSNSOLN.xls".

e. *Position line solution*

- Iterate and edit input data.
- Apply topographic-isostatic and lunar corrections as appropriate.

6.10 Spreadsheets

A series of spreadsheets in Excel was written to accommodate all the computations up to and including the determination of astronomical latitude and longitude. There are summarised in Table 6.4, below:

Table 6.4 Spreadsheets used for the determination of astronomical latitude and longitude.

Workbook	Mb	Spreadsheet	Remarks
FK5_1_2.xls	0.1		A spreadsheet to collect and edit bright star data, not only FK5 but also YBSC and SAO.
FK5J2000.xls	0.8	FK5	FK5_1_2.xls reformatted for use in ...
		FK5 J2000 to target	Input is time and date of proposed or actual observations. Output is α and δ at target epoch. Output is input to ...
		First selection	Selects 95 starts. Input is also station latitude, max zenith angle and star magnitude range. Output is star data for selected stars for input to PREDICT.xls
MCBJ2000.xls	11.7	MCB	MCB data set of 6694 stars.
		MCB 2000	Input is time & date of observations. Output is α and δ at target epoch. Output is input to ...
		First selection	Selects 95 starts. Input is also station latitude, max zenith angle and star magnitude range. Output is star data for selected stars for input to PREDICT.xls ...
PREDICT.xls	3.9		Other input is latitude, longitude, date, max zenith angle, range of E & W azimuth, GMT at start, time between stars, approx azimuth of first star, horizontal offset from star to crosshair, expected time and zenith angle observation standard errors. Output is an observing programme of 50 stars in order of time such that input criteria are satisfied and the stars increase progressively in azimuth. Spreadsheet output lists azimuth, zenith angle, and time to precisions of 1", 1" and $0^s.1$. Assumed standard errors in input data and standard errors in the assumption of standard refraction conditions give position error ellipse data and a diagram based upon the least squares design.

		Predict Polaris	Input data are provisional values of position, date, R at 0^h on 1 January of year of observations, GMT of start and time interval between determinations and α and δ of Polaris. Output data are a listing of azimuths and zenith angles.
POSNSOLN.xls	0.2		Input data are; 1. Provisional values of position, collimation, refraction coefficient, observation quality. 2. Date of first observation, horizontal offset, stopwatch correction. 3. Star data may be copied from PREDICT.xls. 4. Observations of stopwatch and zenith angles. Least squares iteration is by macro. Output is; 1. Adjusted position, collimation and refraction coefficient. 2. Position error ellipse data and diagram. 3. Worst standard residual. 4. Adjusted observation quality. 5. Conventional position lines graphic.
Convert video time to GPS time.xls	14.5		Input data is approx GPS start time of data (to nearest second) and frame period in ms. Output is time for each video frame.
Equation of motion of star on screen 5 parameter.xls	3.5		Input data is selected section of saved video row mean pixel values, row of theodolite horizontal crosshair, provisional value of C. Output is frame time star crosses horizontal crosshair.

6.11 Summary

Using the theory developed in Chapter 4 and the updated star data from Chapter 5, observing and computing processes have been developed in this chapter. The balance of stars has been considered in terms of the direction of balance based on errors in computed refraction coefficient and errors in computed collimation. The productivity of various observing and technology combinations was reviewed and approaches to automating the observing and computing process identified.

In the photodiode method, which turned out to be unsuccessful because of the instability of the sensitive diode selected, the issues of precise timing of star observations, radio time signal delays, the detection of star passage over the theodolite crosshair and the determination of time of star passage over the theodolite crosshair were considered. Theory is now in place should it ever become more practical to use a sensitive photodiode.

In the video camera method, the method finally selected because it worked, the issues of precise linkage of time to a video frame, determination of the motion of the image of the star, determination of the theodolite horizontal crosshair in the video image and determination of the time of star image passing the horizontal crosshair image were considered.

The methods developed in this chapter will be applied in the practical determination of an astronomical position and described in Chapter 10.

One correction, not described in any of the foregoing, is that associated with the effect of lunar gravitation and barycentric centrifugal force on deviation of the vertical and that is discussed in the next chapter. To correct observed astronomical position on the earth's surface, as described in this chapter, to that which would have been observed on the geoid, it is necessary to apply a topographic-isostatic correction and a simple method for computing this correction. That topic is examined in Chapter 8.

Chapter 7

The Effect of Lunar Gravitation and Barycentric Centrifugal Force on Deviation of the Vertical

7.1 Introduction

The earth and moon orbit around their own barycentre. The barycentre is within the earth. Because of this orbit, there is a centrifugal effect that varies with time and place. It has a variable effect upon the local direction of the vertical. This barycentric effect is evaluated to a first order and formulae for the correction of observations of the vertical are derived.

Although the moon appears to orbit around the earth, in fact, moon and earth orbit around their own barycentre. Assuming circular orbits and a homogeneous spherical earth then, at the earth's centre, the gravitational attraction of the moon is exactly balanced by the centrifugal acceleration of the earth's mass centre around the barycentre.

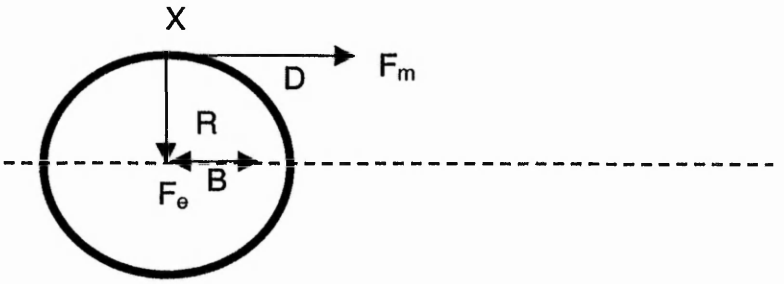

Figure 7.1 The balance of Earth-Lunar gravitation and centrifugal force.

The plane of the earth and moon's orbit passes through the mass centre of both and their barycentre. In Figure 7.1 point X is on the earth's surface and is also on the normal to the plane of the earth and moon's orbit that passes through the earth's centre.

The effect of the moon's gravitational attraction upon the deviation of the vertical is given by:

$$\chi_{mg} = \tan^{-1}(F_m/F_e)$$

where F_e is the gravitational attraction of the earth *and*

F_m is the gravitational attraction of the moon

Newton's Law gives:

$$F_e = GM_e/R^2 \quad \text{and} \quad F_m = GM_m/D^2$$

where M_e and M_m are the masses of the earth and moon respectively

R is radius of the earth

D is distance between the mass centres

Therefore

$$\chi_{mg} = \tan^{-1}\left(\frac{M_m R^2}{M_e D^2}\right)$$

With values from Seidelmann (1992) of

$M_e/M_m = 0.012300034^{-1}$

D = 384400000 metres,

and assuming

R = 6369000 metres,

this gives

χ_{mg} = 0".696 towards the moon.

The effect of the centrifugal acceleration of the earth's mass centre around the earth-moon barycentre is given by:

$$\chi_{ca} = \tan^{-1}(B\omega_m^2/g)$$

where B is the distance from earth mass centre to barycentre

ω_m is the sidereal mean motion

With values from Seidelmann (1992) of

B = 4671000 metres

$\omega_m = 2.6617\ 10^{-6}$ rads s^{-1},

and taking a mean value of g = 9.81 m s^{-2},

this gives

χ_{ca} = 0".696 away from the moon.

Therefore at point X, defined in Figure 7.1 above, the gravitational attraction of the moon is in balance with the centrifugal force due to the orbit around the barycentre.

At any other point on the earth, the forces will not be in balance and therefore the components of correction to the deviation must be computed separately.

7.2 The effect of the moon's gravitational attraction upon the deviation of the vertical

From above, the maximum value of χ_{mg} is 0".696 and will occur when the moon is on the observer's horizon. When the moon is at an elevation of h_m, the deviation in the direction of the moon will be:

$$\chi_{mg} = 0".696 \cos h_m$$

and the deviation at right angles to the line, ζ_{mg}, will be zero.

If the azimuth of the moon from the observer is A_m, since

$$\chi_{mg} = -(\xi_{mg}\cos A_m + \eta_{mg}\sin A_m) \quad \text{and}$$

$$\zeta_{mg} = (\xi_{mg}\sin A_m - \eta_{mg}\cos A_m) = 0$$

then

$$\eta_{mg} = -\chi_{mg}\sin A_m = -0".696 \cos h_m \sin A_m \quad \text{and}$$

$$\xi_{mg} = -\chi_{mg}\cos A_m = -0".696 \cos h_m \cos A_m$$

The azimuth of the moon, A_m, can be found from spherical trigonometry:

$$\cot A_m = (\sin \phi_P \cos t_m - \cos \phi_P \tan \delta_m) \operatorname{cosec} t_m$$

where t_m, the hour angle of the moon is given by:

$$t_m = GAST + \lambda_P - RA_m$$

Find the elevation of the moon, h_m, from:

$$\sin h_m = \cos \delta_m \cos \phi_P \cos t_m + \sin \delta_m \sin \phi_P$$

The topocentric right ascension and declination of the moon may be found at the US Naval Observatory's "Web Version of MICA" – the Multiyear Interactive Computer Almanac at USNO (1997c) or on the CD version of MICA 1990 – 2005 (MICA, 1998)

If the moon is to the south of the observer, then the correction to the observed astronomical latitude will be numerically negative. If the moon is to the east of the observer, then the correction to the observed astronomical longitude will be numerically positive.

7.3 The Effect of Centrifugal Acceleration of the Observation Point around the Barycentric Rotation Axis upon the Deviation of the Vertical

By redefining the term B in the formula for χ_{ca} in section 7.1 an equivalent formula for the effect of centrifugal acceleration of the observation point around the barycentric rotation axis upon the deviation of the vertical is:

$$\chi_{ca} = \pm \tan^{-1}(B\omega_m^2 \cos h_b / g)$$

where

B is now the shortest distance between the barycentric rotation axis and the observation point

h_b is the elevation of the line describing the shortest distance between the barycentric rotation axis and the observation point

ω_m and g are respectively 2.6617 10^{-6} rads s^{-1} and 9.81 m s^{-2}.

See Figure 7.2, below.

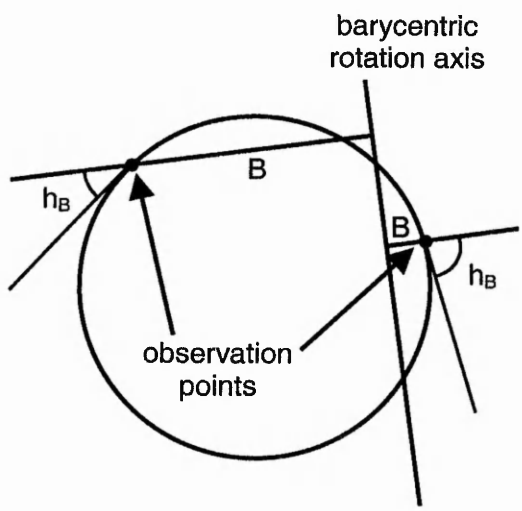

Figure 7.2 Shortest distance between the barycentric rotation axis and the observation point, line B, and the elevation of the extension of that line, h_B, for two points on the surface of the earth.

It is useful to describe the following co-ordinate systems, see Figure 7.3, below.

Topocentric

The origin is at the observation point. X is up, Y is east, Z is north.

Geocentric

The geocentric Cartesian co-ordinates of the observation point ϕ_P, λ_P are given by:

$$\mathbf{X_{gP}} \begin{bmatrix} X_{gP} \\ Y_{gP} \\ Z_{gP} \end{bmatrix} = \begin{bmatrix} (\nu_P + h_P) \cos\phi_P \cos\lambda_P \\ (\nu_P + h_P) \cos\phi_P \sin\lambda_P \\ (\nu_P (1 - e^2) + h_P) \sin\phi_P \end{bmatrix}$$

where

$$\nu_P = \frac{a}{(1 - e^2 \sin^2\phi_P)^{\frac{1}{2}}}$$

Orbital

The earth mass centre is the origin of this system. The positive, X_O, axis passes through the barycentre and the moon. The Z_O axis is parallel to the barycentric rotation axis such that the Z_O co-ordinate of the earth's North Pole is positive. The Y_O axis lies in the lunar orbital plane making a right-handed co-ordinate system.

From Seidelmann (1992), therefore, the orbital co-ordinates of the barycentre are:

$$\mathbf{X_{oB}} \begin{bmatrix} X_{oB} \\ Y_{oB} \\ Z_{oB} \end{bmatrix} = \begin{bmatrix} B \\ 0 \\ 0 \end{bmatrix} = \begin{bmatrix} 4671000 \text{ metres} \\ 0 \text{ metres} \\ 0 \text{ metres} \end{bmatrix}$$

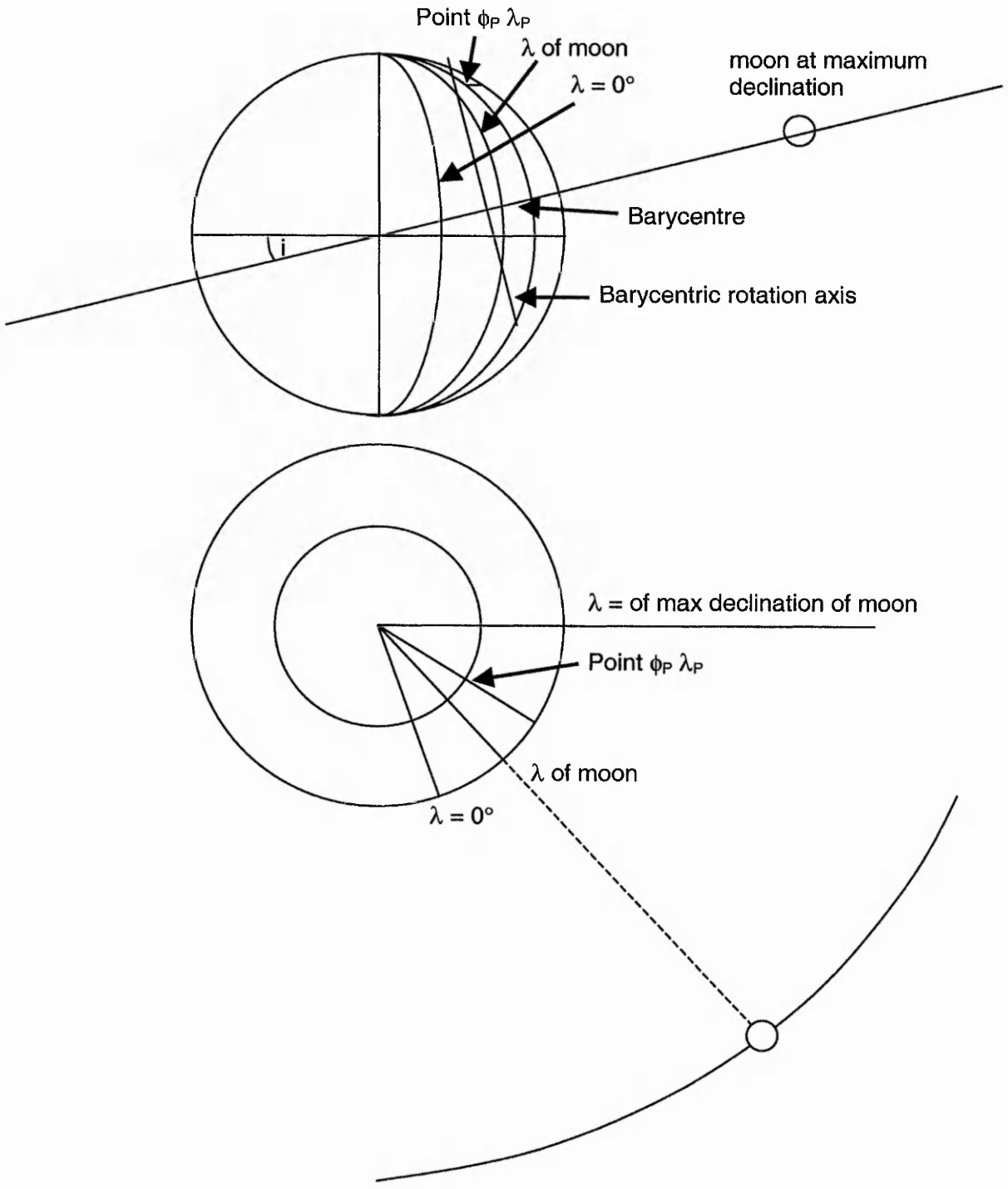

Figure 7.3 The spatial relationship between Earth and Moon (not to scale)

7.4 The Relationship between the Geocentric, Orbital and Topocentric Co-ordinate Systems

The relationship between the Geocentric and Orbital Co-ordinate systems may be found by first considering the spherical triangle with corners at the North Celestial Pole (NCP), the moon at the time of observation, when its declination is δ_m, and the moon at its maximum declination (δ_{max}). See Figure 7.4, below.

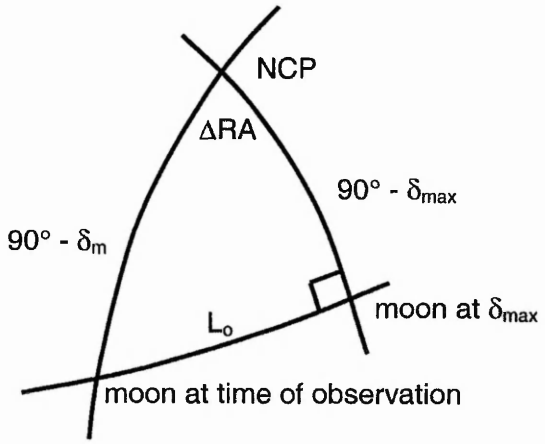

Figure 7.4 The spatial relationship between the Earth and the Moon in the astronomical triangle.

From application of the spherical sine rule:

$$\sin L_o = \cos \delta_m \sin \Delta RA$$

where $\Delta RA = RA_{@\delta max} - RA_m \quad (= \lambda_{max} - \lambda_m)$

and $RA_{@\delta max}$ is the right ascension of the moon when it is at its maximum declination

RA_m is the right ascension of the moon

λ_{max} is the longitude of the moon when it is at its maximum declination

λ_m is the longitude of the moon

L_o is the angular passage of the moon with respect to the earth's mass centre in the orbital plane. It will also be the angular passage of the moon with respect to the barycentre in the orbital plane since the earth's centre, the barycentre and the moon always form a straight line in the orbital plane.

Since both the geocentric and the orbital co-ordinate systems have their origins at the mass centre of the earth then only rotations are required to convert from one system to the other. Therefore for a point, P:

$$\mathbf{X}_{oP} = \mathbf{R}_Z(-L_o)\,\mathbf{R}_Y(-\delta_{max})\,\mathbf{R}_Z(\lambda_{max})\,\mathbf{X}_{gP}$$

$$\mathbf{X}_{oP} = \mathbf{R}_Z(-L_o)\,\mathbf{R}_Y(-\delta_{max})\,\mathbf{R}_Z(RA_{@\delta max} - GAST)\,\mathbf{X}_{gP}$$

If, for the sake of brevity, $RA_{@\delta max} - GAST$ is written as d, then

$$\begin{bmatrix} X_{oP} \\ Y_{oP} \\ Z_{oP} \end{bmatrix} = \begin{bmatrix} \cos L_o & -\sin L_o & 0 \\ \sin L_o & \cos L_o & 0 \\ 0 & 0 & 1 \end{bmatrix} \begin{bmatrix} \cos\delta_{max} & 0 & \sin\delta_{max} \\ 0 & 1 & 0 \\ -\sin\delta_{max} & 0 & \cos\delta_{max} \end{bmatrix} \begin{bmatrix} \cos d & \sin d & 0 \\ -\sin d & \cos d & 0 \\ 0 & 0 & 1 \end{bmatrix} \begin{bmatrix} X_{gP} \\ Y_{gP} \\ Z_{gP} \end{bmatrix}$$

$$\begin{bmatrix} X_{oP} \\ Y_{oP} \\ Z_{oP} \end{bmatrix} = \begin{bmatrix} \cos L_o\cos\delta_{max}\cos d + \sin L_o\sin d & \cos L_o\cos\delta_{max}\sin d - \sin L_o\cos d & \cos L_o \sin\delta_{max} \\ \sin L_o \cos\delta_{max} \cos d - \cos L_o\sin d & \sin L_o \cos\delta_{max}\sin d + \cos L_o\cos d & \sin L_o \sin\delta_{max} \\ -\sin\delta_{max} \cos d & -\sin\delta_{max} \sin d & \cos\delta_{max} \end{bmatrix} \begin{bmatrix} X_{gP} \\ Y_{gP} \\ Z_{gP} \end{bmatrix}$$

and in reverse

$$\mathbf{X}_{gP} = \mathbf{R}_Z(GAST - RA_{@\delta max})\,\mathbf{R}_Y(\delta_{max})\,\mathbf{R}_Z(L_o)\,\mathbf{X}_{oP}$$

$$\begin{bmatrix} X_{gP} \\ Y_{gP} \\ Z_{gP} \end{bmatrix} = \begin{bmatrix} \cos L_o\cos\delta_{max}\cos d + \sin L_o\sin d & \sin L_o \cos\delta_{max} \cos d - \cos L_o\sin d & -\sin\delta_{max} \cos d \\ \cos L_o\cos\delta_{max}\sin d - \sin L_o\cos d & \sin L_o \cos\delta_{max}\sin d + \cos L_o\cos d & -\sin\delta_{max} \sin d \\ \cos L_o \sin\delta_{max} & \sin L_o \sin\delta_{max} & \cos\delta_{max} \end{bmatrix} \begin{bmatrix} X_{oP} \\ Y_{oP} \\ Z_{oP} \end{bmatrix}$$

The length and vector components of the observation point to the nearest point, N, on the barycentric rotation axis is most easily found in the orbital co-ordinate system. Therefore N_o is given by:

$$\mathbf{X}_{oN} = \begin{bmatrix} X_{oN} \\ Y_{oN} \\ Z_{oN} \end{bmatrix} = \begin{bmatrix} B \\ 0 \\ Z_{oP} \end{bmatrix}$$

The distance PN is therefore

$$D_{PN} = ((X_{oN} - X_{oP})^2 + (Y_{oN} - Y_{oP})^2)^{1/2}$$

$$= ((B - X_{oP})^2 + Y_{oP}^2)^{1/2}$$

The vector PN in the orbital co-ordinate system is

$$\mathbf{v}_{oPN} = \begin{bmatrix} X_{oN} - X_{oP} \\ Y_{oN} - Y_{oP} \\ Z_{oN} - Z_{oP} \end{bmatrix} = \begin{bmatrix} B - X_{oP} \\ -Y_{oP} \\ 0 \end{bmatrix}$$

The same vector in the geocentric co-ordinate system will be:

$$\mathbf{v}_{gPN} = \mathbf{R}_Z(GAST - RA_{max})\,\mathbf{R}_Y(\delta_{max})\,\mathbf{R}_Z(L_o)\,\mathbf{v}_{oPN}$$

And in the topocentric system

$$\mathbf{v}_{tPN} = \mathbf{R}_Y(-\phi)\,\mathbf{R}_Z(\lambda_P)\,\mathbf{v}_{gPN}$$

$$\begin{bmatrix} X_{vtPN} \\ Y_{vtPN} \\ Z_{vtPN} \end{bmatrix} = \begin{bmatrix} \cos\phi_P & 0 & \sin\phi_P \\ 0 & 1 & 0 \\ -\sin\phi_P & 0 & \cos\phi_P \end{bmatrix} \begin{bmatrix} \cos\lambda_P & \sin\lambda_P & 0 \\ -\sin\lambda_P & \cos\lambda_P & 0 \\ 0 & 0 & 1 \end{bmatrix} \begin{bmatrix} X_{vgPN} \\ Y_{vgPN} \\ Z_{vgPN} \end{bmatrix}$$

$$\begin{bmatrix} X_{vtPN} \\ Y_{vtPN} \\ Z_{vtPN} \end{bmatrix} = \begin{bmatrix} \cos\phi_P \cos\lambda_P & \cos\phi_P \sin\lambda_P & \sin\phi_P \\ -\sin\lambda_P & \cos\lambda_P & 0 \\ -\sin\phi_P \cos\lambda_P & -\sin\phi_P \sin\lambda_P & \cos\phi_P \end{bmatrix} \begin{bmatrix} X_{vgPN} \\ Y_{vgPN} \\ Z_{vgPN} \end{bmatrix}$$

The azimuth of PN is given by:

$$\tan(A_{tPN}) = Y(\mathbf{v}_{tPN})/Z(\mathbf{v}_{tPN})$$

The elevation of PN is given by:

$$\tan(h_{tPN}) = \frac{X(\mathbf{v}_{tPN})}{(Y(\mathbf{v}_{tPN})^2 + Z(\mathbf{v}_{tPN})^2)^{½}}$$

The centrifugal acceleration gives a deviation effect in the horizontal plane of

$$\chi_{ca} = \tan^{-1}(\cos h_{tPN} D_{PN} \omega_m^2 / g)$$

The component parts in the north-south and east-west directions are:

$$\eta_{ca} = -\chi_{ca} \sin A_{tPN} \quad \text{and}$$

$$\xi_{ca} = -\chi_{ca} \cos A_{tPN}$$

If N is to the south of the observer then the correction to the observed astronomical latitude will be numerically positive. If N is to the east of the observer then the correction to the observed astronomical longitude will be numerically negative.

7.5 The variation of Lunar Right Ascension and Declination

Approximate values of $RA_{@\delta max}$, δ_{max}, RA_m, and δ_m can be found from analysis of data available at USNO (1997c) using "apparent co-ordinates: geocentric RA & Dec wrt equator of date" or on the CD version at MICA (1998).

An example of the variation of the right ascension and declination of the moon for a period of 33 days is in Figure 7.5, below. The near sine curve is declination and the near straight line is right ascension. Where right ascension returns to 0^h, an increment of 24^h has been added to preserve continuity.

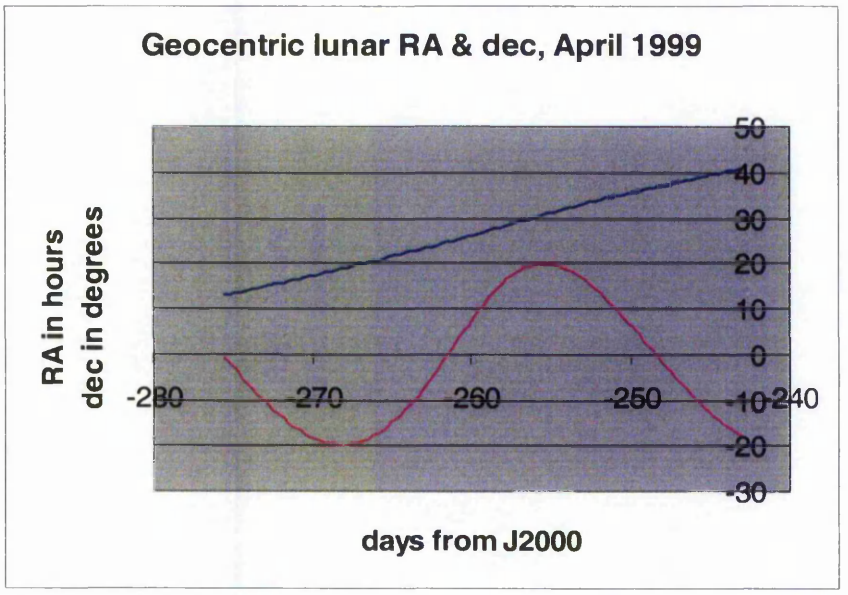

Figure 7.5 Geocentric Right Ascension and Declination of the Moon in April 1999. The upper near straight line is Right Ascension; the lower sinusoidal line is Declination.

A spreadsheet was written to find $RA_{@\delta max}$, δ_{max}, RA_m, and δ_m from a set of 99 date/times, right ascensions and declinations. 99 epochs is the largest data set that can be recovered from the Internet site. In each case the data was modelled to:

$$(RA \text{ or } \delta) - M\,d - C - A\cos(W(d - B)) - E\cos(F(d - G)) = 0$$

where	d is the	date in days from J2000
	M	overall slope
	C	offset from 0
	A	amplitude of the main harmonic
	W	frequency of the main harmonic
	B	phase of the main harmonic
	E	amplitude of the second harmonic
	F	frequency of the second harmonic
	G	amplitude of the second harmonic

A best fit was achieved by least squares.

Typical examples of some of the values were:

	RA		δ	
M	0.88	hours/day	0.0079	deg/day
A	0.45	hours	19.77	deg
W	0.2362	rads/day	0.2321	rads/day
E	0.09	hours	1.09	deg
F	0.4658	rads/day	0.4852	rads/day

The last equation does not fully model the changes of right ascension and declination. However, with RMS values for the residuals of the order of 30^s and 200" respectively, it is an indication that the spreadsheet is sufficient for extracting values of right ascension and declination for the calculation of the effect of lunar gravitation upon astronomical position.

7.6 Magnitude and Direction of Lunar Deviation

Figure 7.6, below, shows the Geocentric Right Ascension and Declination of the Moon in April 1999. On the following pages in Figures 7.7 to 7.10, show respectively the values of the distance from the observation point to the barycentric rotation axis, deviation due to lunar gravitation, deviation due to centrifugal acceleration about the barycentric axis and total deviation.

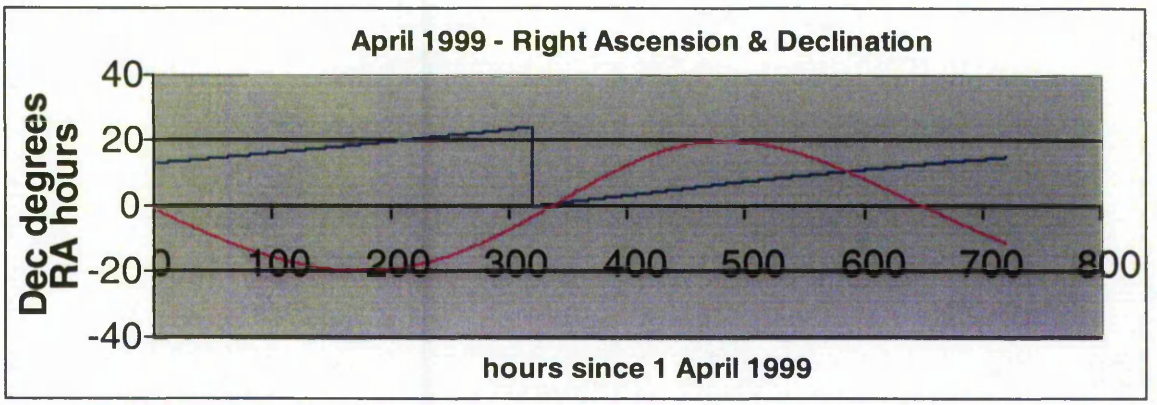

Figure 7.6 Geocentric Right Ascension and Declination of the Moon in April 1999 with time shown in hours from the start of the month.

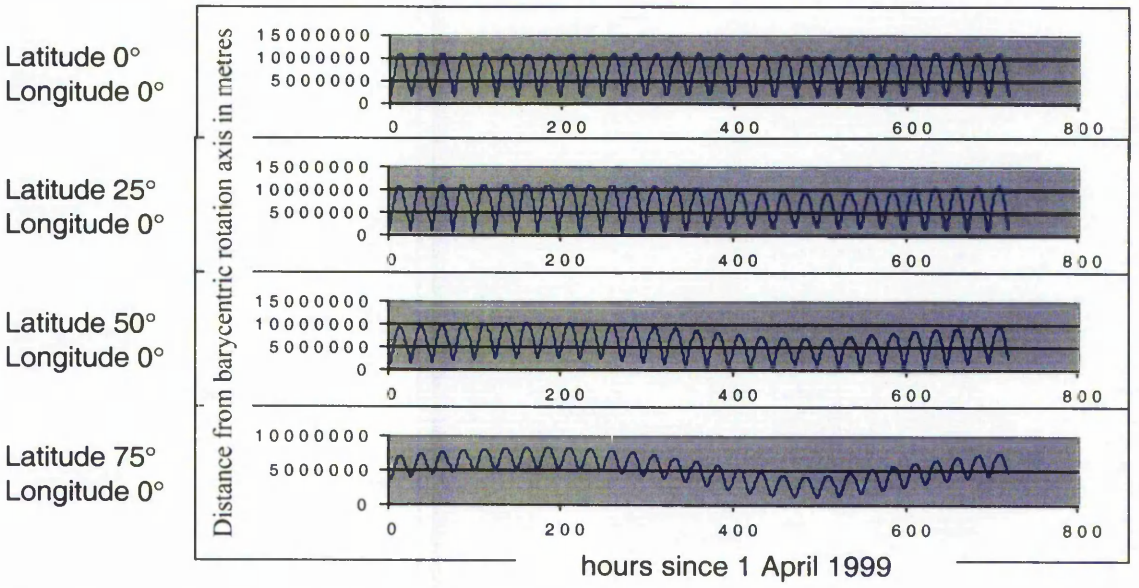

Figure 7.7 Distance from point to barycentric rotation axis.

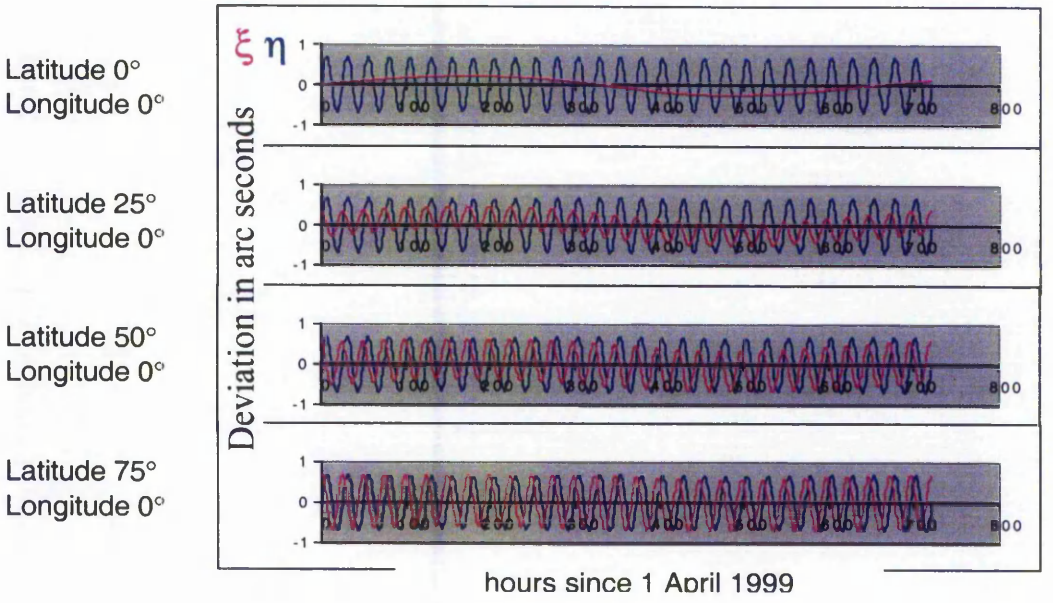

Figure 7.8 Deviation due to lunar gravitation.

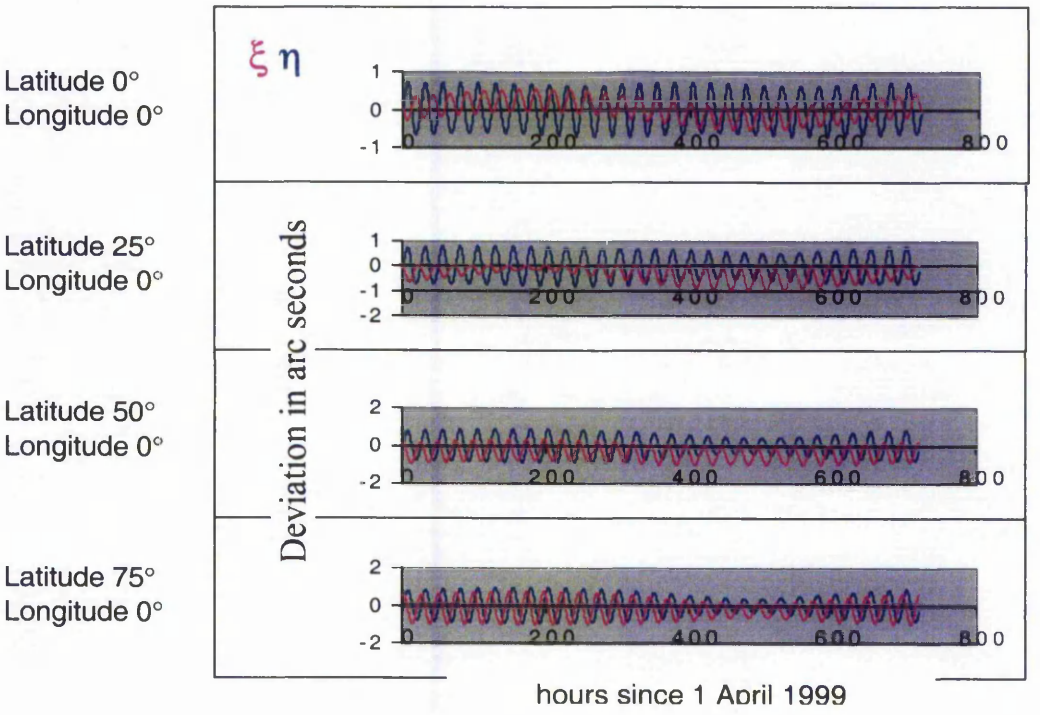

Figure 7.9 Deviation due to centrifugal acceleration about barycentric rotation axis. The x-axis is in hours from 1 April 1999.

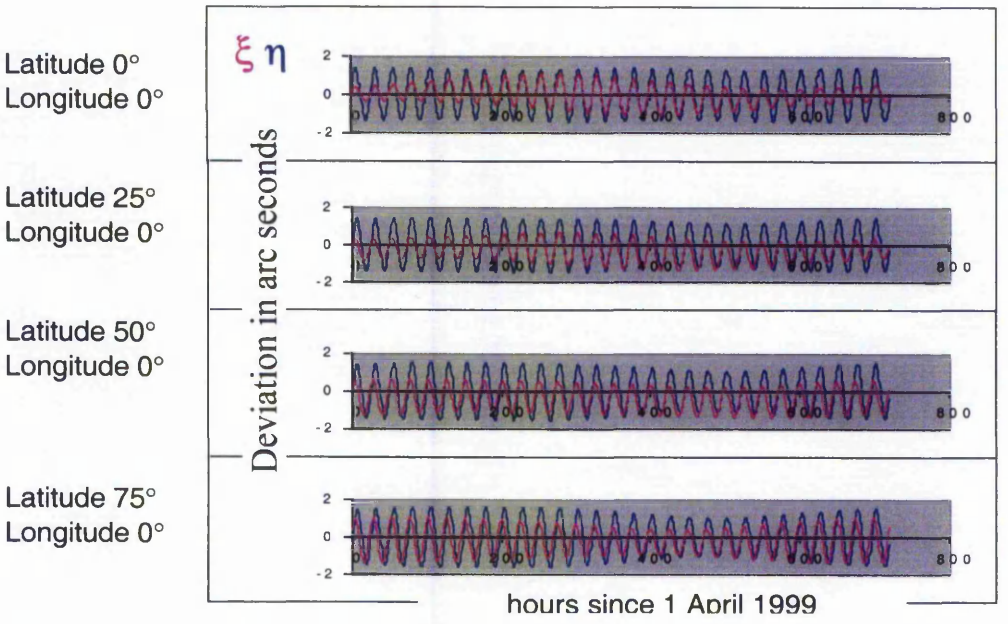

Figure 7.10 Total lunar deviation. The x-axis is in hours from 1 April 1999.

It is clear from the above that the mean of a month's worth of η is zero. That applies to η due to lunar gravitation and η, due to lunar centrifugal effects. In addition, the mean of a

month's worth of ξ due to lunar gravitation is also zero. However, the mean of a month's worth of ξ due to lunar centrifugal effects is not zero. Mean values for a lunar cycle's worth of ξ due to lunar centrifugal effects starting on 1 April 1999 were computed for different values of latitude. The graph of results is at Figure 7.11, below.

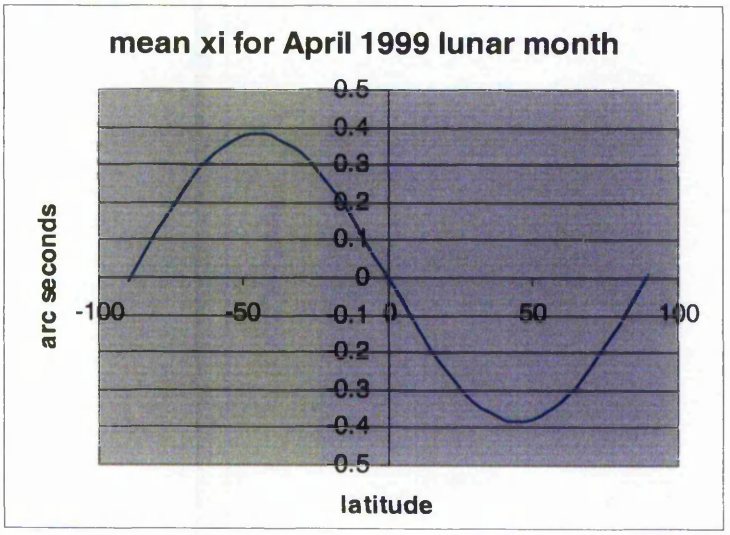

Figure 7.11 Mean ξ for April 1999.

If separation is computed from the above deviations then, as Figure 7.12, shows, almost 12 metres of the earth's equatorial bulge are due to the mean lunar centrifugal effect.

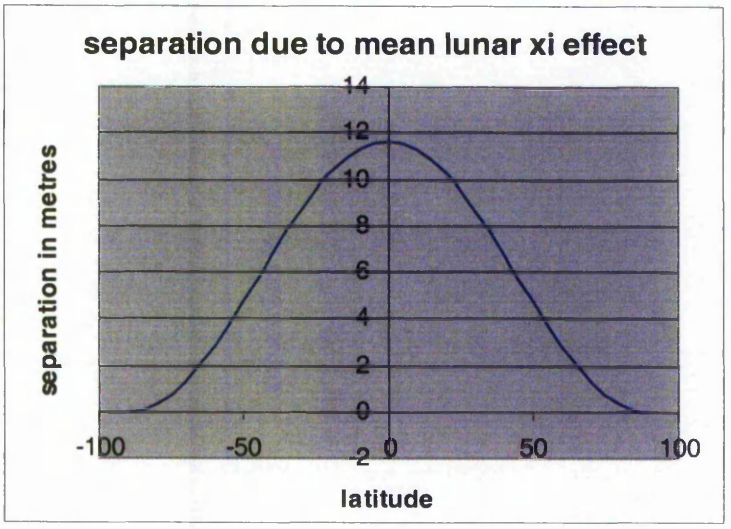

Figure 7.12 Separation due to the mean lunar ξ effect.

This would suggest that a correction based on the graph of mean ξ, Figure 7.11 above, should be applied to all lunar ξ reductions to remove the permanent lunar ξ effect.

However, the data above is only based upon the maximum declination of the moon in April and the maximum declination varies.

According to Walker (2001), the orbit of the moon has an inclination of 5°.145 with respect to the ecliptic. Therefore, the maximum declination of the moon in any one particular orbit will lie within the range of the obliquity of the ecliptic plus or minus the inclination of the moon's orbit with respect to the ecliptic. This range of maximum declination in practice is 18°.15 to 28°.72 (King, 1999).

The data above relates to an arbitrary period where the maximum declination is close to the lower limit. It is therefore appropriate to find the mean values for a lunar cycle's worth of ξ due to lunar centrifugal effects for several representative periods within the full range of declination during the 18.6 years when the ascending node of the orbit of the moon precesses through a full circle. The effect can be seen in the graph of lunar declination for the 16 years for which MICA (1998) is valid. See Figure 7.13, below.

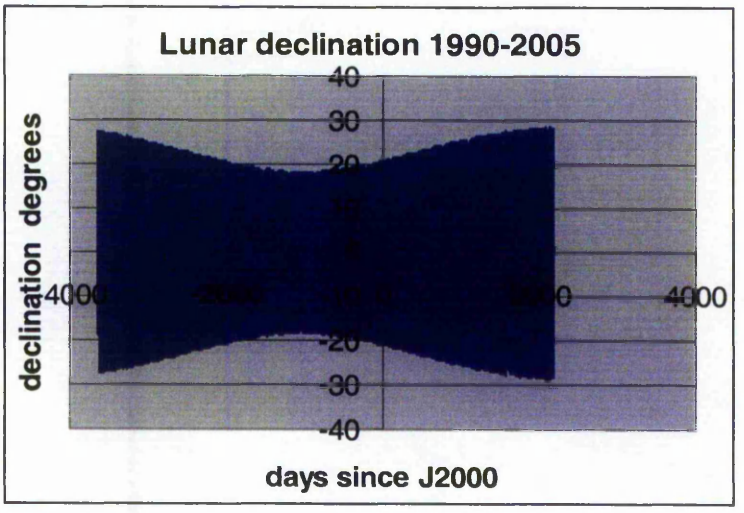

Figure 7.13 Lunar Declination for 1990 to 2005.

Using MICA (1998), the mean values of ξ due to lunar centrifugal effects were computed for 10º increments of latitude for the lunar months starting, respectively, on the following arbitrarily chosen dates:

1 February 1990	=	-3621.5	days after J2000
1 May 1992		-2801.5	
1 May 1997		-975.5	
1 August 2001		577.5	
1 November 2005		2130.5	

The results, graphically displayed, were all very similar. See Figure 7.14, below.

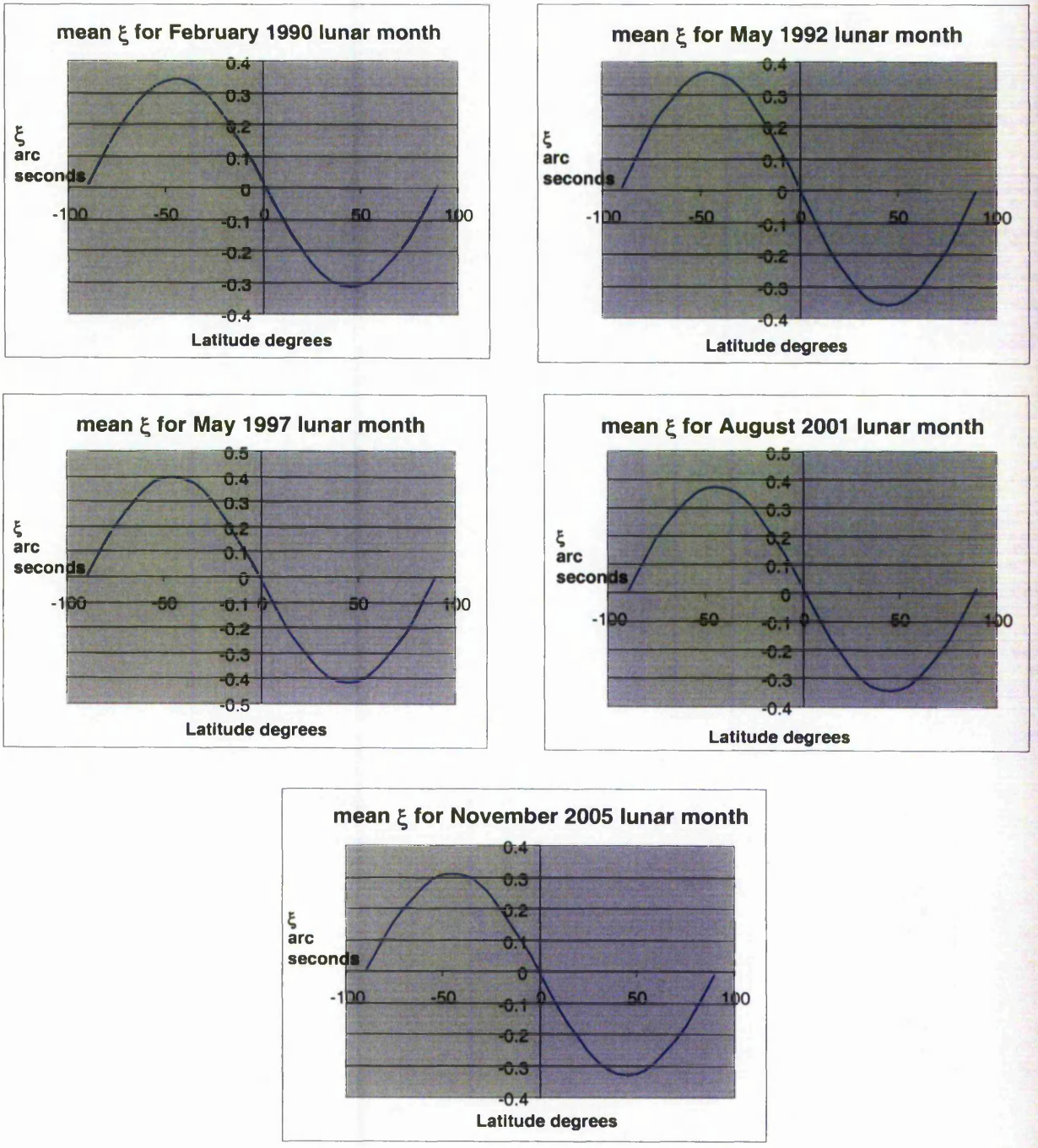

Figure 7.14 Mean ξ for five arbitrary lunar months between February 1990 and November 2005.

There is a slight lack of north-south symmetry in the above data. This is most probably due to the approximate nature of the modelled lunar orbit. However, a least squares fit of the mean of the above data to the sine curve:

$$\xi_{mean} = M \sin(2\phi)$$

gives $M = 0".357 \pm 0".002$

However, again because of the approximate nature of the modelled lunar orbit, a more reasonable value for M and its uncertainty might be 0".36 ± 0".02.

ξ_{mean} is to be taken as the permanent lunar ξ effect and should be applied to all computed values of the lunar ξ correction.

7.7 Summary

In this chapter the effect of the moon's gravitational attraction upon the deviation of the vertical was considered with particular reference to the effect of centrifugal acceleration of the observation point around the barycentric rotation axis upon the deviation of the vertical. The geocentric, orbital and topocentric co-ordinate systems and their relationships were reviewed and formulae that describe the effect of the moon's gravitational attraction upon the deviation of the vertical were developed. The variations of actual Lunar Right Ascension and Declination were examined and this lead to the numerical evaluation of the magnitude and direction of the Lunar Deviation effect. Although this effect is at the sub-arc second level, it will have a systematic effect on all astronomical observations taken over a short period such as the 1-2 hours used in the method described in Chapter 6 because the moon will be in substantially the same part of the sky.

Chapter 8

The Topographic-Isostatic Effect

8.1 Introduction

Astronomical position is observed on the ground surface but slope of the geoid is computed at the geoid. The reduction of observed astronomical position includes a component to account for the different attractions of the surrounding topography on the ground surface compared with that at the geoid. In this chapter, the usual method of determining this topographic-isostatic effect is reviewed and a new simpler method is developed that avoids the need for a complete local terrain model.

8.2 The Topographic-Isostatic Effect Upon Astronomical Position

The observation of astronomical position is made on the surface of the ground. The computation of separation is undertaken by considering the slope of the geoid, at the geoid. Reduction of the observed astronomical position involves computation of the downward continuation of the vertical. This has two components: that due to the divergence of equipotential surfaces away from the poles and that due to different values of the horizontal attraction of the topography at the observation and computation points. The latter is the subject of this chapter.

8.3 The Topography as Right Rectangular Prisms

The topography may be considered as a series of right rectangular prisms that have defined density and axes parallel to, or at right angles to, the vertical at the observation point. The densities of topography, sea/lakes and mantle are quite different. If the boundaries between these can be estimated, and values ascribed to the densities between the boundaries, then a single right rectangular prism can be treated as the sum of its component parts where the parts form a vertical stack of individual right rectangular prisms. The practical boundaries of such a stack would be the highest point of the topography and the lowest point of the Mohorovicic discontinuity or Moho, the boundary surface that separates the Earth's crust from the underlying mantle. Above and below, there will be horizontal symmetry. Figure 8.1,

below, shows the horizontal components of attraction of a right rectangular prism at an observation point and at a computation point.

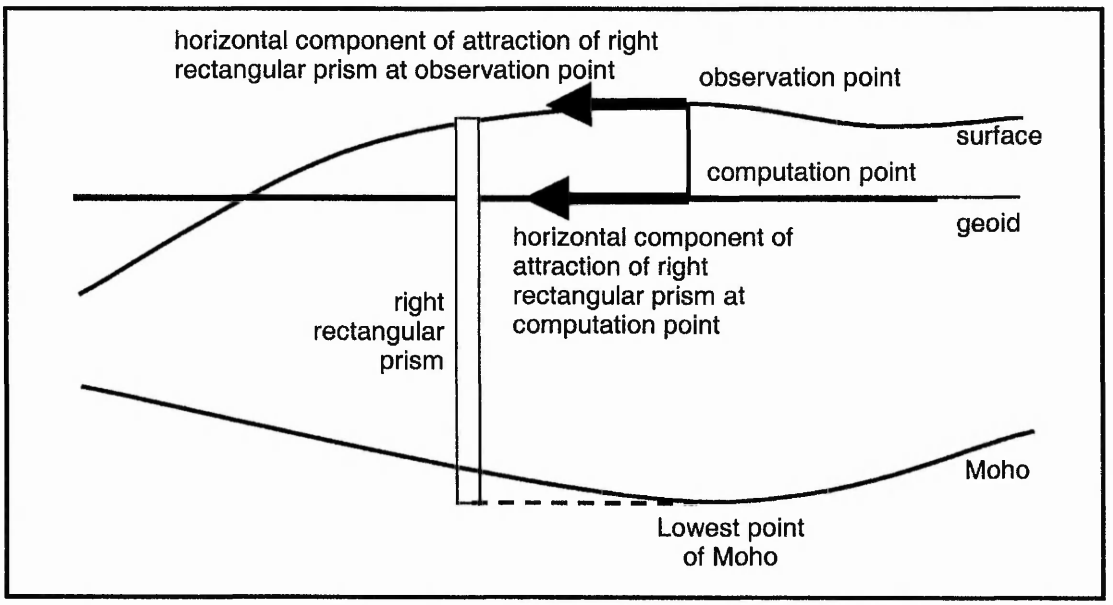

Figure 8.1 Horizontal components of attraction of a right rectangular prism at an observation point and a computation point.

According to Volcano (2001) the Moho is at a depth of 5-10 km beneath the ocean floor and about 35 km below the continents although down to 60 km below mountains.

However, this simple model may not be quite so useful for the representation of the Moho. There is now some doubt concerning the form of the Moho as a smooth surface. Mooney and Meissner (1992) proposed that the Moho consisted of a laminiferous transition zone 3-5 km wide. Brittain (Brittain et al 1996) elaborates further upon this idea where discontinuities or steps in the Moho are also considered.

Tziavos & Andritsanos (1998) quote Nagy (1966) and Tsoulis (1997) for the formula for the attraction of a right rectangular prism as:

$$T_z(P) = G\rho \left| \left| \left| x \ln(y+r) + y \ln(x+r) - z \tan^{-1} \frac{xy}{zr} \right|_{x_1}^{x_2} \right|_{y_1}^{y_2} \right|_{z_1}^{z_2}$$

where $T_z(P)$ is the attraction of a right rectangular prism in the direction z at point P, the origin of the x,y,z right-handed co-ordinate system defined by the user.

G is the universal gravitational constant (Georgia 2001) $6.672\ 10^{-8}\ cm^3\ g^{-1}\ s^{-2}$

ρ is the density of the right rectangular prism, assumed constant.

$x_1 \ldots z_2$ describe the extent of the right rectangular prism

r is the distance of P from a unit element of the right rectangular prism.

When $(x^2 + y^2 + z^2)^{½}$ is substituted for r into the equation above:

$$T_z(P) = G\rho \left| \begin{array}{c} \\ \\ \end{array} \right| x \ln(y+(x^2+y^2+z^2)^{½}) + y \ln(x+(x^2+y^2+z^2)^{½}) - z \tan^{-1}\left(\frac{xy}{z(x^2+y^2+z^2)^{½}}\right) \left|\begin{array}{ccc} x_2 & y_2 & z_2 \\ & & \\ x_1 & y_1 & z_1 \end{array}\right.$$

Nagy (1966) derives a similar formula except that the $\tan^{-1}(..)$ term is replaced by a different $\sin^{-1}(..)$ term. However, whereas the $\tan^{-1}(..)$ term above is interchangeable in x and y, Nagy's $\sin^{-1}(..)$ term is not, and the formula must therefore be considered doubtful even though Nagy declares that both formulae are identical, that is, his formula is identical to a formula quoted from Haáz (1953) and similar to the one above.

The formula above is for the vertical component of attraction. What is required here are eastward and northward components. These may be derived from the above formula by interchanging axes so that the formulae for the eastward and northward attractions are respectively:

$$T_x(P) = G\rho \left| \begin{array}{c} \\ \\ \end{array} \right| y \ln(z+(x^2+y^2+z^2)^{½}) + z \ln(y+(x^2+y^2+z^2)^{½}) - x \tan^{-1}\left(\frac{yz}{x(x^2+y^2+z^2)^{½}}\right) \left|\begin{array}{ccc} y_2 & z_2 & x_2 \\ & & \\ y_1 & z_1 & x_1 \end{array}\right.$$

$$T_y(P) = G\rho \left| \begin{array}{c} \\ \\ \end{array} \right| z \ln(x+(x^2+y^2+z^2)^{½}) + x \ln(z+(x^2+y^2+z^2)^{½}) - y \tan^{-1}\left(\frac{zx}{y(x^2+y^2+z^2)^{½}}\right) \left|\begin{array}{ccc} z_2 & x_2 & y_2 \\ & & \\ z_1 & x_1 & y_1 \end{array}\right.$$

In all cases x_1 and x_2, y_1 and y_2, z_1 and z_2, must be on the same side of their respective axes. If they are not then the prism must be split into 2 prisms, on the positive and negative sides of the axis.

Expanding the expression for $T_x(P)$ above leads to:

$$T_x(P) = G\rho \left| \begin{array}{c} \\ \end{array} \right| y_2 \ln(z+(x^2+y_2^2+z^2)^{½}) + z \ln(y_2+(x^2+y_2^2+z^2)^{½}) - x \tan^{-1}\left(\frac{y_2 z}{x(x^2+y_2^2+z^2)^{½}}\right)$$

$$- y_1 \ln(z+(x^2+y_1^2+z^2)^{½}) - z \ln(y_1+(x^2+y_1^2+z^2)^{½}) + x \tan^{-1}\left(\frac{y_1 z}{x(x^2+y_1^2+z^2)^{½}}\right) \left|\begin{array}{cc} z_2 & x_2 \\ & \\ z_1 & x_1 \end{array}\right.$$

$$= G\rho \Big| y_2 \ln(z_2+(x^2+y_2^2+z_2^2)^{1/2}) + z_2 \ln(y_2+(x^2+y_2^2+z_2^2)^{1/2}) - x\tan^{-1}\left(\frac{y_2z_2}{x(x^2+y_2^2+z_2^2)^{1/2}}\right)$$

$$- y_1 \ln(z_2+(x^2+y_1^2+z_2^2)^{1/2}) - z_2 \ln(y_1+(x^2+y_1^2+z_2^2)^{1/2}) + x\tan^{-1}\left(\frac{y_1z_2}{x(x^2+y_1^2+z_2^2)^{1/2}}\right)$$

$$- y_2 \ln(z_1+(x^2+y_2^2+z_1^2)^{1/2}) - z_1 \ln(y_2+(x^2+y_2^2+z_1^2)^{1/2}) + x\tan^{-1}\left(\frac{y_2z_1}{x(x^2+y_2^2+z_1^2)^{1/2}}\right)$$

$$+ y_1 \ln(z_1+(x^2+y_1^2+z_1^2)^{1/2}) + z_1 \ln(y_1+(x^2+y_1^2+z_1^2)^{1/2}) - x\tan^{-1}\left(\frac{y_1z_1}{x(x^2+y_1^2+z_1^2)^{1/2}}\right) \Big|_{x_1}^{x_2}$$

$$= G\rho \Big\{ y_2\ln(z_2+(x_2^2+y_2^2+z_2^2)^{1/2}) + z_2\ln(y_2+(x_2^2+y_2^2+z_2^2)^{1/2}) - x_2\tan^{-1}\left(\frac{y_2z_2}{x_2(x_2^2+y_2^2+z_2^2)^{1/2}}\right)$$

$$- y_1\ln(z_2+(x_2^2+y_1^2+z_2^2)^{1/2}) - z_2\ln(y_1+(x_2^2+y_1^2+z_2^2)^{1/2}) + x_2\tan^{-1}\left(\frac{y_1z_2}{x_2(x_2^2+y_1^2+z_2^2)^{1/2}}\right)$$

$$- y_2\ln(z_1+(x_2^2+y_2^2+z_1^2)^{1/2}) - z_1\ln(y_2+(x_2^2+y_2^2+z_1^2)^{1/2}) + x_2\tan^{-1}\left(\frac{y_2z_1}{x_2(x_2^2+y_2^2+z_1^2)^{1/2}}\right)$$

$$+ y_1\ln(z_1+(x_2^2+y_1^2+z_1^2)^{1/2}) + z_1\ln(y_1+(x_2^2+y_1^2+z_1^2)^{1/2}) - x_2\tan^{-1}\left(\frac{y_1z_1}{x_2(x_2^2+y_1^2+z_1^2)^{1/2}}\right)$$

$$- y_2\ln(z_2+(x_1^2+y_2^2+z_2^2)^{1/2}) - z_2\ln(y_2+(x_1^2+y_2^2+z_2^2)^{1/2}) + x_1\tan^{-1}\left(\frac{y_2z_2}{x_1(x_1^2+y_2^2+z_2^2)^{1/2}}\right)$$

$$+ y_1\ln(z_2+(x_1^2+y_1^2+z_2^2)^{1/2}) + z_2\ln(y_1+(x_1^2+y_1^2+z_2^2)^{1/2}) - x_1\tan^{-1}\left(\frac{y_1z_2}{x_1(x_1^2+y_1^2+z_2^2)^{1/2}}\right)$$

$$+ y_2\ln(z_1+(x_1^2+y_2^2+z_1^2)^{1/2}) + z_1\ln(y_2+(x_1^2+y_2^2+z_1^2)^{1/2}) - x_1\tan^{-1}\left(\frac{y_2z_1}{x_1(x_1^2+y_2^2+z_1^2)^{1/2}}\right)$$

$$- y_1\ln(z_1+(x_1^2+y_1^2+z_1^2)^{1/2}) - z_1\ln(y_1+(x_1^2+y_1^2+z_1^2)^{1/2}) + x_1\tan^{-1}\left(\frac{y_1z_1}{x_1(x_1^2+y_1^2+z_1^2)^{1/2}}\right) \Big\}$$

and similarly $T_y(P)$ may be found by exchanging x, y and z.

$$T_y(P) = G\rho \Big\{ z_2\ln(x_2+(y_2^2+z_2^2+x_2^2)^{1/2}) + x_2\ln(z_2+(y_2^2+z_2^2+x_2^2)^{1/2}) - y_2\tan^{-1}\left(\frac{z_2x_2}{y_2(y_2^2+z_2^2+x_2^2)^{1/2}}\right)$$

$$- z_1\ln(x_2+(y_2^2+z_1^2+x_2^2)^{1/2}) - x_2\ln(z_1+(y_2^2+z_1^2+x_2^2)^{1/2}) + y_2\tan^{-1}\left(\frac{z_1x_2}{y_2(y_2^2+z_1^2+x_2^2)^{1/2}}\right)$$

$$- z_2\ln(x_1+(y_2^2+z_2^2+x_1^2)^{1/2}) - x_1\ln(z_2+(y_2^2+z_2^2+x_1^2)^{1/2}) + y_2\tan^{-1}\left(\frac{z_2x_1}{y_2(y_2^2+z_2^2+x_1^2)^{1/2}}\right)$$

$$+ z_1\ln(x_1+(y_2^2+z_1^2+x_1^2)^{1/2}) + x_1\ln(z_1+(y_2^2+z_1^2+x_1^2)^{1/2}) - y_2\tan^{-1}\left(\frac{z_1x_1}{y_2(y_2^2+z_1^2+x_1^2)^{1/2}}\right)$$

$$- z_2 \ln(x_2+(y_1^2+z_2^2+x_2^2)^{1/2}) - x_2 \ln(z_2+(y_1^2+z_2^2+x_2^2)^{1/2}) + y_1 \tan^{-1}\left(\frac{z_2 x_2}{y_1(y_1^2+z_2^2+x_2^2)^{1/2}}\right)$$

$$+ z_1 \ln(x_2+(y_1^2+z_1^2+x_2^2)^{1/2}) + x_2 \ln(z_1+(y_1^2+z_1^2+x_2^2)^{1/2}) - y_1 \tan^{-1}\left(\frac{z_1 x_2}{y_1(y_1^2+z_1^2+x_2^2)^{1/2}}\right)$$

$$+ z_2 \ln(x_1+(y_1^2+z_2^2+x_1^2)^{1/2}) + x_1 \ln(z_2+(y_1^2+z_2^2+x_1^2)^{1/2}) - y_1 \tan^{-1}\left(\frac{z_2 x_1}{y_1(y_1^2+z_2^2+x_1^2)^{1/2}}\right)$$

$$- z_1 \ln(x_1+(y_1^2+z_1^2+x_1^2)^{1/2}) - x_1 \ln(z_1+(y_1^2+z_1^2+x_1^2)^{1/2}) + y_1 \tan^{-1}\left(\frac{z_1 x_1}{y_1(y_1^2+z_1^2+x_1^2)^{1/2}}\right) \Big\}$$

If only the topography above the geoid is to be considered, then formulae for computation of $T_x(P)$ and $T_y(P)$ depend upon whether the point of computation P is above (Case I) or below (Case II) the top of the right rectangular prism. In Figure 8.2, below, z_P is the height of point P and z_M is the height of the right rectangular prism. When $z_P < z_M$ the attraction of the prism must be considered as the sum of the part above z_P and the part below it as far as the attraction at the point is concerned.

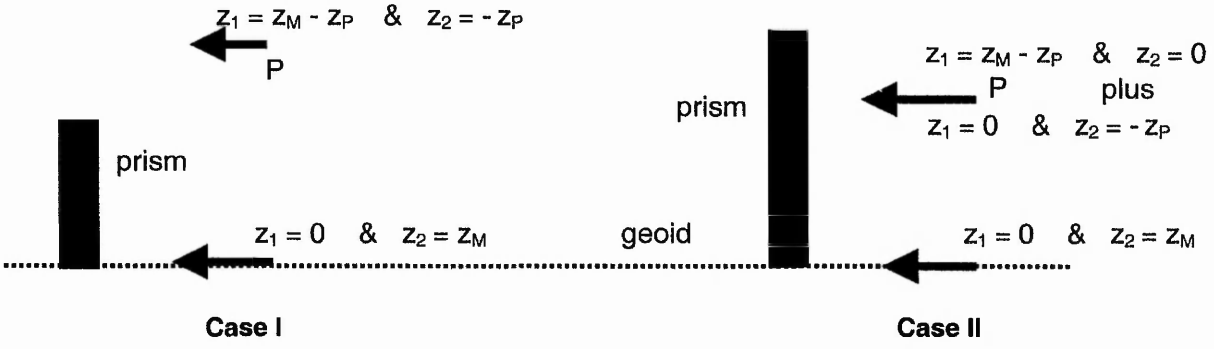

Figure 8.2 The attraction of a right rectangular prism at the geoid and at the computation point.

In Case I, the differences between the attraction at the geoid and at the point are:

$$T_x(P) = G\rho \Big\{ y_2 \ln((x_2^2+y_2^2)^{1/2}) - y_1 \ln((x_2^2+y_1^2)^{1/2}) - y_2 \ln((x_1^2+y_2^2)^{1/2}) + y_1 \ln((x_1^2+y_1^2)^{1/2})$$

$$- y_2 \ln(z_M+(x_2^2+y_2^2+z_M^2)^{1/2}) - z_M \ln(y_2+(x_2^2+y_2^2+z_M^2)^{1/2}) + x_2 \tan^{-1}\left(\frac{y_2 z_M}{x_2(x_2^2+y_2^2+z_M^2)^{1/2}}\right)$$

$$+ y_1 \ln(z_M+(x_2^2+y_1^2+z_M^2)^{1/2}) + z_M \ln(y_1+(x_2^2+y_1^2+z_M^2)^{1/2}) - x_2 \tan^{-1}\left(\frac{y_1 z_M}{x_2(x_2^2+y_1^2+z_M^2)^{1/2}}\right)$$

$$+ y_2 \ln(z_M+(x_1^2+y_2^2+z_M^2)^{1/2}) + z_M \ln(y_2+(x_1^2+y_2^2+z_M^2)^{1/2}) - x_1 \tan^{-1}\left(\frac{y_2 z_M}{x_1(x_1^2+y_2^2+z_M^2)^{1/2}}\right)$$

$$- y_1 \ln(z_M + (x_1^2 + y_1^2 + z_M^2)^{1/2}) - z_M \ln(y_1 + (x_1^2 + y_1^2 + z_M^2)^{1/2}) + x_1 \tan^{-1}\left(\frac{y_1 z_M}{x_1 (x_1^2 + y_1^2 + z_M^2)^{1/2}}\right) \Big\}$$

$$- G\rho \Big\{ y_2 \ln(-z_P + (x_2^2 + y_2^2 + z_P^2)^{1/2}) - z_P \ln(y_2 + (x_2^2 + y_2^2 + z_P^2)^{1/2}) + x_2 \tan^{-1}\left(\frac{y_2 z_P}{x_2 (x_2^2 + y_2^2 + z_P^2)^{1/2}}\right)$$

$$- y_1 \ln(-z_P + (x_2^2 + y_1^2 + z_P^2)^{1/2}) + z_P \ln(y_1 + (x_2^2 + y_1^2 + z_P^2)^{1/2}) - x_2 \tan^{-1}\left(\frac{y_1 z_P}{x_2 (x_2^2 + y_1^2 + z_P^2)^{1/2}}\right)$$

$$- y_2 \ln(z_M - z_P + (x_2^2 + y_2^2 + (z_M - z_P)^2)^{1/2}) - (z_M - z_P) \ln(y_2 + (x_2^2 + y_2^2 + (z_M - z_P)^2)^{1/2}) + x_2 \tan^{-1}\left(\frac{y_2 (z_M - z_P)}{x_2 (x_2^2 + y_2^2 + (z_M - z_P)^2)^{1/2}}\right)$$

$$+ y_1 \ln(z_M - z_P + (x_2^2 + y_1^2 + (z_M - z_P)^2)^{1/2}) + (z_M - z_P) \ln(y_1 + (x_2^2 + y_1^2 + (z_M - z_P)^2)^{1/2}) - x_2 \tan^{-1}\left(\frac{y_1 (z_M - z_P)}{x_2 (x_2^2 + y_1^2 + (z_M - z_P)^2)^{1/2}}\right)$$

$$- y_2 \ln(-z_P + (x_1^2 + y_2^2 + z_P^2)^{1/2}) + z_P \ln(y_2 + (x_1^2 + y_2^2 + z_P^2)^{1/2}) - x_1 \tan^{-1}\left(\frac{y_2 z_P}{x_1 (x_1^2 + y_2^2 + z_P^2)^{1/2}}\right)$$

$$+ y_1 \ln(-z_P + (x_1^2 + y_1^2 + z_P^2)^{1/2}) - z_P \ln(y_1 + (x_1^2 + y_1^2 + z_P^2)^{1/2}) + x_1 \tan^{-1}\left(\frac{y_1 z_P}{x_1 (x_1^2 + y_1^2 + z_P^2)^{1/2}}\right)$$

$$+ y_2 \ln(z_M - z_P + (x_1^2 + y_2^2 + (z_M - z_P)^2)^{1/2}) + (z_M - z_P) \ln(y_2 + (x_1^2 + y_2^2 + (z_M - z_P)^2)^{1/2}) - x_1 \tan^{-1}\left(\frac{y_2 (z_M - z_P)}{x_1 (x_1^2 + y_2^2 + (z_M - z_P)^2)^{1/2}}\right)$$

$$- y_1 \ln(z_M - z_P + (x_1^2 + y_1^2 + (z_M - z_P)^2)^{1/2}) - (z_M - z_P) \ln(y_1 + (x_1^2 + y_1^2 + (z_M - z_P)^2)^{1/2}) + x_1 \tan^{-1}\left(\frac{y_1 (z_M - z_P)}{x_1 (x_1^2 + y_1^2 + (z_M - z_P)^2)^{1/2}}\right) \Big\}$$

$$T_y(P) = G\rho \Big\{ x_2 \ln((y_2^2 + x_2^2)^{1/2}) - z_M \ln(x_2 + (y_2^2 + z_M^2 + x_2^2)^{1/2}) - x_2 \ln(z_M + (y_2^2 + z_M^2 + x_2^2)^{1/2}) + y_2 \tan^{-1}\left(\frac{z_M x_2}{y_2 (y_2^2 + z_M^2 + x_2^2)^{1/2}}\right)$$

$$- x_1 \ln((y_2^2 + x_1^2)^{1/2}) + z_M \ln(x_1 + (y_2^2 + z_M^2 + x_1^2)^{1/2}) + x_1 \ln(z_M + (y_2^2 + z_M^2 + x_1^2)^{1/2}) - y_2 \tan^{-1}\left(\frac{z_M x_1}{y_2 (y_2^2 + z_M^2 + x_1^2)^{1/2}}\right)$$

$$- x_2 \ln((y_1^2 + x_2^2)^{1/2}) + z_M \ln(x_2 + (y_1^2 + z_M^2 + x_2^2)^{1/2}) + x_2 \ln(z_M + (y_1^2 + z_M^2 + x_2^2)^{1/2}) - y_1 \tan^{-1}\left(\frac{z_M x_2}{y_1 (y_1^2 + z_M^2 + x_2^2)^{1/2}}\right)$$

$$+ x_1 \ln((y_1^2 + x_1^2)^{1/2}) - z_M \ln(x_1 + (y_1^2 + z_M^2 + x_1^2)^{1/2}) - x_1 \ln(z_M + (y_1^2 + z_M^2 + x_1^2)^{1/2}) + y_1 \tan^{-1}\left(\frac{z_M x_1}{y_1 (y_1^2 + z_M^2 + x_1^2)^{1/2}}\right) \Big\}$$

$$- G\rho \Big\{ -z_P \ln(x_2 + (y_2^2 + z_P^2 + x_2^2)^{1/2}) + x_2 \ln(-z_P + (y_2^2 + z_P^2 + x_2^2)^{1/2}) + y_2 \tan^{-1}\left(\frac{z_P x_2}{y_2 (y_2^2 + z_P^2 + x_2^2)^{1/2}}\right)$$

$$- (z_M - z_P) \ln(x_2 + (y_2^2 + (z_M - z_P)^2 + x_2^2)^{1/2}) - x_2 \ln(z_M - z_P + (y_2^2 + (z_M - z_P)^2 + x_2^2)^{1/2}) + y_2 \tan^{-1}\left(\frac{(z_M - z_P) x_2}{y_2 (y_2^2 + (z_M - z_P)^2 + x_2^2)^{1/2}}\right)$$

$$+ z_P \ln(x_1 + (y_2^2 + z_P^2 + x_1^2)^{1/2}) - x_1 \ln(-z_P + (y_2^2 + z_P^2 + x_1^2)^{1/2}) - y_2 \tan^{-1}\left(\frac{z_P x_1}{y_2 (y_2^2 + z_P^2 + x_1^2)^{1/2}}\right)$$

$$+ (z_M - z_P) \ln(x_1 + (y_2^2 + (z_M - z_P)^2 + x_1^2)^{1/2}) + x_1 \ln(z_M - z_P + (y_2^2 + (z_M - z_P)^2 + x_1^2)^{1/2}) - y_2 \tan^{-1}\left(\frac{(z_M - z_P) x_1}{y_2 (y_2^2 + (z_M - z_P)^2 + x_1^2)^{1/2}}\right)$$

$$+ z_P \ln(x_2 + (y_1^2 + z_P^2 + x_2^2)^{1/2}) - x_2 \ln(-z_P + (y_1^2 + z_P^2 + x_2^2)^{1/2}) - y_1 \tan^{-1}\left(\frac{z_P x_2}{y_1 (y_1^2 + z_P^2 + x_2^2)^{1/2}}\right)$$

$$+ (z_M - z_P) \ln(x_2 + (y_1^2 + (z_M - z_P)^2 + x_2^2)^{1/2}) + x_2 \ln(z_M - z_P + (y_1^2 + (z_M - z_P)^2 + x_2^2)^{1/2}) - y_1 \tan^{-1}\left(\frac{(z_M - z_P) x_2}{y_1 (y_1^2 + (z_M - z_P)^2 + x_2^2)^{1/2}}\right)$$

$$- z_P \ln(x_1 + (y_1^2 + z_P^2 + x_1^2)^{1/2}) + x_1 \ln(-z_P + (y_1^2 + z_P^2 + x_1^2)^{1/2}) + y_1 \tan^{-1}\left(\frac{z_P x_1}{y_1 (y_1^2 + z_P^2 + x_1^2)^{1/2}}\right)$$

$$- (z_M - z_P) \ln(x_1 + (y_1^2 + (z_M - z_P)^2 + x_1^2)^{1/2}) - x_1 \ln(z_M - z_P + (y_1^2 + (z_M - z_P)^2 + x_1^2)^{1/2}) + y_1 \tan^{-1}\left(\frac{(z_M - z_P) x_1}{y_1 (y_1^2 + (z_M - z_P)^2 + x_1^2)^{1/2}}\right) \Big\}$$

In Case II the differences between the attraction at the geoid and at the point are:

$$T_x(P) = G\rho \Big\{ y_2 \ln((x_2^2+y_2^2)^{1/2}) - y_1 \ln((x_2^2+y_1^2)^{1/2}) - y_2 \ln((x_1^2+y_2^2)^{1/2}) + y_1 \ln((x_1^2+y_1^2)^{1/2})$$
$$- y_2 \ln(z_M+(x_2^2+y_2^2+z_M^2)^{1/2}) - z_M \ln(y_2+(x_2^2+y_2^2+z_M^2)^{1/2}) + x_2 \tan^{-1}\left(\frac{y_2 z_M}{x_2(x_2^2+y_2^2+z_M^2)^{1/2}}\right)$$
$$+ y_1 \ln(z_M+(x_2^2+y_1^2+z_M^2)^{1/2}) + z_M \ln(y_1+(x_2^2+y_1^2+z_M^2)^{1/2}) - x_2 \tan^{-1}\left(\frac{y_1 z_M}{x_2(x_2^2+y_1^2+z_M^2)^{1/2}}\right)$$
$$+ y_2 \ln(z_M+(x_1^2+y_2^2+z_M^2)^{1/2}) + z_M \ln(y_2+(x_1^2+y_2^2+z_M^2)^{1/2}) - x_1 \tan^{-1}\left(\frac{y_2 z_M}{x_1(x_1^2+y_2^2+z_M^2)^{1/2}}\right)$$
$$- y_1 \ln(z_M+(x_1^2+y_1^2+z_M^2)^{1/2}) - z_M \ln(y_1+(x_1^2+y_1^2+z_M^2)^{1/2}) + x_1 \tan^{-1}\left(\frac{y_1 z_M}{x_1(x_1^2+y_1^2+z_M^2)^{1/2}}\right) \Big\}$$

$$- G\rho \Big\{ y_2 \ln((x_2^2+y_2^2)^{1/2}) - y_1 \ln((x_2^2+y_1^2)^{1/2}) - y_2 \ln((x_1^2+y_2^2)^{1/2}) + y_1 \ln((x_1^2+y_1^2)^{1/2})$$
$$- y_2 \ln(z_M-z_P+(x_2^2+y_2^2+(z_M-z_P)^2)^{1/2}) - (z_M-z_P) \ln(y_2+(x_2^2+y_2^2+(z_M-z_P)^2)^{1/2}) + x_2 \tan^{-1}\left(\frac{y_2(z_M-z_P)}{x_2(x_2^2+y_2^2+(z_M-z_P)^2)^{1/2}}\right)$$
$$+ y_1 \ln(z_M-z_P+(x_2^2+y_1^2+(z_M-z_P)^2)^{1/2}) + (z_M-z_P) \ln(y_1+(x_2^2+y_1^2+(z_M-z_P)^2)^{1/2}) - x_2 \tan^{-1}\left(\frac{y_1(z_M-z_P)}{x_2(x_2^2+y_1^2+(z_M-z_P)^2)^{1/2}}\right)$$
$$+ y_2 \ln(z_M-z_P+(x_1^2+y_2^2+(z_M-z_P)^2)^{1/2}) + (z_M-z_P) \ln(y_2+(x_1^2+y_2^2+(z_M-z_P)^2)^{1/2}) - x_1 \tan^{-1}\left(\frac{y_2(z_M-z_P)}{x_1(x_1^2+y_2^2+(z_M-z_P)^2)^{1/2}}\right)$$
$$- y_1 \ln(z_M-z_P+(x_1^2+y_1^2+(z_M-z_P)^2)^{1/2}) - (z_M-z_P) \ln(y_1+(x_1^2+y_1^2+(z_M-z_P)^2)^{1/2}) + x_1 \tan^{-1}\left(\frac{y_1(z_M-z_P)}{x_1(x_1^2+y_1^2+(z_M-z_P)^2)^{1/2}}\right) \Big\}$$

$$- G\rho \Big\{ y_2 \ln(-z_P+(x_2^2+y_2^2+z_P^2)^{1/2}) - z_P \ln(y_2+(x_2^2+y_2^2+z_P^2)^{1/2}) + x_2 \tan^{-1}\left(\frac{y_2 z_P}{x_2(x_2^2+y_2^2+z_P^2)^{1/2}}\right)$$
$$- y_1 \ln(-z_P+(x_2^2+y_1^2+z_P^2)^{1/2}) + z_P \ln(y_1+(x_2^2+y_1^2+z_P^2)^{1/2}) - x_2 \tan^{-1}\left(\frac{y_1 z_P}{x_2(x_2^2+y_1^2+z_P^2)^{1/2}}\right)$$
$$- y_2 \ln((x_2^2+y_2^2)^{1/2}) + y_1 \ln((x_2^2+y_1^2)^{1/2}) + y_2 \ln((x_1^2+y_2^2)^{1/2}) - y_1 \ln((x_1^2+y_1^2)^{1/2})$$
$$- y_2 \ln(-z_P+(x_1^2+y_2^2+z_P^2)^{1/2}) + z_P \ln(y_2+(x_1^2+y_2^2+z_P^2)^{1/2}) - x_1 \tan^{-1}\left(\frac{y_2 z_P}{x_1(x_1^2+y_2^2+z_P^2)^{1/2}}\right)$$
$$+ y_1 \ln(-z_P+(x_1^2+y_1^2+z_P^2)^{1/2}) - z_P \ln(y_1+(x_1^2+y_1^2+z_P^2)^{1/2}) + x_1 \tan^{-1}\left(\frac{y_1 z_P}{x_1(x_1^2+y_1^2+z_P^2)^{1/2}}\right) \Big\}$$

$$T_y(P) = G\rho \Big\{ x_2 \ln((y_2^2+x_2^2)^{1/2}) - z_M \ln(x_2+(y_2^2+z_M^2+x_2^2)^{1/2}) - x_2 \ln(z_M+(y_2^2+z_M^2+x_2^2)^{1/2}) + y_2 \tan^{-1}\left(\frac{z_M x_2}{y_2(y_2^2+z_M^2+x_2^2)^{1/2}}\right)$$
$$- x_1 \ln((y_2^2+x_1^2)^{1/2}) + z_M \ln(x_1+(y_2^2+z_M^2+x_1^2)^{1/2}) + x_1 \ln(z_M+(y_2^2+z_M^2+x_1^2)^{1/2}) - y_2 \tan^{-1}\left(\frac{z_M x_1}{y_2(y_2^2+z_M^2+x_1^2)^{1/2}}\right)$$
$$- x_2 \ln((y_1^2+x_2^2)^{1/2}) + z_M \ln(x_2+(y_1^2+z_M^2+x_2^2)^{1/2}) + x_2 \ln(z_M+(y_1^2+z_M^2+x_2^2)^{1/2}) - y_1 \tan^{-1}\left(\frac{z_M x_2}{y_1(y_1^2+z_M^2+x_2^2)^{1/2}}\right)$$
$$+ x_1 \ln((y_1^2+x_1^2)^{1/2}) - z_M \ln(x_1+(y_1^2+z_M^2+x_1^2)^{1/2}) - x_1 \ln(z_M+(y_1^2+z_M^2+x_1^2)^{1/2}) + y_1 \tan^{-1}\left(\frac{z_M x_1}{y_1(y_1^2+z_M^2+x_1^2)^{1/2}}\right) \Big\}$$

$$- G\rho \Big\{ x_2 \ln((y_2^2+x_2^2)^{1/2}) - x_1 \ln((y_2^2+x_1^2)^{1/2}) - x_2 \ln((y_1^2+x_2^2)^{1/2}) + x_1 \ln((y_1^2+x_1^2)^{1/2})$$
$$- (z_M-z_P) \ln(x_2+(y_2^2+(z_M-z_P)^2+x_2^2)^{1/2}) - x_2 \ln(z_M-z_P+(y_2^2+(z_M-z_P)^2+x_2^2)^{1/2}) + y_2 \tan^{-1}\left(\frac{(z_M-z_P)x_2}{y_2(y_2^2+(z_M-z_P)^2+x_2^2)^{1/2}}\right)$$

$$+ (z_M-z_P)\ln(x_1+(y_2^2+(z_M-z_P)^2+x_1^2)^{½})+x_1\ln(z_M-z_P+(y_2^2+(z_M-z_P)^2+x_1^2)^{½})-y_2\tan^{-1}\left(\frac{(z_M-z_P)x_1}{y_2(y_2^2+(z_M-z_P)^2+x_1^2)^{½}}\right)$$

$$+ (z_M-z_P)\ln(x_2+(y_1^2+(z_M-z_P)^2+x_2^2)^{½})+x_2\ln(z_M-z_P+(y_1^2+(z_M-z_P)^2+x_2^2)^{½})-y_1\tan^{-1}\left(\frac{(z_M-z_P)x_2}{y_1(y_1^2+(z_M-z_P)^2+x_2^2)^{½}}\right)$$

$$- (z_M-z_P)\ln(x_1+(y_1^2+(z_M-z_P)^2+x_1^2)^{½})-x_1\ln(z_M-z_P+(y_1^2+(z_M-z_P)^2+x_1^2)^{½})+y_1\tan^{-1}\left(\frac{(z_M-z_P)x_1}{y_1(y_1^2+(z_M-z_P)^2+x_1^2)^{½}}\right)\}$$

$$- G\rho\{-z_P\ln(x_2+(y_2^2+z_P^2+x_2^2)^{½}) + x_2\ln(-z_P+(y_2^2+z_P^2+x_2^2)^{½}) + y_2\tan^{-1}\left(\frac{z_Px_2}{y_2(y_2^2+z_P^2+x_2^2)^{½}}\right)$$

$$+ z_P\ln(x_1+(y_2^2+z_P^2+x_1^2)^{½}) - x_1\ln(-z_P+(y_2^2+z_P^2+x_1^2)^{½}) - y_2\tan^{-1}\left(\frac{z_Px_1}{y_2(y_2^2+z_P^2+x_1^2)^{½}}\right)$$

$$+ z_P\ln(x_2+(y_1^2+z_P^2+x_2^2)^{½}) - x_2\ln(-z_P+(y_1^2+z_P^2+x_2^2)^{½}) - y_1\tan^{-1}\left(\frac{z_Px_2}{y_1(y_1^2+z_P^2+x_2^2)^{½}}\right)$$

$$- z_P\ln(x_1+(y_1^2+z_P^2+x_1^2)^{½}) + x_1\ln(-z_P+(y_1^2+z_P^2+x_1^2)^{½}) + y_1\tan^{-1}\left(\frac{z_Px_1}{y_1(y_1^2+z_P^2+x_1^2)^{½}}\right)$$

$$- x_2\ln((y_2^2+x_2^2)^{½}) + x_1\ln((y_2^2+x_1^2)^{½}) + x_2\ln((y_1^2+x_2^2)^{½}) - x_1\ln((y_1^2+x_1^2)^{½})\}$$

Case II simplifies slightly to:

$$T_x(P) = G\rho\{ - y_2\ln(z_M+(x_2^2+y_2^2+z_M^2)^{½}) - z_M\ln(y_2+(x_2^2+y_2^2+z_M^2)^{½}) + x_2\tan^{-1}\left(\frac{y_2z_M}{x_2(x_2^2+y_2^2+z_M^2)^{½}}\right)$$

$$+ y_1\ln(z_M+(x_2^2+y_1^2+z_M^2)^{½}) + z_M\ln(y_1+(x_2^2+y_1^2+z_M^2)^{½}) - x_2\tan^{-1}\left(\frac{y_1z_M}{x_2(x_2^2+y_1^2+z_M^2)^{½}}\right)$$

$$+ y_2\ln(z_M+(x_1^2+y_2^2+z_M^2)^{½}) + z_M\ln(y_2+(x_1^2+y_2^2+z_M^2)^{½}) - x_1\tan^{-1}\left(\frac{y_2z_M}{x_1(x_1^2+y_2^2+z_M^2)^{½}}\right)$$

$$- y_1\ln(z_M+(x_1^2+y_1^2+z_M^2)^{½}) - z_M\ln(y_1+(x_1^2+y_1^2+z_M^2)^{½}) + x_1\tan^{-1}\left(\frac{y_1z_M}{x_1(x_1^2+y_1^2+z_M^2)^{½}}\right)\}$$

$$- G\rho\{-y_2\ln(z_M-z_P+(x_2^2+y_2^2+(z_M-z_P)^2)^{½})-(z_M-z_P)\ln(y_2+(x_2^2+y_2^2+(z_M-z_P)^2)^{½})$$

$$+x_2\tan^{-1}\left(\frac{y_2(z_M-z_P)}{x_2(x_2^2+y_2^2+(z_M-z_P)^2)^{½}}\right)$$

$$+ y_1\ln(z_M-z_P+(x_2^2+y_1^2+(z_M-z_P)^2)^{½}) + (z_M-z_P)\ln(y_1+(x_2^2+y_1^2+(z_M - z_P)^2)^{½})$$

$$- x_2\tan^{-1}\left(\frac{y_1(z_M - z_P)}{x_2(x_2^2+y_1^2+(z_M - z_P)^2)^{½}}\right)$$

$$+ y_2\ln(z_M-z_P+(x_1^2+y_2^2+(z_M-z_P)^2)^{½}) + (z_M-z_P)\ln(y_2+(x_1^2+y_2^2+(z_M-z_P)^2)^{½})$$

$$- x_1\tan^{-1}\left(\frac{y_2(z_M-z_P)}{x_1(x_1^2+y_2^2+(z_M-z_P)^2)^{½}}\right)$$

$$- y_1\ln(z_M-z_P+(x_1^2+y_1^2+(z_M-z_P)^2)^{½}) - (z_M-z_P)\ln(y_1+(x_1^2+y_1^2+(z_M-z_P)^2)^{½})$$

$$+ x_1\tan^{-1}\left(\frac{y_1(z_M-z_P)}{x_1(x_1^2+y_1^2+(z_M-z_P)^2)^{½}}\right)\}$$

$$- G\rho\{y_2\ln(-z_P+(x_2^2+y_2^2+z_P^2)^{½}) - z_P\ln(y_2+(x_2^2+y_2^2+z_P^2)^{½}) + x_2\tan^{-1}\left(\frac{y_2z_P}{x_2(x_2^2+y_2^2+z_P^2)^{½}}\right)$$

$$- y_1\ln(-z_P+(x_2^2+y_1^2+z_P^2)^{\frac{1}{2}}) + z_P\ln(y_1+(x_2^2+y_1^2+z_P^2)^{\frac{1}{2}}) - x_2\tan^{-1}\left(\frac{y_1z_P}{x_2(x_2^2+y_1^2+z_P^2)^{\frac{1}{2}}}\right)$$

$$- y_2\ln((x_2^2+y_2^2)^{\frac{1}{2}}) + y_1\ln((x_2^2+y_1^2)^{\frac{1}{2}}) + y_2\ln((x_1^2+y_2^2)^{\frac{1}{2}}) - y_1\ln((x_1^2+y_1^2)^{\frac{1}{2}})$$

$$- y_2\ln(-z_P+(x_1^2+y_2^2+z_P^2)^{\frac{1}{2}}) + z_P\ln(y_2+(x_1^2+y_2^2+z_P^2)^{\frac{1}{2}}) - x_1\tan^{-1}\left(\frac{y_2z_P}{x_1(x_1^2+y_2^2+z_P^2)^{\frac{1}{2}}}\right)$$

$$+ y_1\ln(-z_P+(x_1^2+y_1^2+z_P^2)^{\frac{1}{2}}) - z_P\ln(y_1+(x_1^2+y_1^2+z_P^2)^{\frac{1}{2}}) + x_1\tan^{-1}\left(\frac{y_1z_P}{x_1(x_1^2+y_1^2+z_P^2)^{\frac{1}{2}}}\right)\Big\}$$

$$T_y(P) = G\rho\Big\{ - z_M\ln(x_2+(y_2^2+z_M^2+x_2^2)^{\frac{1}{2}}) - x_2\ln(z_M+(y_2^2+z_M^2+x_2^2)^{\frac{1}{2}}) + y_2\tan^{-1}\left(\frac{z_Mx_2}{y_2(y_2^2+z_M^2+x_2^2)^{\frac{1}{2}}}\right)$$

$$+ z_M\ln(x_1+(y_2^2+z_M^2+x_1^2)^{\frac{1}{2}}) + x_1\ln(z_M+(y_2^2+z_M^2+x_1^2)^{\frac{1}{2}}) - y_2\tan^{-1}\left(\frac{z_Mx_1}{y_2(y_2^2+z_M^2+x_1^2)^{\frac{1}{2}}}\right)$$

$$+ z_M\ln(x_2+(y_1^2+z_M^2+x_2^2)^{\frac{1}{2}}) + x_2\ln(z_M+(y_1^2+z_M^2+x_2^2)^{\frac{1}{2}}) - y_1\tan^{-1}\left(\frac{z_Mx_2}{y_1(y_1^2+z_M^2+x_2^2)^{\frac{1}{2}}}\right)$$

$$- z_M\ln(x_1+(y_1^2+z_M^2+x_1^2)^{\frac{1}{2}}) - x_1\ln(z_M+(y_1^2+z_M^2+x_1^2)^{\frac{1}{2}}) + y_1\tan^{-1}\left(\frac{z_Mx_1}{y_1(y_1^2+z_M^2+x_1^2)^{\frac{1}{2}}}\right)\Big\}$$

$$- G\rho\Big\{ - (z_M-z_P)\ln(x_2+(y_2^2+(z_M-z_P)^2+x_2^2)^{\frac{1}{2}}) - x_2\ln(z_M-z_P+(y_2^2+(z_M-z_P)^2+x_2^2)^{\frac{1}{2}})$$

$$+ y_2\tan^{-1}\left(\frac{(z_M-z_P)x_2}{y_2(y_2^2+(z_M-z_P)^2+x_2^2)^{\frac{1}{2}}}\right)$$

$$+ (z_M-z_P)\ln(x_1+(y_2^2+(z_M-z_P)^2+x_1^2)^{\frac{1}{2}}) + x_1\ln(z_M-z_P+(y_2^2+(z_M-z_P)^2+x_1^2)^{\frac{1}{2}})$$

$$- y_2\tan^{-1}\left(\frac{(z_M-z_P)x_1}{y_2(y_2^2+(z_M-z_P)^2+x_1^2)^{\frac{1}{2}}}\right)$$

$$+ (z_M-z_P)\ln(x_2+(y_1^2+(z_M-z_P)^2+x_2^2)^{\frac{1}{2}}) + x_2\ln(z_M-z_P+(y_1^2+(z_M-z_P)^2+x_2^2)^{\frac{1}{2}})$$

$$- y_1\tan^{-1}\left(\frac{(z_M-z_P)x_2}{y_1(y_1^2+(z_M-z_P)^2+x_2^2)^{\frac{1}{2}}}\right)$$

$$- (z_M-z_P)\ln(x_1+(y_1^2+(z_M-z_P)^2+x_1^2)^{\frac{1}{2}}) - x_1\ln(z_M-z_P+(y_1^2+(z_M-z_P)^2+x_1^2)^{\frac{1}{2}})$$

$$+ y_1\tan^{-1}\left(\frac{(z_M-z_P)x_1}{y_1(y_1^2+(z_M-z_P)^2+x_1^2)^{\frac{1}{2}}}\right)\Big\}$$

$$- G\rho\Big\{ -z_P\ln(x_2+(y_2^2+z_P^2+x_2^2)^{\frac{1}{2}}) + x_2\ln(-z_P+(y_2^2+z_P^2+x_2^2)^{\frac{1}{2}}) + y_2\tan^{-1}\left(\frac{z_Px_2}{y_2(y_2^2+z_P^2+x_2^2)^{\frac{1}{2}}}\right)$$

$$+ z_P\ln(x_1+(y_2^2+z_P^2+x_1^2)^{\frac{1}{2}}) - x_1\ln(-z_P+(y_2^2+z_P^2+x_1^2)^{\frac{1}{2}}) - y_2\tan^{-1}\left(\frac{z_Px_1}{y_2(y_2^2+z_P^2+x_1^2)^{\frac{1}{2}}}\right)$$

$$+ z_P\ln(x_2+(y_1^2+z_P^2+x_2^2)^{\frac{1}{2}}) - x_2\ln(-z_P+(y_1^2+z_P^2+x_2^2)^{\frac{1}{2}}) - y_1\tan^{-1}\left(\frac{z_Px_2}{y_1(y_1^2+z_P^2+x_2^2)^{\frac{1}{2}}}\right)$$

$$- z_P\ln(x_1+(y_1^2+z_P^2+x_1^2)^{\frac{1}{2}}) + x_1\ln(-z_P+(y_1^2+z_P^2+x_1^2)^{\frac{1}{2}}) + y_1\tan^{-1}\left(\frac{z_Px_1}{y_1(y_1^2+z_P^2+x_1^2)^{\frac{1}{2}}}\right)$$

$$- x_2\ln((y_2^2+x_2^2)^{\frac{1}{2}}) + x_1\ln((y_2^2+x_1^2)^{\frac{1}{2}}) + x_2\ln((y_1^2+x_2^2)^{\frac{1}{2}}) - x_1\ln((y_1^2+x_1^2)^{\frac{1}{2}})\Big\}$$

Therefore the formulae for Case I and Case II are identical.

Because of the attraction of the prism at P, the astronomical latitude determined at P will be less than the astronomical latitude that would be determined at the equivalent point on the geoid, see Figure 8.3, below. Therefore, if there is a positive mass imbalance to the north, i.e. P is on a southward-facing slope, then the topographic-isostatic deviation correction to be applied to the astronomical latitude observed at P, will be positive.

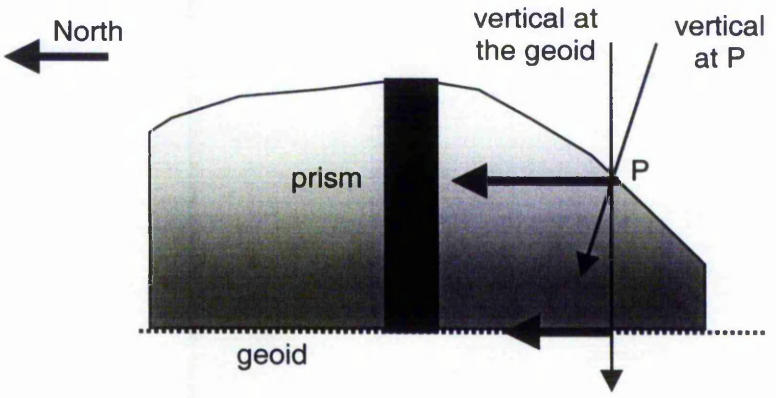

Figure 8.3 The sign of the topographic-isostatic deviation correction.

Similarly, if the mass imbalance is to the east, i.e. P is on a westward-facing slope, then the topographic-isostatic deviation correction to be applied to the astronomical longitude observed at P will be positive. The graphics at Annex A show topographic-isostatic deviation effects.

8.4 Calculation of the components of the topographic-isostatic effect using right rectangular blocks

To calculate the components of the topographic-isostatic effect upon astronomical position, the area needs to be divided up into blocks where each block is assumed to have constant height. The greater effects will be nearer the point of investigation and therefore the blocks should be smallest nearest to the point of investigation. In addition, the block boundaries must not cross the x or y axes through the point of investigation. One, but not the only, solution to this problem would be to divide the area under consideration according to Figure 8.4, below.

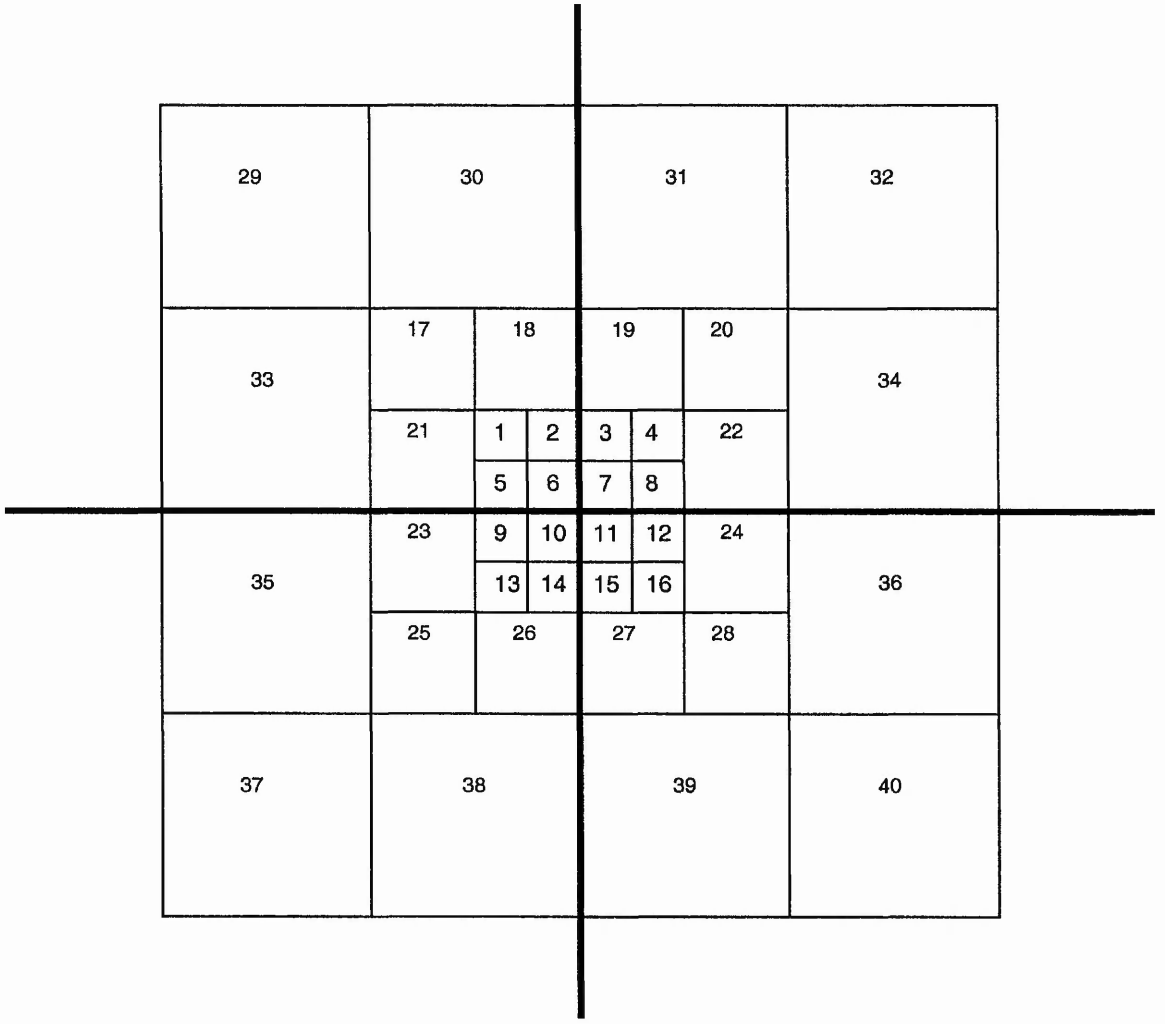

Figure 8.4 Block divisions for the computation of topographic-isostatic effect.

Each successive outer ring of blocks adds 12 blocks but quadruples the area.

Such an approach needs a Digital Elevation Model (DEM). One DEM in the public domain is the "Global Land One-km Base Elevation (GLOBE)" which may be found at GLOBE (2001). This is referred to as a 1 km model but elevations are available on a grid of 30 arc seconds of latitude and longitude, which is, for example, every 930 metres of latitude and 560 metres of longitude at the latitude of Nottingham. The DEM is relative to mean sea level vertically and WGS84 horizontally. The quoted precision of the DEM is variable. Hastings & Dunbar (1998) report on reviews of the work of others that, in test areas in Australia and Japan, 6m RMS error has been achieved while, for more remote areas RMS, errors rise to 100 metres with a worst case of a 300 metres error in Antarctica. It is believed that the overall design objective of 18 metres RMS has been met. Berry (1999) reports similar errors and

indicates that some of the errors are related to the terrain because satellite altimeters, which were used to collect the observational data, are designed to work well over ice and water but not over rugged terrain. Altimeter failure may occur where there is a high terrain variation. In areas where there is a rapid change of height, the computed DEM may lack sufficient high frequency information to fully reflect the roughness of the terrain.

8.5 Numerical Investigation of the Topographic-Isostatic Effect Using Right Rectangular Blocks

Three test areas were investigated. They were a low elevation area of gently undulating topography (Nottingham), a more rugged area (Aviemore, Scotland), and an extreme mountainous area, at least in European terms (Mt Blanc). With reference to Figure 8.4, the contributions of the inner four squares (squares 6, 7, 10 & 11), the first ring (squares 1-5, 8, 9, 12-16) and those of the second ring (squares 17-28) were considered. In each case, the sample size exceeded 12500 computation points. The results, in Table 8.1, for east-west deviation corrections were obtained.

Table 8.1 Deviations for the topographic-isostatic effect for three sample areas.

	Nottingham	Aviemore	Mt Blanc
Latitude range (degrees)	52.5 to 53.5	56.5 to 57.5	45.0 to 46.0
Longitude range (degrees)	-1.5 to -0.5	-4.0 to -3.0	6.5 to 7.5
Highest point (metres)	277	1292	4570
Lowest point (metres)	7	26	296
Mean terrain height	78	420	2018
Roughness [1] (metres)	37	201	718
Inner 4 Squares (arc seconds)			
East-west deviation			
Highest	0.651	3.044	7.260
Lowest	-0.783	-3.190	-6.672
RMS	0.110	0.576	2.203
North-south deviation			
Highest	0.818	3.311	8.292
Lowest	-0.833	-4.379	-8.421
RMS	0.145	0.950	3.295
First ring (arc seconds)			
East-west deviation			
Highest	0.023	0.952	4.524
Lowest	-0.027	-1.089	-4.321
RMS	0.002	0.134	1.298
North-south deviation			
Highest	0.013	0.532	4.707
Lowest	-0.014	-0.845	-4.749
RMS	0.001	0.097	1.426
Second ring (arc seconds)			
East-west deviation			
Highest	0.006	0.428	4.398
Lowest	-0.009	-0.444	-4.374
RMS	0.002	0.074	1.159
North-south deviation			
Highest	0.005	0.246	4.890
Lowest	-0.005	-0.290	-4.397
RMS	0.001	0.048	1.134
Squares 1-28 (arc seconds)			
East-west deviation			
Highest	0.656	4.202	14.045
Lowest	-0.817	-4.599	-14.247
RMS	0.110	0.774	4.425
North-south deviation			
Highest	0.833	3.979	16.984
Lowest	-0.845	-5.461	-16.220
RMS	0.146	1.081	5.645

[1] Roughness is defined as the RMS of (point height – sample mean height)

The three blocks of Nottingham, Aviemore and Mt Blanc are in order of increasing terrain height and roughness. In the undulating, low terrain, Nottingham Block, only the inner four squares have significant effect. In the medium topography of the Aviemore Block, the inner 4 squares and first and second ring have significant effect although it is doubtful if the third ring would also be significant. In the high rough terrain of the Mt Blanc Block, all the computed elements are significant. Since the RMS of the first and second rings are significant then it is more than likely that further rings would also be significant. The RMS of blocks 1-28 is close to the sum of the separate RMS of the inner four squares, the first ring and the second ring. This indicates that there are significant systematic effects in the data and therefore the DEM is not sufficiently dense and the number of blocks inadequate as far as the Mt Blanc Block is concerned.

The data suggests that the density of the GLOBE DEM model is sufficient for the Nottingham Block and just sufficient for the Aviemore Block. On that basis, it would appear that the GLOBE DEM is adequate for the computation of astronomical topographic-isostatic deviation corrections at the 0".1 level for the whole of the UK. The last sentence cannot be considered conclusive and further work is required to evaluate the effect of a denser DEM especially in rough terrain. However, other conclusions below suggest that the GLOBE DEM model may not be sufficient in rough terrain.

Research is reported at Landmap (2000) for the production of a 30m DEM for the UK but the product was not expected to be available until later in 2001.

Clearly there will be a correlation between slope and the magnitude of the topographic-isostatic deviation. The six graphs in Figure 8.5 below were derived from east-west and north-south subsets of the data in the three blocks described above. The east-west slope was computed as the difference in height between the points east and west of the point under investigation divided by the distance between them, and similarly for the north-south slope. All the graphs show that there is a strong correlation between slope and topographic-isostatic deviation. The correlation appears strongest in the Nottingham block and weakest in the Mt Blanc block.

Superficially, it would appear that an estimate of topographic-isostatic deviation could be found from the general slope of the ground at the point of observation. Examination of the graphs suggests that such an estimate would have a standard error of the order of better than ±25% of its true value ±0".05 for the Nottingham block

and better than ±25% of its true value ±0".1 for the Mt Blanc block. No consideration of the height of the point under investigation has been made in this investigation.

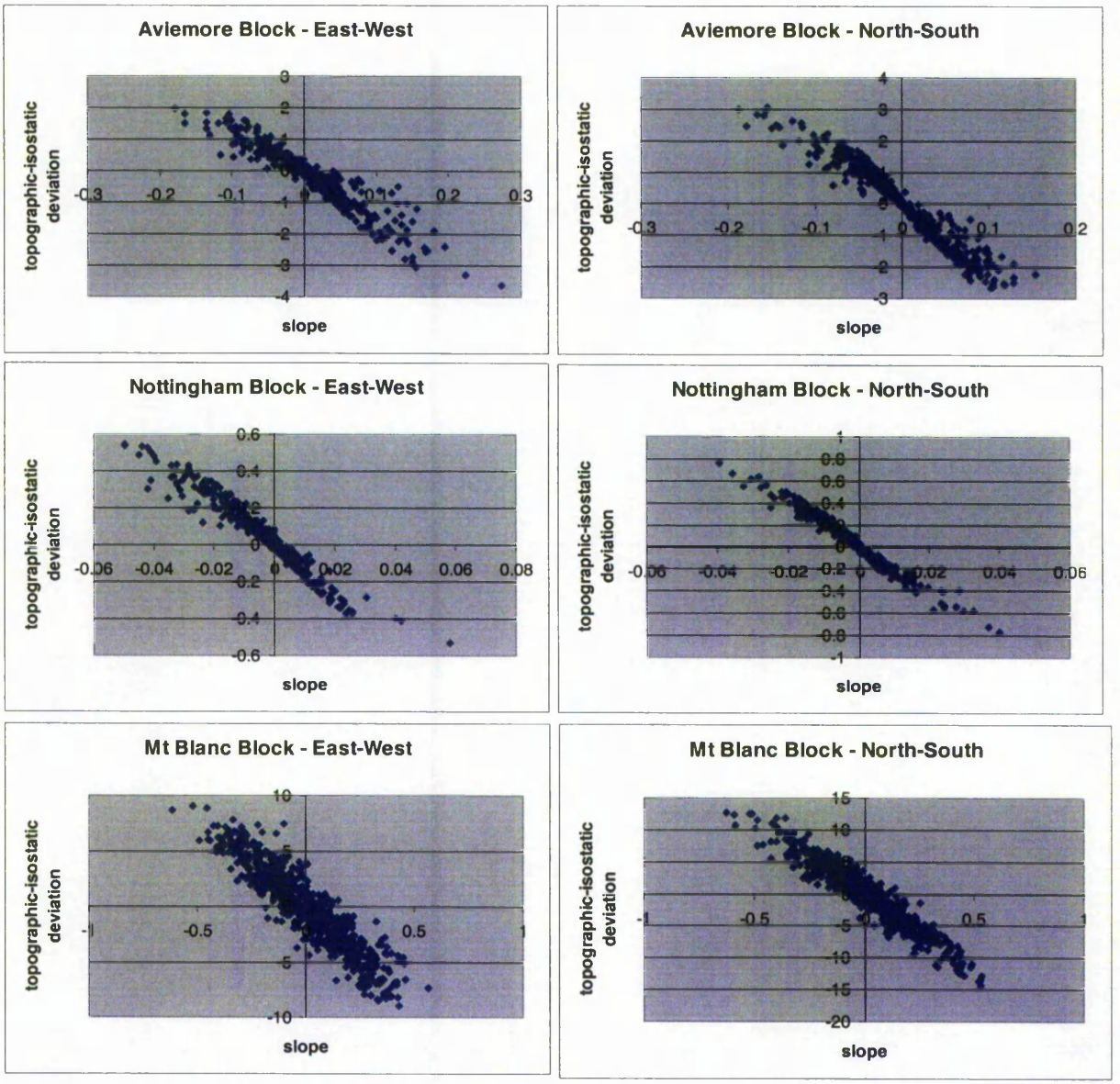

Figure 8.5 Six graphs showing the relationship between ground slope and topographic-isostatic deviation.

8.6 The topographic-isostatic effect from the slope of the ground

An alternative approach to determining the topographic-isostatic correction could be developed by considering only the slope of the ground in the region of observation

point. Such an approach would be more sensitive to the local form of the topography but would take virtually no notice of distant topographic features. It would also assume that the topography at right angles to the line of greatest slope is linear and consistent, e.g. there are no bends in the hills, see Figures 8.6 and 8.7, below.

The force of attraction of a mass at one point to a unit mass at another, as stated in Bomford (1980), is:

$$F = G \int\int\int \rho \cos\theta \, r^{-2} \, dv$$

where F is the force of attraction

ρ is the density of the material

θ is the angle between the axis of the force and the direction to the element dv

r is the distance from the unit mass to the elemental mass dv

In Figure 8.6, below, the attraction to a unit mass at point P of a rod of linear density σ, along the line normal to the rod is considered.

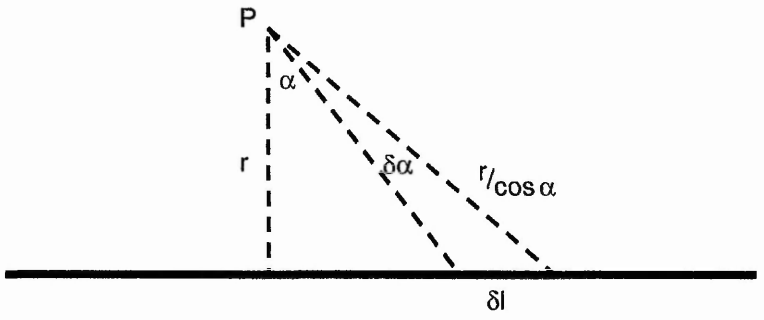

Figure 8.6 The attraction of a rod to a point.

The above formula may be rewritten as:

$$\begin{aligned} F &= G \sigma \int \cos\alpha \, (r \cos^{-1}\alpha)^{-2} \, dl \\ &= G \sigma \int \cos\alpha \, (r \cos^{-1}\alpha)^{-2} \, r \, (\cos\alpha)^{-2} \, d\alpha \\ &= G \sigma \, r^{-1} \int \cos\alpha \, d\alpha \\ &= G \sigma \, r^{-1} \, [\sin\alpha_2 - \sin\alpha_1] \end{aligned}$$

where α_1 and α_2 are at the angles subtended at the ends of the rod. If the rod is long compared with r:

$$F \approx 2 G \sigma r^{-1}$$

Now consider a part of a wall made up of rods.

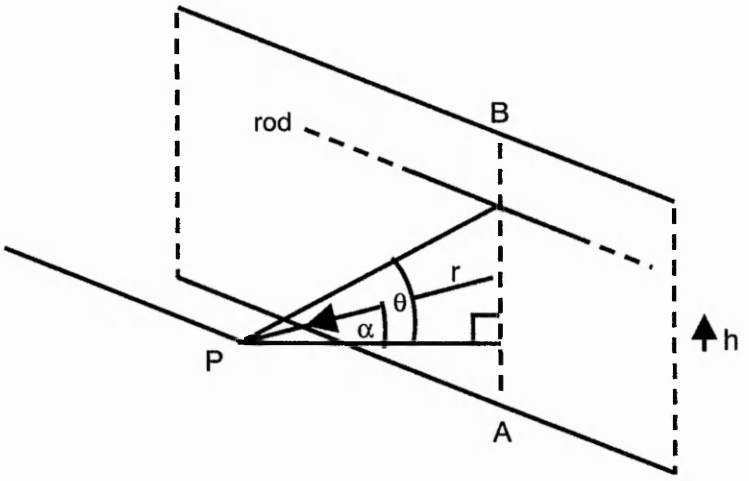

Figure 8.7 The attraction of a wall of rods to a point.

The direction of interest for the computation of attraction makes an angle of α with the normal to the wall.

The component of attraction, at P, in the direction of interest of one rod is:

$$F = 2 G \sigma \cos(\theta - \alpha) (r \cos\alpha \sec\theta)^{-1}$$

where σ is now the area density.

The component of attraction in the direction of interest of a wall made up of a series of rods is:

$$\begin{aligned} F &= 2 G \sigma \int \cos(\theta - \alpha) (r \cos\alpha \sec\theta)^{-1} dh \\ &= 2 G \sigma \int \cos(\theta - \alpha) (r \cos\alpha \sec\theta)^{-1} r \cos\alpha \sec^2\theta \, d\theta \\ &= 2 G \sigma \int \cos(\theta - \alpha) \sec\theta \, d\theta \\ &= 2 G \sigma \int (\cos\theta \cos\alpha + \sin\theta \sin\alpha)) \sec\theta \, d\theta \\ &= 2 G \sigma \int (\cos\alpha + \tan\theta \sin\alpha) \, d\theta \\ &= 2 G \sigma [(\theta_2 - \theta_1) \cos\alpha + (\ln(\sec\theta_2) - \ln(\sec\theta_1)) \sin\alpha] \end{aligned}$$

Finally consider a solid, infinitely long, wedge made up of parallel walls each at variable distance t from point P:

$$\begin{aligned} F &= 2 G \rho \int [(\theta_2 - \theta_1) \cos\alpha + (\ln(\sec\theta_2) - \ln(\sec\theta_1)) \sin\alpha] \, dt \\ &= 2 G \rho t [(\theta_2 - \theta_1) \cos\alpha + (\ln(\sec\theta_2) - \ln(\sec\theta_1)) \sin\alpha] \end{aligned}$$

where ρ is the volumetric density.

Figure 8.8, below, represents a cross-section of a hill through a point P. The maximum slope is in the plane of the page. The topography is approximated by a series of infinitely long wedges perpendicular to the plane of the page.

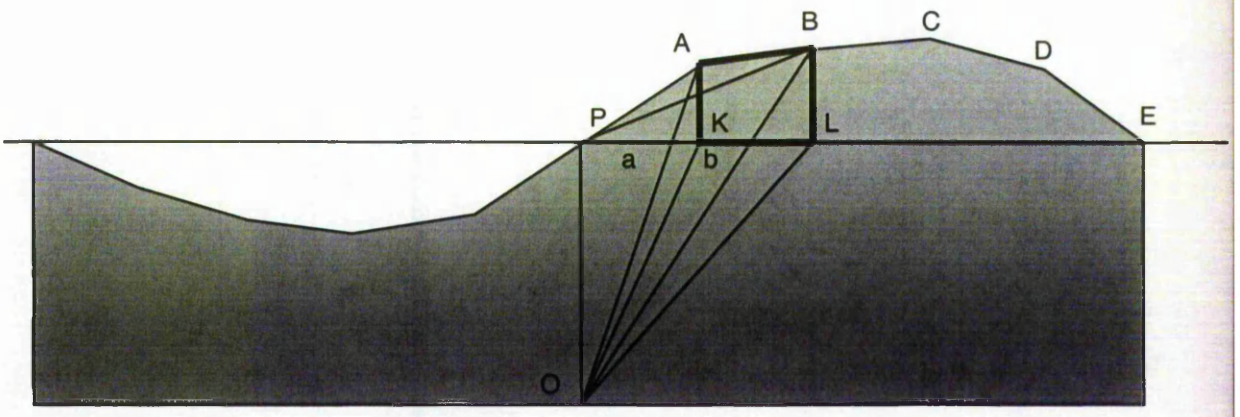

Figure 8.8 Topography approximated by wedges.

The heights of a number of points along the line of greatest slope are found. The points are at multiples of a chosen horizontal distance, d.

The horizontal attractions at P (F_P) and at O (F_O) of the wedge ABKL are the sums of the attraction of triangular wedges as follows:

$$F_P = F_{PAB} + F_{PBL} - F_{PAK}$$
$$F_O = F_{OAB} + F_{OBL} - F_{OAK} - F_{OKL}$$

In Figure 8.8, above, a and b are the horizontal distances of A and B from P or O. h_P is the height of P above O etc. In Table 8.2, below, α, θ_1 and θ_2 are as in Figure 8.7, above.

The topographic-isostatic correction is therefore a function of the difference between F_P and F_O.

Table 8.2 Parameters for the computation of topographic-isostatic correction by wedges.

wedge	α	θ_1	θ_2	t
PAB	$\tan^{-1}((b-a)/(h_A-h_B))$	$\alpha - \tan^{-1}((h_A-h_P)/a)$	$\alpha - \tan^{-1}((h_B-h_P)/b)$	$b\cos\theta_2/\cos(\alpha-\theta_2)$
PBL	0	$-\tan^{-1}((h_B-h_P)/b)$	0	b
PAK	0	$-\tan^{-1}((h_A-h_P)/a)$	0	a
OAB	$\tan^{-1}((b-a)/(h_A-h_B))$	$\alpha - \tan^{-1}(h_A/a)$	$\alpha - \tan^{-1}(h_B/b)$	$b\cos\theta_2/\cos(\alpha-\theta_2) + h_P\cos\alpha$
OBL	0	$-\tan^{-1}(h_B/b)$	$-\tan^{-1}(h_P/b)$	b
OAK	0	$-\tan^{-1}(h_A/a)$	$-\tan^{-1}(h_P/a)$	a
OKL	$\frac{1}{2}\pi$	$\tan^{-1}(a/h_P)$	$\tan^{-1}(b/h_P)$	h_P

In Table 8.2, above, a, θ_1, θ_2 and t are as defined in the equation for a solid, infinitely long, wedge made up of parallel walls each at variable distance t from point P, above.

Masses close to the observation point will have more effect than masses at a distance. However, it is necessary to determine when distant masses have negligible effect. In Figure 8.9, below, several non-symmetrical simple longitudinal profiles are examined. Symmetrical longitudinal profiles will have zero topographic-isostatic correction.

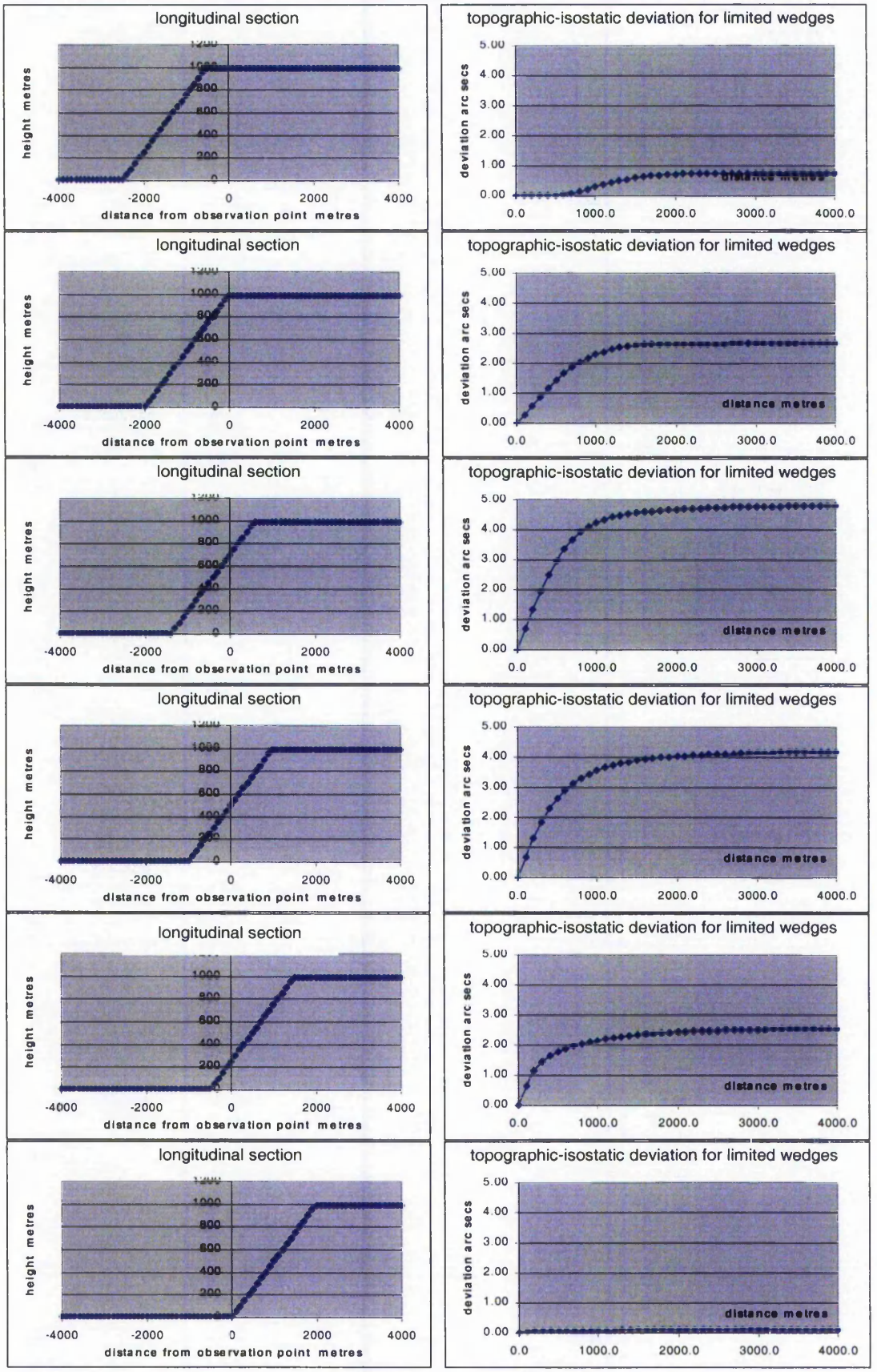

Figure 8.9 Topographic-isostatic deviations associated with symmetrical simple longitudinal profiles.

In Figure 8.9 above, the observation point is at different positions relative to a steep slope rising from near sea level to almost 1000 m. In all cases, 95% of the topographic-isostatic deviation, derived from consideration of the topography out to 4 km from the point, may be found by considering the longitudinal section only out to 2 km from the point. The graphs in Figure 8.9, above, suggest that the topographic-isostatic deviation is almost fully computed at 4 km. The greatest topographic-isostatic deviation is about a quarter of the way from the top of the slope.

The tentative conclusion and an approximate "rule of thumb" that arises from this simulation study is that it is prudent to create a longitudinal section along the line of greatest slope with a length equal to at least twice the height of the highest point on the section.

8.7 Investigation of the topographic-isostatic effect of simple topographical features

Hills are not normally straight sided but have slopes that change relatively smoothly with distance. In the following, the topographic-isostatic deviation at the foot of a sinusoidal straight ridge running perpendicular to the direction of interest is computed using only the topography out to a given distance.

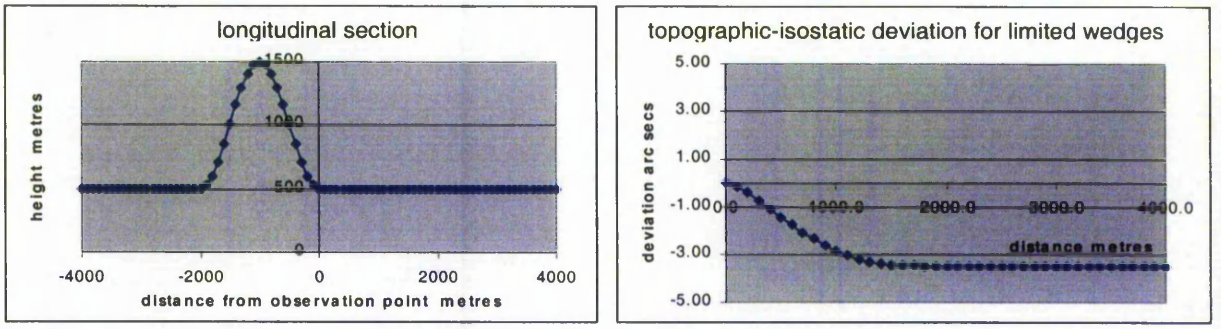

Figure 8.10 Topographic-isostatic deviation relative to position on a sinusoidal ridge.

In Figure 8.10 above, the position of investigation is 1000 metre horizontally from the top of the ridge. The deviation is computed on the basis of taking account of topography out to a given distance. Figure 8.11 shows the full (with consideration out to 4km) topographic-isostatic deviation computed for observation points across the ridge.

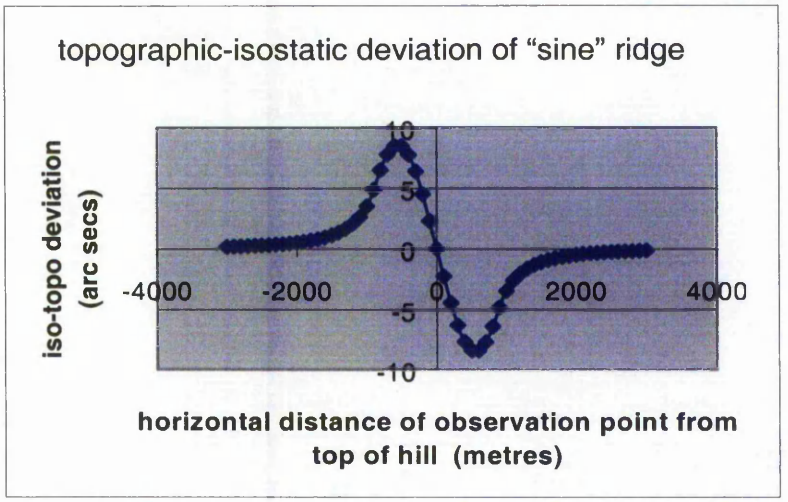

Figure 8.11 Topographic-isostatic deviation computed for observation points across a sinusoidal ridge.

From the graph in Figure 8.11, it is apparent that the greatest values of topographic-isostatic deviation may be found just less than halfway up either side of the ridge. However, these are also the points where the rates of change of topographic-isostatic deviation are the least. This implies that to minimise errors in the computed value of topographic-isostatic deviation the best observing points are where there is an even slope, i.e. zero rate of change and this will occur on the steepest part of the ridge.

This conclusion was reviewed by studying the topographic-isostatic effect of a ridge in the shape of an embankment.

From Figures 8.12 and 8.13 below, it is apparent that the greatest values of topographic-isostatic deviation may be found about halfway up either side of the ridge. However the greatest rate of change of topographic-isostatic deviation is near the ends of the slopes, i.e. where the change of slope is greatest. This confirms the earlier conclusion that the best observing points are well away from a rapidly changing slope.

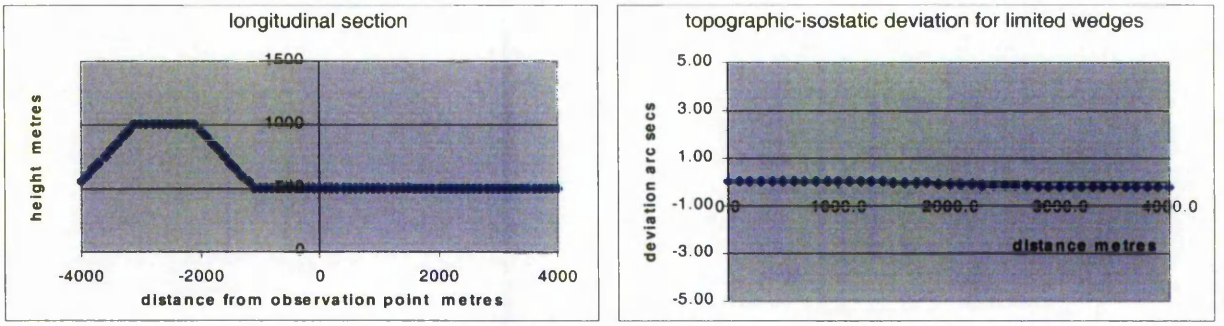

Figure 8.12 Topographic-isostatic deviation relative to position on an embankment type ridge.

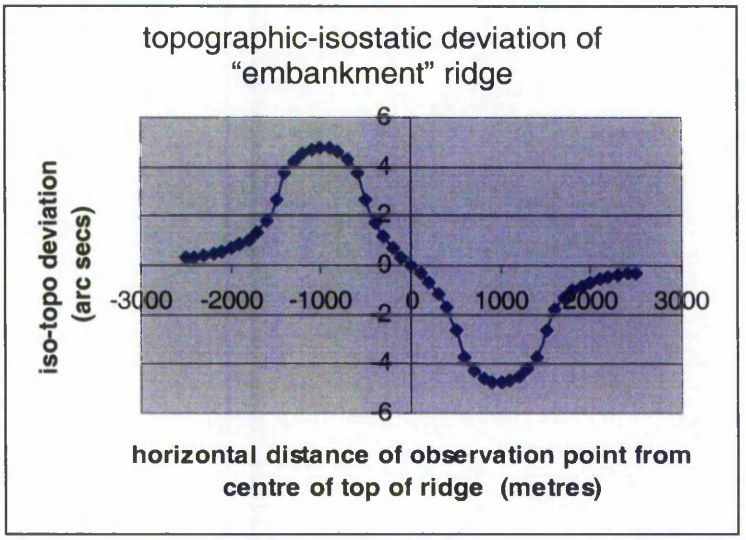

Figure 8.13 Topographic-isostatic deviation computed for observation points across an embankment-type ridge.

8.8 Graphical evaluation

These simple conclusions were further examined by computing the topographic-isostatic corrections at six points in the Preseli Mountains in Wales. See Figure 8.14, below. Three of the sites, Mirianog Ganot, Waunlwyd Farm and Trehenry were chosen because they were on steep, but reasonably even, slopes where the infinitely long wedge assumption would be reasonably valid. The other three sites, Dinas Head, Island Farm and Dinas Cross, are where deviation of the vertical had been observed as part of a student field course but topographic-isostatic corrections had not yet been applied. The flat parts of the longitudinal section in two of the latter three are over the sea where no submarine height information is available.

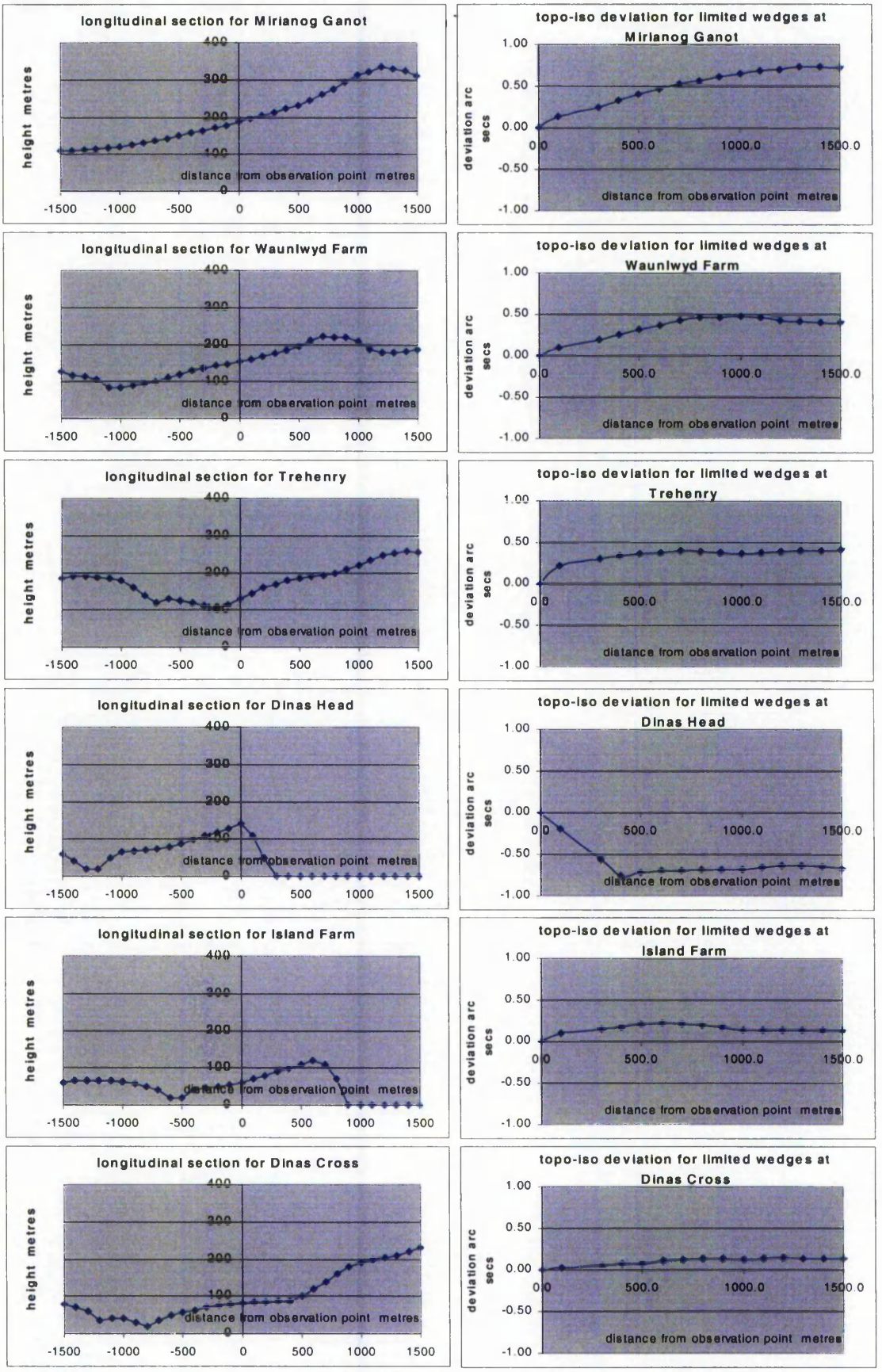

Figure 8.14 Topographic-isostatic corrections for six sites in the Preseli Mountains in Wales.

In each pair of graphs in Figure 8.14, the left of the pair shows the longitudinal profile along the line of greatest slope. The right hand graph shows the topographic-isostatic correction computed based on wedges, limited in distance from the observation point. In each case, the width of each wedge is 100 metres.

Examination of the graphs in Figure 8.14 suggests that it is prudent to create a longitudinal section along the line of greatest slope in length at least four times the height of the highest point along that section. However, in this context it is worth returning to the underlying assumption that infinitely long wedges can represent the topography. While this is reasonably valid near the point of computation, it becomes less valid with increasing distance along the longitudinal section. In Section 8.6 it was shown that for a rod the attraction was:

$$F = G \sigma r^{-1} [\sin\alpha_2 - \sin\alpha_1]$$

To simplify the formulae, α_2 and α_1 were taken to be +90º and -90º respectively. On moving out along the longitudinal section on a convex slope, e.g. on a spur, the values of α will decrease in magnitude and so the distant wedges will have a smaller contribution than that assumed. Therefore, distant topography will make less contribution than assumed and the 95% contribution cut-off point, described above, will be achieved sooner. In a valley the situation will be reversed. Therefore, there is little to be gained by using a longitudinal section of more than four times the greatest height for the calculation of topographic-isostatic deviation.

The accuracy of this method of determining the topographic-isostatic correction depends upon the validity of the assumption that infinitely long wedges, perpendicular to the line of greatest slope, can represent the topography. Overall, it is tentatively estimated that the method will give a solution to ± 10% ± 0".1 of its true value in topography similar to that found in the UK. Further investigation is required to confirm this value. There has been no comparison with solutions found from a DEM using as none of sufficient density was available at the time of writing.

8.9 Summary

In this chapter the topographic-isostatic effect upon astronomical position was reviewed, in particular with the topography represented as right rectangular prisms, and these were used to calculate the components of the topographic-isostatic effect. A numerical investigation of the topographic-isostatic effect using right rectangular blocks was undertaken and, although results were obtained, the amount of

computation required was large if more than a few blocks around each point were to be used. An alternative approach was examined, namely that of finding the topographic-isostatic effect from the slope of the ground, and this was reviewed by evaluating it for topographical features and actual ground profiles. With astronomical position able to be computed as the sub-arc second level, as in Chapter 6 then, if that position is to be used to determine the geoid this effect must be accounted for.

Chapter 9

The Astrogeodetic Geoid Model

9.1 The Astrogeodetic Geoid

In previous chapters methods for the determination of astronomical position have been developed and discussed. It is now appropriate to consider how astronomical position, and hence deviation of the vertical, derived at a number of points can be used to create a geoid model.

The concept of astrogeodetic levelling for geoid determination is extremely simple. At any point, and in a given direction, the slope of the geoid is the same as the deviations of the vertical. The deviation of the vertical may be found as:

north-south deviation	ξ	=	$(\phi_A - \phi_G)$
east-west deviation	η	=	$(\lambda_A - \lambda_G) \cos \phi$

where ϕ and λ are latitude and longitude respectively and subscripts A and G refer to astronomical and geodetic quantities respectively. In practice it does not matter whether the latitude in the $\cos\phi$ term is astronomical or geodetic; the effect of the difference is negligibly small.

Astronomical position may be found by various methods of which "Position Lines" is the most efficient field survey method because both components ξ and η are found at the same time. The true value of an astronomical position is effectively unique, as long as all necessary corrections are applied to reduce observations to a common reference frame, and tectonic plate movements and deep earth subsurface mass movements are negligibly small.

Geodetic position is only realised through a datum definition, with satellite and/or terrestrial observations adjusted in geodetic networks. This is covered in any textbook of geodesy or advanced surveying such as Bomford (1980), Cooper (1987) or Vanicek and Krakiwsky (1982) or in Breach (1997).

If a new and extensive astrogeodetic geoid is to be observed, then it is likely that geodetic values from terrestrial or satellite observations will already exist or that new values will be observed by GPS.

If GPS is to be used then it is likely that position relative to a control survey station, possibly at the origin of a local GPS or pseudo WGS 84 datum, may be found to ±0.01 m (with post processing) while the astronomical observations are taking place.

The classical approach to determining an astrogeodetic geoid by astrogeodetic levelling (as explained in Bomford (1980), Vanicek and Krakiwsky (1982) or Robbins (1976)) is to observe deviation of the vertical at a series of sites spread approximately equally between two nodal points. A diagram of an astrogeodetic network appears similar to that of a conventional levelling network. The reason for this form of network is that observations, at a single station, by non-automated methods take most of a night. It is therefore necessary to minimise the number of stations in a network.

The difference in geoid height between two successive stations, A and B, is found as:

$$\delta N = \tfrac{1}{2}(\chi_A + \chi_B)L$$

where

χ_A etc, is the deviation of the vertical in the direction of the line at station A in radians

L is the length of the line.

and $\chi_A = -(\xi \cos \alpha + \eta \sin \alpha)$

where α is the azimuth of line.

Such an approach does not make use of the deviation at right angles to the line and so half the observational data is not used. A better approach is to observe deviations at stations in, as near to, a regular grid as possible over the whole of the area of investigation and estimate the deviation at sufficient intermediate points by least squares collocation. Then it is possible to use any route through the network to find the difference in geoid height at any chosen point relative to an origin in the network. With points well distributed over an area, a digital terrain style model of the geoid (a DGM) could be formed, from which a contour plot could be produced.

9.2 Analysis of the Astrogeodetic Geoid Model

9.2.1 Density of observations

In this section, the required density of astronomical observations is considered. The fewer observations that are required the more productive and the more economically viable the system becomes. The main considerations are the

precision of individual deviations of the vertical and the way deviation of the vertical changes with position. Two quite different approaches to the problem are considered below.

9.2.2 *Kaula's rule of thumb*

Vanicek and Krakiwsky (1972) report that Kaula (1966) found an empirical relationship between wavelengths and amplitudes of elements of geoid models. For a geoid profile expressed as a trigonometric Fourier series, on average, the relationship between the wavelength and amplitude is given by:

$$A_n \cong R\, n^{-2}\, 10^{-5}$$

where A_n is the amplitude of the n*th* Fourier coefficient

R is the radius of the earth

n an integer, is the number of waves in a complete circumference

If a mean value of R is taken as 6370000 metres then:

$$A_n \cong 63.7\, n^{-2} \text{ metres} \qquad (n>1)$$

Brown et al (1972) showed this to be true for features longer than about 500 km. That implies it holds for values for n up to about 40. Assuming this is true for *all* values of n then the maximum amplitude would be

$$\Sigma A_n \cong 63.7\, \Sigma n^{-2} \text{ metres}$$

But since $\Sigma n^{-2} = \pi^2/6$ if n takes all integer values from 1 to ∞, then

$$\Sigma A_n \cong 63.7\, (\pi^2/6 - 1) \text{ metres}$$

$$\cong 41.08 \text{ metres}$$

This is less than the maximum separation of 105m of the geoid from a best fitting ellipsoid stated by Vanicek and Krakiwsky (1982).

If the form of the n^{th} undulation is

$$y = 63.7\, n^{-2} \sin\left(\frac{x n}{R}\right)$$

so

$$\frac{dy}{dx} = 63.7\, n^{-1} R^{-1} \cos\left(\frac{x n}{R}\right)$$

So, θ_n, the maximum slope of the waveform n, will be:

$$\theta_n \cong 63.7\ n^{-1} R^{-1} \text{ radians}$$

and therefore the maximum slope with all the waveforms included will be

$$\Sigma\theta_n \cong 10^{-5} \Sigma\ n^{-1} \text{ radians} \cong 2".06\ \Sigma\ n^{-1}$$

But $\Sigma\ n^{-1}$ is ∞ and therefore it is clear that Kaula's rule of thumb will overestimate the slope and therefore, probably, also the separation. However, since Kaula's rule of thumb appears valid for longer wavelengths, then the upper elements of Table 9.1, below, derived from the above formula, will be appropriate.

Table 9.1 Deviation by Kaula's rule of thumb.

n	Wavelength in kilometres	$\Sigma\theta_n$"
4	10000	4.3
40	1000	8.8
400	100	13.5
4 000	10	18.3
40 000	1	23.0
400 000	0.1	27.7
4 000 000	0.01	32.5

However, since the maximum value of deviation of the vertical is understood to occur in the Himalayas and does not exceed about 60" then Kaula's rule appears to be applicable well beyond the limit suggested by Brown et al (1972).

The maximum rate of change of slope for waveform n is given by:

$$\frac{d^2y}{dx^2} = -63.7\ R^{-2} \sin\left(\frac{x\,n}{R}\right)$$

So, θ_n', the maximum rate of change of slope of the waveform n, will be:

$$\theta_n' \cong -0.000323 \text{ "/km}$$

For n terms, the total maximum rate of change of slope will be n 0.000323 "/km. Table 9.2, below, shows the maximum rate of change of slope

that could be found worldwide based upon n waveforms. If large values of n are valid, the effect of the maximum rate of change of slope will only apply over very short distances and will therefore not cause any serious irregularities in the geoid.

Table 9.2 Rate of change of deviation by Kaula's rule of thumb.

n	wavelength in kilometres	θ_n "/km
4	10000	0.0013
40	1000	0.013
400	100	0.13
4 000	10	1.3
40 000	1	13
400 000	0.1	130
4 000 000	0.01	1300

9.3 The effect of a hemispherical mountain on the deviation of the vertical

In the following, the gravitational effects of a simple hemispherical mountain are considered; that is, as they affect changes in deviation of the vertical. The hemispherical mountain as in Figure 9.1, below, may be considered as a simple model representing an isolated topographical feature.

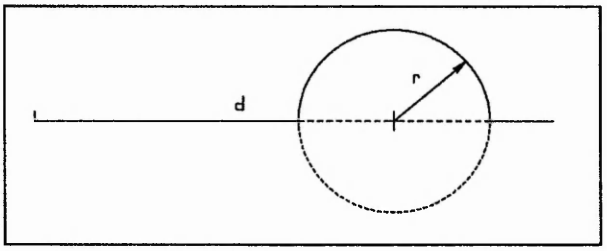

Figure 9.1 A hemispherical mountain.

Assume that the gravitational attraction at any point is made up of two parts, a downward attraction due to the gravitational attraction of the earth and a sideways attraction due to a spherical mountain. The centre of the sphere is in the local horizon

plane. The downward acceleration will be $g \cong 9.8$ m s^{-2}. From Bomford (1980), the sideways acceleration will be:

$$F = G M d^{-2} \quad \text{towards the centre.}$$

where G is the universal gravitational constant, is $6.672\ 10^{-11}$ kg^{-1} m^3 s^{-2}

M is the mass of the mountain

d is the distance from the point to the centre of the sphere

but $$M = \frac{4}{3} \pi r^3 \rho$$

where r is the radius of the sphere

ρ is the density of the sphere

therefore

$$F = \frac{4}{3} G \pi r^3 \rho d^{-2}$$

The deviation of the vertical, in radians will be:

$$\chi = F g^{-1}$$

$$= \frac{4}{3} G \pi r^3 \rho d^{-2} g^{-1}$$

The rate of change of deviation of the vertical towards the centre of the sphere will be:

$$\frac{d\chi}{dd} = -\frac{8}{3} G \pi r^3 \rho d^{-3} g^{-1}$$

The rate of change of deviation of the vertical towards the centre of the sphere will be a maximum at the surface of the sphere, i.e. where d = r. At this point:

$$\frac{d\chi}{dd} = -\frac{8}{3} G \pi \rho g^{-1}$$

If ρ is taken as 2670 kg m^{-3}, a reasonably representative value, then numerical evaluation leads to

$$\frac{d\chi}{dd} = -\frac{8 \pi 6.672\ 10^{-11}}{3 \quad 9.8} \text{ kg}^{-1} \text{ m}^3 \text{ s}^{-2} \text{ 2670 kg m}^{-3} \text{ m}^{-1} \text{ s}^2$$

$$= 1.52\ 10^{-7} \text{ radians m}^{-1} \quad \text{(ignoring the sign)}$$

$$= 0".031 \text{ m}^{-1}$$

$$= 31" \text{ km}^{-1}$$

If a mountain were to exist in this form then the underground half of the sphere would represent a doubling of the underground density. If the underground half of the sphere is now removed that will reduce the sideways acceleration by half but would also create a small upward component of acceleration. However, the upward component would be negligibly small compared with g and therefore would have no significant effect upon the computed deviation of the vertical or its rate of change. Therefore the deviation of the vertical and its maximum rate of change, which is at the surface of the hemisphere, become half their previously determined values and are:

$$\chi = \frac{2}{3} G \pi r^3 \rho d^{-2} g^{-1}$$

$$\frac{d\chi}{dd} = -\frac{4}{3} G \pi \rho g^{-1}$$

and upon evaluation the maximum value of the latter is 16" km^{-1}

If the point of investigation is moved towards the centre of the mountain then the point may be considered to be either in a horizontal tunnel or travelling over the surface of the mountain. If the point is in a horizontal tunnel then the external portion of the mountain, treated as a series of hemispherical shells, will have no gravitational attraction because the gravitational potential inside a spherical shell is constant (Heiskanen and Moritz, 1979). Therefore the deviation of the vertical in the tunnel at a distance d from the centre of the sphere will be:

$$\chi = \frac{4}{3} G \pi \rho d g^{-1}$$

and its rate of change will be

$$\frac{d\chi}{dd} = \frac{4}{3} G \pi \rho g^{-1}$$

which, with the numerical values above, is 16" km^{-1}, but because the mountain is a hemisphere, halves to 8" km^{-1}.

Over the surface of the spherical mountain, the attraction towards the centre of the mountain has the same value but the attraction is always directed towards the centre. On the surface the gravitational attraction is:

$$F = \frac{4}{3} G \pi r \rho$$

In this case the deviation of the vertical is:

$$\chi = F d g^{-1}$$

$$r = \frac{4}{3} G \pi \rho d g^{-1}$$

and its rate of change is:

$$\frac{d\chi}{dd} = \frac{4}{3} G \pi \rho g^{-1}$$

which is the same result as that obtained by treating the point as if it was in a tunnel. Therefore, since the mountain is hemispherical, and not spherical, the deviation of the vertical and the rate of change of deviation of the vertical become:

$$\chi = \frac{2}{3} G \pi \rho d g^{-1}$$

$$\frac{d\chi}{dd} = \frac{2}{3} G \pi \rho g^{-1}$$

The greatest rate of change of deviation of the vertical, from the above, is at the foot of the mountain, that is, where the distance of the station from the centre of the mountain is the same as the radius of the mountain. At this point the value is 16" km^{-1} irrespective of the radius of the mountain. For the geoid to be concave, the rate of change of deviation of the vertical would have to exceed, approximately, 32" km^{-1} in the opposite sense to that of the curvature of the ellipsoid. Since, even with a reasonable variation in the assumed value of ρ, the rate of change of deviation of the vertical will not approach the earth's curvature, the geoid can only be convex when viewed from above.

A sparse set of astrogeodetic observations in the region of a large topographical feature will lead to errors in the computed geoid model for that area, even with errorless observations. Considering only geoid sections from astrogeodetic levelling, Table 9.3, below, was constructed to show the effect of increasing the spacing between observation sites in the region of a hemispherical mountain. Mountains of radii ranging from 100 to 2000 metres were used. In Table 9.3 the geoid height at the top of the mountain is relative to the geoid height at a point 5000 metres from the centre of the mountain. The results below relate only to the errors due to the spacing of the stations in conjunction with the conventional approach to geoid sections and do not include considerations of uncertainty in the individual observations.

Table 9.3 Errors in geoid sections by astrogeodetic levelling with sparse data.

radius of mountain metres		2000		1000		500		200		100	
		At top of mountain									
inter-station distance	stations	geoid height	max error	geoid height	max error	geoid height	max error	geoid height	max error	geoid height	max error
metres	per km	mm	mm	mm	mm	mm	mm	mm	mm	mm	mm
1000	1	173.18	5.67	54.96	5.47	6.87	-6.45	0.44	-1.78	0.05	-0.51
500	2	168.98	1.47	51.00	1.51	14.70	1.38	0.94	-1.28	0.12	-0.45
333	3	168.17	0.66	50.18	0.68	12.49	-0.84	1.44	-0.78	0.18	-0.38
250	4	167.88	0.37	49.88	0.39	13.70	0.38	1.94	-0.28	0.24	-0.32
200	5	167.75	0.24	49.74	0.25	13.01	-0.31	2.44	0.22	0.31	-0.26
100	10	167.57	0.06	49.56	0.06	13.39	0.06	2.28	0.06	0.62	0.06
25	40	167.52	0.00	49.50	0.00	13.33	0.00	2.23	0.00	0.57	0.00
10	100	167.52	0.00	49.49	0.00	13.33	0.00	2.22	0.00	0.56	0.00
2.5	400	167.51	0.00	49.49	0.00	13.33	0.00	2.22	0.00	0.56	0.00
1	1000	167.51	0.00	49.49	0.00	13.33	0.00	2.22	0.00	0.56	0.00

The results indicate that, at the 0.01 mm level, there is no advantage in reducing the inter-station distance below 25 m. The results for the 2000 m and 1000 m mountains are almost identical and suggest that error is not a function of the size of the feature but only of the inter-station distance. Negative values of the error only occur where there is no observation at the foot of the mountain. In fact, for all mountains where the inter-station distance is 100 m, i.e. where there is an observation at the foot of the mountain, the error is 0.06 mm. It would therefore appear that proximity of at least one observation near the foot of the mountain would make a significant difference to the value of the error in the final geoid height of the mountain top.

In the following, the effect of taking the whole set of observations a few metres closer or further away from the centre of the mountain was investigated. In all cases, the radius of the mountain was 1000 m and the inter-station distance was 100 m. The first observation is at 5000 m from the centre of the mountain and the next at (5000 - x)

metres. Therefore, the nearest observation outside the mountain is (1100 - x) m. The final observation is at the top/centre of the mountain.

Table 9.4 The effect of taking a set of observations a few metres closer or further away from the centre of a mountain.

radius of mountain	1000 metres	
inter-station distance	100 metres	
	At top of mountain	
x metres	geoid height mm	max error mm
0	49.556	0.063
10	49.506	0.013
20	49.466	-0.026
30	49.438	-0.055
40	49.420	-0.073
50	49.413	-0.080
60	49.418	-0.075
70	49.434	-0.059
80	49.463	-0.030
90	49.503	0.010
100	49.556	0.063
inter-station distance = 1 metre	49.493	

From Table 9.4 it would appear possible to reduce the error in the geoid height at the top of the mountain by setting the offset x to about 13 metres. In practice, of course this would be quite impossible because mountains are neither symmetrical nor hemispherical. What can be concluded is that errors appear to be bounded to approximately ± the error in the geoid height when an observation is taken at the foot of the mountain.

9.3.1 The rate of change of the deviation of the vertical

The second rate of change of the deviation of the vertical will be:

$$\frac{d^2\chi}{dd^2} = 4\,G\,\pi\,r^3\,\rho\,d^{-4}\,g^{-1}$$

outside a hemispherical mountain. Again this will be a maximum for a minimum value of d, i.e. d = r, in which case:

$$\frac{d^2\chi}{dd^2} = 4\,G\,\pi\,\rho\,r^{-1}\,g^{-1}$$

which, with the values above, becomes $0.047\ r^{-1}$ "m^{-2} if r is in metres.

Rice (1962), as reported in Robbins (1976), found a value of 0.016" km^{-2} over average lines of 22 km. With the formula above, a similar value would be found 7.5 km from the centre of a hemispherical mountain of 1000 m radius. Dean (1980) found a value of 0.008" km^{-2} for work in the UK. The UK has few mountains of 1000 m. However, the value of 0.008 " km^{-2} would also be found 1.5 km from the centre of a hemispherical hill of 100 m radius.

9.4 Geoid Model Simulation

From the foregoing it is apparent that the inter-station distance affects the errors in the geoid height, considered only from the point of view of mathematical approximations in the formulae for geoid sections.

Geoid models were constructed from defined topographic models. This enabled the computation of as extensive and detailed a set of deviations as would be required. Such a detailed set of "errorless" deviations would not have been possible from a DEM of real topography because, in the analysis below, the topography is defined by simple geometric shapes for which exact values of attraction and hence deviation can be computed.

In the following, the effects of uncertainty in the observations are also included.

A topographic model, 10 km by 10 km, was defined by up to 70 hemispherical mountains/hills. The roughness of the model is greater than most realistic topography of similar height ranges but the purpose of the topographic model is merely to generate a geoid model with easily definable deviations. Four models were used.

The algorithm for the deviation at a point inside and outside a hemispherical hill, due to the hill has already been developed. Each deviation has east-west and north-south components. The deviation at a point, due to up to 70 such hills is the sum of the individual deviations.

The geoid and deviation models were formed at a regular grid of 100 m, i.e. for 10201 points in each model. The 100 m spacing can lead to errors of up to 0.00006 m at the top of each mountain or hill due to mathematical errors in the geoid sections formulae as shown above. With up to 70 hills and mountains in the model, the errors will be greater.

The geoid model was formed from the deviations, by successive geoid sections from the southwest corner of the model going north and then east. A second computation starts at the southwest corner and goes east and then north. The difference in the computed values for the same point gives a check upon the validity of the computational method. The mean value from both the computations was accepted. Full data sets for geoid heights and deviations throughout each model were created.

Brief details of the models are in Table 9.5. Diagrammatic representations of the topography are in Figures 9.2 to 9.4. Each hemispherical hill is shown by its circular base. Figures 9.5 to 9.7 show the geoid associated with a topography model.

Table 9.5 Parameters of topography and geoid models.

Model	**1**	**2**	**3**	**4**
	Mountains	**Hills**	**Lowlands**	**Plain**
Max geoid height	0.26405 m	0.05069 m	0.00096 m	0 m
Difference between E-then-N and N-then-E computation. See above	0.00042 m	0.00030 m	0.00017 m	0 m
No of hills	19	70	70	0
height/radius of hills	1 x 2000 m 3 x 1500 m 6 x 1000 m 9 x 500 m	6 x 500 m 21 x 375 m 43 x 250 m	7 x 100 m 63 x 60 m	

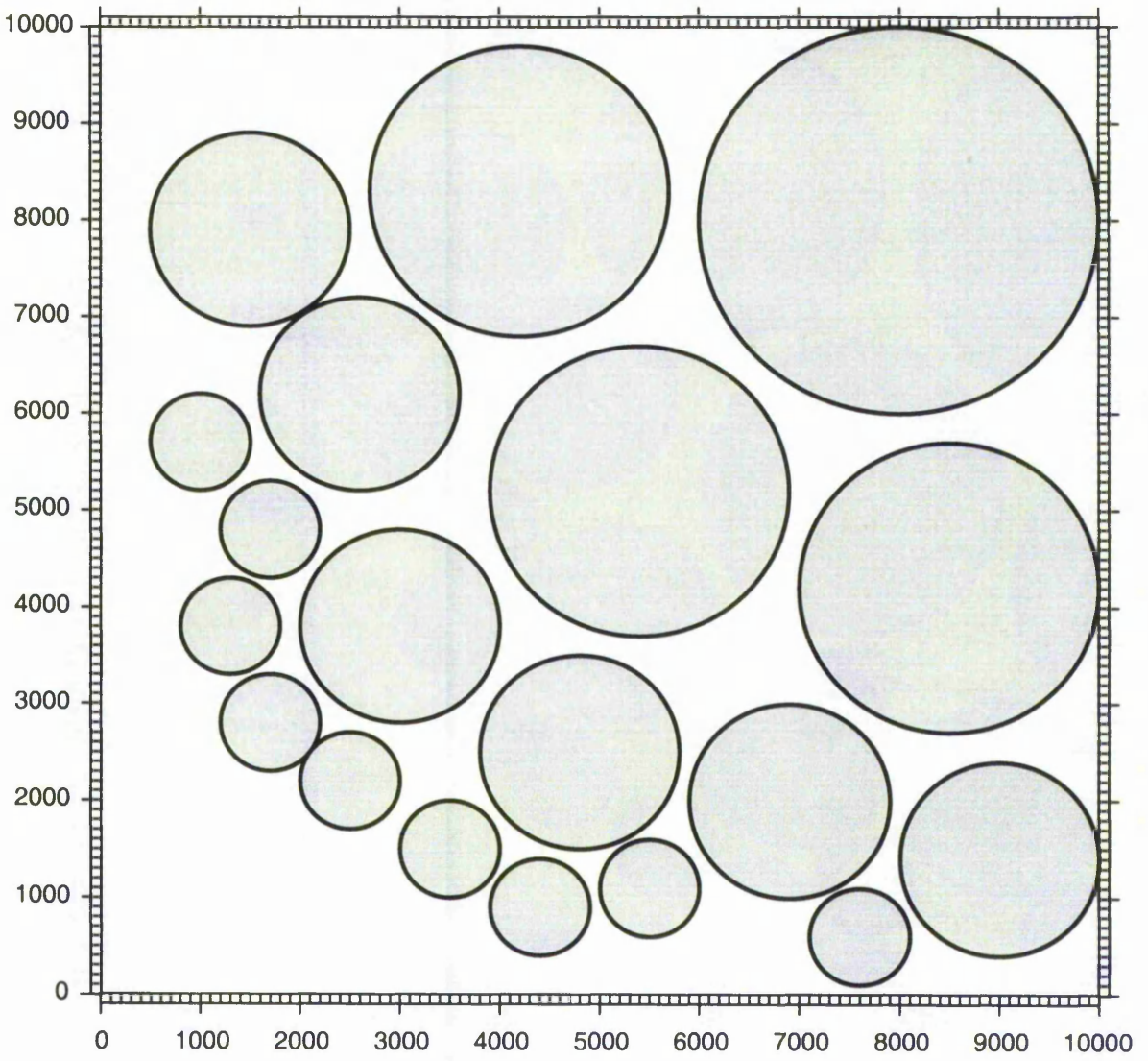

Figure 9.2 Diagrammatic representation of the topography model "Mountains"

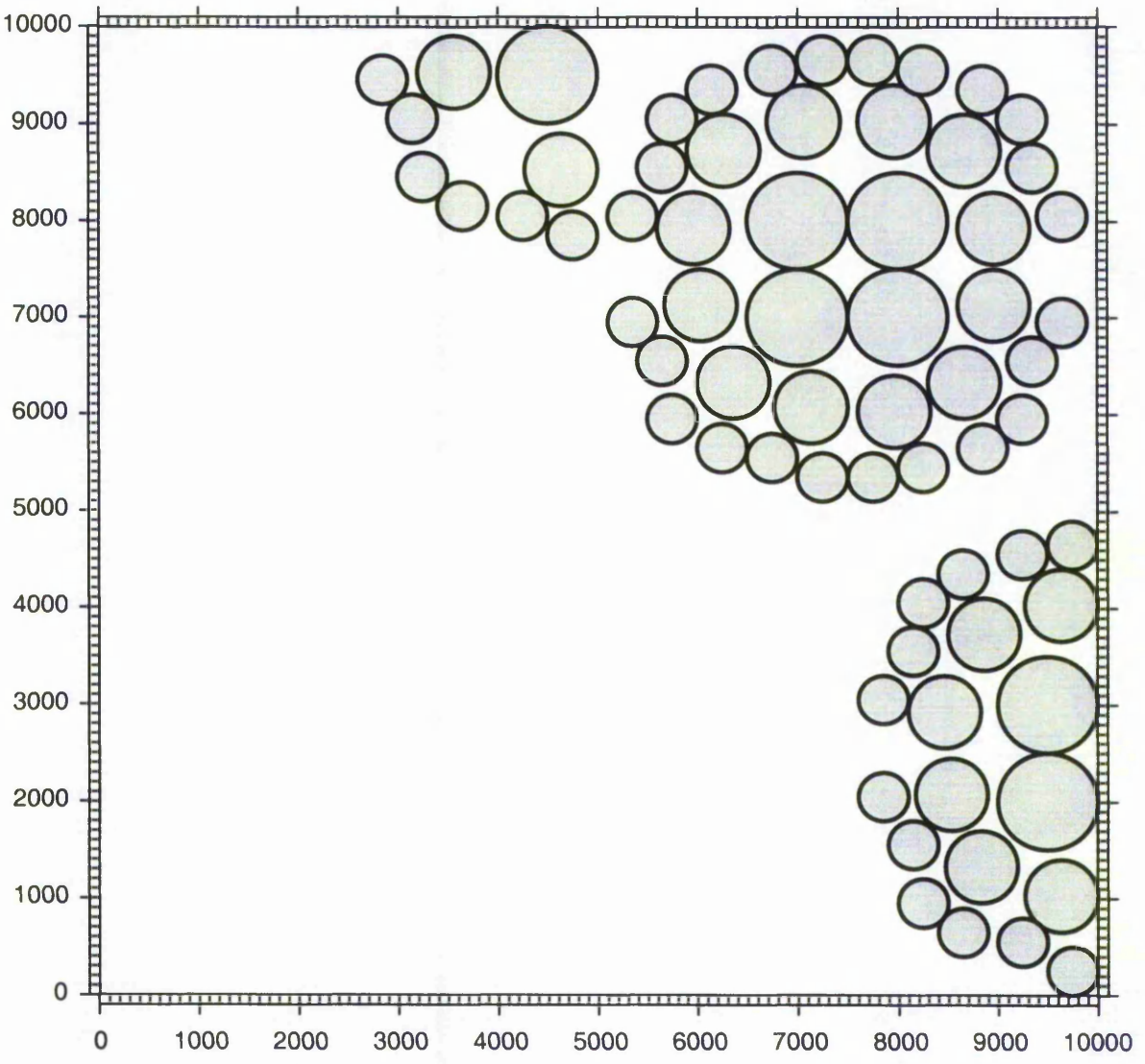

Figure 9.3 Diagrammatic representation of the topography model "Hills"

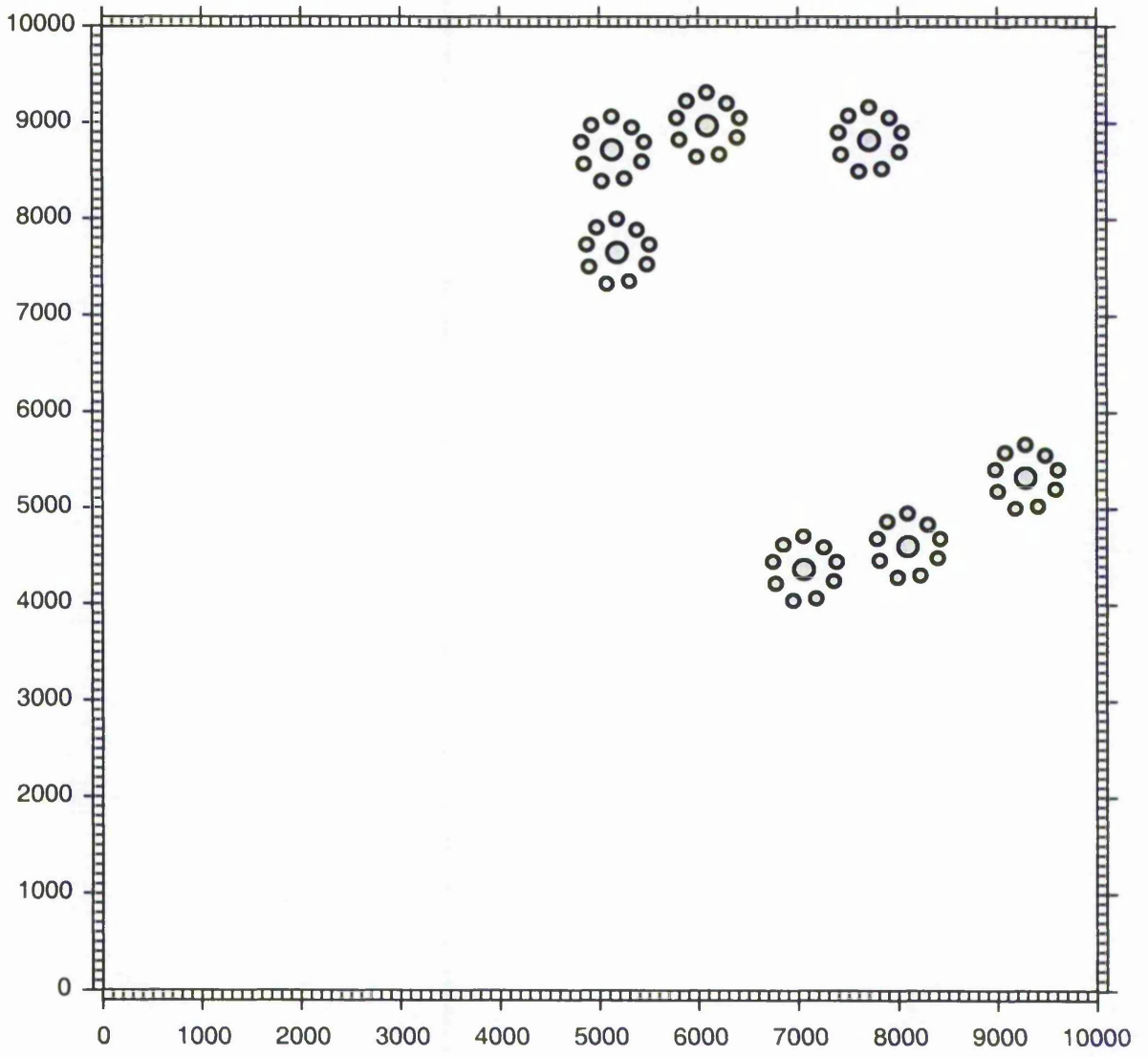

Figure 9.4 Diagrammatic representation of the topography model "Lowlands"

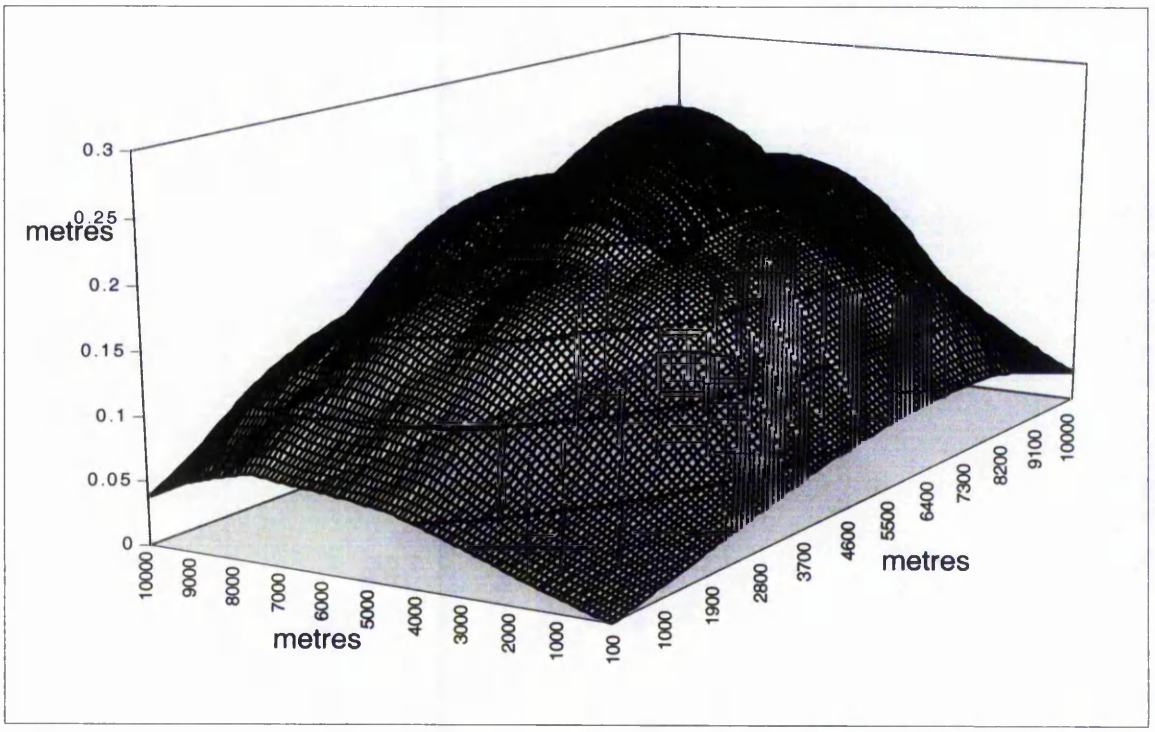

Figure 9.5 The geoid associated with the topography model "Mountains".

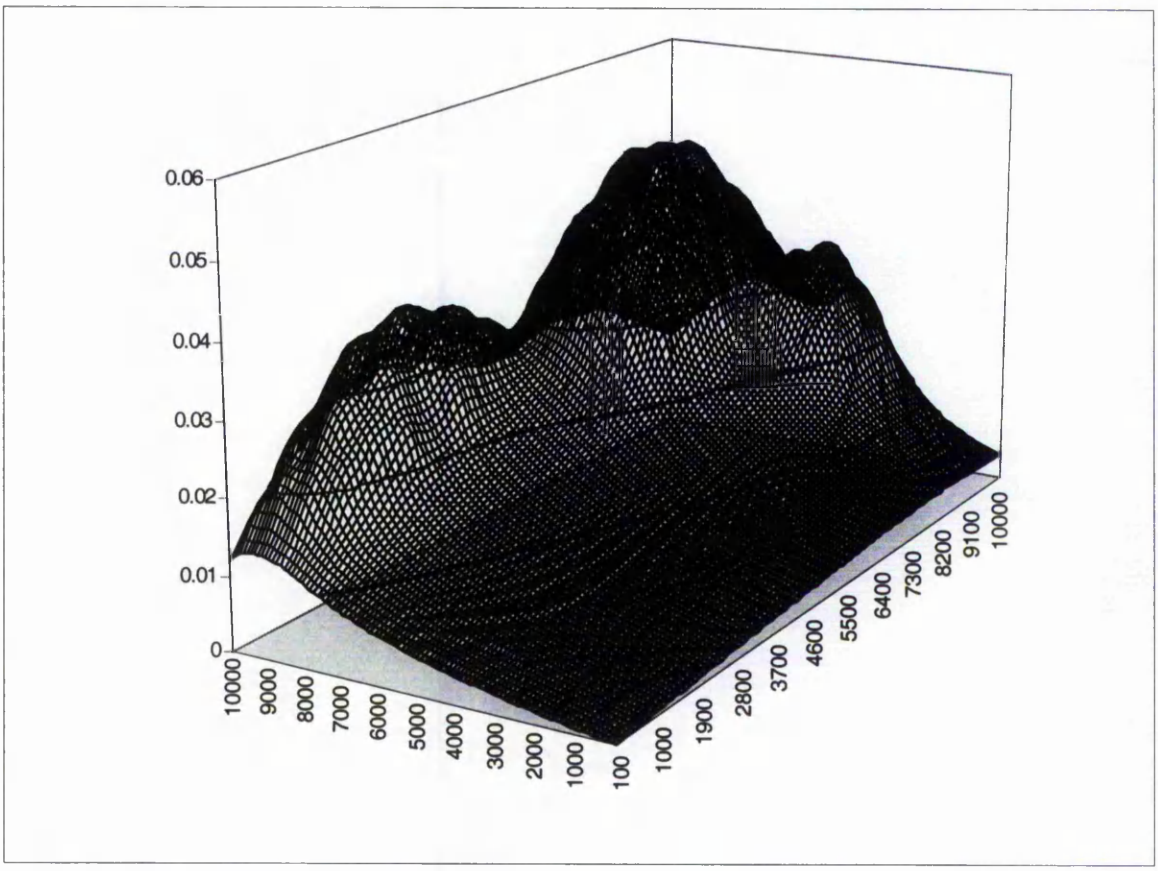

Figure 9.6 The geoid associated with the topography model "Hills".

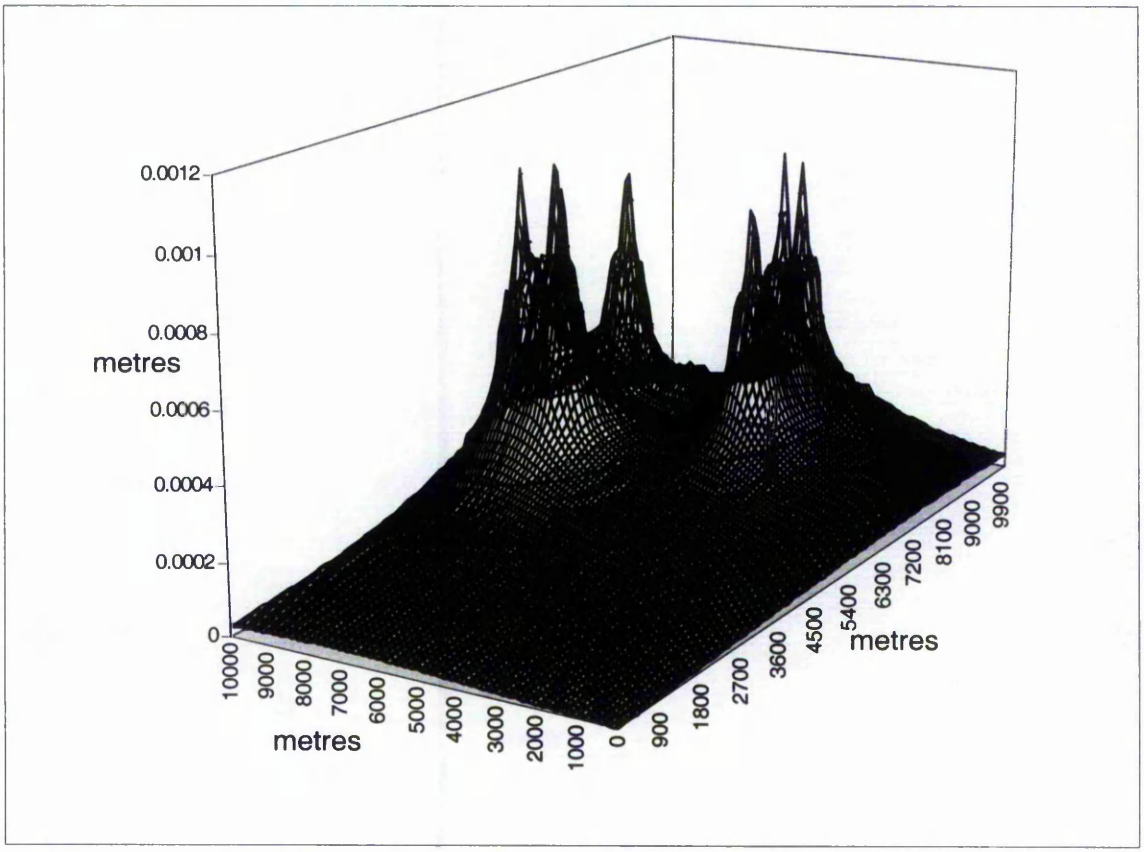

Figure 9.7 The geoid associated with the topography model "Lowlands".

The data sets for the deviations were edited to leave a subset of observations in a regular grid. This reduced set of deviations represents a set of "true" values of simulated observations. Adding random errors to the "true" observations created an "observed" set of simulated observations.

Two simulation studies were undertaken to investigate the relation between RMS error in geoid model, quality of deviation observations, inter-station distance and roughness of the terrain.

- The first study involved modelling the geoid by finding the coefficients of various polynomial expressions to describe (fit) the computed geoid.
- The second study involved developing and using an interpolation algorithm to provide sufficient computed values of deviation to form a geoid by conventional astrogeodetic levelling.

9.5 Geoid Model by Polynomial Coefficients

The geoid could be modelled by any suitable 2 dimensional series such as a series based upon:

$$\sum_{i=1}^{i=k}\sum_{j=0}^{j=i} a_{ij}\, e^{(i-j)}\, n^{j} \quad = \quad a_{10}e + a_{11}n + a_{20}e^2 + a_{21}en + a_{22}n^2 + a_{30}e^3 + \ldots + a_{kk}n^k$$

e and n are the easting and northing of the point. The co-ordinates of the southwest corner of the block are (0,0).

The number of terms in the model depends on how far the series is taken. If the maximum values of i and j are k then there are k^2-1 terms. The "-1" removes the singular term, a_{00}, and equivalent to the datum defect of a 1 dimensional network. It will be impossible to find a_{00} from slope information alone. The original geoid model contains 10201 heights, i.e. 101 rows and columns. The selected "observed" observations will be one of those in Table 9.6, below.

Table 9.6 Numbers of "observations" of η and ξ in the cut down sets of "true" values.

Selected fraction of total number of rows and columns f	No of rows and columns r = 101 x f (rounded up)	No of η and ξ "observations" $2r^2$
1/2	51	5202
1/3	34	2312
1/4	26	1352
1/5	21	882
1/6	17	578
1/8	13	338
1/10	11	242
1/12	9	162
1/15	7	98
1/20	6	72
1/25	5	50
1/33	4	32
1/50	3	18

For a good fit, k should be large but less than r. If k is too small, there will be excessive smoothing and little can be concluded about the relationships between the quality of the fit, inter-station distance and quality of the observations.

The object of the next part of this investigation is to reconstruct the geoid model from the computed polynomial coefficients and compare the reconstructed geoid model with the original geoid model in terms of the root mean square (RMS) differences between them at a 100-metre spacing.

When the observation equations can be expressed in the form:

$$\mathbf{Ax} = \mathbf{b} + \mathbf{v}$$

The least squares solution for the parameters is:

$$\mathbf{x} = (\mathbf{A}^T\sigma_{bb}^{-1}\mathbf{A})^{-1}\mathbf{A}^T\sigma_{bb}^{-1}\mathbf{b}$$

where $\mathbf{x}$ is the vector of corrections to provisional values of the parameters.

$\mathbf{A}$ is a matrix of the observation equations partially differentiated with respect to the parameters.

$\mathbf{b}$ is a vector of "observed minus computed" observations.

σ_{bb} is the covariance matrix of the observations.

The dimensions of the matrices, e.g. M, in the form no of rows **M** no of columns, are:

$\frac{1}{2}k(k+3)\ \mathbf{x}\ 1$, $2r^2\ \mathbf{A}\ \frac{1}{2}k(k+3)$, $2r^2\ \mathbf{b}\ 1$, $2r^2\ \sigma_{bb}\ 2r^2$.

The matrices are defined as follows:

x is the vector of corrections to the deviation model coefficients

$$\mathbf{x} = [\,\delta a_{10}\ \delta a_{11}\ \delta a_{20}\ \delta a_{21}\ \delta a_{22}\ \ldots\ \delta a_{kk}]^T$$

The observations are of deviation, therefore in terms of the geoid model, defined above:

$$\xi = \frac{dH}{dn} \qquad \eta = \frac{dH}{de}$$

where η and ξ are in radians

H, n, and e are in metres

$$\frac{dH}{dn} = H'_n$$

$$= \sum_{i=1}^{i=k} \sum_{j=1}^{j=i} j\, a_{ij}\, e^{(i-j)}\, n^{(j-1)}$$

$$= a_{11} + a_{21}e + 2a_{22}n + a_{31}e^2 + 2a_{32}en + 3a_{33}n^2 + a_{41}e^3 + 2a_{42}e^2n + 3a_{43}en^2 + 4a_{44}n^3 + \ldots + ka_{kk}n^{(k-1)}$$

$$\frac{dH}{de} = H'_e$$

$$= \sum_{i=1}^{i=k} \sum_{j=0}^{j=(i-1)} (i-j)\, a_{ij}\, e^{(i-j-1)}\, n^j$$

$$= a_{10} + 2a_{20}e + a_{21}n + 3a_{30}e^2 + 2a_{31}en + a_{32}n^2 + 4a_{40}e^3 + 3a_{41}e^2n + 2a_{42}en^2 + a_{43}n^3 \ldots + a_{k(k-1)}n^{(k-1)}$$

$$\mathbf{A} = [\, \mathbf{A}_\xi \;\; \mathbf{A}_\eta \,]^T$$

Therefore a row of $\mathbf{A}_\xi$ is given by:

$$\mathbf{A}_\xi = [\, 0\ 1\ 0\ e\ 2n\ 0\ e^2\ 2en\ 3n^2\ 0\ e^3\ 2e^2n\ 3en^2\ 4n^3\ \ldots\ kn^{(k-1)} \,]$$

and a row of $\mathbf{A}_\eta$ is given by:

$$\mathbf{A}_\eta = [\, 1\ 0\ 2e\ n\ 0\ 3e^2\ 2en\ n^2\ 0\ 4e^3\ 3e^2n\ 2en^2\ n^3 \ldots\ n^{(k-1)}\ 0 \,]$$

$$\mathbf{b} = \begin{bmatrix} o_{\xi 1} - c_{\xi 1} \\ o_{\xi 2} - c_{\xi 2} \\ \ldots \\ o_{\eta 1} - c_{\eta 1} \\ o_{\eta 2} - c_{\eta 2} \\ \ldots \end{bmatrix}$$

In this study, σ_{bb} is assumed to be an identity matrix. This ignores any difference in quality of the observations. If all observations are of the same quality and only the parameters, but not their quality, are to be computed then σ_{bb} is not required.

The relationship was investigated between the topography as defined by the four models, density of the observations, number of terms in the polynomial approximation of the model and fit of the model derived from the computed values of the polynomial coefficients with the errorless model. The RMS heights of the geoid models, where height is with respect to the southwest corner of the model, are in Table 9.7 below:

Table 9.7 RMS heights of the geoid models.

Model	RMS height
mountains	0.163097 m
hills	0.022843 m
lowlands	0.000219 m
plain	0.0 m

In each case in the original models, geoid heights were computed at 100 m spacing. "Observations" to construct an estimated model were taken at spacings of 500 m, 700 m, 1000 m, 1500 m and 2500 m.

The random errors applied to the "true observations" to obtain the "observed observations" were 0", 0".1, 0".3, 1" and 3". To minimise the complexity of the "random error" algorithm for the application of errors to the true "observations" in the Excel spreadsheet, the error was applied as:

$$\pm k * (RAND() - 0.5)$$

where k is the range for maximum error

RAND() takes any value between 0 and 1 with equal probability.

This distribution is of course not normally distributed but the standard error of the observations will be 0.288 k. In the study, specific values of k are used. Table 9.8, below, shows k with its equivalent standard errors.

Table 9.8 k factor and equivalent standard error.

k	standard error
0"	0"
0".1	0".03
0".3	0".09
1"	0".29
3"	0".86

Polynomials of powers of the easting and northing and their products up to 12 were investigated. The relationship between the maximum power and the number of terms in the polynomial expression is in Table 9.9, below.

Table 9.9 Power, number of terms and polynomial coefficients for a geoid model.

Maximum power	Number of terms	Polynomial expression, coefficients of ...
0	0	
1	2	e n
2	5	e n e^2 en n^2
3	9	e n e^2 en n^2 e^3 e^2n en^2 n^3
4	14	e n e^2 en n^2 e^3 e^2n en^2 n^3 e^4 e^3n e^2n^2 en^3 n^4
5	20	e n e^2 en n^2 e^3 e^2n en^2 n^3 e^4 e^3n e^2n^2 en^3 n^4 e^5 e4n e^3n^2 ... n^5
6	27	e n e^2 en n^2 e^3 e^2n en^2 n^3 e^4 e^3n e^2n^2 en^3 n^4 e^5 e4n e^3n^2 ... n^6
7	35	e n e^2 en n^2 e^3 e^2n en^2 n^3 e^4 e^3n e^2n^2 en^3 n^4 e^5 e4n e^3n^2 ... n^7
8	44	e n e^2 en n^2 e^3 e^2n en^2 n^3 e^4 e^3n e^2n^2 en^3 n^4 e^5 e4n e^3n^2 ... n^8
9	54	e n e^2 en n^2 e^3 e^2n en^2 n^3 e^4 e^3n e^2n^2 en^3 n^4 e^5 e^4n e^3n^2 ... n^9
10	65	e n e^2 en n^2 e^3 e^2n en^2 n^3 e^4 e^3n e^2n^2 en^3 n^4 e^5 e^4n e^3n^2 ... n^{10}
11	77	e n e^2 en n^2 e^3 e^2n en^2 n^3 e^4 e^3n e^2n^2 en^3 n^4 e^5 e^4n e^3n^2 ... n^{11}
12	90	e n e^2 en n^2 e^3 e^2n en^2 n^3 e^4 e^3n e^2n^2 en^3 n^4 e^5 e^4n e^3n^2 ... n^{12}

The relationship between the maximum power, p, and the number of terms in the polynomial expression, n, is

$$n = (p + 1)*(p + 2)/2 - 1$$

Superficially, there would appear to be 1200 possible combinations to test, i.e. powers to 12, 5 different spacings, 4 different models and 5 values for k. Of those, only 751 combinations were tested. Where conclusions could be drawn, further data was not derived. At the time of the investigation, observations and computations had been made to determine deviation to ± 0".3 (latitude) and therefore this study was aimed at finding the quality of geoid that could be determined with this precision of observation and what could be achieved if realistic improvements could be made to the precision of observations. The full set of numerical results is at Annex B, RMS Solutions For Tests Of Polynomial Geoid Models.

The numerical values of the polynomial coefficients were derived from least squares estimations. Since up to 90 coefficients were estimated, the matrix inversion routines of Excel, limited to matrices of dimensions of 50 could not be used. Solutions for the **x** vector of coefficients were attempted initially by the method of Jacobi, for computational simplicity. The method failed because the terms on the leading diagonal of the normal equations matrix were not dominant. Solutions by Gauss-Seidel were possible, but only when the number of coefficients was very small. For computations of coefficients involving powers greater than 3, the convergence was unacceptably slow and the method had to be abandoned. The final working solution was by Choleski's method. Choleski was the most complex solution to programme in a spreadsheet. A check upon the correctness of the programming was to take the output of a 90-parameter Choleski solution as the input to a Gauss-Seidel solution. The Gauss-Seidel solution did not diverge or change the solution.

The author's conclusions from this part of the study were as follows.

- There is a practical limit to the number of coefficients that can be computed using a soreadsheet. Accumulated rounding errors in the Choleski solution meant that in the 90-parameter solution the last term in the lower triangular matrix, **L**, was the square root of a small negative number. This was arbitrarily changed to make it the square root of a small positive number. The power of 12, or 90-parameter solution, must therefore be treated with caution, as must other high power solutions.
- The observations are not of the property to be derived, that is the observations are of the slope of the geoid. The property to be derived is the geoid height. The following simple example in two dimensions illustrates the problem.

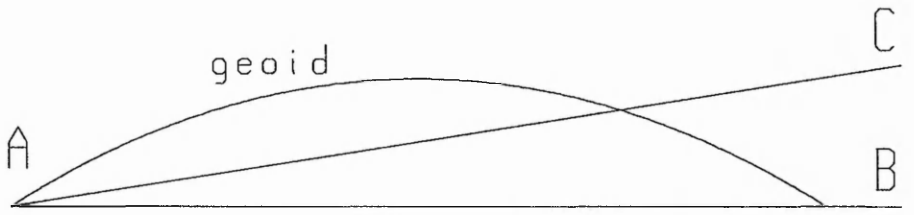

Figure 9.8 An illustration of a geoid model based upon observations of slope or height.

In Figure 9.8, the geoid is the curved line and is symmetrical about the centre of the figure. The model of the geoid is to be a straight line constrained to fit the geoid at the point A. Because the geoid is symmetrical, a least squares solution based upon observations of slope at A and B would compute the geoid as the line AB. By contrast, if the observations had been of geoid height, the least squares fit would lead to a geoid model of line AC. In three dimensions, with a more complex geoid and with more parameters in the solution, the effect is more difficult to analyse. This may account for the fact that adding more terms to the polynomial geoid model does not always improve the RMS solution. Many of the graphs at Annex B show anomalous peaks at individual "maximum powers of polynomial" and this phenomena is probably the cause.

- With the mountains model and 500 m inter-station distance (mountains at 500 m), the graphs at Annex B show that there is little to be gained with terms in the polynomial expression of powers beyond 6. If the observation error range is increased to 10", only then does the least squares solution become significantly affected by the errors in the observations beyond a power of 5. A 1" error range produces a solution very similar to that of errorless observations. The best RMS solution, at about 0.0065 m, is about 4.0% of the geoid model RMS.
- With the hills model and 500 m inter-station distance (hills at 500 m), more coefficients produce a better model up to powers of 10. This is possibly because the topography is still rugged but more complex: 70 features in the hills model compared with 19 in the mountains model. The 0".3 solutions are substantially the same as the observationally errorless, 0" error range, solutions and only marginally better than the 1" error range solutions. The best RMS solution, at about 0.0010 m, is about 4.4% of the geoid model RMS.

- With the lowlands model and 500 m inter-station distance (lowlands at 500 m), more terms in the polynomial model are justified only if the observations are of the highest quality. The maximum useful power of polynomial coefficients / error range cut off is in Table 9.10, below. The assessment is very subjective.

Table 9.10 The maximum useful power for observations of a given quality in the "Lowlands" model.

error range	maximum useful power
0"	12
0".1	9
0".3	4
1"	2

The reason for the change of maximum useful power with error range is that with such a small and irregular model, in terms of feature size to inter-station distance, observational errors dominate over the underlying geoid slope signal. The best RMS solution, at about 0.00006 m, is about 27% of the geoid model RMS. With a 1" error range there is barely any improvement over no model at all.

- With all the plain models, the RMS statistics are only functions of the effects of errors in the observations. Generally throughout the study, the more terms in the polynomial expression the worse the solution in RMS terms since the least squares solution, by definition, gives a best fit to the data provided. In *very* approximate terms the RMS is related to the maximum power of the polynomial, the error range, and the inter-station distance by the following expression.

$$\text{RMS} \approx \frac{p * e * d}{4 * 10^6}$$

where p is the maximum power of a term in the polynomial expression.
e is the standard error of slope observations in arc seconds.
d is the inter-station distance in metres.

- In the mountains with inter-station distance of 700 m, the RMS solutions are only marginally worse than the mountains with inter-station distance of 500 m RMS solutions. The mountains with inter-station distances of 1000 m, 1500 m and 2500 m RMS solutions, although similar, are significantly worse than the mountains with inter-station distance of 700 m RMS solutions. This indicates that about 700 m is the optimum spacing for this topography. Throughout there is nothing to be gained by improving the quality of observations from the 1" error range.
- With the hills model, a more realistic rugged topography representative of some mountainous parts of England and Wales, there appears to be a limit to the usefulness of improved observations, that is dependant upon the inter-station distance, as in Table 9.11, below.

Table 9.11 The optimisation of inter-station distance and quality of observations associated with the "hills" model.

inter-station distance	approximate best RMS	minimum useful error range
500 m	0.001 m	0".3
700 m	0.002 m	1"
1000 m	0.003 m	1"
1500 m	0.004 m	1"

- With the hills model, the maximum useful power in the polynomial terms depends upon the inter-station distance as in Table 9.12, below.

Table 9.12 The optimisation of inter-station distance and maximum useful power in the polynomial expansion associated with the "hills" model.

inter-station distance	maximum useful power
500 m	10
700 m	8
1000 m	7
1500 m	6

This is because there are fewer observations if the inter-station distance is greater and also because a polynomial with too many terms will model the noise rather than the signal.

- The lowlands model has very short wavelength features. Therefore, only a high density of observations can adequately model the geoid. All the lowlands solutions are dominated by noise. If the inter-station distance is 1000 m or greater, then the polynomial model gives RMS values greater than if there had been no model at all. At 700 m inter-station distance the maximum error range above which observations become pointless is 0".1 and the maximum error range for a 500 m inter-station distance is 0".3. However, these solutions have RMS agreement with the geoid better than 0.00015 m. Although there appears to very little to be gained by observing geoid slope when the geoid is so smooth, it must be remarked that these models do not reflect the long wavelength slope that will apply to most parts of the real geoid.

- Overall the quality of RMS agreement depends upon the quality of observations, the inter-station distance, the nature of the topography and hence the geoid and the number of terms in the polynomial expansion of the geoid. This study suggests that a sub-millimetric geoid can easily be achieved in moderate topography such as that found in most of England with inter-station distances up to 700 m and observations equivalent to an error range of 0".3, i.e. a standard error of 0".1. With an error range of 1", equivalent to a standard error of 0".3, a geoid at the 0.002 m level is achievable.

  At the other extreme, in mountainous country, with an inter-station distance of up to 700 m and with an error range of 1", equivalent to a standard error of 0".3, the quality of geoid that can be achieved is, in RMS terms, about 4-5% of the difference in geoid height from the origin of the survey.

All these conclusions relate to an area of investigation of 10 kilometres square. To extend these conclusions to larger areas would require re-examination of the parameters of this study.

9.6 Geoid Model by Interpolation of deviations

In this study, a full block of 101 by 101 deviation values for both north-south and east-west directions was developed from the available "observations". The algorithm chosen was such that intermediate values of deviation were determined as a weighted average of all "observed" deviation values in the block. The weight, w, applied for each "observed" value was defined by:

$$w = (l \{1 + g_1^{(l/g_2)} g_3^{-1}\})^{-1}$$

where l is the distance between the "observation" and the interpolation point and is given by:

$$l^2 = (E_i - E_o)^2 + (N_i - N_o)^2$$

where the subscripts refer to the "observed" and the interpolated points.

The constants g_1, g_2 and g_3 may be selected for convenience.

This weight algorithm was chosen because:

It gives smooth and continuous values for deviation and hence the geoid, throughout the model.

Weighting is near inverse linear with distance in the local region of the interpolation point but the weights of points only a little beyond a critical value, g_2, soon become very small.

If g_2 is too large, there will be excessive smoothing. If g_2 is too small then interpolated points will tend to take the value of the nearest "observed" point and a plot of interpolated deviations would appear as a checkerboard of steps rather than a smooth but undulating surface.

The chosen values of g_1 and g_3 were 100 and 1000 respectively. g_2 was chosen to be 0.6s where s is the approximate average distance between "observations". For a grid arrangement, s was taken as the distance between adjacent points in the grid. The coefficient of l, $\{1 + g_1^{(l/g_2)} g_3^{-1}\}$, therefore varies with the distance l as in Table 9.13 and Figures 9.9 and 9.10, below.

Table 9.13 l and its coefficient in the weight function.

l	coefficient $\{1 + g_1^{(l/g_2)} g_3^{-1}\}^{-1}$
0.0s	0.99900
0.2s	0.99538
0.4s	0.97891
0.6s	0.90909
0.8s	0.68298
1.0s	0.31701
1.2s	0.09091
1.4s	0.02109
1.6s	0.00462
1.8s	0.00100
2.0s	0.00021

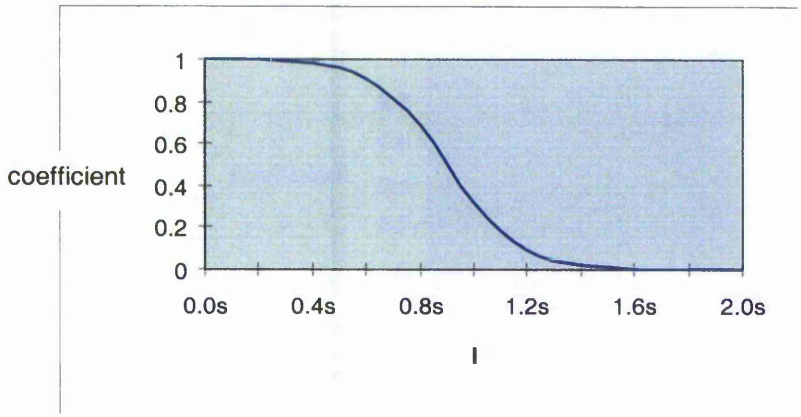

Figure 9.9 l and its coefficient in the weight function.

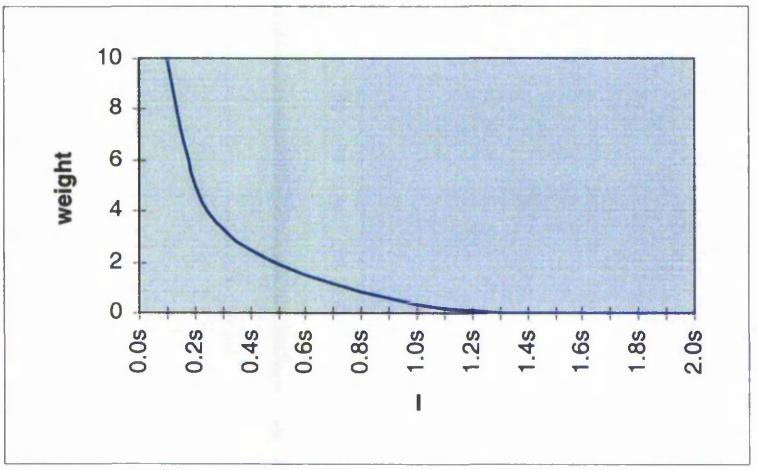

Figure 9.10 l and the weight function.

g_2 was optimised to be 0.6s because that was the value that gave a best fit for the mountains model with a spacing of 500 m between observations and with 0".0 random error applied to the "observations".

Once again, the variables to be investigated were:

Inter-observation distance - 500 m 700 m 1000 m 1500 m 2500 m.

Size of random "error" in the observations - 0" 0".1 0".3 1" 3".

Topographic model, i.e. mountains, hills, lowlands and plain, as defined earlier.

The total number of solutions was therefore 100. RMS values of the difference between the geoid derived from the full set of 10201 "true" observations and the set of 10201 "observations" reconstructed by interpolation from the subset implied by the inter-station distance. The RMS results are in Table 9.14, below.

Table 9.14 RMS difference between the geoid derived from a full set of "true" observations and a set of 10201 interpolated "observations".

RMS values are in metres					
Mountains					
distance	error 0"	0.1"	0.3"	1"	3"
500m	0.001137	0.001148	0.001212	0.003005	0.006290
700m	0.002656	0.002495	0.002733	0.006471	0.005688
1000m	0.003375	0.003343	0.003476	0.004332	0.007127
1500m	0.006779	0.006809	0.006499	0.007162	0.009155
2500m	0.030270	0.030389	0.029893	0.034240	0.045467
Hills					
distance	error 0"	0.1"	0.3"	1"	3"
500m	0.000459	0.000486	0.000664	0.001582	0.004750
700m	0.001798	0.001808	0.001758	0.002120	0.008012
1000m	0.001227	0.001231	0.001563	0.002353	0.006973
1500m	0.002357	0.002456	0.002545	0.003707	0.008251
2500m	0.004568	0.004483	0.005076	0.004712	0.010067
Lowlands					
distance	error 0"	0.1"	0.3"	1"	3"
500m	0.000104	0.000239	0.000508	0.002742	0.004806
700m	0.000139	0.000318	0.000696	0.00146	0.004375
1000m	0.000265	0.000321	0.000702	0.001617	0.006973
1500m	0.000446	0.000548	0.000927	0.003566	0.009210
2500m	0.000215	0.000643	0.000963	0.003542	0.015912
Plain					
distance	error 0"	0.1"	0.3"	1"	3"
500m	0.0	0.000126	0.000407	0.001199	0.003514
700m	0.0	0.000169	0.000445	0.001831	0.008974
1000m	0.0	0.000229	0.001157	0.001821	0.006133
1500m	0.0	0.000250	0.000789	0.003569	0.015089
2500m	0.0	0.000308	0.000818	0.003562	0.005505

From these results it would appear that the RMS value of the difference between the "true" and computed geoid is a function of the 3 variables: inter-observation distance, size of random "error" in the observations, and size of the topographic model. The problem is to find the relationship so that the numerical quality of a computed geoid may be found given the values of the variables and so the quality of output may be determined before observations are taken. With such a relationship known it would be possible to select values for inter-observation distance and quality of observation given knowledge of the terrain for a desired quality of geoid model. Inter-observation distance and size of random "error" in the observations may easily be expressed numerically. Finding a single numerical value to describe the terrain is more difficult. For this part of the investigation, it is taken as the simple statistic, the difference in height between the highest and lowest point in the topographic model.

The form of the function is not clear from the above data. A function of the form:

$$RMS^2 = a\, t^x\, k^y\, f^z$$

where a is a constant
t is the terrain height
k is the observation "error"
f is the inter-observation distance

cannot be possible because if any of t, k or f are 0 then the RMS must be 0 and that does not fit the above data. Similarly a function of the form:

$$RMS^2 = a\, t^x + b\, k^y + c\, f^z$$

where a, b and c are constants

also cannot be possible because unless t, k *and* f are 0, then the RMS cannot be 0 and that also does not fit the data associated with the plain model.

The function: $RMS^2 = a\, t^u\, k^v + b\, t^w\, f^x + c\, k^y\, f^z$

where a, b, c, u, v, w, x, y and z are constants

was investigated with a view to finding which of the terms are applicable and finding their values. To avoid large and small terms in the various least squares solutions below, the units of t and f are taken as kilometres, k as seconds of arc and the RMS is in millimetres. The 100 RMS values above lead to 100 observation equations to solve for up to 9 unknowns. The model is well over-determined. The least squares solution for the above model is in Table 9.15, below. Significant statistics are in bold type.

Table 9.15 Least squares determination of the parameters in the model

$$a\,t^u\,k^v + b\,t^w\,f^x + c\,k^y\,f^z - RMS^2 = 0.$$

x vector	values
a	0.03839
b	0.02975
c	1.59614
u	**5.90211**
v	1.42173
w	2.78161
x	6.76521
y	1.53668
z	1.00305

coefficients of correlation

b	c	u	v	w	x	y	z	
-0.05747	-0.10839	**-1.00000**	-0.00015	0.23835	0.00921	-0.03623	0.26974	a
	-0.05027	0.05585	0.27579	-0.20542	-0.97915	0.05813	-0.04445	b
		0.10761	0.15176	0.15352	0.01903	-0.93848	-0.24688	c
			-0.00473	-0.23855	-0.00754	0.03697	-0.26954	u
				0.03585	-0.28530	-0.16024	-0.01423	v
					0.00305	-0.19513	0.18502	w
						-0.01812	0.00545	x
							-0.03889	y

$(A^TA)^{-1}$

a	b	c	u	v	w	x	y	z
22.24031	-0.00676	-0.10569	-835.587	-0.00038	0.27538	0.03879	-0.01970	0.07138
	0.00062	-0.00026	0.24677	0.00380	-0.00125	-0.02181	0.00017	-0.00006
		0.04275	3.94245	0.01734	0.00778	0.00351	-0.02237	-0.00286
			31394.4	-0.46275	-10.3547	-1.19329	0.75531	-2.67992
				0.30543	0.00485	-0.14084	-0.01021	-0.00044
					0.06002	0.00067	-0.00551	0.00254
						0.79791	-0.00187	0.00027
							0.01329	-0.00025
symmetrical								0.00315

The solution became unstable as convergence approached and a solution was only achieved with increasing values of under-relaxation. The reason is that as convergence approached the coefficient of correlation between a and u tended towards

1.0 exactly. This implies that there is not a unique solution for a and u and either could be fixed at any value and convergence still achieved. The value of u is unexpectedly large and the variances of a and u are out of sympathy with the variances of the other parameters. If there is a functional relationship between the RMS and the variables t, k and f, then a cannot be fixed. Therefore, in the next model (Table 9.16 below) u is arbitrarily set to 2 and a remains free.

Table 9.16 Least squares determination of the parameters in the model

$$a\,t^2 k^v + b\,t^w f^x + c\,k^y f^z - RMS^2 = 0.$$

x vector	values
a	3.35131
b	1.42E-06
c	4.33055
v	1.87770
w	**10.32924**
x	13.91542
y	2.07967
z	1.10917

coefficients of correlation

b	c	v	w	x	y	z	
-0.00435	-0.20562	-0.99167	0.00292	0.26401	0.20178	0.03795	a
	-0.16587	0.00222	**-1.00000**	-0.02210	0.17001	-0.11673	b
		0.20469	0.16588	0.00092	-0.98185	-0.13758	c
			-0.00093	-0.23768	-0.20688	-0.01772	v
				0.01669	-0.17002	0.11667	w
					-0.00253	0.01300	x
						-0.02296	y

$(A^TA)^{-1}$

a	b	c	v	w	x	y	z
0.12693	-2.00E-06	-0.0144	-0.03400	1.37092	0.50765	0.00295	0.00015
	1.69E-06	-4.2E-05	2.77E-07	-1.71260	-0.00015	9.06E-06	-1.7E-06
		0.03866	0.00387	42.99935	0.00098	-0.00792	-0.00030
			0.00926	-0.11793	-0.12346	-0.00082	-1.9E-05
				1738080	118.747	-9.19613	1.70208
					29.1268	-0.00056	0.00077
						0.00168	-1.0E-05
symmetrical							0.00012

Again, the convergence is unstable, and this time it is because of the -1.0 coefficient of correlation between b and w. Again, the value and variance of w are unreasonably large. Again, b cannot be fixed if the functional relationship is to be found. Therefore, in the next model, Table 9.17, w is arbitrarily set to 2 and b remains free.

Table 9.17 Least squares determination of the parameters in the model

$$a\,t^2 k^v + b\,t^2 f^x + c\,k^y f^\alpha - RMS^2 = 0.$$

x vector	values
a	5.23738
b	1.09E-05
c	2.62721
v	1.78656
x	**18.6132**
y	2.84053
z	1.03932

coefficients of correlation

b	c	v	x	y	z	
-0.27001	-0.20221	-0.98979	0.27000	0.20105	0.03186	a
	-0.00800	0.24100	**-1.00000**	0.00774	-0.00794	b
		0.20333	0.00800	-0.99687	-0.06089	c
			-0.24100	-0.20493	-0.01003	v
				-0.00774	0.00793	x
					-0.00470	y

$(A^TA)^{-1}$

a	b	c	v	x	y	z
0.12620	-3.2E-05	-0.01459	-0.02160	3.21780	0.00502	8.96E-05
	1.12E-07	-5.4E-07	4.95E-06	-0.01122	1.82E-07	-2.10E-08
		0.04128	0.00254	0.05451	-0.01424	-9.80E-05
			0.00378	-0.49649	-0.00089	-4.90E-06
				1125.04	-0.01826	0.002107
					0.00494	-2.60E-06
symmetrical						6.27E-05

Yet again, the convergence is unstable, and this time it is because of the -1.0 coefficient of correlation between b and x. Again, the value and variance of x are unreasonably large. b cannot be fixed if the functional relationship is to be found.

Therefore, in the next model, Table 9.18, below, x is arbitrarily set to 2 and b remains free.

Table 9.18 **Least squares determination of the parameters in the model $a\,t^2 k^v + b\,t^2 f^2 + c\,k^y f^\alpha - RMS^2 = 0$.**

x vector	values
a	0.00179
b	2.40715
c	0.99631
v	**6.41904**
y	1.44545
z	1.05737

coefficients of correlation

b	c	v	y	z	
-0.29772	-0.18316	**-1.00000**	0.17245	0.05702	a
	-0.07227	0.29746	0.09658	-0.10104	b
		0.18316	-0.92865	-0.30006	c
			-0.17253	-0.05688	v
				-0.01020	y

$(A^TA)^{-1}$

a	b	c	v	y	z
0.12764	-0.00589	-0.01289	-64.7185	0.01078	0.00193
	0.00306	-0.00079	2.98264	0.00093	-0.00053
		0.03881	6.53636	-0.03201	-0.00560
			32814.6	-5.46894	-0.97555
				0.03062	-0.00017
symmetrical					0.00896

The convergence is still unstable, this time it is because of the -1.0 coefficient of correlation between a and v. Again the value and variance of v are unreasonably large. a cannot be fixed if the functional relationship is to be found. Therefore, in the next model, Table 9.19, below, v is arbitrarily set to 2 and a remains free.

Table 9.19 Least squares determination of the parameters in the model $a\,t^2k^2 + b\,t^2f^2 + c\,k^y f^\alpha - RMS = 0$.

x vector	values
a	1.07096
b	39.4333
c	0.94267
y	3.73133
z	1.14774

coefficients of correlation

b	c	y	z	
-0.33066	0.01020	-0.01843	0.16586	a
	-0.11694	0.11859	-0.08447	b
		-0.99945	-0.02159	c
			-0.00680	y

$(A^TA)^{-1}$

a	b	c	y	z
0.00163	-0.00071	7.80E-05	-0.00013	5.53E-05
	0.00282	-0.00115	0.00113	-3.70E-05
		0.03443	-0.03322	-3.30E-05
			0.03209	-1.00E-05
symmetrical				6.8E-05

Although convergence is no longer unstable, the coefficient of correlation between c and y is very close to -1.0. Although the values and variances of c and y are not unreasonably large, the value of y is unlikely because an integer value would be expected if there were a truly functional relationship. c cannot be fixed if the functional relationship is to be found. Therefore, in the next model (Table 9.20 below) y is arbitrarily set to 2 and c remains free.

Table 9.20 Least squares determination of the parameters in the model $a\,t^2k^2 + b\,t^2f^2 + c\,k^2f^z - RMS^2 = 0$.

x vector	values	σ		σ_0
a	1.12976	1.97460		48.8733
b	39.2367	2.57943		
c	6.19348	1.99911		
z	1.16071	0.40835		

coefficients of correlation			
b	c	z	
-0.32908	-0.24237	0.16812	a
	0.04498	-0.08704	b
		-0.86195	c

$(A^TA)^{-1}$			
a	b	c	z
0.00163	-0.00070	-0.00040	5.68E-05
	0.00279	9.71E-05	-3.80E-05
		0.00167	-0.00029
symmetrical			6.98E-05

Now, of the original 9 parameters only a, b, c and z are still free. This time convergence is achieved and there are no excessively large coefficients of correlation or unreasonably large variances. However the coefficients a, b and c are significantly different in size and it is worth comparing them with their own standard errors. b and c are at least 3 times the size of their standard errors, a is less than its own standard error and therefore there is little evidence that a exists at all. In the next model (Table 9.21 below) a is set to zero.

Table 9.21 Least squares determination of the parameters in the model

$$b\,t^2 f^2 + c\,k^2 f^z - RMS^2 = 0.$$

x vector	values	σ		σ_0
b	39.7217	2.43575		48.7037
c	6.45624	1.93053		
z	1.12585	0.38697		

coefficients of correlation

c	z	
-0.03840	-0.03582	b
	-0.84990	c

$(A^TA)^{-1}$

b	c	z
0.002484	-7.6E-05	-1.4E-05
	0.00156	-0.00027
symmetrical		6.27E-05

Again, convergence is achieved without any anomalies. σ_0 improves slightly indicating that the removal of the term containing a has not had a detrimental effect upon the solution. The standard errors of b and c remain much the same. The value of z could reasonably be expected to be an integer and if so, given the values above will have a value of 1. The final model, Table 9.22, below, assumes this and solves for the coefficients b and c.

Table 9.22 Least squares determination of the parameters in the model

$$b\,t^2 f^2 + c\,k^2 f - RMS^2 = 0.$$

x vector	values	σ	σ_0
b	39.8409	2.42361	48.5039
c	6.68700	1.57051	

coefficient of correlation

c	
-0.09213	b

$(A^TA)^{-1}$

c	b
0.00246	-0.00015
-0.00015	0.00103

This time the coefficient of correlation shows that b and c are substantially un-correlated. The standard errors of b and c are much smaller than the values of b and c indicating that it is reasonable to assume that the terms do indeed exist. However the standard errors of b and c are sufficiently large to cast doubt upon the values of b and c much beyond 1 significant figure. It is therefore concluded that the functional relationship is:

$$RMS^2 = 40\left(t^2 f^2 + \frac{k^2 f}{6}\right)$$

This must be viewed as an empirical non-analytical relationship because of the assumptions that u, v, w, x and y take the values of 2. Given that k is the "random error" defined earlier then if k is to be defined in terms of standard error then the relationship becomes:

$$RMS^2 = 40\,t^2 f^2 + 75\,e^2 f$$

where e is the standard error of an observation of deviation of the vertical.

9.7 Geoid Model - from deviations to geoid heights

Earlier, it was stated that geoid models were constructed from the model deviation data by, either computing east then north, or north then east from the origin, the southwest corner. Such an approach relies heavily upon an absence of errors in the deviation observations along the southern and western edges of the block. A better approach might be to compute the geoid height of any point as the mean of:

The geoid height of the point to the south and the mean of the north-south deviations at that and the new point, times distance, and ...

The geoid height of the point to the west and the mean of the east-west deviations at that and the new point, times distance.

In Figure 9.11, below, letters stand for geoid heights and numbers for computed difference heights.

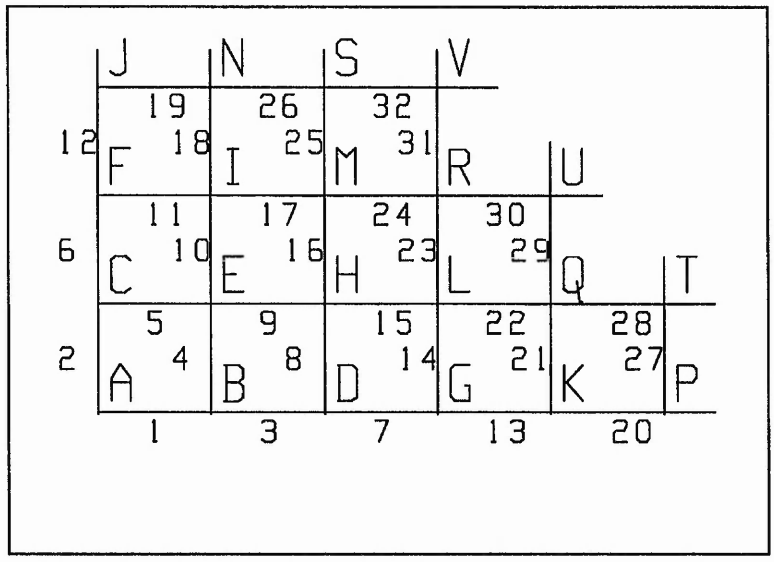

Figure 9.11 Progressive Nodes diagram.

In this ***progressive nodes*** approach, for example:

H = ½(E + 9 + D + 8)

Developing the first few heights from the southwest corner:

B = A+1

C = A+2

D = B+3

$$= \quad A+1+3$$

$$E = \tfrac{1}{2}(B+4+C+5)$$

$$= \tfrac{1}{2}(A+1+4+A+2+5)$$

$$= A+\tfrac{1}{2}(1+2+4+5)$$

$$F = A+2+6$$

$$G = A+1+3+7$$

$$H = \tfrac{1}{2}(D+8+E+9)$$

$$= \tfrac{1}{2}(A+1+3+8+A+\tfrac{1}{2}(1+2+4+5)+9)$$

$$= A+\tfrac{1}{2}(1+3+8+9+\tfrac{1}{2}(1+2+4+5)) \quad \text{etc.}$$

However, this does not reflect the expected symmetry of the situation. Considering the only two possible routes from A to H it would be expected that the following difference geoid heights would have equal weight in the solution; 1 and 9, 3 and 5, 2 and 8. This clearly is not the case. The east-then-north-and-north-then-east approach would give equal weight to the difference geoid heights 1, 2, 3, 5, 8 and 9 but would ignore 4. If the argument is developed further it can be shown that R in the progressive nodes approach is:

$$R = A+(1+\tfrac{1}{2}(2+3+7+14+15+16+17+23+24 +\tfrac{1}{2}(1+3+4+5+8+9+\tfrac{1}{2}(1+2+3+6+8+9+10+11))))$$

but in the east-then-north-and-north-then-east approach:

$$R = A+\tfrac{1}{2}(1+2+3+6+7+11+14+17+23+24)$$

The relative weights of all the difference geoid heights involved in the determination of R for the different approaches are in Table 9.23, below.

Table 9.23 Relative weights of difference geoid heights in the determination of R.

difference geoid heights	weight in "progressive nodes"	weight in "east-then-north-and-north-then-east"
1	0.1719	0.1
2	0.0781	0.1
3	0.1094	0.1
4	0.0313	0
5	0.0313	0
6	0.0156	0.1
7	0.0625	0.1
8	0.0469	0
9	0.0469	0
10	0.0156	0
11	0.0156	0.1
14	0.0625	0.1
15	0.0625	0
16	0.0625	0
17	0.0625	0.1
23	0.0625	0.1
24	0.0625	0.1

In the case of the computed geoid height of R, it can be seen that a greater number of interpolated difference geoid heights, each with lesser weight, are involved with the progressive nodes approach. The significant drawback is that one of the difference geoid heights, 1, has a much greater weight, negating the desired effect. The above is sufficient to illustrate the possibilities. Analysis of points further from the southwest corner would also be possible.

A third approach would be to use the computed geoid difference heights in a least squares adjustment to find the geoid heights of all the points. Such an approach would be tedious in the computations and the statistical output would be of dubious value because the "observations" are not true observations but are derived from interpolated values and would have high coefficients of correlation between them. The variances and covariances and hence coefficients of correlation would be complex to determine.

A more practical approach, of intermediate rigor, would be to modify the "progressive nodes" method above by taking the variances of the computed geoid heights and the difference geoid heights into account. The following derives the relationships for computing the geoid height Z, given previously computed statistics for W, X and Y.

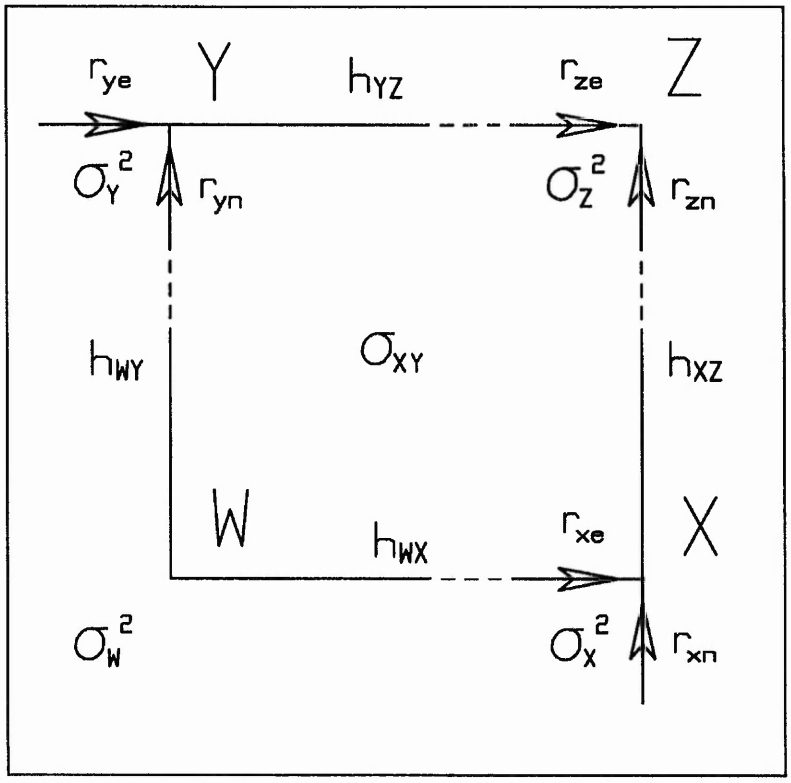

Figure 9.12 Diagram to show finding geoid height given other geoid heights, difference geoid heights and their uncertainties in a Progressive Nodes form.

In Figure 9.12:

h_{WY} etc. is the geoid height difference based upon the interpolated deviation values.

r_{yn} etc. is the proportion of $(W + h_{WY})$ used to compute Y.

(In the progressive nodes method $r_{yn} = ½$). $r_{yn} + r_{ye} = 1$.

σ_W^2 etc. is the computed variance of W.

σ_{XY} is the computed covariance between X and Y.

σ_h^2 etc. is the variance of all geoid height differences between adjacent points based upon interpolated deviation values.

The following are all derived from simple propagation of error formulae for variances and covariances. If Z was computed from $Y + h_{YZ}$, then the variance of Z would be given by:

$$\sigma_Z^2 = \sigma_Y^2 + \sigma_h^2$$

Similarly if Z was computed from $X + h_{XZ}$, then the variance of Z would be given by:

$$\sigma_Z^2 = \sigma_X^2 + \sigma_h^2$$

Therefore the different computed values for Z must be combined in a weighted mean solution based upon the variances of the solutions where:

$$r_{ze} = \frac{\sigma_X^2 + \sigma_h^2}{\sigma_X^2 + \sigma_Y^2 + 2\sigma_h^2}$$

$$r_{zn} = \frac{\sigma_Y^2 + \sigma_h^2}{\sigma_X^2 + \sigma_Y^2 + 2\sigma_h^2}$$

and so the geoid height Z is:

$$Z = r_{ze}(Y + h_{YZ}) + r_{zn}(X + h_{XZ})$$

Similarly X and Y will have already been found from:

$$X = r_{xe}(W + h_{WX}) + \ldots$$

$$Y = r_{yn}(W + h_{WY}) + \ldots$$

and so:

$$\sigma_{XY} = r_{yn} r_{xe} \sigma_W^2$$

The variance of Z may be derived as follows.

$$\sigma_Z^2 = r_{ze}^2\sigma_Y^2 + r_{zn}^2\sigma_X^2 + (r_{ze}^2 + r_{zn}^2)\sigma_h^2 + 2r_{ze}r_{zn}\sigma_{XY}$$

$$= r_{ze}^2\sigma_Y^2 + r_{zn}^2\sigma_X^2 + (r_{ze}^2 + r_{zn}^2)\sigma_h^2 + 2r_{ze}r_{zn}r_{yn}r_{xe}\sigma_W^2$$

If the geoid heights and their variances are computed in a northeast direction starting from the southwest corner, then all terms required for a particular geoid height have already been computed. The statistical limitation of the method is that the computed geoid heights depend only upon the computed geoid height differences to the south

and to the west of the point under investigation. In a least squares solution, a computed geoid height is affected at least to some extent by *all* "observations".

Providing that stations I, J, and K are consecutive stations east-west or north-south then h_{IJ} and h_{JK} share a common deviation observation at J. Therefore there will be a covariance between h_{IJ} and h_{JK}. d_I (etc) is the deviation at I with a variance of σ_d^2, and the geoid height differences h_{IJ} and h_{JK} are:

$$h_{IJ} = \tfrac{1}{2}s(d_I + d_J) \quad \text{and}$$

$$h_{JK} = \tfrac{1}{2}s(d_J + d_K)$$

where s is the distance between I and J.

The variances of h_{IJ} and h_{JK} and covariance between them are:

$$\sigma_{hIJ}^2 = \sigma_{hJK}^2 = \tfrac{1}{2}s^2\sigma_d^2$$

$$\sigma_{hIhJ} = \tfrac{1}{4}s^2\sigma_d^2 = \tfrac{1}{2}\sigma_{hIJ}^2$$

The above formulae when revised to take account of the covariance between computed geoid height differences are below.

$$\sigma_Z^2 = \sigma_Y^2 + \tfrac{1}{2}s^2\sigma_d^2$$

$$\sigma_Z^2 = \sigma_X^2 + \tfrac{1}{2}s^2\sigma_d^2$$

$$r_{ze} = \frac{\sigma_X^2 + \tfrac{1}{2}s^2\sigma_d^2}{\sigma_X^2 + \sigma_Y^2 + s^2\sigma_d^2}$$

$$r_{zn} = \frac{\sigma_Y^2 + \tfrac{1}{2}s^2\sigma_d^2}{\sigma_X^2 + \sigma_Y^2 + s^2\sigma_d^2}$$

$$Z = r_{ze}(Y + \tfrac{1}{2}s(d_{Ye} + d_{Ze})) + r_{zn}(X + \tfrac{1}{2}s(d_{Xn} + d_{Zn}))$$

where d_{Ye} is the deviation at Y in the east-west direction, etc.

In Figure 9.13, below, if the point of U is to the west of Y and the point of V is south of X, then X and Y will have already been found from:

$$X = r_{xe}(W + \tfrac{1}{2}s(d_{We} + d_{Xe})) + r_{xn}(V + \tfrac{1}{2}s(d_{Vn} + d_{Xn}))$$

$$Y = r_{ye}(U + \tfrac{1}{2}s(d_{Ue} + d_{Ye})) + r_{yn}(W + \tfrac{1}{2}s(d_{Wn} + d_{Yn}))$$

so:

$$\sigma_{XY} = r_{yn}r_{xe}\sigma_W^2$$

ignoring covariance terms, and similarly

$$\sigma_{UW} = r_{wn}r_{ue}\sigma_S^2$$

$$\sigma_{WV} = r_{vn}r_{we}\sigma_T^2$$

The covariance σ_{UV}, which is more complex to calculate will be smaller and for the purpose of this computation is assumed 0.

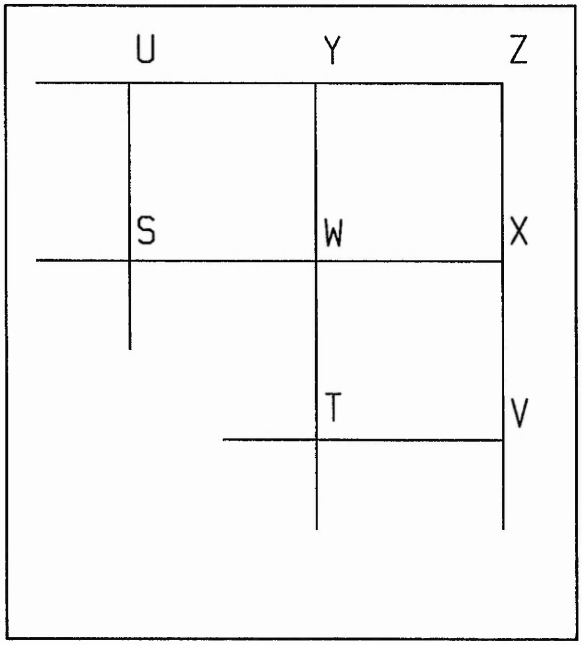

Figure 9.13 Diagram to show stations leading to Z in a Progressive Nodes form.

S and T are the geoid heights west and south of W respectively. Substituting for X and Y into Z gives:

$$\begin{aligned} Z &= r_{ze}(r_{ye}(U + \tfrac{1}{2}s(d_{Ue} + d_{Ye})) + r_{yn}(W + \tfrac{1}{2}s(d_{Wn} + d_{Yn})) + \tfrac{1}{2}s(d_{Ye} + d_{Ze})) \\ &\quad + r_{zn}(r_{xe}(W + \tfrac{1}{2}s(d_{We} + d_{Xe})) + r_{xn}(V + \tfrac{1}{2}s(d_{Vn} + d_{Xn})) + \tfrac{1}{2}s(d_{Xn} + d_{Zn})) \\ &= r_{ze}r_{ye}U + (r_{ze}r_{yn} + r_{zn}r_{xe})W + r_{zn}r_{xn}V \\ &\quad + \tfrac{1}{2}s\{r_{ze}[r_{ye}d_{Ue} + (1 + r_{ye})d_{Ye} + r_{yn}(d_{Wn} + d_{Yn}) + d_{Ze}] \\ &\quad + r_{zn}[r_{xe}(d_{We} + d_{Xe}) + r_{xn}d_{Vn} + (1 + r_{xn})d_{Xn} + d_{Zn}]\} \end{aligned}$$

The now more complete variance of Z may be derived as follows.

$$\begin{aligned} \sigma_Z^2 &= r_{ze}^2r_{ye}^2\sigma_U^2 + (r_{ze}r_{yn} + r_{zn}r_{xe})^2\sigma_W^2 + r_{zn}^2r_{xn}^2\sigma_V^2 \\ &\quad + \tfrac{1}{2}s^2\{r_{ze}^2[r_{ye}^2 + 1 + r_{ye} + 2r_{yn}^2] + r_{zn}^2[r_{xn}^2 + 1 + r_{xn} + 2r_{xe}^2]\}\sigma_d^2 \\ &\quad + 2(r_{ze}r_{yn} + r_{zn}r_{xe})(r_{ze}r_{ye}r_{wn}r_{ue}\sigma_S^2 + r_{zn}r_{xn}r_{vn}r_{we}\sigma_T^2) + (0) \end{aligned}$$

The (0) term represents terms that have been ignored and are assumed zero. In fact, they contain covariances between S and T etc. and are likely to be positive. Therefore, the value of σ_Z^2, but not Z will be underestimated. To compensate, the numerical coefficient of the penultimate term in the above equation is changed from 2 to 3 for the practical work as described below.

The east-then-north-and-north-then-east method of geoid determination was numerically compared with the progressive nodes approach to determine how much better a solution could be obtained from the progressive nodes model.

In the following, eight different estimates of geoid height were derived; four based on east-then-north-and-north-then-east models and four based upon progressive nodes models. Each determination was based on the same 300 pairs of deviation data sets derived from original 101 by 101 grids of north-south and east-west deviations of the mountains model with 500 metre inter-station distances and with a 3" "random error"

East-then-north-and-north-then-east models

1 East then north.

The geoid height of the northeast corner is derived from a conventional line of astrogeodetic levelling from the southwest corner of the block to the southeast corner then to the northeast corner.

2 North then east.

As model 1 but via the northwest corner.

3 Mean of southwest to centre.

The geoid height of the centre of the block is derived from the mean of two lines of astrogeodetic levelling, both starting at the south-west corner and ending at the centre of the block, co-ordinates (5000, 5000) metres, similar to the routes 1 and 2 above. One goes east then north, the other, north then east.

4 Mean of southwest to northeast to centre.

The mean geoid height of the northeast corner from 1 and 2 above is accepted. Then from the north-east corner two lines of astrogeodetic levelling, both ending at the centre of the block, co-ordinates (5000, 5000) metres, run respectively via points

(10000, 5000) and (5000, 10000). The mean geoid height is taken.

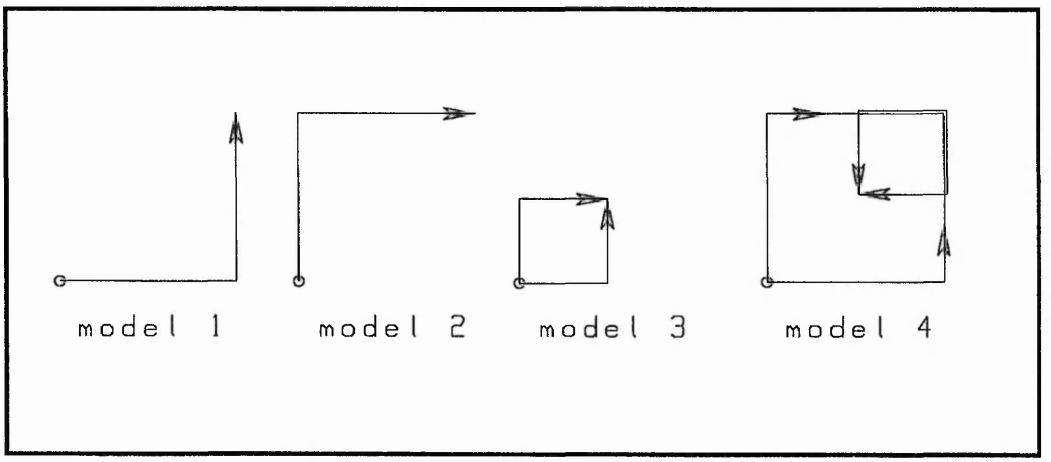

Figure 9.14 Diagram to show astrogeodetic models 1 to 4.

Progressive nodes models

5 Southwest to northeast.

The geoid height of the northeast corner is computed from the southwest corner.

6 Northeast to southwest.

The geoid height of the southwest corner is computed from the northeast corner.

7 Southwest to centre.

The geoid height of the centre (5000, 5000) is computed from the southwest corner.

8 Southwest to northeast to centre.

The geoid height of the centre (5000, 5000) is computed from the northeast corner. The geoid height of the northeast corner is taken from model 5 above.

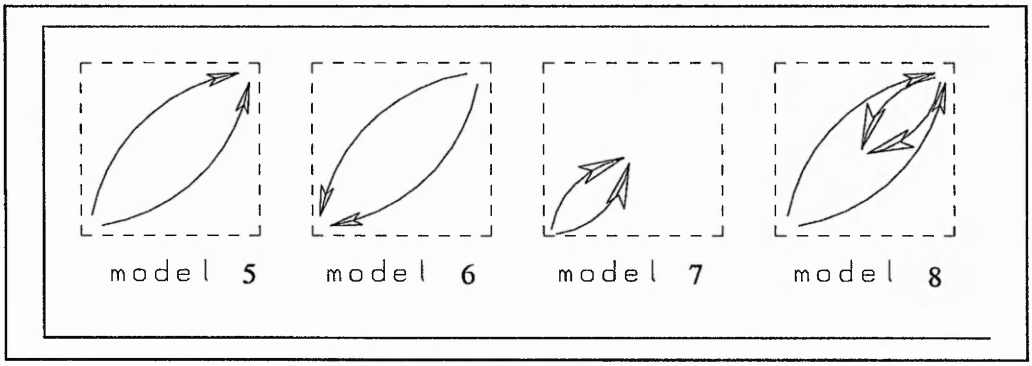

Figure 9.15 Diagram to show astrogeodetic models 5 to 8.

The results are in Table 9.24 below. All units are metres.

Table 9.24 Comparison of the east-then-north-and-north-then-east method with the progressive nodes method of geoid determination.

model	1	2	3	4	5	6	7	8
Mean geoid height	0.083828	0.083893	0.237670	0.237831	0.083348	0.083307	0.237492	0.237477
σ	0.005915	0.005669	0.002811	0.004264	0.001334	0.001299	0.001102	0.001111
σ of mean	0.000339	0.000325	0.000161	0.000245	0.000077	0.000075	0.000063	0.000064

The statistics relating to appropriate differences in the models are in Table 9.25 below.

Table 9.25 Statistics relating to the differences in the models in Table 9.24.

model	1 - 2	3 - 4	5 - 6	7 - 8
mean	-0.000066	-0.000160	0.000041	0.000016
σ	0.008099	0.004291	0.001021	0.000921
σ of mean	0.000464	0.000246	0.000059	0.000053

In the following section, statistics taken from the above two tables are quoted as printed. This is to aid reference to the tables and does not indicate that the statistics concerned are valid to the number of places of decimal quoted.

From the above it is clear that models 1 and 2 should produce the same answer. In both models the geoid height of the north-east corner depends upon an astrogeodetic

levelling line of 200 legs each of 100 metres with standard errors of 0".86. Thus the expected difference of geoid height from the two routes would be:

$$0.86\ 206265^{-1}\ 200^{½}\ 100\ 2^{½} \quad = \quad 0.00834 \text{ metres}$$

This is similar to the differences of the models 1 and 2 value, 0.008099 metres in the table above and suggests that the spreadsheets involved have been written correctly.

Models 3 and 4 are alternative routes to the centre of the block. The standard error of the difference of the routes, at 0.004291 metres, indicates that if the mean of the two results is taken then its own standard error will be 0.0030 metres.

Models 5 and 6 give relative geoid heights of opposite corners by working through the block from opposite corners. As such, they should give the same results. If the geoid heights had been derived from a least squares adjustment of the whole data set then there would be no difference between the solutions. The actual difference between the solutions therefore indicates the limitations of the progressive nodes approach. The standard error of the difference of the solutions at 0.001021 metres indicates that if the mean of the two results is taken then its own standard error will be 0.00072 metres. This is approximately a fourfold improvement over the equivalent models 1 and 2 solution. The equivalent least squares solution would contain 10200 unknowns and 20402 observation equations. As such it would be well beyond the capability of the major commercial least squares survey package Star*Net. See Annex E of the Star*Net manual (Star*Net, 1991).

Models 7 and 8 are alternative processes for finding the geoid height of the centre of the block. The standard error of the difference processes, at 0.000921 metres, indicates that if the mean of the two results is taken then its own standard error will be 0.00065 metres. If this process may be considered as equivalent to the models 3 and 4 approach then this process also shows a better than fourfold improvement over the conventional computation of astrogeodetic levelling.

9.8 Summary

Astrogeodetic deviations as described in theoretical terms in Chapter 4 with the practical procedures of Chapter 6 and small corrections described in Chapters 7 and 8 may now be used to find the form of the geoid. In this chapter the astrogeodetic geoid model was reviewed in terms of the density of observations and Kaula's rule of thumb. Starting with a consideration of the effect of a hemispherical mountain on the deviation of the vertical, a geoid model simulation was constructed with four different models.

The route from deviation data to geoid model was considered in terms of polynomial coefficients, interpolation of deviations and progressive nodes. The overall conclusion is that although polynomial coefficients, derived from a least squares treatment of deviation observations, should theoretically produce the most rigorous solution for the form of the geoid, a more practical solution may be to use the technique of progressive nodes described in this chapter. This is because least squares solutions for the solution of large sets of polynomial coefficients are vulnerable to the accumulation of rounding errors and a tendency for "noise" to be modelled as "signal".

In the next chapter a practical exercise is described to show how a determination of astronomical position can be made.

Chapter 10

A Practical Determination of Astronomical Position

10.1 Introduction

To show that the process described in earlier chapters, especially Chapter 6, would produce useful results, a determination of the deviation of the vertical at a site in Nottinghamshire was undertaken; the date for this was 20 July 2000. The video camera method, described in Section 6.6, was used with a Pulnix black and white camera mounted on the telescope of a Wild T2000 electronic theodolite. The intermediate results, described in Section 10.2 below, are presented according to the aide memoire of Section 6.9.1. The elements from the aide memoire are in red.

10.2 Intermediate results - preparation

a. *Predictions*

Estimate WGS84 position with handheld GPS.

Latitude: N 53° 4' 46".0 Longitude: W 1° 10' 15".9

In UK only, find slope of the geoid from Grid InQuest, (2001)

-2".2 17".5

Apply slope to WGS84 position to find an estimate of the astronomical position.

Latitude: N 53° 4' 44" Longitude: W 1° 9' 58"

Select start date and time for observations.

GMT 20:45

Use spreadsheets:

"MCBJ2000.xls" to update star data and find a suitable star set.

"PREDICT.xls" to identify Polaris, orient horizontal circle, prepare and print observing programme.

Time GMT	Zenith	Az
HH.MMSS	DD.MMSS	DD.MMSS
20.4500	37.3241	0.3733
20.4800	37.3223	0.3822
20.5100	37.3205	0.3911
20.5400	37.3146	0.4000
20.5700	37.3127	0.4048
21.0000	37.3108	0.4135
21.0300	37.3048	0.4223
21.0600	37.3028	0.4310
21.0900	37.3007	0.4356
21.1200	37.2946	0.4442
21.1500	37.2925	0.4528
21.1800	37.2903	0.4613
21.2100	37.2841	0.4658
21.2400	37.2819	0.4742
21.2700	37.2756	0.4826
21.3000	37.2733	0.4909
21.3300	37.2709	0.4952
21.3600	37.2646	0.5034
21.3900	37.2622	0.5116
21.4200	37.2557	0.5157
21.4500	37.2532	0.5238
21.4800	37.2507	0.5318
21.5100	37.2442	0.5357
21.5400	37.2416	0.5437
21.5700	37.2350	0.5515
22.0000	37.2324	0.5553
22.0300	37.2258	0.5631
22.0600	37.2231	0.5708
22.0900	37.2203	0.5744
22.1200	37.2136	0.5820
22.1500	37.2108	0.5855
22.1800	37.2040	0.5930
22.2100	37.2012	1.0004
22.2400	37.1944	1.0037
22.2700	37.1915	1.0110
22.3000	37.1846	1.0142
22.3300	37.1816	1.0213
22.3600	37.1747	1.0244
22.3900	37.1717	1.0315
22.4200	37.1647	1.0344
22.4500	37.1617	1.0413
22.4800	37.1546	1.0442
22.5100	37.1516	1.0509
22.5400	37.1445	1.0536
22.5700	37.1414	1.0603
23.0000	37.1342	1.0629

Figure 10.1 Polaris prediction programme for 20 July 2000.

Star/mag No	RA HH.MMSSs	Declination DD.MMSS	Time GMT HH.MMSSs	Zenith DD.MMSS	Az DD.MMSS	star passage across screen
1432001403.0	14.3205455	38.1843217	21.0600	28.5147	253.5931	1.05
1347010101.9	13.4732772	49.1902433	21.0800	29.4010	282.2427	1.08
1524016203.3	15.2456903	58.5815125	21.1000	14.3351	303.2654	0.90
1404005803.7	14.0423525	64.2250135	21.1200	25.0547	314.1524	0.79
1623015602.7	16.2401246	61.3108049	21.1400	10.0427	330.5930	0.50
1520012103.0	15.2044863	71.5020650	21.1600	22.0045	338.1124	0.40
1948004803.8	19.4814540	70.1611702	21.1800	24.4226	31.0827	-0.59
2118012402.5	21.1838179	62.3509627	21.2000	32.5023	48.2935	-0.85
1917002203.8	19.1708839	53.2216383	21.2200	18.2424	76.3908	-1.12
2041009501.3	20.4128440	45.1655022	21.2400	33.4844	82.0308	-1.12
1944020902.9	19.4500952	45.0759670	21.2600	25.0812	93.2402	-1.14
1756012702.2	17.5638602	51.2933502	21.2800	5.5618	101.5412	-1.20
1858022903.3	18.5858780	32.4133053	21.3200	26.3755	130.2438	-0.88
1823013003.9	18.2343894	21.4621676	21.3400	33.1418	154.4141	-0.51
1630002802.8	16.3014752	21.2933380	21.3600	33.2428	204.3504	0.43
1642013703.5	16.4255404	38.5534074	21.3800	16.1332	213.5953	0.58
1542009903.8	15.4245852	26.1755819	21.4000	33.3124	227.4332	0.80
1527013603.7	15.2750918	29.0632599	21.4200	33.0851	236.1315	0.91
1515007203.5	15.1531270	33.1906221	21.4400	31.4207	245.3321	0.99
1501014003.5	15.0157744	40.2340299	21.4600	28.5956	259.5526	1.08
1524016203.3	15.2456903	58.5815125	21.4800	19.2516	301.0357	0.94
1404005803.7	14.0423525	64.2250135	21.5000	29.1235	314.0559	0.79
1520012103.0	15.2044863	71.5020650	21.5200	24.1356	333.4744	0.48
1912012403.1	19.1236936	67.3951233	21.5400	17.5558	27.2250	-0.53
2128012203.2	21.2843967	70.3338404	21.5600	29.4913	33.2612	-0.62
2118012402.5	21.1838179	62.3509627	21.5800	28.3037	49.4813	-0.86
1917002203.8	19.1708839	53.2216383	22.0000	12.4816	80.0923	-1.15
1929016503.8	19.2945002	51.4356519	22.0200	14.4204	85.3642	-1.16
2022005902.2	20.2216099	40.1531291	22.0400	27.5159	102.2810	-1.11
1858022903.3	18.5858780	32.4133053	22.0800	23.0118	146.2403	-0.66
1836020600.0	18.3658512	38.4713053	22.1000	15.3254	153.1609	-0.56
1715000503.1	17.1503669	24.5032579	22.1200	29.3909	202.3340	0.40
1739009503.8	17.3929913	46.0036497	22.1400	8.1222	213.1507	0.53
1641004802.9	16.4118744	31.3622852	22.1600	26.2906	224.2630	0.75
1642013703.5	16.4255404	38.5534074	22.1800	20.2805	235.0008	0.88
1730008502.8	17.3028054	52.1819428	22.2000	6.1353	267.0630	0.99
1524016203.3	15.2456903	58.5815125	22.2200	23.4836	301.1205	0.94
1623015602.7	16.2401246	61.3108049	22.2400	17.0246	310.3949	0.82
1753012503.7	17.5334113	56.5235392	22.2600	5.0554	320.3938	0.60
1520012103.0	15.2044863	71.5020650	22.2800	26.4532	330.5604	0.54
1948004803.8	19.4814540	70.1611702	22.3000	19.4711	21.4213	-0.43
2128012203.2	21.2843967	70.3338404	22.3200	26.5241	32.1230	-0.60
2249009903.5	22.4944230	66.1156180	22.3400	33.5511	41.2412	-0.74
2118012402.5	21.1838179	62.3509627	22.3600	24.0749	49.5809	-0.87
2210015903.3	22.1054224	58.1203142	22.3800	30.4512	58.0036	-0.96
1917002203.8	19.1708839	53.2216383	22.4000	6.5049	83.0723	-1.20
1929016503.8	19.2945002	51.4356519	22.4200	8.4105	93.2246	-1.19
2114015003.7	21.1449829	38.0248417	22.4400	31.0815	102.3929	-1.11
2022005902.2	20.2216099	40.1531291	22.4600	21.5300	115.1843	-1.04

Figure 10.2 Star prediction observing programme for 20 July 2000.

10.3 Intermediate results – data collection

b. *Prepare T2000 and data recording system*

c. *Collect data*

Time GMT HH.MMSS	Observed Zenith DD.MMSSs
21.0600	start
21.0800	
21.1000	14.33551
21.1200	25.05470
21.1400	10.04261
21.1600	22.00473
21.1800	24.42242
21.2000	32.50264
21.2200	18.24276
21.2400	33.49014
21.2600	25.08178
21.2800	5.56174
21.3000	light on
21.3200	26.37583
21.3400	33.14171
21.3600	33.24377
21.3800	16.13318
21.4000	33.31240
21.4200	33.08519
21.4400	31.42052
21.4600	28.59570
21.4800	19.25133
21.5000	29.12378
21.5200	24.13568
21.5400	17.55563
21.5600	29.49116
21.5800	28.30384
22.0000	12.48170
22.0200	14.42082
22.0400	27.51588
22.0600	light on
22.0800	23.01172
22.1000	15.32520
22.1200	29.39074
22.1400	8.12231
22.1600	26.29080
22.1800	20.28033
22.2000	6.13563
22.2200	23.48382
22.2400	17.02447
22.2600	5.05568
22.2800	26.45338
22.3000	19.47120
22.3200	26.52418
22.3400	33.55133
22.3600	24.07470
22.3800	30.45118

22.4000	6.50429
22.4200	8.41068
22.4400	31.08170
22.4600	21.53010
22.4800	light on

Figure 10.3 Observed zenith angles. 20 July 2000.

10.4 Intermediate results – data processing

d. *Compute data*

Open saved file as a spreadsheet in Excel

Figures 10.4 to 10.7 illustrate fragments of the data.

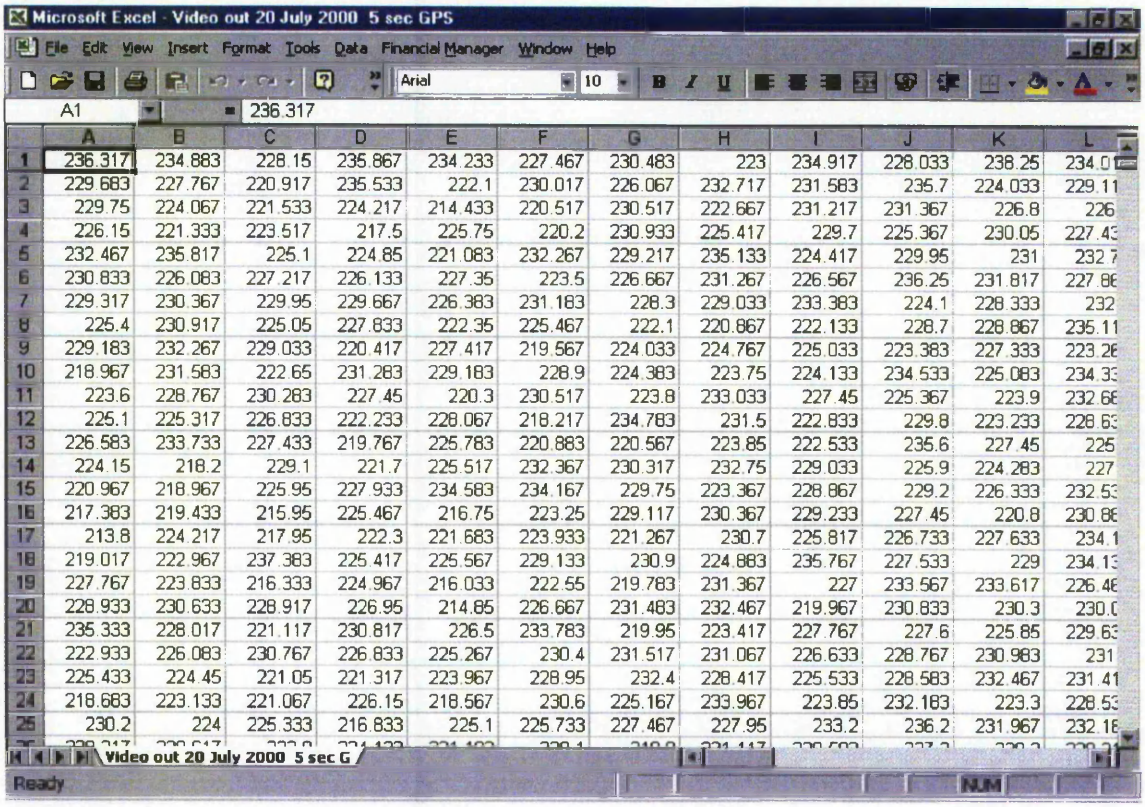

	A	B	C	D	E	F	G	H	I	J	K	L
1	236.317	234.883	228.15	235.867	234.233	227.467	230.483	223	234.917	228.033	238.25	234.0
2	229.683	227.767	220.917	235.533	222.1	230.017	226.067	232.717	231.583	235.7	224.033	229.11
3	229.75	224.067	221.533	224.217	214.433	220.517	230.517	222.667	231.217	231.367	226.8	226
4	226.15	221.333	223.517	217.5	225.75	220.2	230.933	225.417	229.7	225.367	230.05	227.43
5	232.467	235.817	225.1	224.85	221.083	232.267	229.217	235.133	224.417	229.95	231	232.7
6	230.833	226.083	227.217	226.133	227.35	223.5	226.667	231.267	226.567	236.25	231.817	227.86
7	229.317	230.367	229.95	229.667	226.383	231.183	228.3	229.033	233.383	224.1	228.333	232
8	225.4	230.917	225.05	227.833	222.35	225.467	222.1	220.867	222.133	228.7	228.867	235.11
9	229.183	232.267	229.033	220.417	227.417	219.567	224.033	224.767	225.033	223.383	227.333	223.26
10	218.967	231.583	222.65	231.283	229.183	228.9	224.383	223.75	224.133	234.533	225.083	234.33
11	223.6	228.767	230.283	227.45	220.3	230.517	223.8	233.033	227.45	225.367	223.9	232.68
12	225.1	225.317	226.833	222.233	228.067	218.217	234.783	231.5	222.833	229.8	223.233	228.63
13	226.583	233.733	227.433	219.767	225.783	220.883	220.567	223.85	222.533	235.6	227.45	225
14	224.15	218.2	229.1	221.7	225.517	232.367	230.317	232.75	229.033	225.9	224.283	227
15	220.967	218.967	225.95	227.933	234.583	234.167	229.75	223.367	228.867	229.2	226.333	232.53
16	217.383	219.433	215.95	225.467	216.75	223.25	229.117	230.367	229.233	227.45	220.8	230.86
17	213.8	224.217	217.95	222.3	221.683	223.933	221.267	230.7	225.817	226.733	227.633	234.1
18	219.017	222.967	237.383	225.417	225.567	229.133	230.9	224.883	235.767	227.533	229	234.13
19	227.767	223.833	216.333	224.967	216.033	222.55	219.783	231.367	227	233.567	233.617	226.48
20	228.933	230.633	228.917	226.95	214.85	226.667	231.483	232.467	219.967	230.833	230.3	230.0
21	235.333	228.017	221.117	230.817	226.5	233.783	219.95	223.417	227.767	227.6	225.85	229.63
22	222.933	226.083	230.767	226.833	225.267	230.4	231.517	231.067	226.633	228.767	230.983	231
23	225.433	224.45	221.05	221.317	223.967	228.95	232.4	228.417	225.533	228.583	232.467	231.41
24	218.683	223.133	221.067	226.15	218.567	230.6	225.167	233.967	223.85	232.183	223.3	228.53
25	230.2	224	225.333	216.833	225.1	225.733	227.467	227.95	233.2	236.2	231.967	232.18

Figure 10.4 Screen plot of segment of video data, LED for crosshair illumination. 20 July 2000.

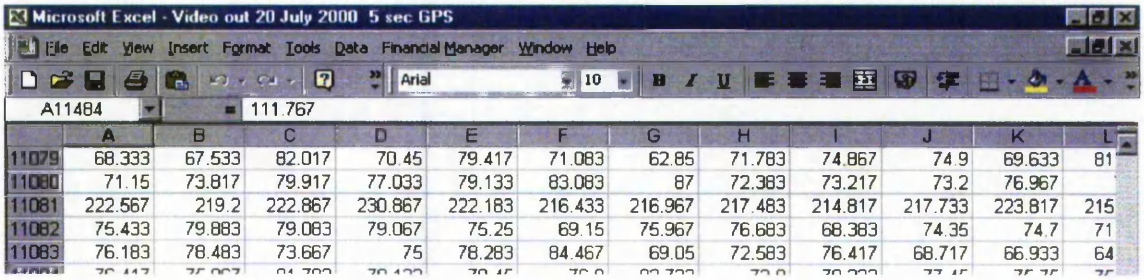

	A	B	C	D	E	F	G	H	I	J	K	L
11079	68.333	67.533	82.017	70.45	79.417	71.083	62.85	71.783	74.867	74.9	69.633	81
11080	71.15	73.817	79.917	77.033	79.133	83.083	87	72.383	73.217	73.2	76.967	
11081	222.567	219.2	222.867	230.867	222.183	216.433	216.967	217.483	214.817	217.733	223.817	215
11082	75.433	79.883	79.083	79.067	75.25	69.15	75.967	76.683	68.383	74.35	74.7	71
11083	76.183	78.483	73.667	75	78.283	84.467	69.05	72.583	76.417	68.717	66.933	64

Figure 10.5 Partial Screen plot of segment of video data with a GPS flash at row 11081, LED for crosshair illumination off. 20 July 2000.

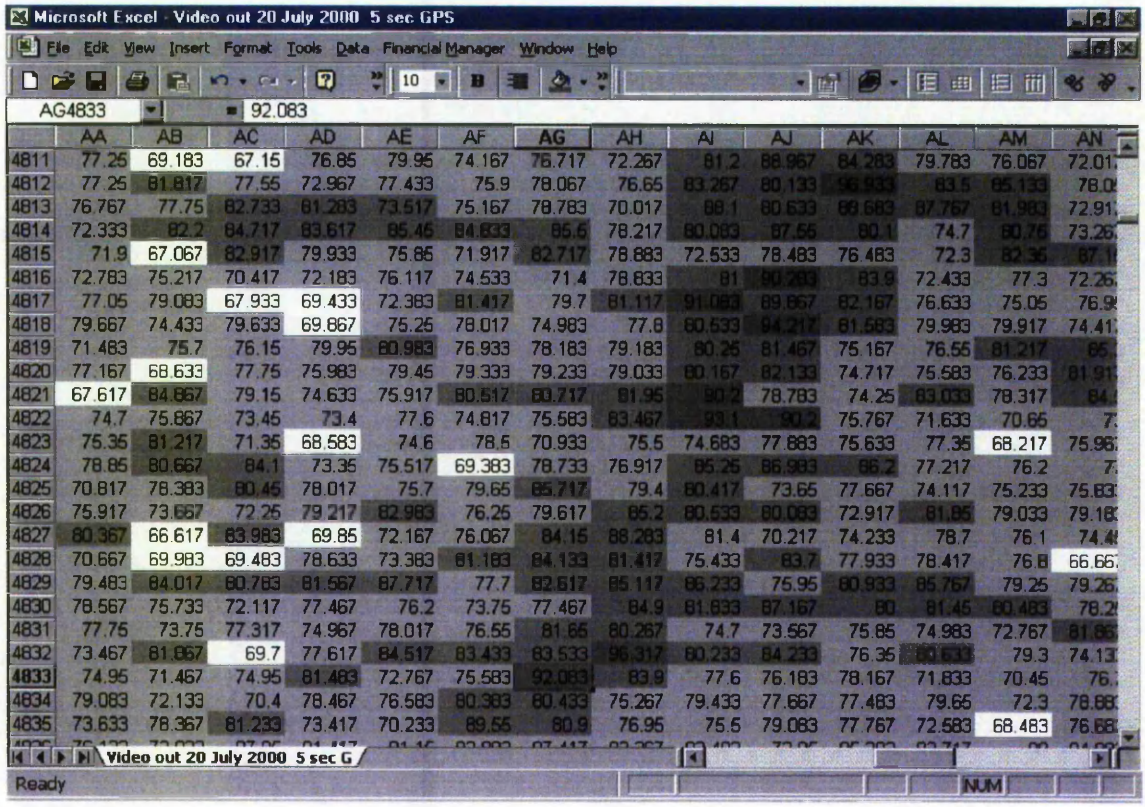

	AA	AB	AC	AD	AE	AF	AG	AH	AI	AJ	AK	AL	AM	AN
4811	77.25	69.183	67.15	76.85	79.95	74.167	76.717	72.267	81.2	88.967	84.283	79.783	76.067	72.01
4812	77.25	81.817	77.55	72.967	77.433	75.9	78.067	76.65	83.267	80.133	96.933	83.5	85.133	78.0
4813	76.767	77.75	82.733	81.283	73.517	75.167	78.783	70.017	88.1	80.633	89.683	87.767	81.983	72.91
4814	72.333	82.2	84.717	83.617	85.45	84.833	85.6	78.217	80.083	87.55	80.1	74.7	80.76	73.26
4815	71.9	67.067	82.917	79.933	75.85	71.917	82.717	78.883	72.533	78.483	76.483	72.3	82.35	87.1
4816	72.783	75.217	70.417	72.183	76.117	74.533	71.4	78.833	81	80.283	83.9	72.433	77.3	72.26
4817	77.05	79.083	67.933	69.433	72.383	81.417	79.7	81.117	91.083	89.867	82.167	76.633	75.05	76.9
4818	79.667	74.433	79.633	69.867	75.25	78.017	74.983	77.8	80.533	94.217	81.583	79.983	79.917	74.41
4819	71.483	75.7	76.15	79.95	80.983	76.933	78.183	79.183	80.25	81.467	75.167	76.55	81.217	65.
4820	77.167	68.633	77.75	75.983	79.45	79.333	79.233	79.033	80.167	82.133	74.717	75.583	76.233	81.91
4821	67.617	84.867	79.15	74.633	75.917	80.517	80.717	81.95	80.2	78.783	74.25	83.033	78.317	84.
4822	74.7	75.867	73.45	73.4	77.6	74.817	75.583	83.467	93.1	90.2	75.767	71.633	70.65	7
4823	75.35	81.217	71.35	68.583	74.6	78.5	70.933	75.5	74.683	77.883	75.633	77.35	68.217	75.96
4824	78.85	80.667	84.1	73.35	75.517	69.383	78.733	76.917	85.25	86.983	86.2	77.217	76.2	7
4825	70.817	78.383	80.45	78.017	75.7	79.65	85.717	79.4	80.417	73.65	77.667	74.117	75.233	75.83
4826	75.917	73.667	72.25	79.217	82.983	76.25	79.617	85.2	80.533	80.083	72.917	81.85	79.033	79.18
4827	80.367	66.617	83.983	69.85	72.167	76.067	84.15	88.283	81.4	70.217	74.233	78.7	76.1	74.4
4828	70.667	69.983	69.483	78.633	73.383	81.183	84.133	81.417	75.433	83.7	77.933	78.417	76.8	66.66
4829	79.483	84.017	80.783	81.567	87.717	77.7	82.617	85.117	86.233	75.95	80.933	85.767	79.25	79.26
4830	78.567	75.733	72.117	77.467	76.2	73.75	77.467	84.9	81.633	87.167	80	81.45	80.483	78.2
4831	77.75	73.75	77.317	74.967	78.017	76.55	81.65	80.267	74.7	73.567	75.85	74.983	72.767	81.65
4832	73.467	81.867	69.7	77.617	84.517	83.433	83.533	96.317	80.233	84.233	76.35	80.633	79.3	74.13
4833	74.95	71.467	74.95	81.483	72.767	75.583	92.083	83.9	77.6	76.183	78.167	71.833	70.45	76.
4834	79.083	72.133	70.4	78.467	76.583	80.383	80.433	75.267	79.433	77.667	77.483	79.65	72.3	78.68
4835	73.633	78.367	81.233	73.417	70.233	89.55	80.9	76.95	75.5	79.083	77.767	72.583	68.483	76.68

Figure 10.6 Screen plot of typical video data with shading to highlight values. 20 July 2000.

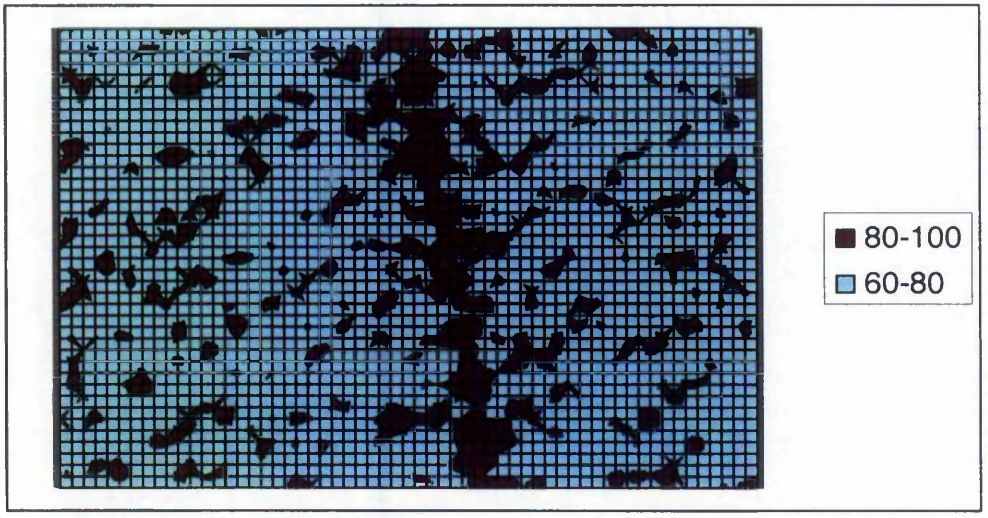

Figure 10.7 Graphical plot of the video data on and surrounding Figure 10.6 with 41 frames (along vertical axis) by 60 rows (along horizontal axis) with video row mean pixel values in the range 60-80 and 80-100. 20 July 2000.

Copy data to spreadsheet "Convert video time to GPS time". Follow on-screen instructions. Output is a set of parameters to convert frame number to GPS time.

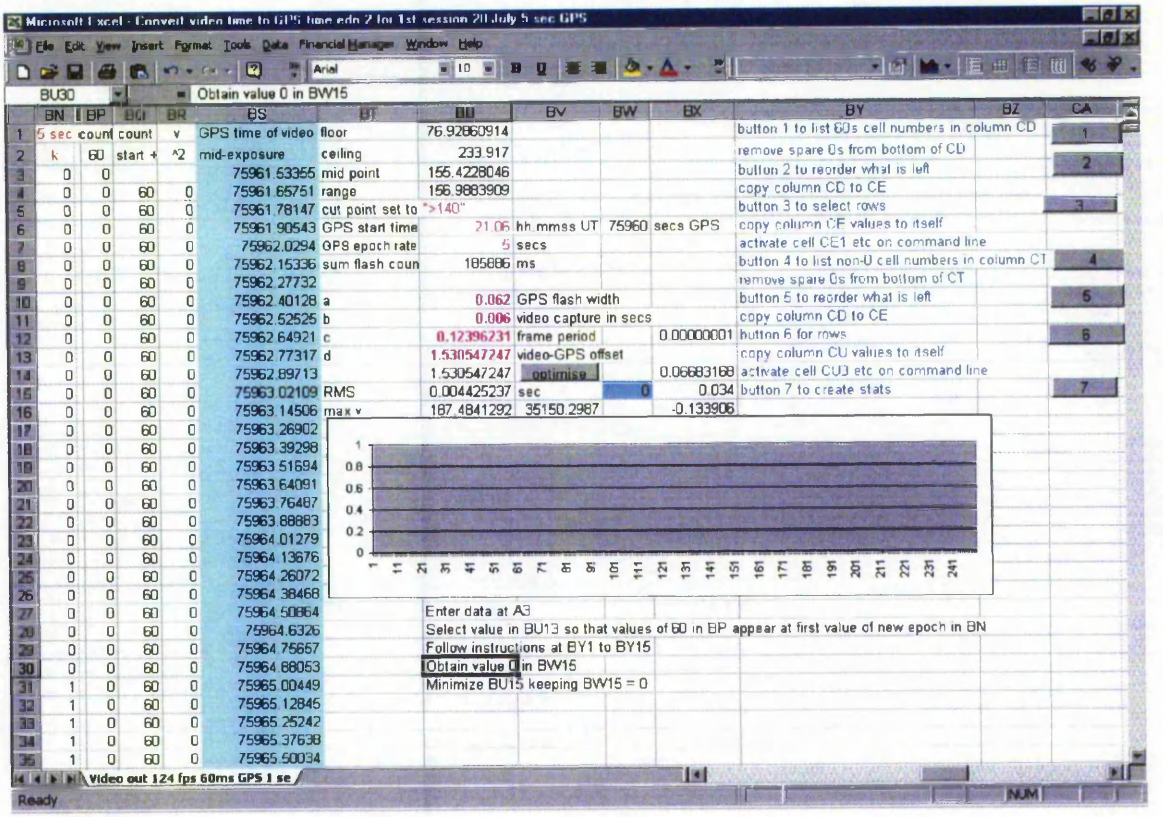

Figure 10.8 Detail of the spreadsheet "Convert video time to GPS time" showing elements of operating instruction. 20 July 2000.

In Figure 10.8, video data has been entered and occupies the block A3:BH29436. The parameters in pink are adjusted until there are no spikes in the graph. Instructions at cell BU27 and below are followed. Instructions at cell BY1 and below, including the seven macros activated by the buttons in column CA, are followed. Then the time of video frame exposure, excluding those frames when the crosshair illumination is on, are displayed near the top of the columns CN and CV. Column CN lists the row numbers and column CV lists the associated GPS times of the video exposure. A detail of the relevant part of the spreadsheet is shown in Figure 10.9 below.

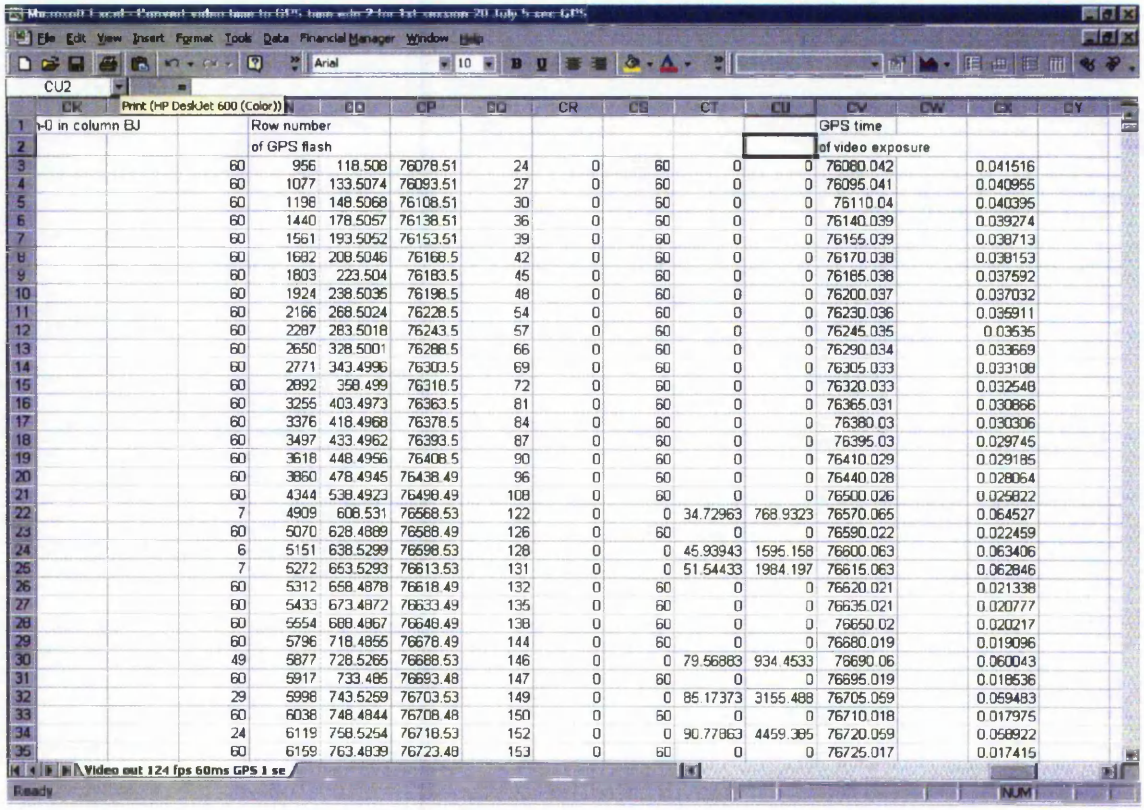

	CK			CO	CP	CQ	CR	CS	CT	CU	CV	CW	CX	CY
1	=0 in column BJ			Row number							GPS time			
2				of GPS flash							of video exposure			
3			60	956	118.508	76078.51	24	0	60	0	0	76080.042		0.041516
4			60	1077	133.5074	76093.51	27	0	60	0	0	76095.041		0.040955
5			60	1198	148.5068	76108.51	30	0	60	0	0	76110.04		0.040395
6			60	1440	178.5057	76138.51	36	0	60	0	0	76140.039		0.039274
7			60	1561	193.5052	76153.51	39	0	60	0	0	76155.039		0.038713
8			60	1682	208.5046	76168.5	42	0	60	0	0	76170.038		0.038153
9			60	1803	223.504	76183.5	45	0	60	0	0	76185.038		0.037592
10			60	1924	238.5035	76198.5	48	0	60	0	0	76200.037		0.037032
11			60	2166	268.5024	76228.5	54	0	60	0	0	76230.036		0.035911
12			60	2287	283.5018	76243.5	57	0	60	0	0	76245.035		0.03535
13			60	2650	328.5001	76288.5	66	0	60	0	0	76290.034		0.033669
14			60	2771	343.4996	76303.5	69	0	60	0	0	76305.033		0.033108
15			60	2892	358.499	76318.5	72	0	60	0	0	76320.033		0.032548
16			60	3255	403.4973	76363.5	81	0	60	0	0	76365.031		0.030866
17			60	3376	418.4968	76378.5	84	0	60	0	0	76380.03		0.030306
18			60	3497	433.4962	76393.5	87	0	60	0	0	76395.03		0.029745
19			60	3618	448.4956	76408.5	90	0	60	0	0	76410.029		0.029185
20			60	3860	478.4945	76438.49	96	0	60	0	0	76440.028		0.028064
21			60	4344	538.4923	76498.49	108	0	60	0	0	76500.026		0.025822
22			7	4909	608.531	76568.53	122	0	0	34.72963	768.9323	76570.065		0.064527
23			60	5070	628.4889	76588.49	126	0	60	0	0	76590.022		0.022459
24			6	5151	638.5299	76598.53	128	0	0	45.93943	1595.158	76600.063		0.063406
25			7	5272	653.5293	76613.53	131	0	0	51.54433	1984.197	76615.063		0.062846
26			60	5312	658.4878	76618.49	132	0	60	0	0	76620.021		0.021338
27			60	5433	673.4872	76633.49	135	0	60	0	0	76635.021		0.020777
28			60	5554	688.4867	76648.49	138	0	60	0	0	76650.02		0.020217
29			60	5796	718.4855	76678.49	144	0	60	0	0	76680.019		0.019096
30			49	5877	728.5265	76688.53	146	0	0	79.56883	934.4533	76690.06		0.060043
31			60	5917	733.485	76693.48	147	0	60	0	0	76695.019		0.018536
32			29	5998	743.5259	76703.53	149	0	0	85.17373	3155.488	76705.059		0.059483
33			60	6038	748.4844	76708.48	150	0	60	0	0	76710.018		0.017975
34			24	6119	758.5254	76718.53	152	0	0	90.77863	4459.385	76720.059		0.058922
35			60	6159	763.4839	76723.48	153	0	60	0	0	76725.017		0.017415

Figure 10.9 Detail of the spreadsheet "Convert video time to GPS time" showing output results . 20 July 2000.

Select data when external cross hair illumination is "on" and import to spreadsheet "equation of motion of star on screen 5 parameter.xls". Output is picture row value for the crosshair. Compute for all similar data sets.

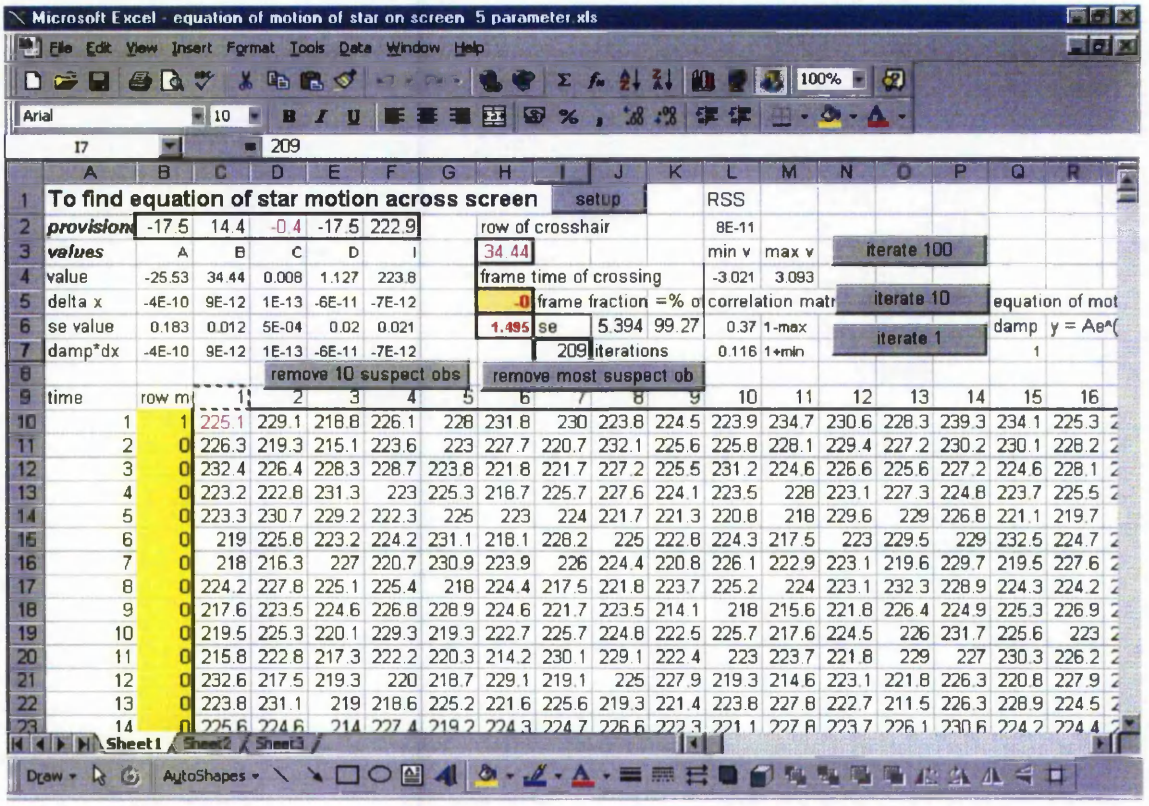

Figure 10.10 Detail of the spreadsheet "equation of motion of star on screen 5 parameter" showing output results . 20 July 2000.

In Figure 10.10, a block of data, 41 rows by 60 columns, is entered at cell C10. The spreadsheet suggests provisional values for the parameters to be solved for in cells B2-F2, less cell D2 that represents the slope of star across the screen, and is taken from the prediction spreadsheet. When using this spreadsheet to find the position of the crosshair as in Figure 10.10, D2 is close to zero. There are macros to calculate provisional values, perform iterations of the least squares solution and to remove suspect observations. Suspect observations are selected on the basis of absolute magnitude divided by the reference variance. In the data shown in Figure 10.10, the centre of the crosshair is at row 34.44. A graphical plot of the input data relating to the solution in Figure 10.10 and a graphical plot showing the locations of the removed data are in Figures 10.11 and 10.12 respectively.

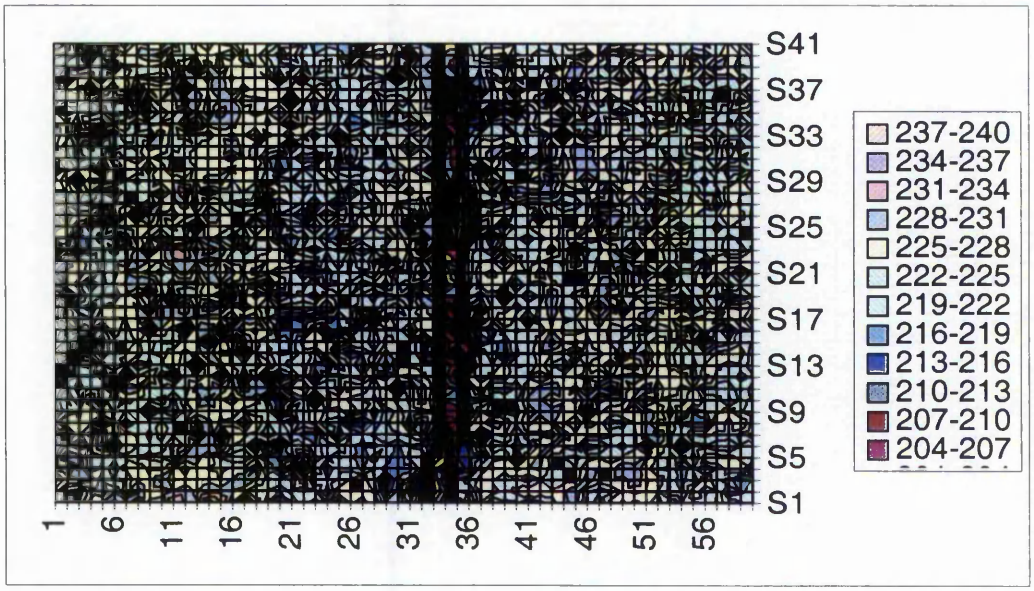

Figure 10.11 A graphical plot of the input data relating to the solution in Figure 10.9. 20 July 2000.

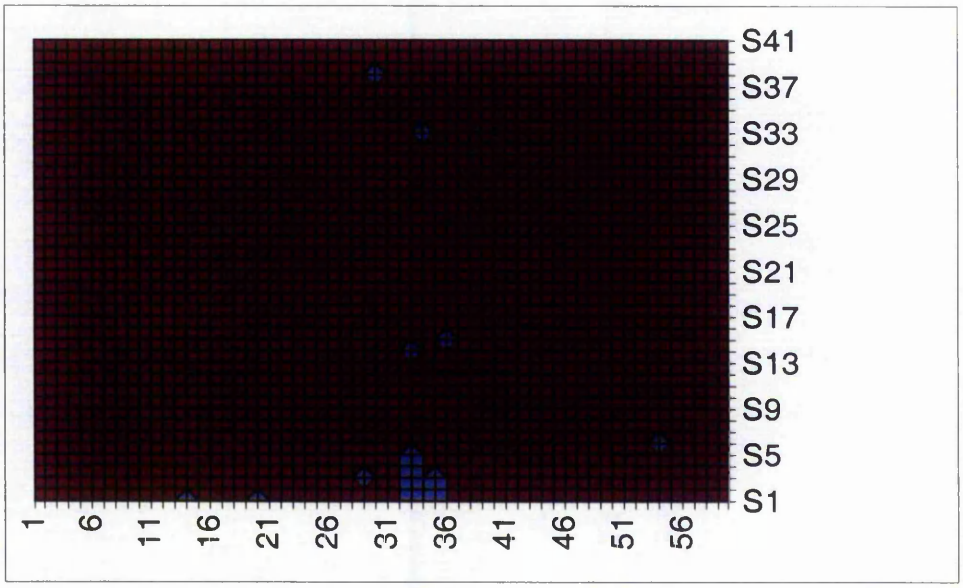

Figure 10.12 A graphical plot showing the locations of the removed data relating to the solution in Figure 10.10. 20 July 2000.

The position of the crosshairs is computed for each occasion that the crosshair illumination is switched on, which is about every half-hour.

As an aid to finding each set of 40 or so rows when a star was passing the crosshair, a graph of the maximum pixel value of each frame can be obtained. An example is shown in Figure 10.13.

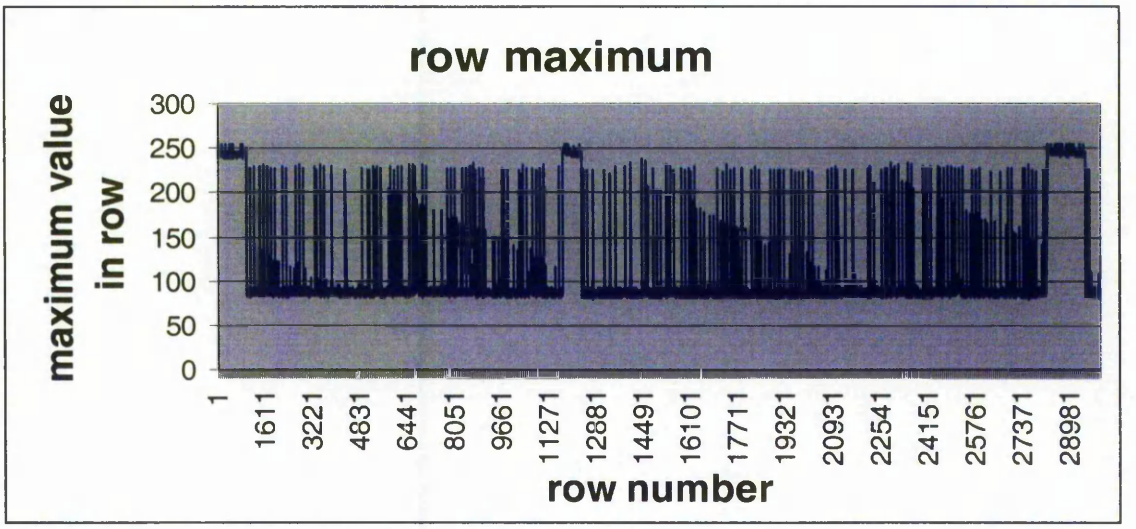

Figure 10.13 Graph maximum pixel value of each frame for 30000 frames. 20 July 2000.

Three periods when the crosshair illumination was switched on can be seen at the beginning, at around row 12000 and almost at the end. The GPS flashes appear as the spikes. However to find the star passages it is necessary to look at the detail of the floor of the data. A section of the data is shown in Figure 10.14, below.

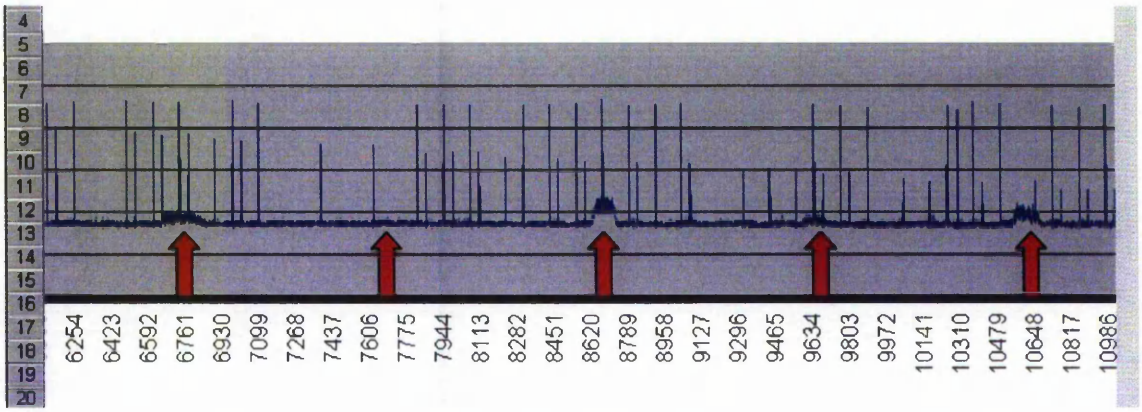

Figure 10.14 Expanded detail from Figure 10.13 showing the passage of 5 stars. 20 July 2000.

In Figure 10.14, the red arrows show the passage of five stars. Three are quite obvious, one, the fourth, barely discernible and another, the second, must be inferred from the positions of the others.

A series of solutions are shown in Figure 10.15. It will be noted that an average solution is obtained for each period that the crosshair illumination is switched on. The graph in Figure 10.16 shows that there is a small drift in the crosshair position during observations. The actual position of the crosshair for a particular star is interpolated from this data.

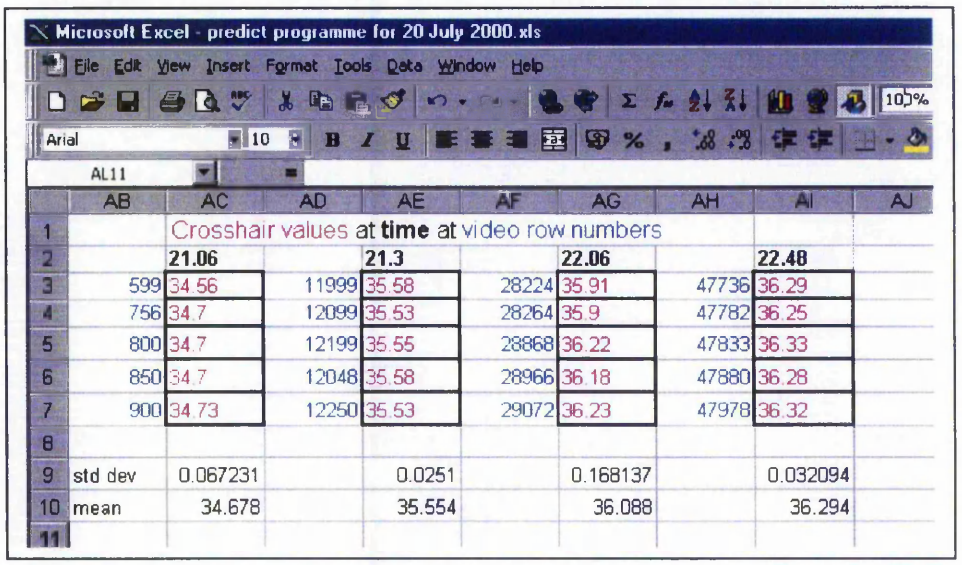

Microsoft Excel - predict programme for 20 July 2000.xls

File Edit View Insert Format Tools Data Window Help

Arial 10 B I U

AL11

	AB	AC	AD	AE	AF	AG	AH	AI	AJ
1		Crosshair values at **time** at video row numbers							
2		**21.06**		**21.3**		**22.06**		**22.48**	
3	599	34.56	11999	35.58	28224	35.91	47736	36.29	
4	756	34.7	12099	35.53	28264	35.9	47782	36.25	
5	800	34.7	12199	35.55	28868	36.22	47833	36.33	
6	850	34.7	12048	35.58	28966	36.18	47880	36.28	
7	900	34.73	12250	35.53	29072	36.23	47978	36.32	
8									
9	std dev	0.067231		0.0251		0.168137		0.032094	
10	mean	34.678		35.554		36.088		36.294	
11									

Figure 10.15 Spreadsheet detail showing collected solutions for the video row position of the crosshairs. 20 July 2000.

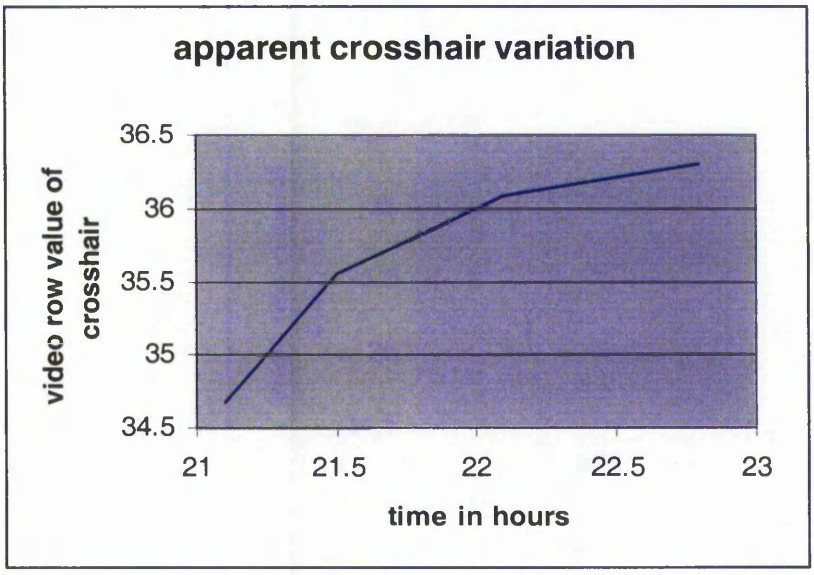

Figure 10.16 Graph showing the drift in position of the crosshairs. 20 July 2000.

Select data for star crossing and import to spreadsheet "equation of motion of star on screen 5 parameter.xls". Output is time, as frame number, for star crossing of horizontal hair.

When using the spreadsheet "equation of motion of star on screen 5 parameter" to find the time that a star crosses the crosshair (see Figure 10.10), the crosshair position interpolated from the data of Figure 10.15 is inserted in cell H3 of the spreadsheet "equation of motion of star on screen 5 parameter". The time in video row numbers, cells A10 to A50, is shown in cell H4 (see Figure 10.10).

Use computed parameters to find GPS time for each star crossing.

20-Jul-2000					
Star/mag No	Observed Zenith	video row of crosshair	frame of transit at crosshair	time of transit at crosshair ss.sss	time of transit at crosshair
1432001403.0	start	34.678			
1347010101.9		34.751			
1524016203.3	14.33551	34.824	1916.466	76199.103	21.0959103
1404005803.7	25.05470	34.897	2877.294	76318.210	21.1158210
1623015602.7	10.04261	34.970	3845.393	76438.217	21.1358217
1520012103.0	22.00473	35.043	4819.897	76559.019	21.1559019
1948004803.8	24.42242	35.116	5781.748	76678.252	21.1758252
2118012402.5	32.50264	35.189	6744.460	76797.592	21.1957592
1917002203.8	18.24276	35.262	7711.703	76917.494	21.2157494
2041009501.3	33.49014	35.335	8667.115	77035.929	21.2355929
1944020902.9	25.08178	35.408	9645.304	77157.188	21.2557188
1756012702.2	5.56174	35.481	10617.973	77277.762	21.2757762
3860036406.2	light on	35.554			
1858022903.3	26.37583	35.584	12548.070	77517.021	21.3157021
1823013003.9	33.14171	35.613	13521.756	77637.722	21.3357722
1630002802.8	33.24377	35.643	14521.031	77761.594	21.3601594
1642013703.5	16.13318	35.673			
1542009903.8	33.31240	35.702			
1527013603.7	33.08519	35.732			
1515007203.5	31.42052	35.762	18364.907	78238.090	21.4358090
1501014003.5	28.59570	35.791	19330.774	78357.821	21.4557821
1524016203.3	19.25133	35.821	20298.740	78477.812	21.4757812
1404005803.7	29.12378	35.851			
1520012103.0	24.13568	35.880	22235.793	78717.934	21.5157934
1912012403.1	17.55563	35.910	23205.359	78838.123	21.5358123
2128012203.2	29.49116	35.940	24176.995	78958.570	21.5558570
2118012402.5	28.30384	35.969	25138.698	79077.785	21.5757785
1917002203.8	12.48170	35.999	26105.170	79197.591	21.5957591
1929016503.8	14.42082	36.029			
2022005902.2	27.51588	36.058	28042.716	79437.773	22.0357773

Figure 10.17 Listing of star data for the time of transit at the crosshair. 20 July 2000.

In Figure 10.17, there are fewer stars than listed in the prediction. The sky was clear at the start of observations but became hazy after the first few stars. Initially some of the less bright stars were lost and eventually the sky clouded over.

Input star co-ordinates (copy from prediction spreadsheet), observed zenith angles & GPS time for all stars into spreadsheet "POSNSOLN with changing refraction and collimation.xls"

Set "S/W correction" as offset between UT and GPS (currently 13 s) + 5n* secs + (UT1R-UTC)**

Input polar motion** and station height.

* This assumes that the GPS flash rate is 5 seconds. n is the integer that leads to the only realistic solution for the computed longitude of the station.

** (UT1R-UTC) and polar motion from GIBS (2001)

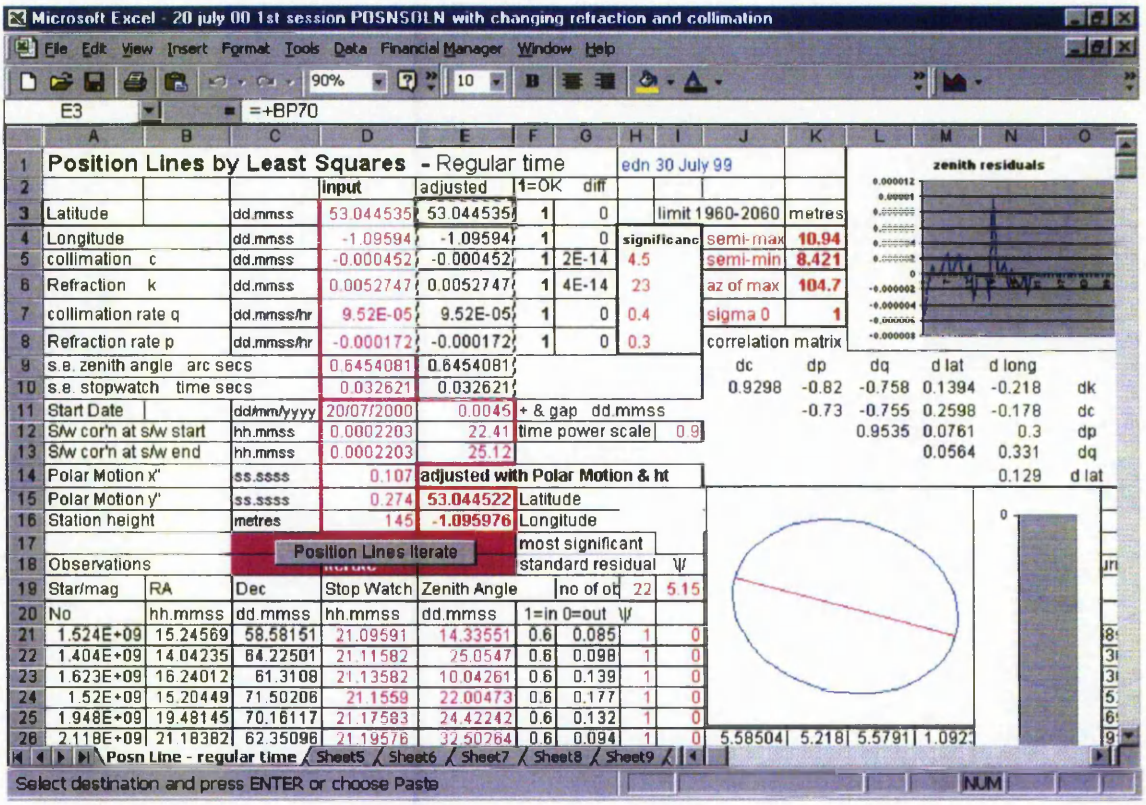

Figure 10.18 Position Line solution with all observations. 20 July 2000.

In Figure 10.18 all observations are used with the following results.

Latitude	53° 04' 45".22	±	0".35
Longitude	-1° 09' 59".76	±	0".77

However, the graph of residuals, Figure 10.19, shows that there is at least one observation with a residual significantly larger than the others.

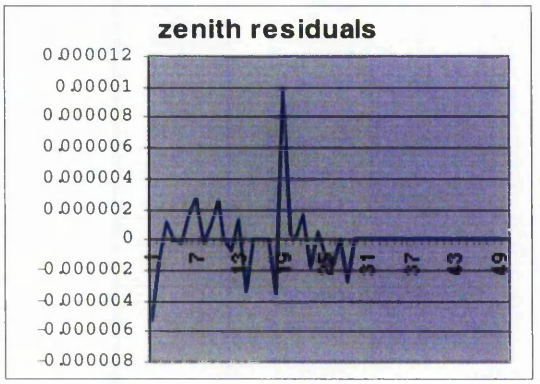

Figure 10.19 Zenith residuals in radians for a Position Line solution with all observations. 20 July 2000.

Cell H19 in Figure 10.18 indicates that the most significant residual is 5.1 times its own standard error and therefore is an outlier that should be rejected. When the adjustment is re-run the results are as follows.

Latitude	53° 04' 44".93	±	0".21
Longitude	-1° 10' 00".71	±	0".49

Find and remove gross errors. Iterate to convergence for astronomical position.

However, the graph of residuals, Figure 10.20, still shows that there is at least one observation with a residual significantly larger than the others.

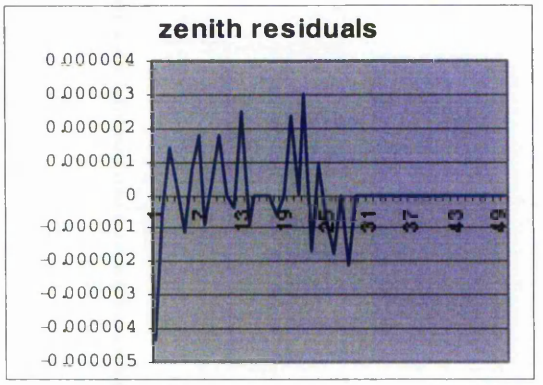

Figure 10.20 Zenith residuals in radians for a Position Line solution with one observation rejected. 20 July 2000.

Cell H19 now indicates that the most significant residual is 4.0 times its own standard error and therefore is an outlier that should be rejected.

10.5 Results

When the adjustment is re-run the results are as follows.

Latitude	53° 04' 44".96	±	0".16
Longitude	-1° 10' 00".44	±	0".24

A detail of the spreadsheet "Position Line Solution" is below at Figure 10.21.

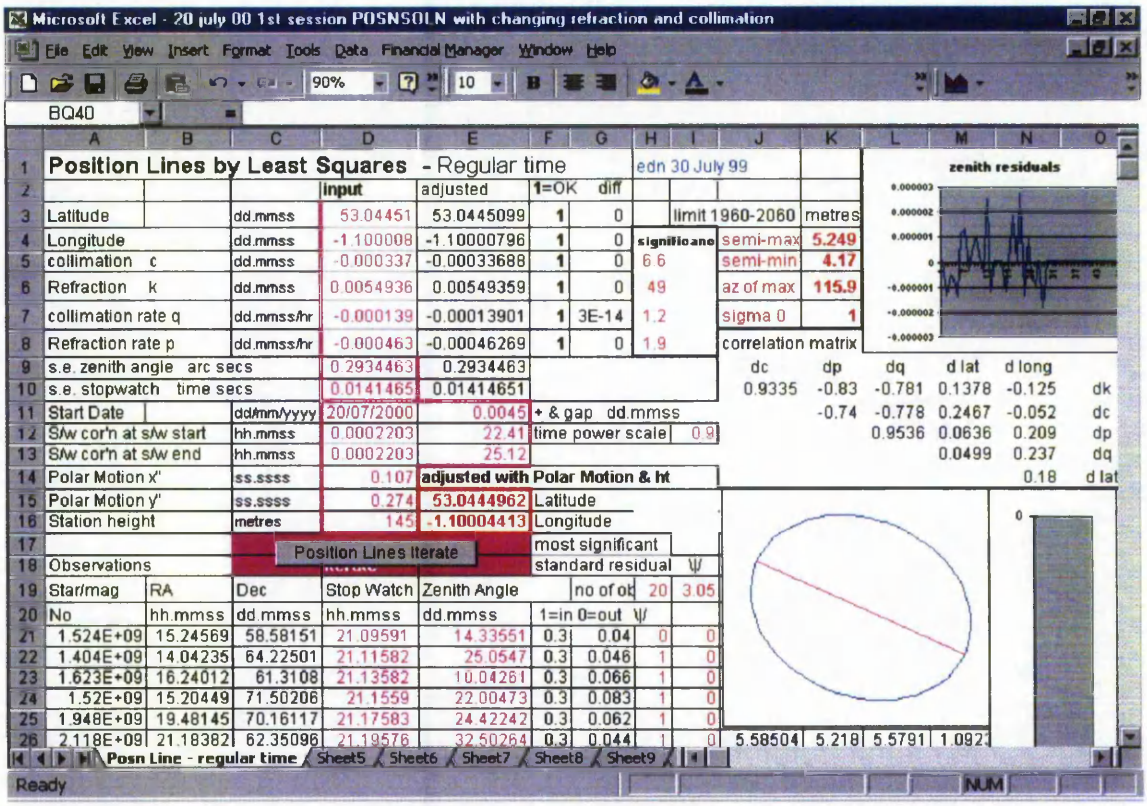

Figure 10.21 Position Line solution with two observations rejected. 20 July 2000.

The graph of residuals in Figure 10.21 indicates that there are no significant residuals and the most significant residual is only 3.05 times its own standard error and therefore the data is accepted as being error free. The position error ellipse in Figure 10.21 has a semi-major axis of 5.25 m which is approximately 0".17 of a latitude arc second.

In this solution, only 22 observations were available and 2 were rejected as outliers. With 20 observations there are 14 degrees of freedom and 6 parameters to solve for. If a full set of 50 good observations were available then the solution semi-major axis would have been of the order of 3.0 m or 0".10 of a latitude arc second.

Once the equipment was all set up the actual solution took less than an hour to observe, however computing time was somewhat greater. 50 good observations would have taken one hour and forty minutes to observe.

In this practical exercise it was noted that the computed standard error of the time that the star crossed the crosshair was related to the magnitude of the star. The brighter the star the better was the solution. A possible future improvement would be to apply weight to the observations in the final Position Line solution according to either the computed standard error of the time that the star crossed the crosshair or, the magnitude of the star.

Finally, apply the topographic-isostatic correction, from Chapter 6, and the correction for lunar gravitation and barycentric centrifugal force, from Chapter 7.

The longitudinal cross-section along the line of steepest slope through the observation point is in Figure 10.22, below. This was derived from the interpolation of contours on a 1:50000 Ordnance Survey map.

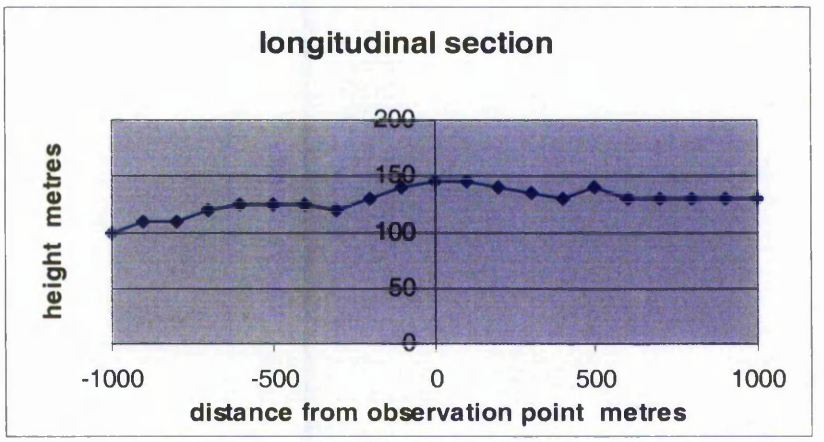

Figure 10.22 Longitudinal cross-section along the line of steepest slope through the observation point.

The computed topographic-isostatic latitude and longitude corrections are respectively +0".01 and +0".11.

At the mean time of observations, the lunar Right Ascension and Declination were $23^h.62$ and -9°.53 respectively. These lead to combined corrections to latitude and longitude for lunar gravitation and barycentric centrifugal force of +0".25 and -0".26 respectively. The final astronomical position is shown in Table 10.1, below.

Table 10.1 Corrected Position Line Solution

	latitude	longitude
Position Line Solution	53° 04' 44".96	-1° 10' 00".44
Topographic-isostatic correction	+0".01	+0".11
Lunar gravitation & barycentric centrifugal force correction	+0".25	-0".26
Corrected Position Line Solution	53° 04' 45".22	-1° 10' 00".59

The GPS position in WGS84 has also been found from just over 115 hours of observations at an epoch rate of 60s, 6908 epochs in all. The final deviation computation is in Table 10.2 below.

Table 10.2 Final Deviation Computation

	latitude	longitude
Corrected Position Line Solution - Astronomical	53° 04' 45".22	-1° 10' 00".59
GPS WGS84 position - Geodetic	53° 04' 46".46	-1° 10' 15".40
	ξ"	η"
Deviation of the vertical	-1".24	+8".90

This compares with the approximate values of deviation of the vertical, derived from data at Ordnance Survey (2001), of -0".7 in latitude and +10".5 in longitude. These are based upon a computation of the average slope of the geoid between points 10" North and South, and points 15" East and West of the observation point. In each case, the distance over which the slope is calculated is approximately 600 metres. A 0.001 m rounding error in one of the points would affect the slope of the geoid and hence deviation of the vertical by 0".35. The difference between the values just described and the author's value of deviation in the meridian is 0".54 and therefore agrees well within the bounds of the combined observational error of the author's observations and the Ordnance Survey's geoid model. The difference in values of deviation in the prime vertical, 1".60, does not agree so well but it is not clear whether that reflects errors in the author's observations and/or method, or errors in the Ordnance Survey's geoid model. The author, although not-unbiased, inclines to the latter.

This exercise shows that the theory and processes developed in earlier chapters can be applied to obtain practical results that could be taken forward with similar observations at other nearby points to compute a local astrogeodetic geoid model.

Chapter 11

Conclusions

11.1 Review of the original aims

The original aims of this study were stated in Chapter 1. As the study developed, so did its direction and therefore not all of the original aims have been addressed.

At the outset it was anticipated that it would be necessary to develop a prediction spreadsheet or software programme for manual video data capture, that is, with the video on a separate mount from the theodolite. Techniques for data capture by video methods would need to be developed. A database of star information that could easily be updated would need to be constructed.

Depending upon the quality of video images, it was anticipated that it would be appropriate to investigate methods for timing to better than 0.04s using characteristics of star-set/star-rise behind the theodolite graticule. Moreover a general least squares analysis would need to be used because the equation that connects the observations of time and the observations of the theodolite circle reading with the unknowns of latitude, longitude, parameters of the refraction model and theodolite vertical collimation contains two inseparable observations. Such a least squares solution would contain a full set of error statistics including the computation of residuals and their standard errors for the determination of outliers and for the true size of the position error ellipse. These are the statistical applications of quality assurance and quality assessment respectively. It was anticipated that such a solution would probably, subject to investigation, have a standard error of the order of ±0".5 - 1".

It was expected that the process would require one hour for observations and two hours for computation per station, leading to a solution better than ±1". Most of the two hours needed for data processing would be involved with abstracting time information from approximately 80 minutes of videotape.

With a video camera mounted on the theodolite, this would eliminate the need for lining up the camera with the theodolite for each star. In turn, it was expected that this would reduce the time per star to about 2 minutes, or 20 stars in 40 minutes.

It was anticipated that a motorised theodolite with video mount, driven by a laptop computer and software, would reduce the acquisition time per star to approximately 6 to 10 seconds per star or 20 stars in 3 minutes plus 15 minutes set up time. This would now be the same time requirement as that for the GPS data capture, a concurrent activity, and possibly similar to the travel time from point to point. Data processing time would also be reduced to about 1 hour per station because there would only be 3 minutes of videotape from which to extract time information.

Neither of these technologies were essential for this investigation but, had they been available, would have dramatically improved the numerical results of the investigation.

The original plan of work included:

a. Design a computer based method for the prediction of star positions for any site and observation start time and hence create a site specific optimised observing programme.

b. Use simulated observations, computed for the observing programme above, to investigate general least squares solutions for the determination of astronomical latitude and longitude.

c. Conduct a short field campaign for the collection of observations, using the observing programme above. Compute astronomical latitudes and longitudes and review the quality and blunder detection statistics of the general least squares solution with a view to system improvement.

d. Compare the solution derived by conventional graphical techniques with the least squares solution.

e. Investigate how on-site solutions, rather than those which are post-processed, may be used to give integrity and quality indicators and to minimise on-site data capture time.

f. Investigate the use of automation in the collection and processing of astronomical data. Technologies and techniques that, at the outset, that may have been available for investigation included:

Video for recording of star crossings.
Abstracting time information from video.
Time tagged theodolite data logging.
Servo/Robotic theodolites for rapid pointing.

g. Investigate and select appropriate statistical methods for the determination of a geoid model from the deviation of the vertical information.

As work progressed, it became apparent that capturing images onto videotape was cumbersome and so an alternative method with a sensitive photodiode and with a video frame capture board was assessed.

In Chapter 1, the aim "to develop a method for the rapid determination of astronomical latitude and longitude including investigation of methods for optimising the selection of observational data and development of field procedures to minimise the time for the collection of observational data" has partly been met. The current version of the method developed by this author involves about two hours of data collection but rather more time spent on data processing per station. This is a significant improvement on traditional techniques that may involve one or two nights of observations and a day of computations. The major improvement is in the order of precision that can be achieved, improving from ±3" to ±0.2" in position. However, there is considerable scope for further improvement in the system, see Section 11.4.

The aim "to investigate the application of rigorous statistical techniques to the precise determination of astronomical latitude and longitude" has been reasonably successful. Least squares analysis by observation equations has been applied for the determination of lunar position, the determination of the time, in video frames, when a star crosses a crosshair and in the construction of geoid models. General least squares has been applied to find position with refraction, vertical collimation and their rates of change included in the parameters to be solved for.

The aim "to develop the application of mathematical techniques for the determination of a geoid model from astronomical deviation of the vertical data of a chosen area" has been attempted. Although several approaches to this problem were developed, which have application to a limited data set over a small area, there is insufficient rigour to justify application to substantial projects, such as those of a national scale.

11.2 Summary of Conclusions

Below is a summary of the main achievements and conclusions from each of the chapters.

In Chapter 4, Position Lines Theory, the least squares approach to position lines (in which refraction, vertical collimation and their rates of change are modelled as

unknowns) was developed and used in a spreadsheet to find astronomical position. Such an approach means that it not necessary to observe meteorological conditions on the ground and make the assumption that observations at one point can be used to model curvature of the optical path from ground to star.

The development of several possible solutions to the evaluation of a personal equation have been considered but it was discovered that the best solution is where estimation of the time that a star passes a crosshair is made without human judgement.

An equation to correct for the effect of an error in horizontal pointing on the observed vertical angle was developed so that an observed near zenith vertical angle could be corrected for the small but systematic error induced by not observing with the star on the theodolite crosshairs.

In Chapter 5, Star Positions, suitable star catalogues were constructed so that the possibility of ambiguity between close stars was avoided and a spreadsheet to update star co-ordinates to the date and time of observations was written to ensure that star data truly referred to the epoch of observation.

A method for detecting the instant of passage of a star across theodolite crosshairs using a photodiode was developed in Chapter 6, Observing and computing processes. Unfortunately, the method could not be tested in practice because the photodiode used was unstable at operating temperatures but the method is now available should, either a more stable diode become available or, a practical means of cooling a diode in the field be developed.

A method for linking GPS and video time by exposure of a GPS timed flash was developed so that there was no "personal equation" effect upon the determination of the timing of star passage over the theodolite crosshairs.

A video based method for detecting the instant of passage of a star across the theodolite crosshairs was developed and implemented in a spreadsheet. This enabled the determination of passage at a sub-video frame epoch level.

The prediction programme was optimised for star balance using a combination of various parameters so that any systematic effect of errors inherent in an unbalanced data set would be minimised.

Productivity with varying levels of automation was considered. It was concluded that the best possible productivity would be that obtainable where theodolite angle data is

captured with a data logger and the theodolite is motorised and programmed to point to stars on command.

Video time was precisely linked to GPS time by using a data capture rate of one frame nominally every 124 ms, that is a data rate slightly different from 8 frames per second. Therefore a precise but practical method to find the instant that a star crosses a theodolite crosshair using a video camera mounted on a theodolite with GPS time input has been developed.

A practical observing and computing aide memoire was written for use in the "field" so that the fairly complex procedure can be completed in the field without omission.

Theory to describe the effect of barycentric lunar gravitation on deviation of the vertical was developed in Chapter 7, The Effect of Lunar Gravitation and Barycentric Centrifugal Force on Deviation of the Vertical. Formulae for the computation of a correction have been derived so that this source of systematic error can now be corrected for. Where astronomical data has been used in the past, derived values of position may need to be corrected.

In Chapter 8, The Topographic-Isostatic Effect, the application of the topographic-isostatic effect on astronomical position was investigated. Formulae for use with a digital elevation model were derived but were of such complexity that application in a simple spreadsheet was not possible.

An approximate "rule of thumb" is that it is prudent to create a longitudinal section along the line of greatest slope in length at least four times the height of the highest point along that section was deduced. It is tentatively suggested that this should give a topographic-isostatic correction to $\pm$ 10% $\pm$ 0".1 of its true value in topography similar to that found in the UK. Therefore, at this level of precision, the computation load is significantly reduced and the need for raw DEM data is now reduced to that "along the line of greatest slope in length at least four times the height of the highest point along that section".

It was found that, to minimise errors in the computed value of topographic-isostatic deviation, the best observing points are where there is an even slope, i.e. zero rate of change of slope.

The application and formulae developed here, using wedges across the local line of greatest slope, although not as rigorous as the DEM approach was much simpler and will give results that are of sufficient precision in non-mountainous areas such as most of UK.

Kaula's rule of thumb was related to the Astrogeodetic Geoid Model in Chapter 9, The Astrogeodetic Geoid Model. The determination of geoid models using polynomial coefficients and "progressive nodes" was examined. It was concluded that the former is the more rigorous approach but computationally much more complex. The latter is likely to produce results that are almost as good, but it was found that the determination of quality statistics is more difficult.

In the practical determination of astronomical position described in Chapter 10, a position solution with a standard error ellipse major axis of ± 0".17 was obtained with 20 observations and it was deduced that 50 good observations, taking 100 minutes to observe with manual pointing of the theodolite, should lead to a solution at the 0".1 level. With the aid of a motorised theodolite, the time of observations would also be significantly reduced. However, local temporal systematic refraction effects might then become more significant.

11.3 Practical Implications

The practical implications of this study are as follows.

- Astronomical position can now be determined to about 0".15 (5 metres) with less than 2 hours worth of observations or, potentially, less than half an hour of observations using a motorised electronic theodolite.
- In turn, this can lead to astronomically derived deviation as an economic data source for the determination of a local precise geoid. This may find a practical application where precise height is required from GPS such as in large engineering projects, for example bridge or tunnel river crossings. Where the engineering project is long and linear, such as with pipeline, canal or river works, the local geoid model is only required in and near the area of the works. In this case, an astrogeodetic geoid will be much easier to construct than a gravitationally derived one because it will require fewer observations.
- How much the process can aid the determination of national or continental geoid models would require further study. However, since precise astronomical position can now be determined with relatively little effort, then astronomy would lend itself more to the provision of a control framework for gravitationally derived geoid models, local independent checks upon gravitationally derived geoid models or the inclusion of astronomical

observations in astro-gravitational geoid models and geoid models derived from mixed observations.

- The system could also have application where change is expected over time in the direction of the vertical at a point, such as in tectonic and volcanic studies. In such cases, astronomical data would give information about change independent from other data sources such as precise levelling, gravity or geophysical measurements.
- There are significant improvements to the usefulness of the system that can be made and they are described in Section 11.4 below.

11.4 Further studies

If a geoid model is to be used with GPS to find orthometric height differences, then the quality of the model must be better than the height difference determined by GPS. With the current and future anticipated improvements in GPS capabilities, the requirement for a millimetre relative geoid will soon arise. For such a geoid to be determined by astrogeodetic means, there will need to be significant improvements in several aspects of the hardware and the data processing techniques.

- The quality of star co-ordinates available from current almanacs is probably not the weakest link in the process. However, any improvement will help, especially in the removal of systematic errors in star co-ordinates.
- Refraction is probably the area that could benefit most from further research. If the observations are made in a short period then there will be less likelihood of the refraction effects being cancelled out than with observations taken over a protracted period of time. Two approaches are possible.
  - ➢ Modelling systematic refraction effects at a given epoch and position due to known meteorological conditions such as the passage of a weather front.
  - ➢ The other is modelling total refraction effects, for example by "2 colour" methods, for the integrated meteorological effect. 2-colour solutions for meteorological effects have been used in EDM instruments such as the Terrameter for the measurement of distance. Observations on 2 frequencies are used with GPS. The problem with such an approach for direction measurement is that the difference in apparent direction of incoming blue and red light is that it will be about 2% of the total refraction effect and therefore to compute the refraction effect to 1" would require measurement of the

difference in altitude of red and blue light from the star to 0".02 - a formidable problem.

- Improved DEMs would aid the computation of the topographic-isostatic effect. Technically this would not be difficult if suitable map data already exists but the time and cost to produce the data sets could be significant. However, the refinement would need to be accompanied by improved density models for the computation of the topographic-isostatic effect. Figure 2 of Heiland et al (1998) suggests that the topographic-isostatic effect could be of several arc seconds in Austria. Marti (1998) suggests that the density of the topography in Switzerland can vary from +0.4 g cm^{-3} to -0.8 g cm^{-3} from the assumed value of 2.67 g cm^{-3}. Taking these two facts together suggests that there could be errors approaching 1" in the computation of the topographic-isostatic effect due to errors in the assumed topographic density.
- Further investigation is required to confirm that the method of finding topographic-isostatic deviation corrections by modelling the topography by infinitely long wedges perpendicular to the line of greatest slope gives a solution to ± 10% of its true value in topography similar to that found in the UK.
- Improve the model for the effect of barycentric lunar gravitation on deviation of the vertical to take account of the fact that the lunar orbit is not circular and therefore lunar gravitation varies. With an elliptical orbit, the earth will accelerate and decelerate during its orbit around the barycentre further complicating the model.
- Improvements to the fundamental observations of vertical angle with electronic theodolites are desirable.

References

Ackroyd, N., Lorimer, R., 1990. **Global Navigation - a GPS users guide.** London: Lloyds of London.

Ádám, J., Denker, H., 1991. **Test Computations for a local Quasigeoid in Hungary using FFT.** Determination of the Geoid Present and Future – IAG Symposium 106, London: Springer-Verlag.

Anon, 1976. **The Astronomical Ephemeris 1978.** London: HMSO.

Anon, 1983. **The Supplement to the Astronomical Almanac 1984.** Washington DC: Nautical Almanac Office USNO & HM Nautical Almanac Office RGO.

Astronomisches Rechen-Institute, 1995. **Apparent Places of Fundamental Stars 1996.** Heidelberg: Astronomisches Rechen-Institute

Barlick, M., Becker, M., Gegout, P., Li, H., Li, Z., Sun, H., Vondrak, J., 1999. **Interannual Variations of the Vertical and their Interpretation.** IAG Special Study Group 5.175. Report to IUGG Conference July 1999 Birmingham.

Barthelmes, F., Dietrich, R., 1991. **Use of Point Masses on Optimized Positions for the Approximation of the Gravity Field.** Determination of the Geoid Present and Future – IAG Symposium 106, London: Springer-Verlag.

BBC, 2001. **BBCTIME.** [online]. British Broadcasting Corporation. Available at <URL:http://www.ubr.com/clocks/timesw/bbctime.html> [Accessed 4 October 2001]

Benciolini, B., Manzino, A., Sansò, F., Sguerso, D., 1991. **ITALGEO '90: Progress Report June '90.** Determination of the Geoid Present and Future – IAG Symposium 106, London: Springer-Verlag.

Berry, P., 1999. **Global digital elevation models – fact or fiction.** Astronomy and Geophysics Vol 40 Issue 3, p10-13. London: Royal Astronomical Society

Blitzkow, D., Cristina, M., Lobianco, B., Fairhead, J., 1997. **Data coverage Improvement for Geoid computation in South America.** Gravity, Geoid and Marine Geodesy, – IAG Symposium 117, London: Springer-Verlag.

Blitzkow, D., Lobianco, M., Fairhead, J., 1999. **The continuous efforts towards a 10 cm resolution geoid for South America.** Poster paper at IUGG99 conference at Birmingham, July 1999.

Bomford, G., 1980. **Geodesy.** 4th edn. Oxford: Oxford University Press

Breach, M., 1985. **Azimuth by the method of multiple timed observations of a Gyrotheodolite without electronic registration.** Bulletin Geodesique Vol 59 No3. Paris: Bureau Centrale l'Association International de Géodésie.

Breach, M., 1997. **Engineering Surveying (1997 edition).** Course notes 800pp. Nottingham: Department of Civil and Structural Engineering, The Nottingham Trent University.

Brenecke, J., Lelgemann, D., Torge, W., Wenzel, H., 1983. **A European Astrogravimetric geoid.** Deutsche Geod. Komm. No 269 Frankfurt/Main.

Brittan, J., Domnesteanu P., Warner M., 1996. **Modelling of 3-D wide-angle seismic data over the Baltic Shield.** [online]. Commission of the European Communities, Brussels. Available at <URL: http://diamond.ge.ic.ac.uk/jb03/jb03/web/babel/babel.html> [Accessed prior to 4 October 2001]

Brookes, B., 1994. **Auto-astro to determine Position and Azimuth.** Nottingham Trent University undergraduate final year project. Nottingham: The Nottingham Trent University.

Brown, R., Vincent, S., Strange, W., 1972. **Undulation spectra for the marine geoid.** Paper presented at the 53rd annual meeting of the American Geophysical Union Washington DC, USA.

Bürki, B., Marti, U., 1991. **The Swiss Geoid Computation: A Status Report.** Determination of the Geoid Present and Future – IAG Symposium 106, London: Springer-Verlag.

Colic, K., Pribicevic, B., Švehla, D., 1998. **First cm-geoid in the Republic of Croatia – The Capital City Zagreb Pilot Project.** Second Continental Workshop on the Geoid in Europe, – 98:4. Helsinki: Reports of the Finnish Geodetic Institute.

Cooper, M., 1987. **Control Surveys in Civil Engineering.** London: Collins.

Cross, P., Holwey, A., Small, L., 1981. **Geodetic Appreciation.** London: North East London Polytechnic (now University of East London).

Davidson, M., 1995. **Astrogeodetic Geoid determination.** Nottingham Trent University undergraduate final year project. Nottingham: The Nottingham Trent University.

Dean, J.D.A., 1980. **The astrogeodetic determination of the geoid in Great Britain, Professional Paper No. 29.** Southampton: Ordnance Survey GB.

Defense Mapping Agency, 1991. **The Department of Defense World Geodetic System 1984: its definition and relationships with local geodetic systems.** Washington DC: United States Defense Mapping Agency

Denker, H., 1991. **GPS Control of the 1989 Gravimetric Quasigeoid for the Federal Republic of Germany.** Determination of the Geoid Present and Future – IAG Symposium 106, London: Springer-Verlag.

Denker, H., 1998. **Evaluation and Improvement of the EGG97 Quasigeoid Model for Europe by GPS and Leveling Data.** Second Continental Workshop on the Geoid in Europe, – 98:4 Helsinki: Reports of the Finnish Geodetic Institute.

Denker, H., Behrend, D., Torge, W., 1997. **The European Quasi-geoid EGG96.** Gravity, Geoid and Marine Geodesy, – IAG Symposium 117, London: Springer-Verlag.

EGG97, 1997. **European Gravimetric (Quasi)Geoid 1997.** [CD-ROM]. Institut für Erdmessung, University of Hannover, Germany / International Association of Geodesy.

EGM96, 1996. NIMA/NASA EGM96, N=M=360 Earth Gravity Model. [online]. US National Imagery and Mapping Agency. Available at <URL: http://164.214.2.59/GandG/wgs-84/egm96.html> [Accessed 28 March 2002]

EGM96, 2001. **The NASA GSFC and NIMA Joint Geopotential Model.** [online]. US National Imagery and Mapping Agency. Available at <URLhttp://cddisa.gsfc.nasa.gov/926/egm96/egm96.html> [Accessed 28 March 2002]

.Eissfeller, B., Hein, G., 1994. **Astrogeodetic Levelling with an Integrated DGPS/CCD Star Camera System.** Kinematic Systems in Geodesy, Geomatics and Navigation, Calgary: University of Calgary.

Featherstone, W., 2000. **Refinement of Gravimetric Geoid Using GPS and Leveling Data.** Journal of Surveying Engineering, May, Volume 126, Issue 2 pp27-56. Reston, VA: The American Society of Civil Engineers

Featherstone, W., Kirby, J., Zhang, K., Kearsley, A., Gilliland, J., 1997. **The Quest for a new Australian Gravimetric Geoid.** Gravity, Geoid and Marine Geodesy, IAG Symposium 117, London: Springer-Verlag.

Forsberg, R., 1991. **A New High-Resolution Geoid of the Nordic Area.** Determination of the Geoid Present and Future – IAG Symposium 106, London: Springer-Verlag.

Forsberg, R., 1998. **Geoid Tayloring to GPS – with example of a 1-cm geoid of Denmark.** Second Continental Workshop on the Geoid in Europe, – 98:4 Reports of the Finnish Geodetic Institute. Helsinki: Finnish Geodetic Institute

Forsberg, R., Kaminskis, J., Solheim, D., 1997. **Geoid of the Nordic and Baltic Region from Gravimetry and Satellite Altimetry, Gravity.** Geoid and Marine Geodesy, – IAG Symposium 117, London: Springer-Verlag.

Fricke, W., Schwan, H., Lederle, T., 1988. **Fifth Fundamental Catalogue (FK5) Part 1 The Basic Fundamental Stars.** Heidelberg: Astronomisches Rechen-Institut.

Fryer, J.G., 1972. **The Australian Geoid,** Australian Surveyor 24 (4). Deakin: The Australian Surveyor.

Fukuda, Y., Kuroda, J., Takabatake, Y., Itoh, J., Murakami, M., 1997. **Improvement of JGEOID 93 by the Geoidal Heights derived from GPS/levelling Survey.** Gravity, Geoid and Marine Geodesy, – IAG Symposium 117, London: Springer-Verlag.

Fukuda, Y., Segawa, J., 1991. **Derivation of the Most Reliable Geoid in the Area of Japan and Some Comments on the Variability of Sea Surface Topography,** Determination of the Geoid Present and Future – IAG Symposium 106, London: Springer-Verlag.

Galileo, 2002. **Galileo Newsletter March 2002 No 19.** [online]. Genesis Office of the European Commission. Available at <URL: http://www.genesis-office.org/indexgl.htm> [Accessed 28 March 2002]

Georgia, 2001. **Scientific Constants.** [online]. Georgia State University. Available at <URL:http://www.gsu.edu/other/constants.html> [Accessed 4 October 2001]

Gerstbach, G., 1999. **Astrogeodetic CDD measurements for centrimetric geoid monitoring.** Poster paper at IUGG99 conference at Birmingham, July 1999.

GIBS, 2001. **International Earth Rotation Service (IERS) Bulletins - Earth Rotation Parameters.** [online]. GPS Informations und Beobachtungssystem, Institute for Applied Geodesy (now Federal Agency for Cartography and Geodesy), Geodetic Research Department. Available at <URL:http://gibs.leipzig.ifag.de/GIBS/MISC/IERS/> [Accessed 4 October 2001]

GLOBE, 2001. **Global Land One-km Base Elevation (GLOBE).** [online]. US National Oceanic & Atmospheric Administration. . Available at <URL:http://www.ngdc.noaa.gov/seg/topo/globe.shtml> [Accessed 5 December 2001]

GOCE, 2002. **Gravity Field and Steady-State Ocean Circulation Mission GOCE.** [online]. European Space Agency. Available at <URL: http://www.esa.int/export/esaLP/goce.html> [Accessed 27 March 2002]

GRACE, 2002. **GRACE Gravity Recovery and Climate Experiment.** [online]. University of Texas. Available at <URL:http://www.csr.utexas.edu/grace/> [Accessed 27 March 2002]

Greenfield, J., 1994. **Auto-astro to determine Position and Azimuth,** Nottingham Trent University undergraduate final year project. Nottingham: The Nottingham Trent University.

Grid InQuest, 2001. **Grid InQuest "A simple 3D datum transformation from WGS84 (ETES89) to OSGB36 British National Grid".** [online]. Quality Engineering and Survey Technology Ltd. Available at <URL:http://www.qualityeng.co.uk/grid_inquest.htm> [Accessed 4 October 2001]

Haáz, I., 1953. **Relations between the potential of the attraction of the mass contained in a finite rectangular prim and its first and second derivatives,** (in Hungarian) Geofizikai Közlemenyek, II, no.7. HU - ISSN 0016-7177. Praha: Akademie věd ČR - Geofyzikální ústav

Hamamatsu, 1996. **Photodiodes.** Enfield: Hamamatsu Photonics UK Limited

Hastings, D., Dunbar, P., 1998. **Development & Assessment of the Global Land One-km Base Elevation Digital Elevation Model (GLOBE).** ISPRS Archives, Vol.32, number 4, pp. 218-221. London: RICS Books.

Hayward, M., 1995. **Astrogeodetic Geoid determination.** Nottingham Trent University undergraduate final year project. Nottingham: The Nottingham Trent University.

Heiland, R., Hofmann-Wellanhof, B., Kienast, G., Kühtreiber, N., 1998. **Recomputation of the Austrian astrogeodetic geoid.** Second Continental Workshop on the Geoid in Europe, – 98:4 Reports of the Finnish Geodetic Institute. Helsinki: Finnish Geodetic Institute

Heiskanen, W., Moritz, H., 1979. **Physical Geodesy.** Graz: Technical University of Austria.

Herring, T., 1987. **Herrings Correction to the IAU 1980 Nutation Series.** BIH Annual Report for 1987. Bureau International de L'Heure Paris. Paris: Bureau International de L'Heure

HMSO 1995. **The Star Almanac for Land Surveyors 1996 (SALS).** London: Her Majesty's Stationary Office.

Hoffleitt, D., 1982. **The Bright Star Catalogue (YBSC).** 4th edition. Yale: Yale University Observatory.

Hofmann-Wellenhof, B., Lichtenegger, H., Collins, J., 1992. **GPS Theory and Practice.** Wien: Springer-Verlag.

Hui, H., Wang, R., Jirong, M., 1999. **Applications of Astonomic Time Latitude Residuals in Geoscience.** Poster paper at IUGG99 conference at Birmingham, July 1999.

IERS, 1998. **International Earth Rotation Service (IERS) Bulletins - Earth Rotation Parameters.** [online]. Available at <URL:http://no5.liepzig.ifag.de/MISC/IERS> [Accessed prior to 4 October 2001]

IERS, 2001. **Fortran sub-routine - Matrix transformation from the terrestrial reference system (TRS) to the celestial reference system (CRS) at the date of observation.** [online]. International Earth Rotation Service (IERS), Central Bureau (IERS/CB). Available at <URL: http://hpiers.obspm.fr/iers/model/clas_transf.f> [Accessed 4 October 2001]

Iliffe, J., Griffiths, W., Message, E., 2000. **Localised Geoid Determination for Engineering Control Surveys.** Survey Review Vol 35 No 275. January 2000. London: Commonwealth Association of Surveying and Land Economy (CASTLE).

Jiang, Z.., 1997. **Geoid determination in France, Gravity.** Geoid and Marine Geodesy, – IAG Symposium 117, London: Springer-Verlag.

JPL. 2002. **Ocean Surface Topography.** [online]. Jet Propulsion Laboratory, NASA. Available at <URL:http://topex-www.jpl.nasa.gov/technology/tandem.html> [Accessed 28 March 2002]

Kahar, J., Kasenda, A., Prijatna, K., 1997. **The Indonesian Geoid Model 1996.** Gravity, Geoid and Marine Geodesy, – IAG Symposium 117, London: Springer-Verlag.

Kaminskis, J., Forsberg, R., 1997. **A new Detailed Geoid for Latvia, Gravity.** Geoid and Marine Geodesy, – IAG Symposium 117, London: Springer-Verlag.

Kaula, W., 1966. **Global harmonic and statistical analysis of gravity.** In *Extension of gravity anomalies to unsurveyed areas.* Ed H. Orlin. American Geophysical Union Monograph 9, Washington DC, USA pp58-67. Washington DC: American Geophysical Union.

Kearsley, A.H.W., Govind R., 1991. **Geoid Evaluation in Australia: Status and Problems.** Determination of the Geoid Present and Future – IAG Symposium 106, London: Springer-Verlag.

Kenyeres, A., Virág., 1998. **Testing of recent geoid models with GPS/levelling in Hungary.** Second Continental Workshop on the Geoid in Europe, – 98:4 Reports of the Finnish Geodetic Institute. Helsinki: Finnish Geodetic Institute.

King, D., 1999. **W5LUU Moon Data for 1999.** [online]. QSL.NET. Available at <URL:http://www.qsl.net/ea6vq/w5luu.html> [Accessed 3 December 2001]

Kühtreiber, N., 1997. **Using Different Digital Terrain Models for a Precise Austrian Geoid.** Gravity, Geoid and Marine Geodesy, – IAG Symposium 117, London: Springer-Verlag.

Landmap, 2000. **LANDMAP Project for the Creation of Satellite Image Map Mosaics and Digital Elevation Models for the British Isles.** [online]. Manchester University / University College London. Available at <URL:http://www.landmap.ac.uk/> [Accessed 4 October 2001]

Leick, A., 1990. **GPS Satellite Surveying.** New York: Wiley.

Leiske, J.H., 1979. **Precession Matrix Based on IAU (1976) System of Astronomical Constants.** Astronomical Astrophysics 73, p282. London: Springer-Verlag.

Lyszkowicz, A., 1991. **Efforts Towards a Preliminary Gravimetric Geoid Computations in Poland Area.** Determination of the Geoid Present and Future – IAG Symposium 106, London: Springer-Verlag.

Majid, A., Kadir, A., Fashir, H., Omar, K.., 1999. **A Regional Gravimetric Co-geoid over South East Asia.** Geomatics Research Australasia, No 71 pp 37-56. Deakin: The Institution of Surveyors, Australia Inc.

NASA, 1997d. **The SKY2000 Master Star Catalog.** [online]. US Naval Aeronautical and Space Administration. Available at <URL:ftp://fdd.gsfc.nasa.gov/pub/skymap/sky2kv2.cat.gz> [Accessed prior to 4 October 2001]

NIMA, 2001. **DoD World Geodetic System 1984, Its Definition and Relationships with Local Geodetic Systems.** National Imagery and Mapping Association, Geospatial Sciences Division. [online]. Available at <URL:http://164.214.2.59/GandG/tr8350_2.html> [Accessed 3 December 2001]

Ollikainen, M., 1998. **GPS levelling results obtained in Finland.** Second Continental Workshop on the Geoid in Europe, – 98:4 Reports of the Finnish Geodetic Institute. Helsinki: Finnish Geodetic Institute.

Ordnance Survey, 2001. **"Co-ordinate converter" for conversion of co-ordinates between OSGB36 plan co-ordinates with height above Ordnance (Newlyn) datum and ETRS89.** Ordnance Survey. [online]. Available at <URL:http://www.gps.gov.uk/convert.asp> [Accessed 4 October 2001]

Ordnance Survey, 2002. **A guide to coordinate systems in Great Britain - 5 Ordnance Survey coordinate systems.** Ordnance Survey. [online]. Available at <URL:http://www.gps.gov.uk/guide5.asp> [Accessed 28 March 2002]

Pâquet, P., Jiang, Z., Everaerts, 1997. **A new Belgian Geoid Determination: BG96.** Gravity, Geoid and Marine Geodesy, – IAG Symposium 117, London: Springer-Verlag.

Rapp, R.H., Nikolaos, K.P., 1991. **OSU89A/B Potential Coefficient Models.** Determination of the Geoid Present and Future – IAG Symposium 106, London: Springer-Verlag.

Rapp, R.H., Sansò, F., ed. 1991. **Determination of the Geoid Present and Future.** – IAG Symposium 106, London: Springer-Verlag.

Rees, W., 1994. **Physics by Example.** Cambridge: Cambridge University Press.

Rice, D.A., 1962. **A geoidal section in the United States.** Bulletin Géodésique No. 65. Paris: Bureau Centrale l'Association International de Géodésie.

Robbins, A., 1976. **Military Engineering Vol XIII Pt IX Field and Geodetic Astronomy.** Hermitage: School of Military Survey.

Rowe, R.D., Salvermoser, R., Stoughton, H.W., Howell, E.A., Raum, J.H., 1985. **An Automated Star Sensor System to Improve Accuracies in Astronomic Position Determinations.** Annual Meetings of the American Congress on Surveying and Mapping and the American Society of Photogrammetry. Washington DC.

Saastamionen, J., 1973a. **Contributions to the theory of atmospheric refraction.** Bulletin Géodésique No. 105. pp 279-298. Paris: Bureau Centrale l'Association International de Géodésie.

Saastamionen, J., 1973b. **Introduction to practical computation of astronomical refraction.** Bulletin Géodésique No. 106. Paris: Bureau Centrale l'Association International de Géodésie.

Segawa, J., Fujimoto, H., Okubo, S., ed. 1997. **Gravity, Geoid and Marine Geodesy.** – IAG Symposium 117, London: Springer-Verlag. pp 383-397

Seidelmann, P.K., 1992. **Explanatory Supplement to the Astronomical Almanac.** Mill Valley California: University Science Books

Sharni, D., Papo, H., Forrai, Y., 1998. **The geoid in Israel: Haifa pilot.** Second Continental Workshop on the Geoid in Europe, – 98:4 Reports of the Finnish Geodetic Institute. Helsinki: Finnish Geodetic Institute.

SLR, 2002. **The Satellite Laser Ranger**. [online]. Royal Observatory Greenwich. Available at <URL:http://www.rog.nmm.ac.uk/leaflets/slr/slr.html > [Accessed 28 March 2002]

Smith, D., Sartori, M., Milbert, D., 2000. **Preliminary Investigations Toward an Improved Geoid Model in Florida.** Surveying and Land Information Systems, Vol.60, No.2, pp109-116. Gaithersburg, Maryland: American Congress on Surveying and Mapping.

Star*Net, 1991. **Star*Net Least Squares Survey Adjustment Program User's Manual.** Oakland California: Starplus Software Inc.

Stokes, G., 1849 **On the Variation of Gravity on the Surface of the Earth.** Transactions of the Cambridge Philosophical Society 8: pp672-695

Tanaka, M., 1997. **Determination of Precise Geoidal Height by GPS observations in and around Sakurajima.** Volcano. Japan, Gravity, Geoid and Marine Geodesy, – IAG Symposium 117, London: Springer-Verlag.

Torge, W., Denker, H., 1991. **Possible Improvements in the Existing European Geoid.** Determination of the Geoid Present and Future – IAG Symposium 106, London: Springer-Verlag.

Torge, W., Denker, H., 1998. **The European Geoid, development over more than 100 years and present status.** Second Continental Workshop on the Geoid in Europe, – 98:4 Reports of the Finnish Geodetic Institute. Helsinki: Finnish Geodetic Institute.

Tsoulis, D., 1997. **A combination method for computing terrain corrections.** Physics and Chemistry of the Earth vol. 23 No. 1 pp 53-58 (s.l.): (s.n.)

Tziavos, I., Andritsanos, 1998. **Recent advances in terrain correction computations.** Second Continental Workshop on the Geoid in Europe, – 98:4 Reports of the Finnish Geodetic Institute. Helsinki: Finnish Geodetic Institute.

Tziavos, I., Arabelos, D., 1991. **Estimation of the Disturbing Potential Components and Comparison with GPS and Astrogeodetic Data.** Determination of the Geoid Present and Future – IAG Symposium 106, London: Springer-Verlag.

Uber, G., 2001. **Clocks and Time: Time Software for PC personal computers for time setting and synchronisation, clock rate correction and time display.** [online]. Gordon T. Uber personal website. Available at <URL:http://www.ubr.com/clocks/timesw/timesw.html> [Accessed 4 October 2001]

UCL, 2002. **WGS84 Geoid Height Computation Using EGM96**. [online]. UCL Geomatics Engineering Research. Available at <URL: http://www.ps.ucl.ac.uk/research/positioning/programs/geoid_height.html> [Accessed 28 March 2002]

Units, 2002. **Non SI units - Nem SI egységek.** [online]. Institute of Experimental Physics, University of Debrecen, Hungary . Available at <URL:http://indykfi.phys.klte.hu/indyKFI/MT/def_nosi.htm> [Accessed 27 March 2002]

USNO, 1997a. **The FK5 Catalogue.** [online]. US Naval Observatory. Available at <URL:http://aries.usno.navy.mil/ad/cdrom/FK5/FK5_1_2.DAT> [Accessed prior to 4 October 2001] redirect to http://ad.usno.navy.mil/ [Accessed 4 October 2001]

USNO, 1997b. **Nutation coefficients and arguments of multiples.** [online]. US Naval Observatory. Available at <URL:http://maia.usno.navy.mil/direct.html> [Accessed prior to 4 October 2001]

USNO, 1997c. **US Naval Observatory's "Web Version of MICA" – Multiyear Interactive Computer Almanac.** [online]. US Naval Observatory. Available at <URL:http://aa.usno.navy.mil/AA/data/docs/WebMICA_2.html> [Accessed 4 October 2001]

Van Flandern, T., 1981. **The Introduction of the improved IAU System of Astronomical Constants Time Scales and Reference Frame into the Astronomical Almanac.** The Supplement to the Astronomical Almanac 1984, London: HMSO.

Vanicek, P., Krakiwsky, E., 1982. **Geodesy: The Concepts.** Amsterdam: North-Holland Publishing Company.

Vanicek, P., Ong, P., Changyou, Z., 1991. **New Gravimetric Geoid for Canada: the "UNB '90" Solution,** Determination of the Geoid Present and Future – IAG Symposium 106, London: Springer-Verlag.

Vermeer, M., Ádám J., ed. 1998. **Second Continental Workshop on the Geoid in Europe at Budapest.** – 98:4 Reports of the Finnish Geodetic Institute. Helsinki: Finnish Geodetic Institute.

Véronneau, M., 1997. **The GSD95 Geoid Model for Canada.** Gravity, Geoid and Marine Geodesy, – IAG Symposium 117, London: Springer-Verlag.

VizieR, 1997. **VizieR Catalogue search page for the Smithsonian Astrophysical Observatory Star Catalogue. Data selected in FK5/J2000 system.** [online]. Available at <URL:http://vizier.u-strasbg.Fr/cgi-bin/wcbCatSelectPg?SAO> [Accessed prior to 4 October 2001]

Volcano, 2001. **Volcanic and Geologic Terms.** [online]. Available at <URL:http://volcano.und.nodak.edu/vwdocs/glossary.html> [Accessed 4 October 2001]

Walker, J., 2001. **The Inconstant Moon.** [online]. Fourmilab, Switzerland. Available at <URL:http://www.fourmilab.ch/earthview/moon_ap_per.html> [Accessed 4 October 2001]

Wei, Z., 1999. **A combined adjustment of astro-geodetic network and GPS network in China.** Poster paper at IUGG99 conference at Birmingham, July 1999.

Wells, D., (ed.) 1986. **Guide to GPS Positioning.** Canadian GPS Associates. (s.l.): (s.n.)

Wielen, R., Lederle, T., Schwam, H., 1994. **Apparent Places of Fundamental Stars 1996.** Heidelberg: Astronomisches Rechen-Institut.

Yang, Z., Chen, Y., 2001. **Determination of Hong Kong Gravimetric Geoid.** Survey Review, Vol.36, No.279, January, pp23-34. London: Commonwealth Association of Surveying and Land Economy (CASTLE).

Zhang, K., Featherstone, W., 1997. **A Preliminary Evaluation of the Terrain Effects on the Gravimetric Geoid Determination in Australia.** Gravity, Geoid and Marine Geodesy, – IAG Symposium 117, London: Springer-Verlag.

Zhang, K., Featherstone, W., Stewart, M., Dodson, A., 1998. **A new gravimetric geoid of Australia.** Second Continental Workshop on the Geoid in Europe, – 98:4 Reports of the Finnish Geodetic Institute. Helsinki: Finnish Geodetic Institute.

Annexes

Annex A Elevation and Topographic-Isostatic Graphics

Annex B RMS Solutions for Tests of Polynomial Geoid Models

Annex A

Elevation and Topographic-Isostatic Graphics

This annex contains graphics that relate to Chapter 8 and is concerned with the topographic-isostatic effect upon astronomical position.

Block – Nottingham

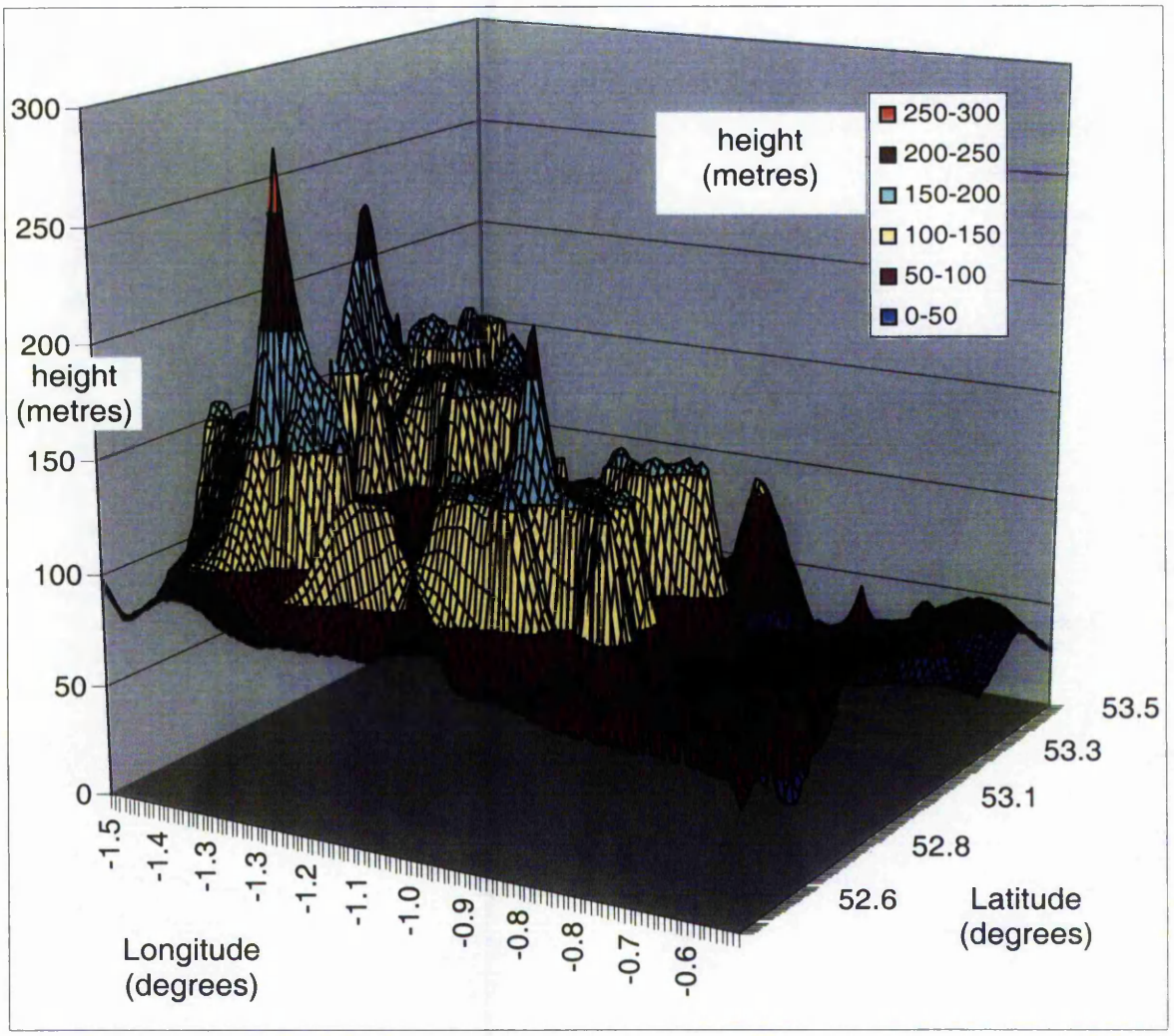

Nottingham Block elevation model

Block - Nottingham

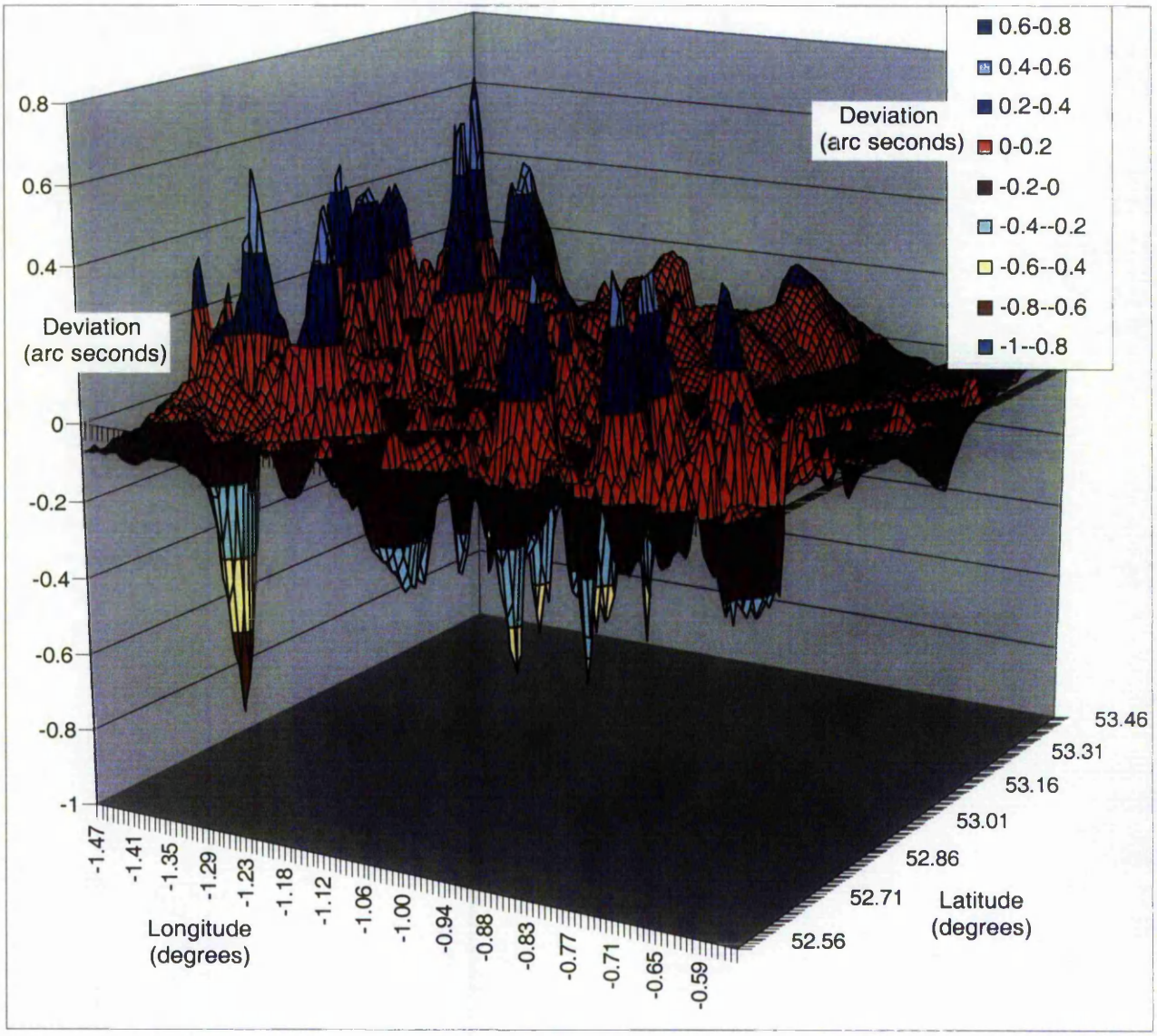

Nottingham Block east-west topographic-isostatic deviation

Block - Nottingham

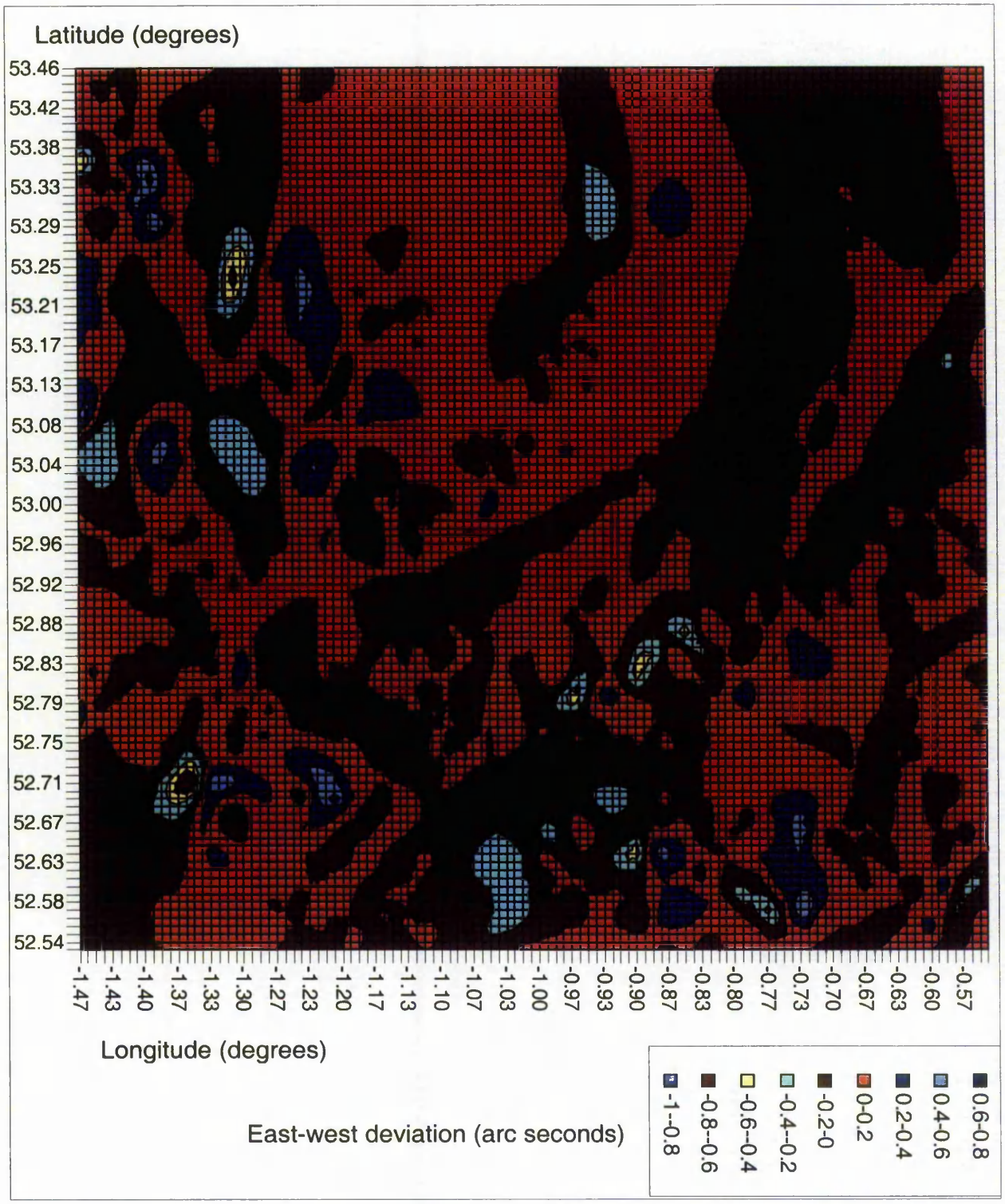

Nottingham Block east-west topographic-isostatic deviation contours

Block - Nottingham

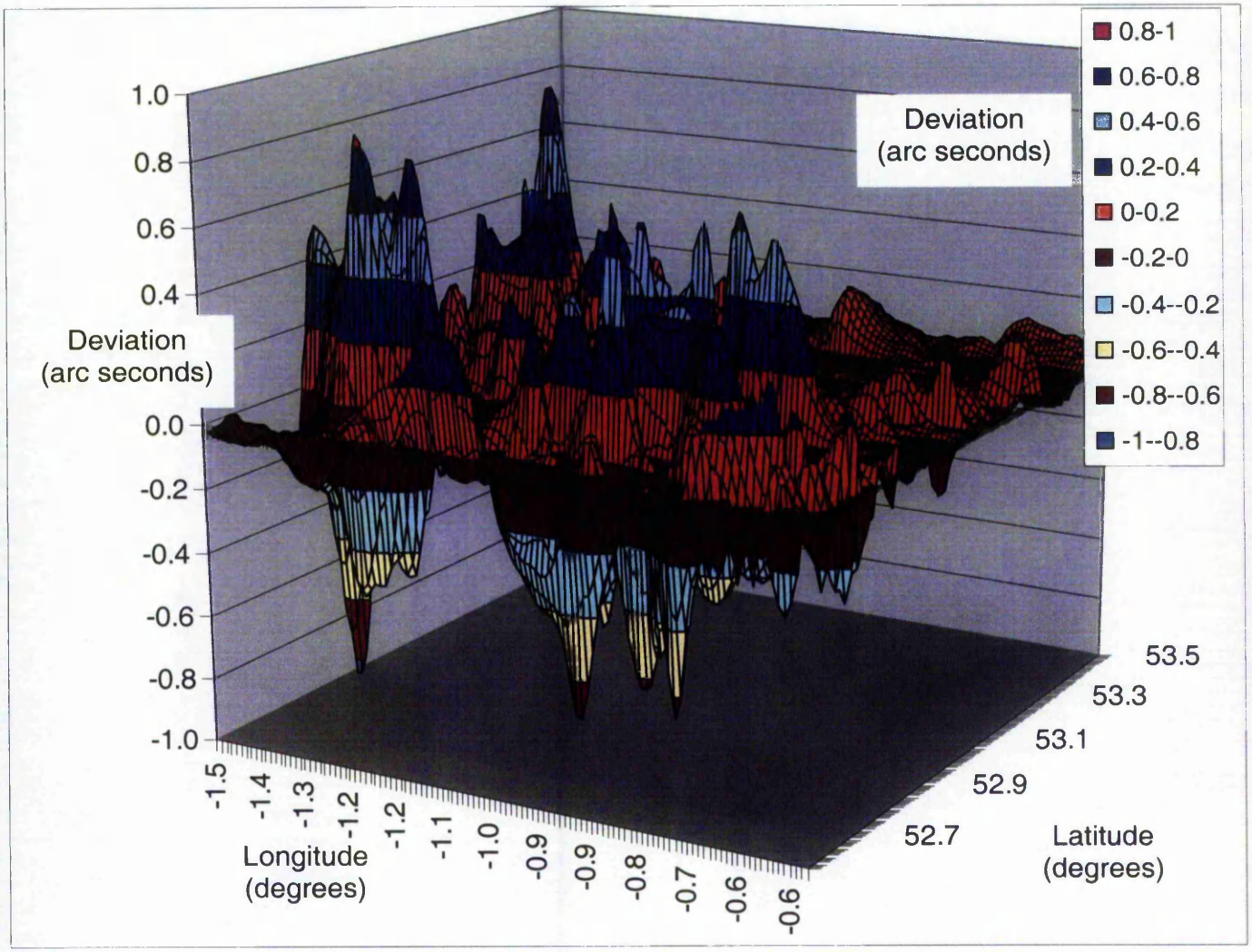

Nottingham Block north-south topographic-isostatic deviation

Block - Nottingham

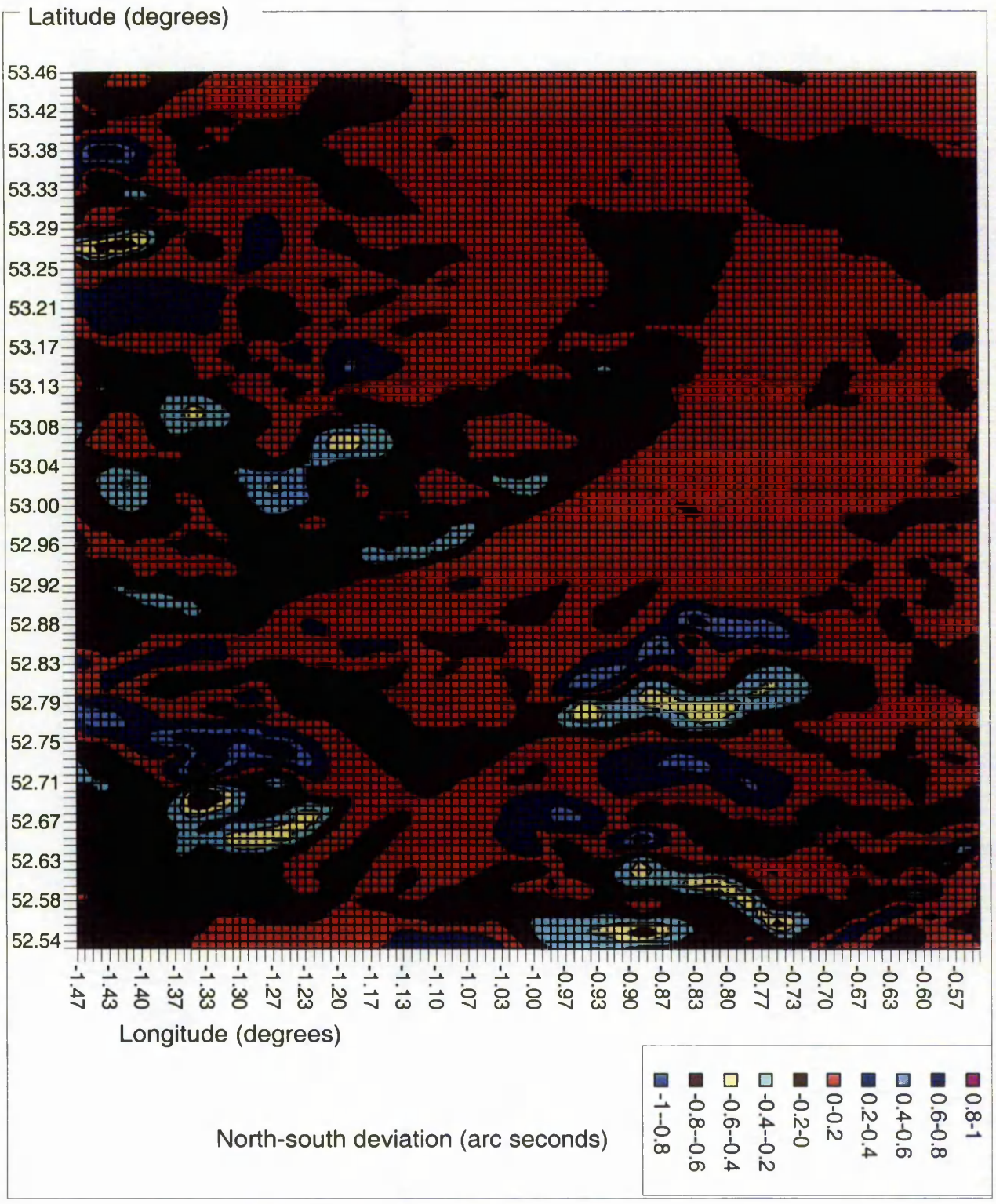

Nottingham Block north-south topographic-isostatic deviation contours

Block – Aviemore

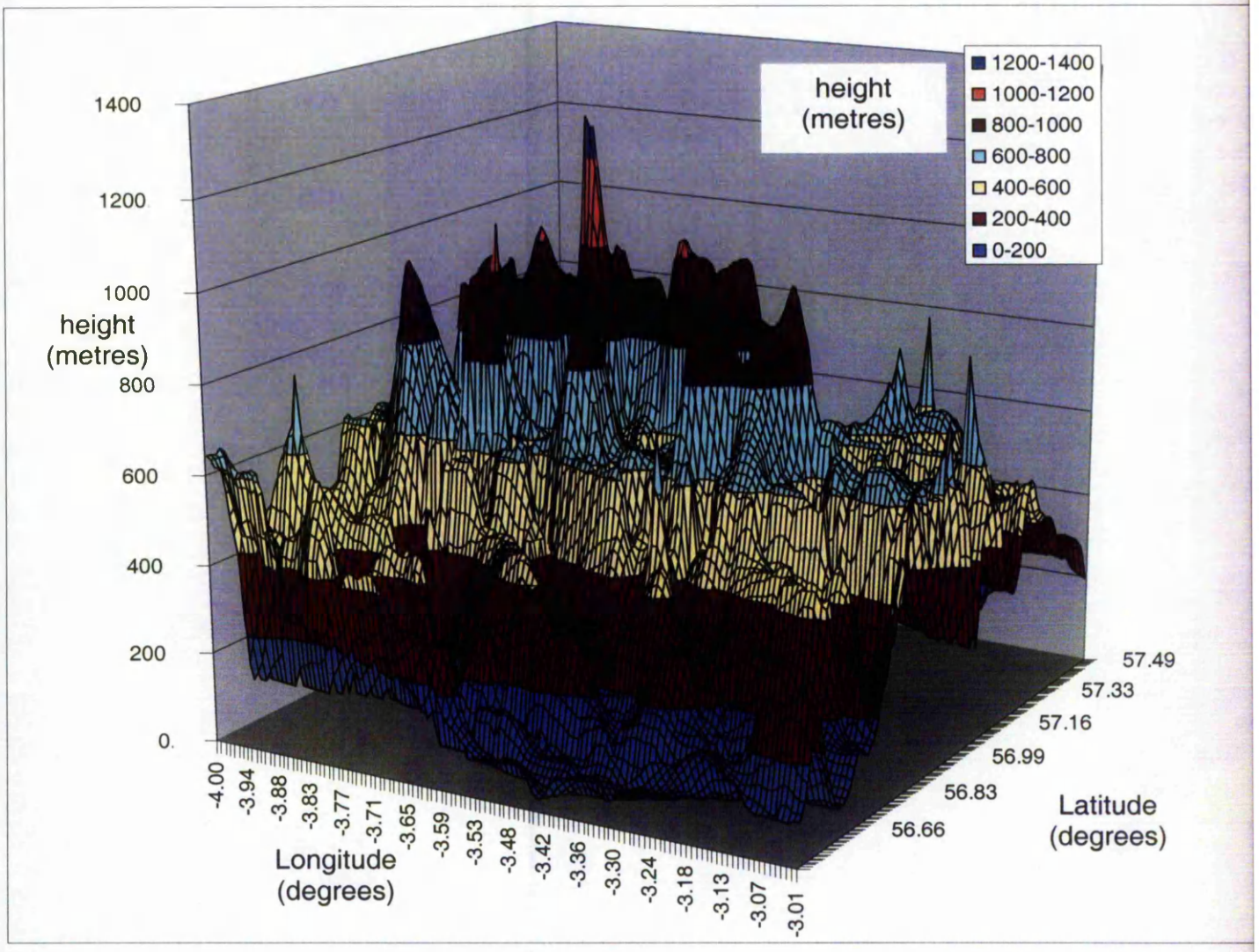

Aviemore Block elevation model

Block - Aviemore

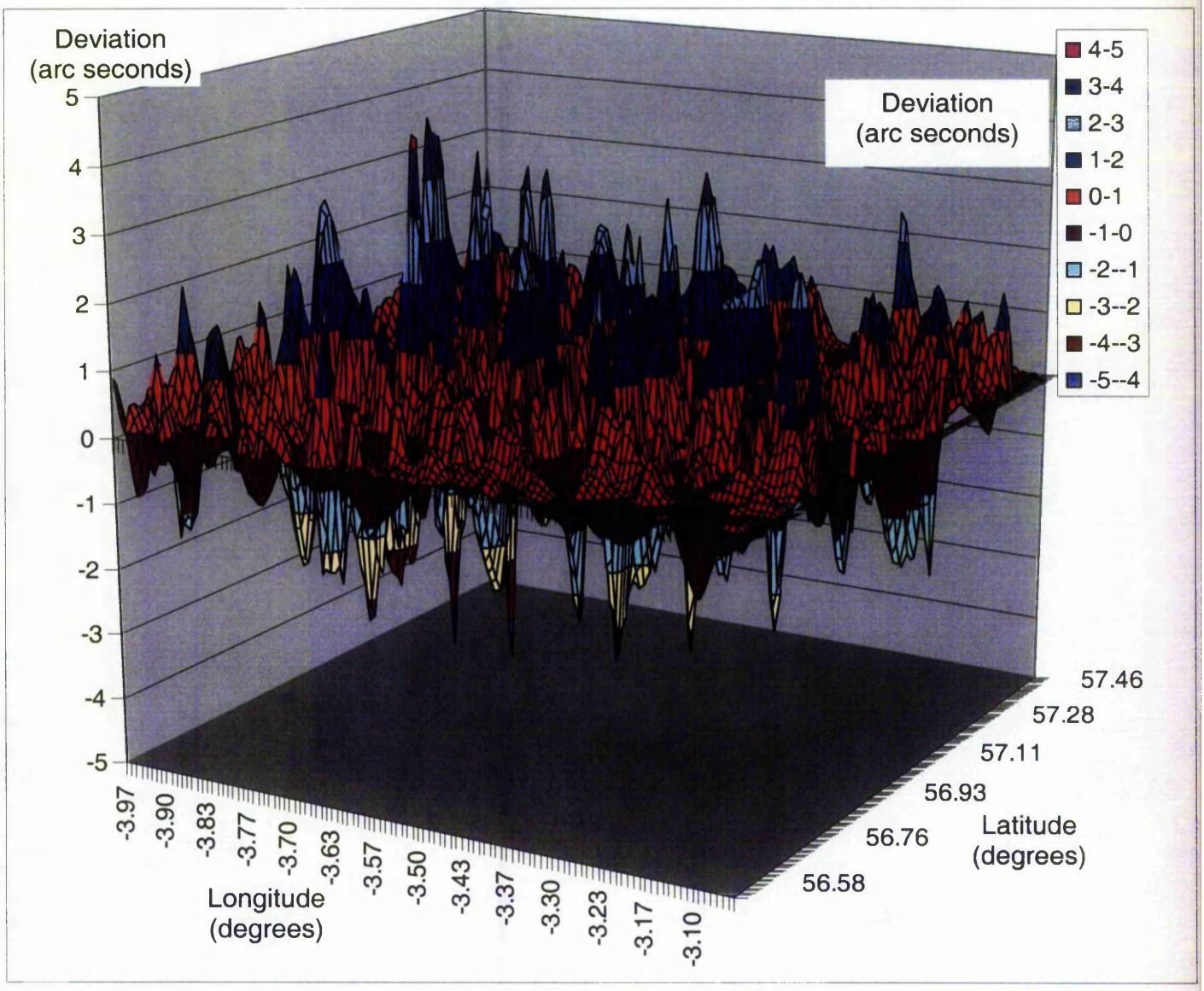

Aviemore Block east-west topographic-isostatic deviation

Block - Aviemore

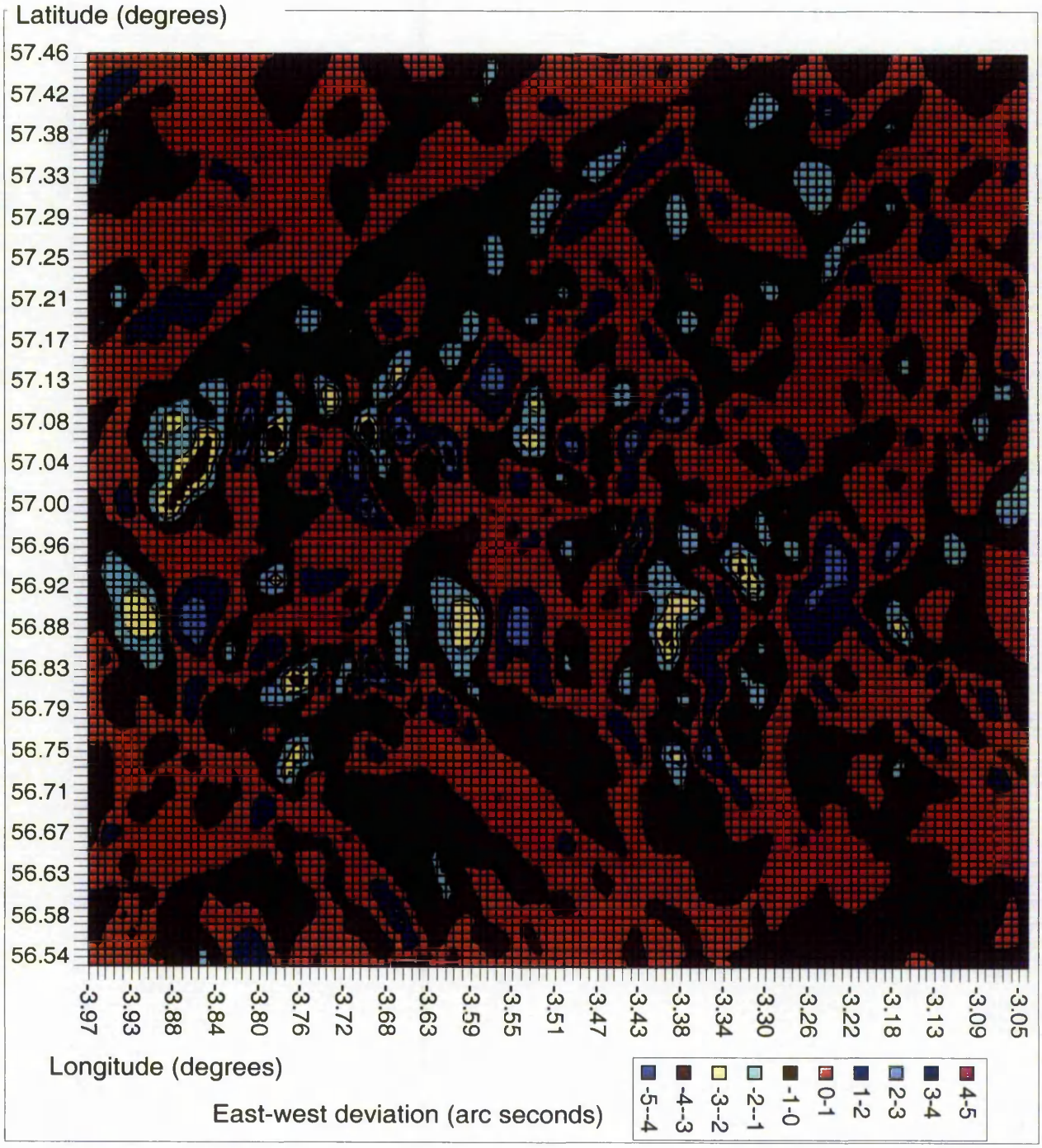

Aviemore Block east-west topographic-isostatic deviation contours

Block - Aviemore

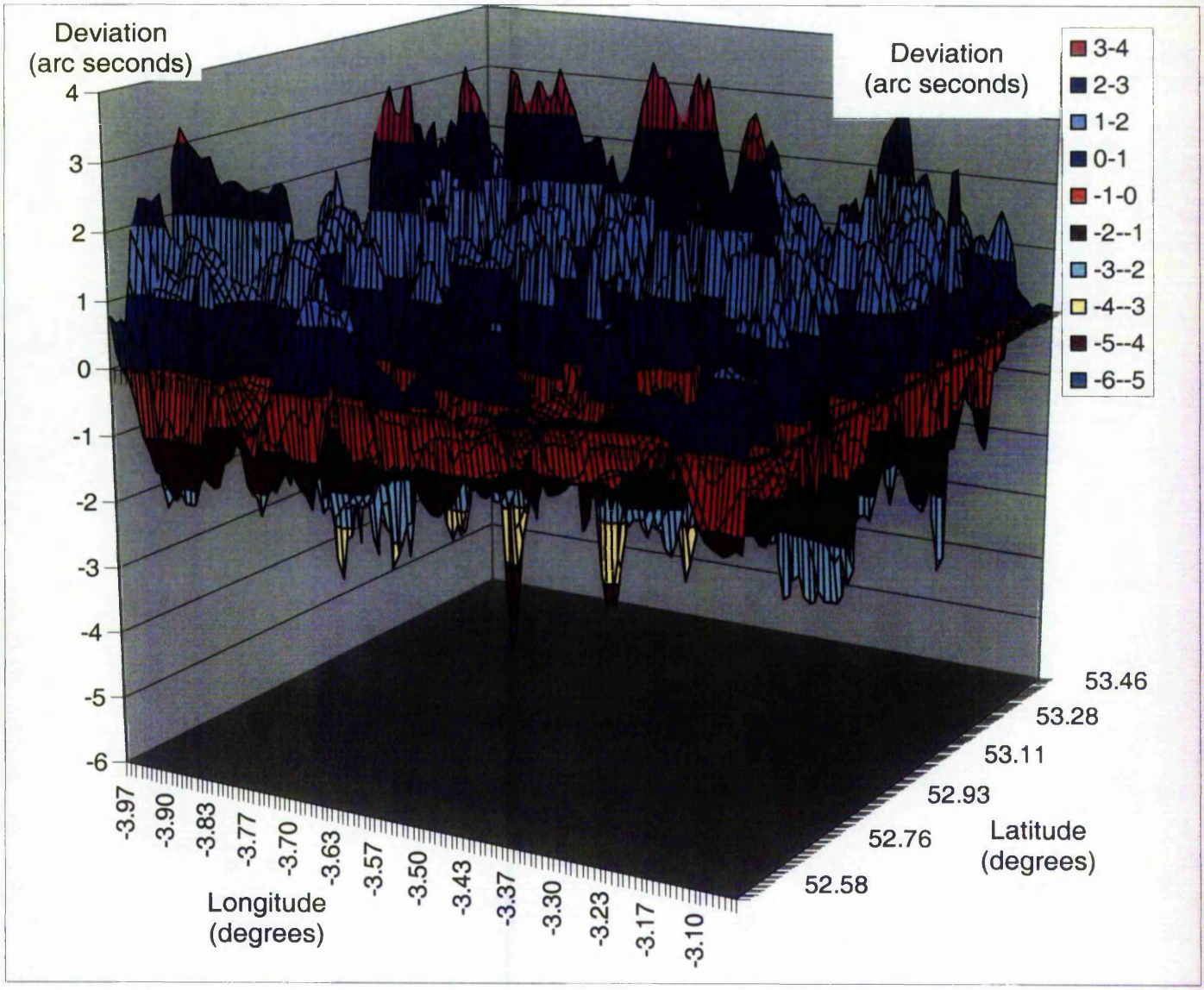

Aviemore Block north-south topographic-isostatic deviation

Block - Aviemore

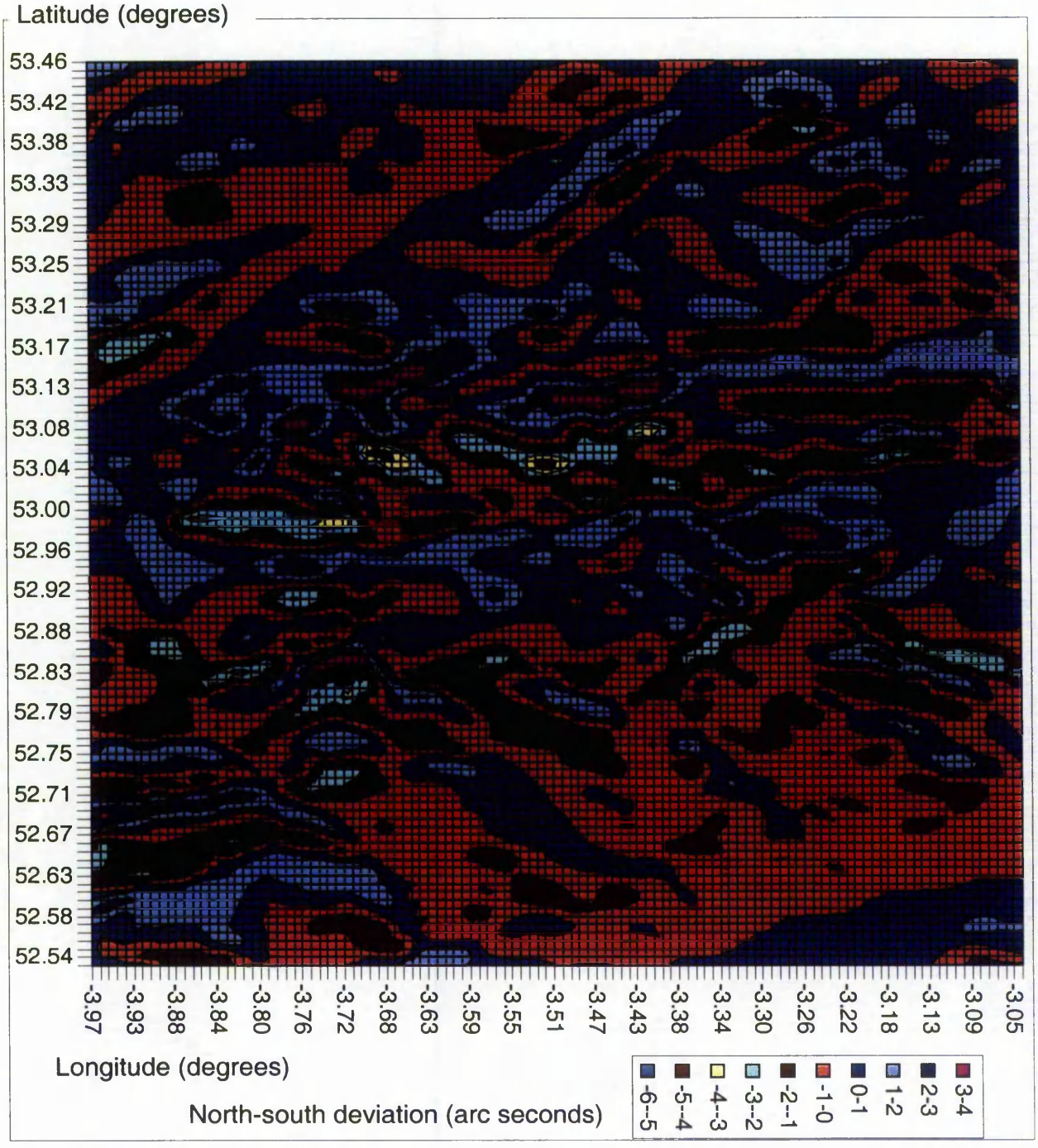

Aviemore Block north-south topographic-isostatic deviation contours

Block – Mt Blanc

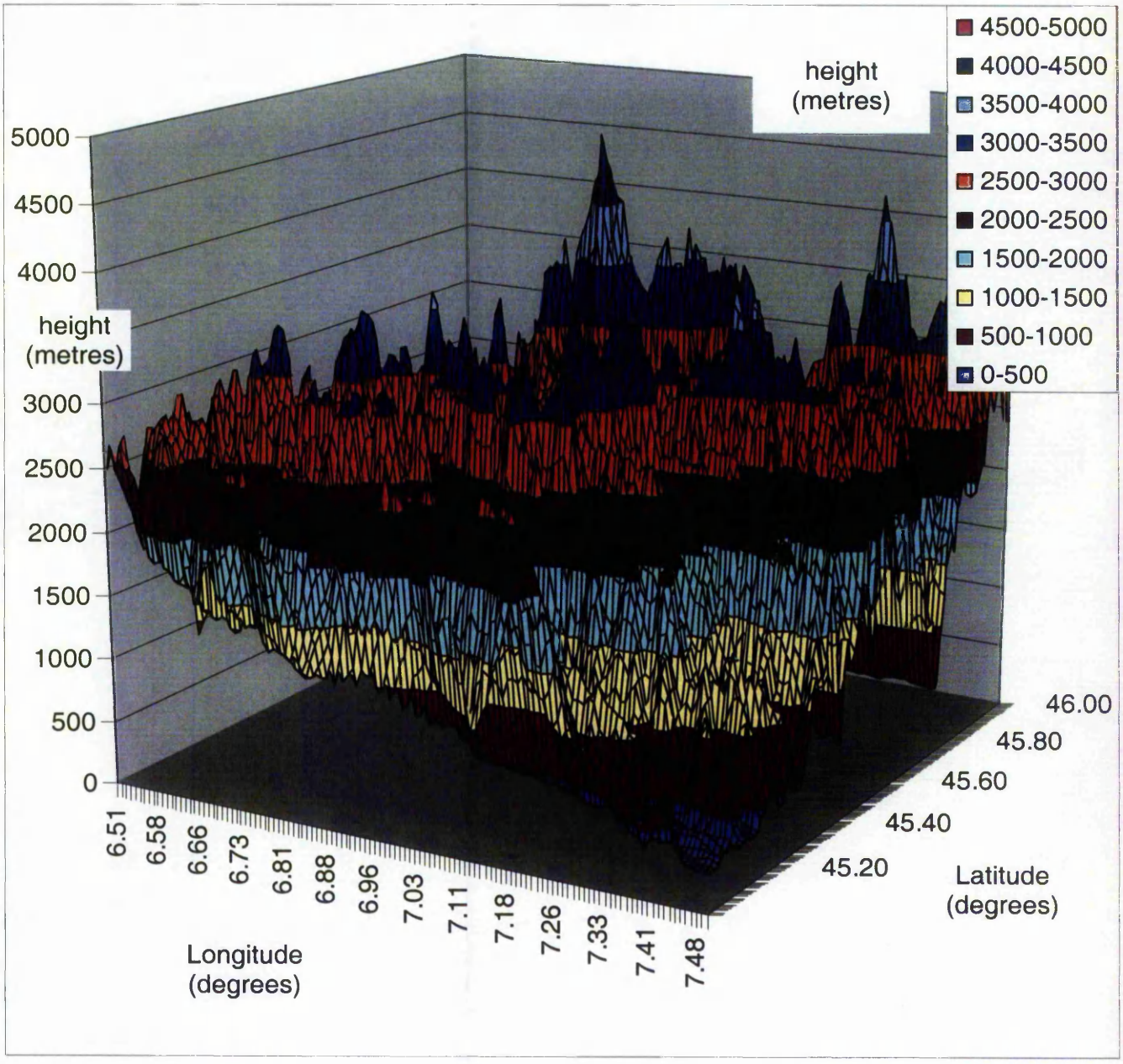

Mt Blanc Block elevation model

Block – Mt Blanc

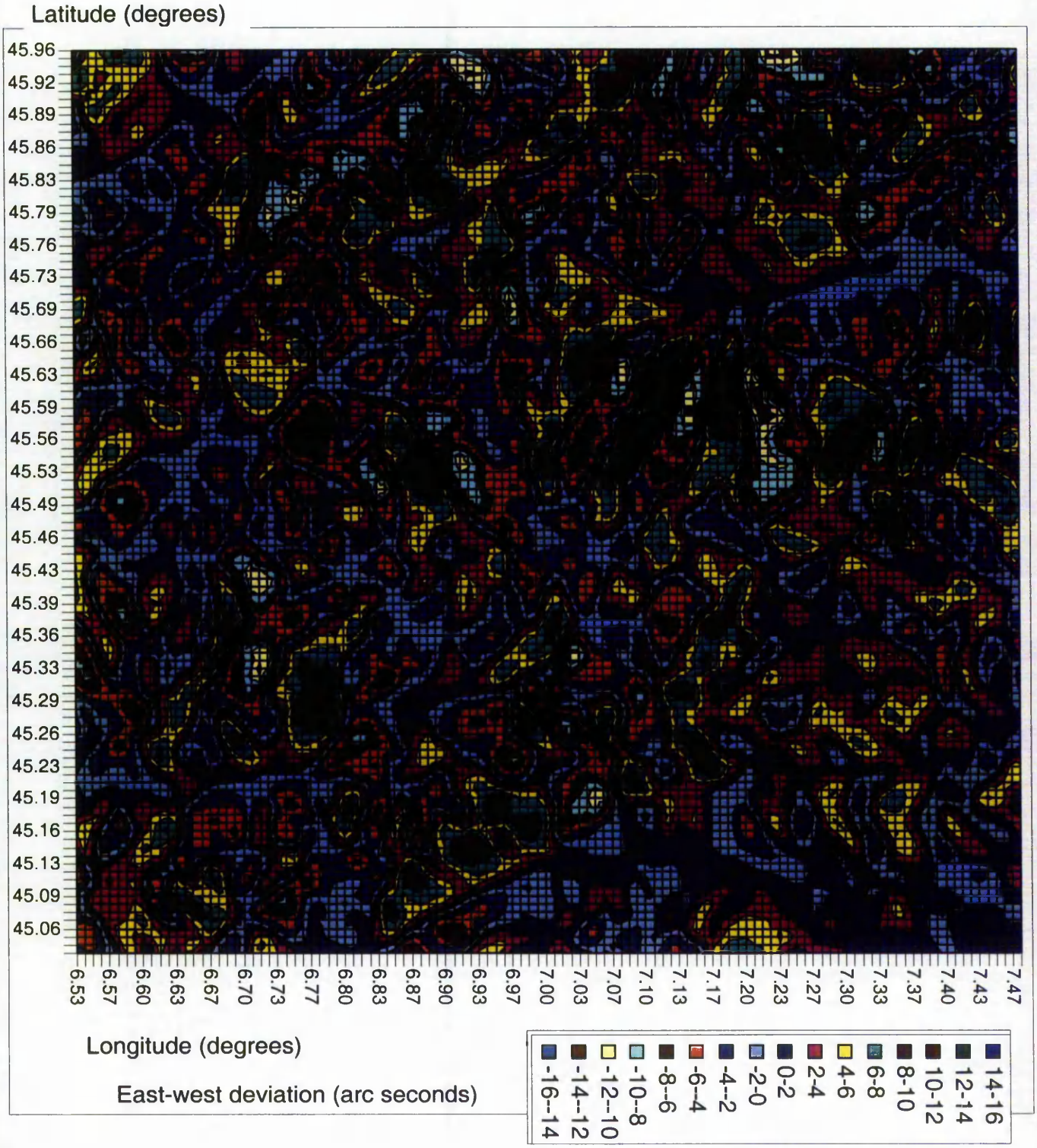

Mt Blanc Block east-west topographic-isostatic deviation contours

Block - Mt Blanc

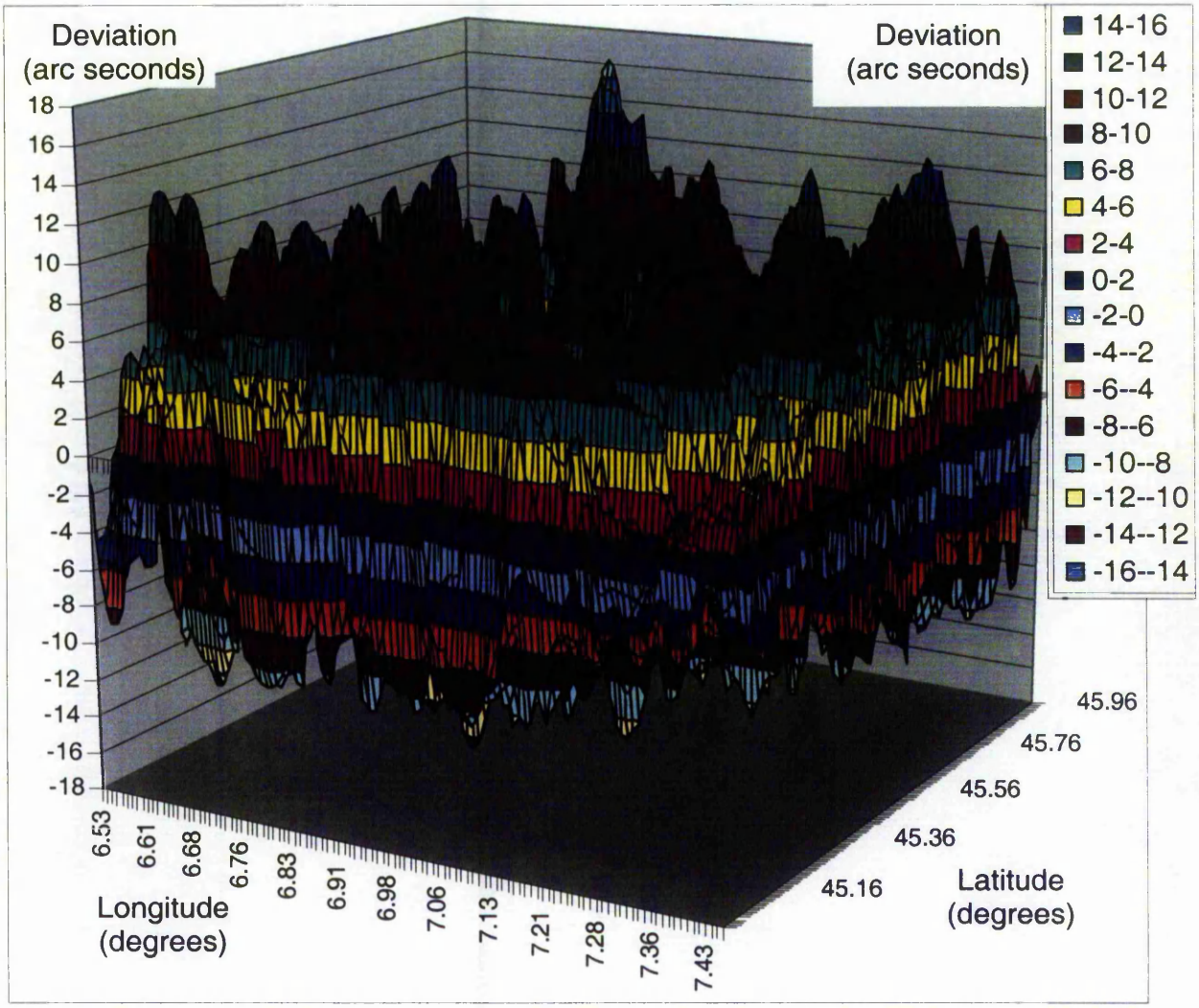

Mt Blanc Block north-south topographic-isostatic deviation

Block – Mt Blanc

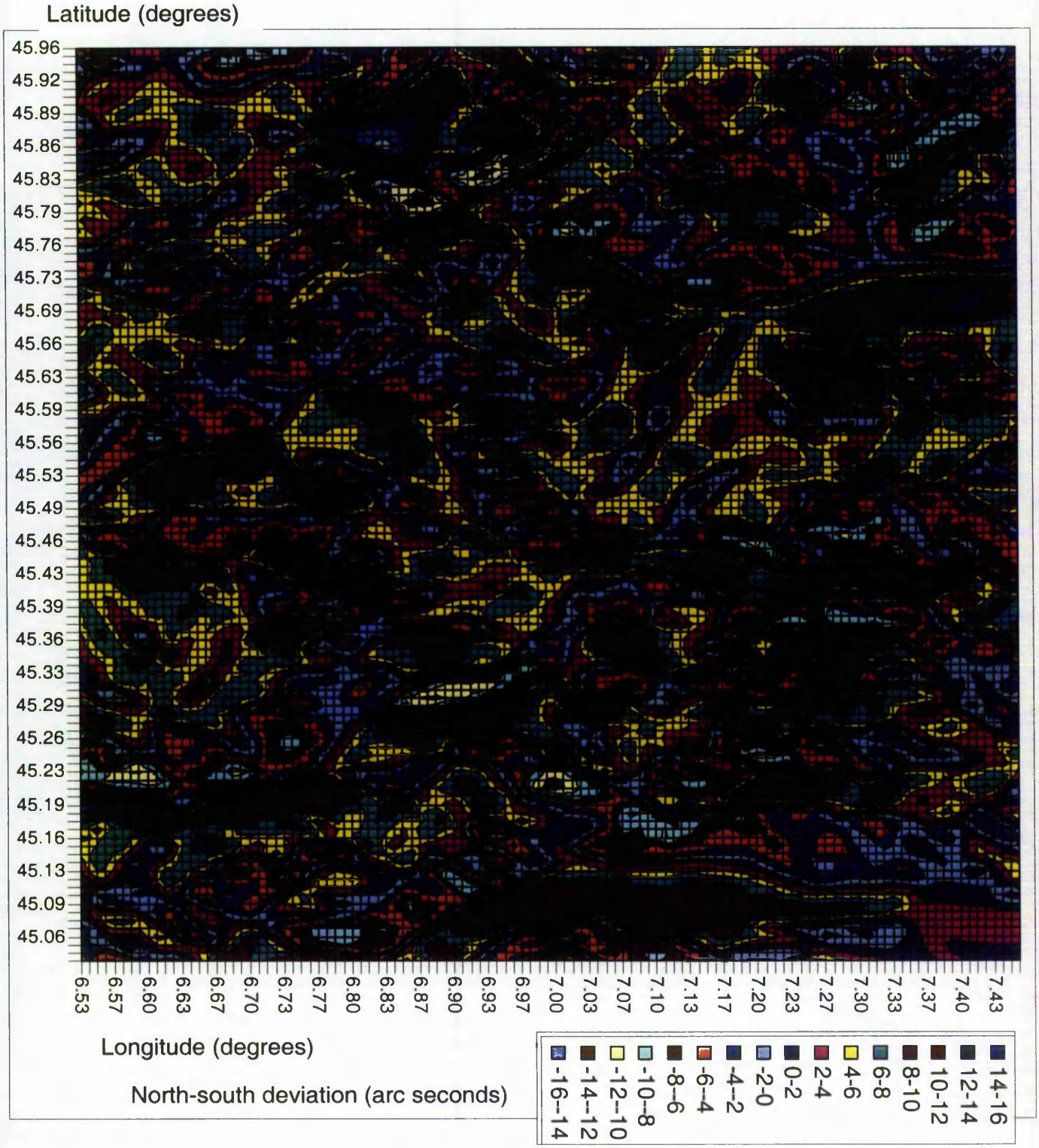

Mt Blanc Block north-south topographic-isostatic deviation contours

Annex B

RMS Solutions for Tests of Polynomial Geoid Models

The graphs in this Annex relate to the text in the Section 10.5 entitled "Geoid Model by Polynomial Coefficients".

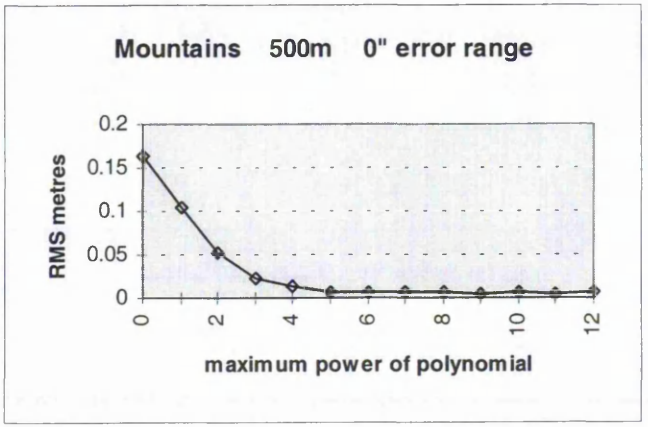
Mountains 500m 0" error range
RMS metres
0.2
0.15
0.1
0.05
0
0 2 4 6 8 10 12
maximum power of polynomial

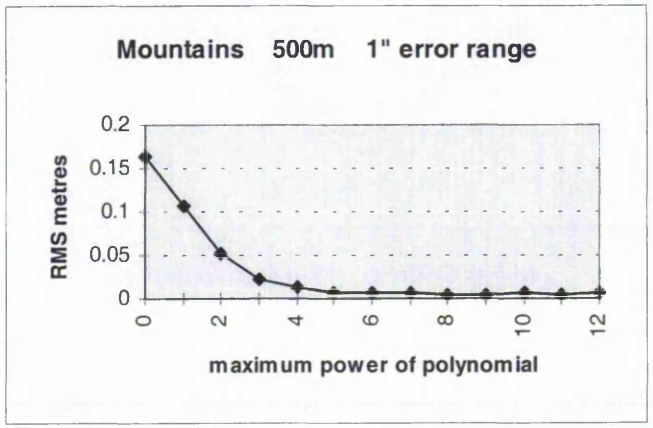
Mountains 500m 1" error range
RMS metres
0.2
0.15
0.1
0.05
0
0 2 4 6 8 10 12
maximum power of polynomial

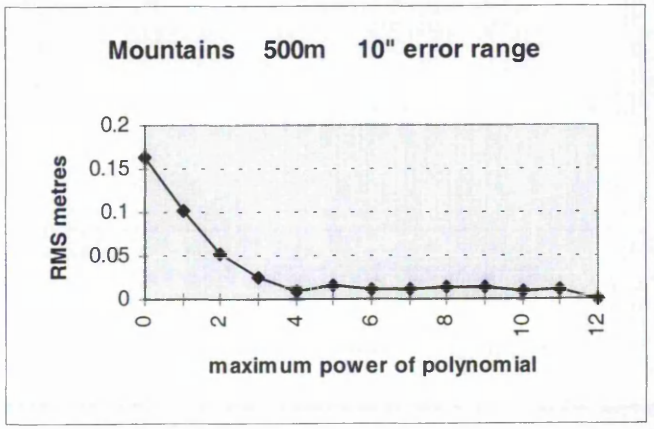
Mountains 500m 10" error range
RMS metres
0.2
0.15
0.1
0.05
0
0 2 4 6 8 10 12
maximum power of polynomial

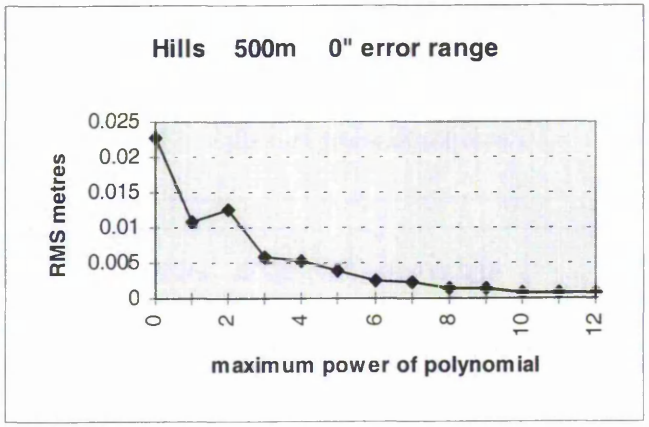
Hills 500m 0" error range
RMS metres
0.025
0.02
0.015
0.01
0.005
0
0 2 4 6 8 10 12
maximum power of polynomial

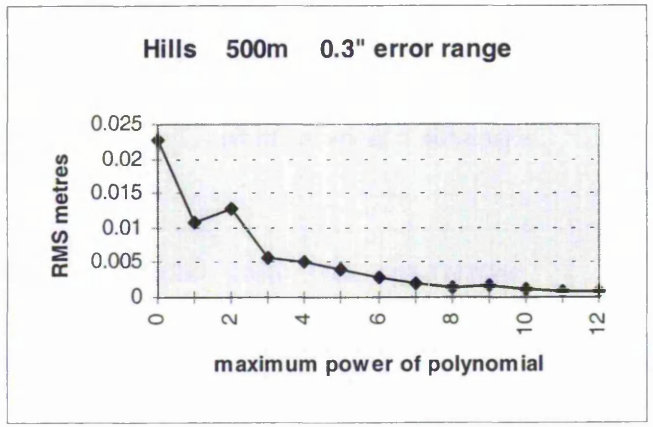
Hills 500m 0.3" error range
RMS metres
0.025
0.02
0.015
0.01
0.005
0
0 2 4 6 8 10 12
maximum power of polynomial

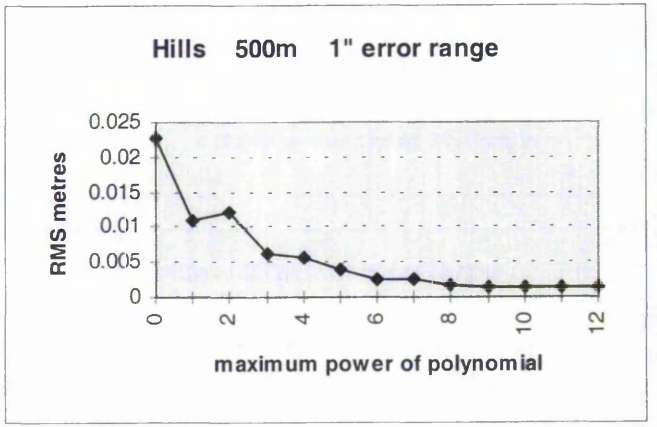
Hills 500m 1" error range
RMS metres
0.025
0.02
0.015
0.01
0.005
0
0 2 4 6 8 10 12
maximum power of polynomial

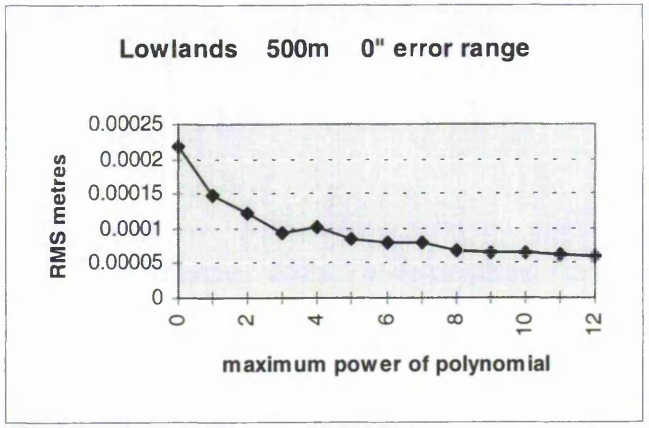
Lowlands 500m 0" error range
RMS metres
0.00025
0.0002
0.00015
0.0001
0.00005
0
0 2 4 6 8 10 12
maximum power of polynomial

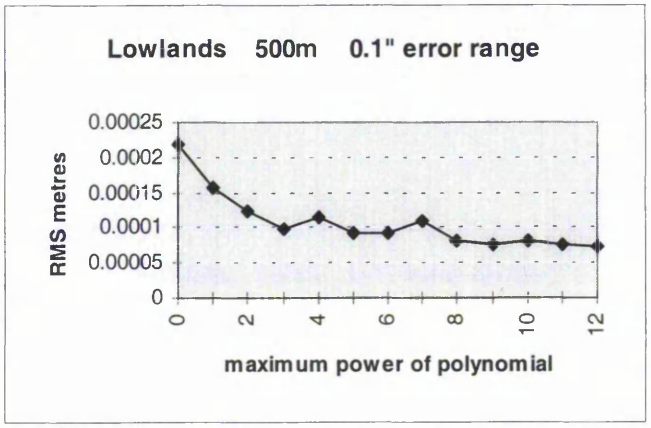
Lowlands 500m 0.1" error range
RMS metres
0.00025
0.0002
0.00015
0.0001
0.00005
0
0 2 4 6 8 10 12
maximum power of polynomial

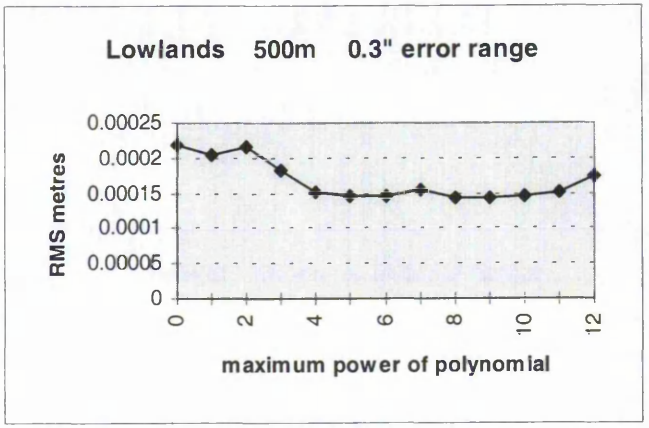
Lowlands 500m 0.3" error range
RMS metres
0.00025
0.0002
0.00015
0.0001
0.00005
0
0 2 4 6 8 10 12
maximum power of polynomial

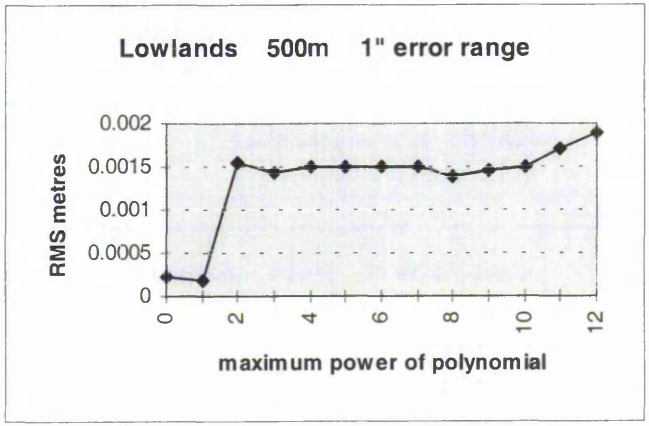
Lowlands 500m 1" error range
RMS metres
0.002
0.0015
0.001
0.0005
0
0 2 4 6 8 10 12
maximum power of polynomial

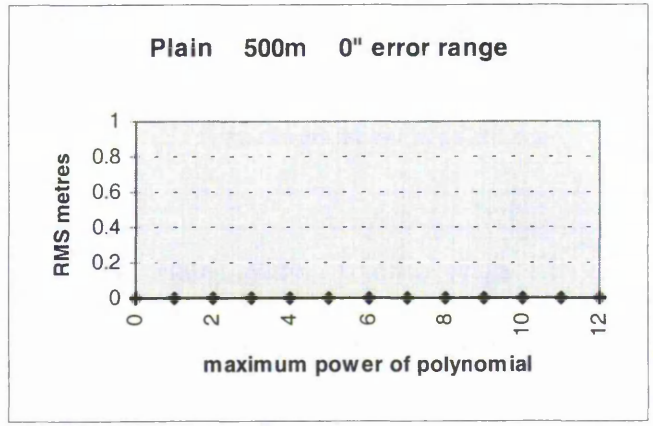
Plain 500m 0" error range
RMS metres
1
0.8
0.6
0.4
0.2
0
0 2 4 6 8 10 12
maximum power of polynomial

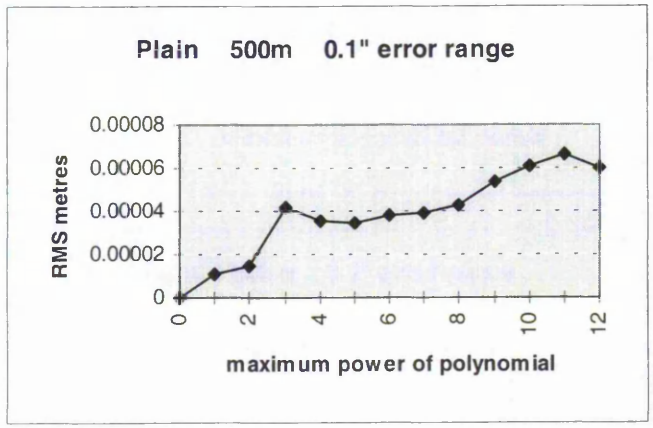
Plain 500m 0.1" error range
RMS metres
0.00008
0.00006
0.00004
0.00002
0
0 2 4 6 8 10 12
maximum power of polynomial

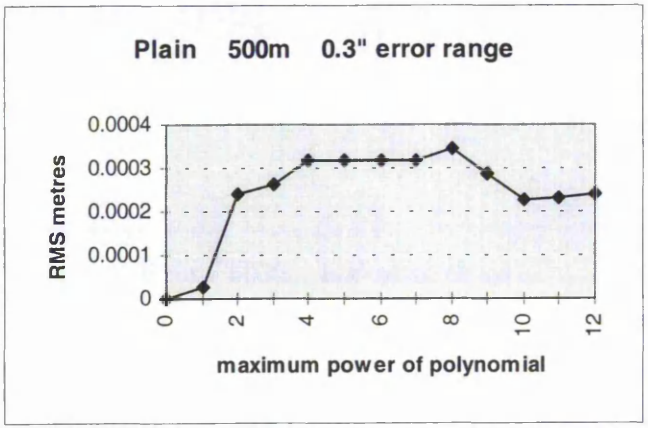
Plain 500m 0.3" error range
RMS metres
0.0004
0.0003
0.0002
0.0001
0
0 2 4 6 8 10 12
maximum power of polynomial

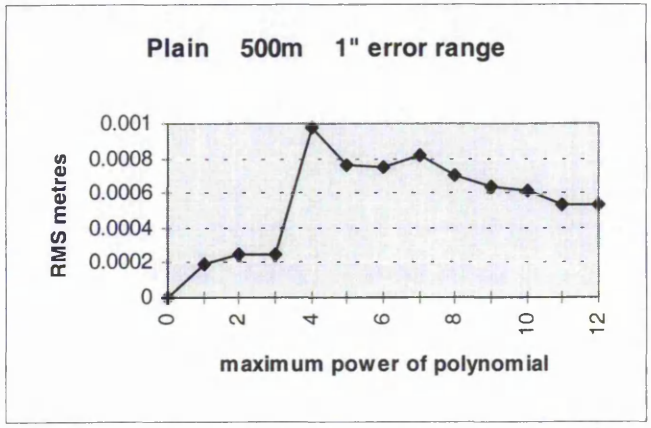
Plain 500m 1" error range
RMS metres
0.001
0.0008
0.0006
0.0004
0.0002
0
0 2 4 6 8 10 12
maximum power of polynomial

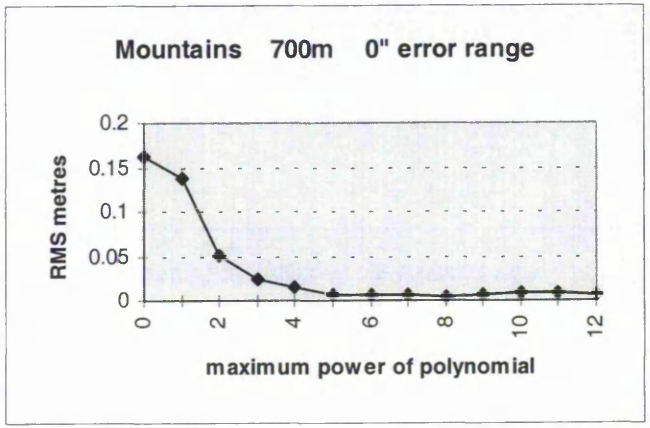
Mountains 700m 0" error range
RMS metres
0.2
0.15
0.1
0.05
0
0 2 4 6 8 10 12
maximum power of polynomial

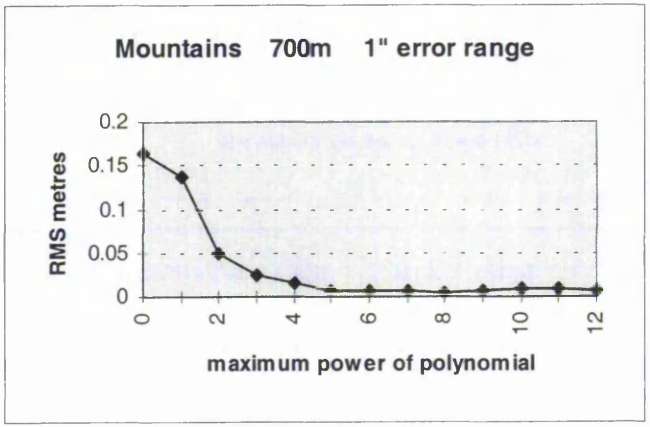
Mountains 700m 1" error range
RMS metres
0.2
0.15
0.1
0.05
0
0 2 4 6 8 10 12
maximum power of polynomial

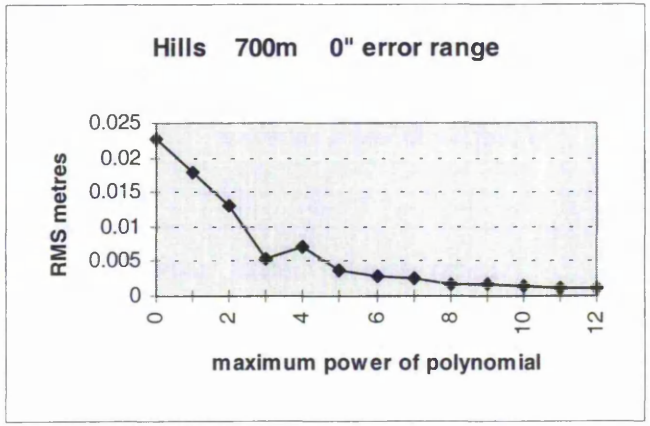
Hills 700m 0" error range
RMS metres
0.025
0.02
0.015
0.01
0.005
0
0 2 4 6 8 10 12
maximum power of polynomial

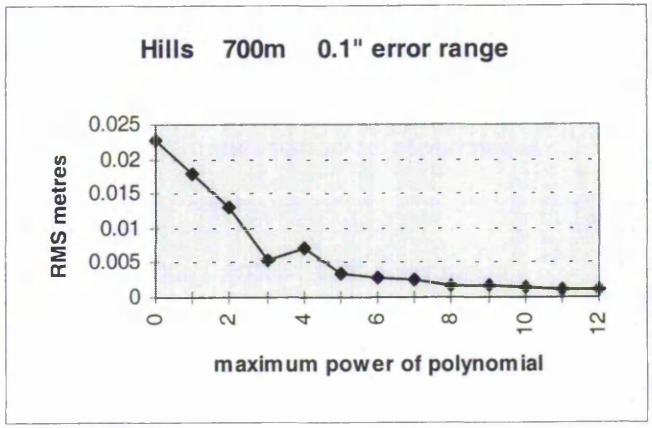
Hills 700m 0.1" error range
RMS metres
0.025
0.02
0.015
0.01
0.005
0
0 2 4 6 8 10 12
maximum power of polynomial

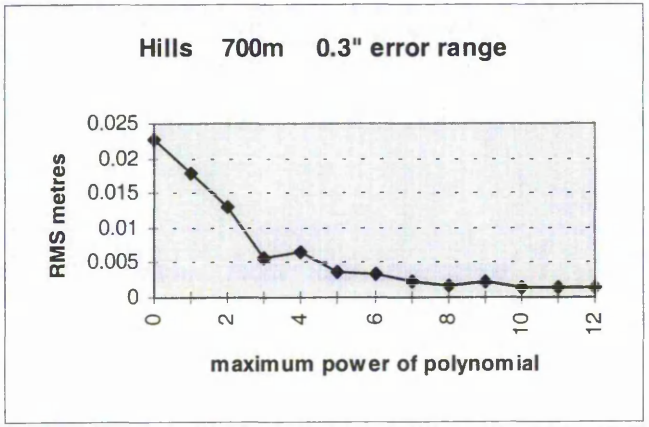
Hills 700m 0.3" error range
RMS metres
0.025
0.02
0.015
0.01
0.005
0
0 2 4 6 8 10 12
maximum power of polynomial

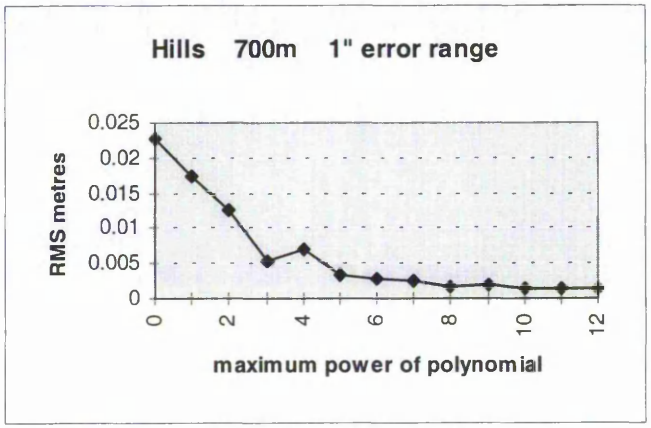
Hills 700m 1" error range
RMS metres
0.025
0.02
0.015
0.01
0.005
0
0 2 4 6 8 10 12
maximum power of polynomial

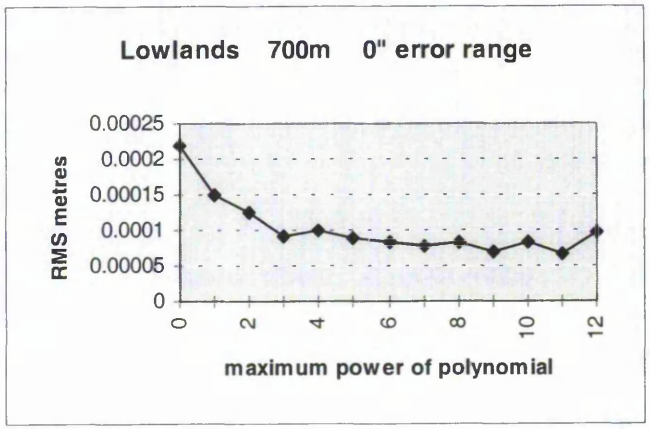
Lowlands 700m 0" error range
RMS metres
0.00025
0.0002
0.00015
0.0001
0.00005
0
0 2 4 6 8 10 12
maximum power of polynomial

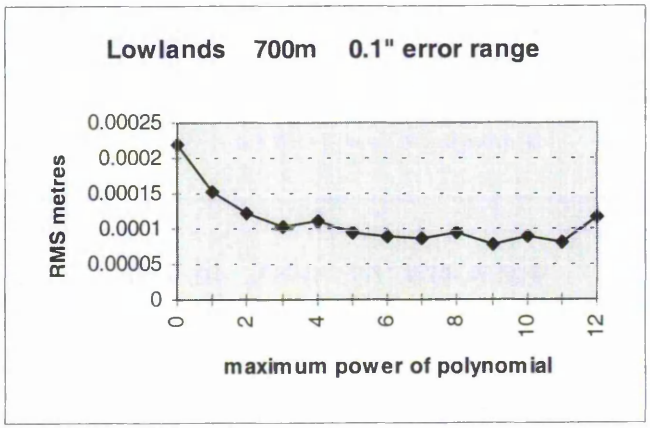
Lowlands 700m 0.1" error range
RMS metres
0.00025
0.0002
0.00015
0.0001
0.00005
0
0 2 4 6 8 10 12
maximum power of polynomial

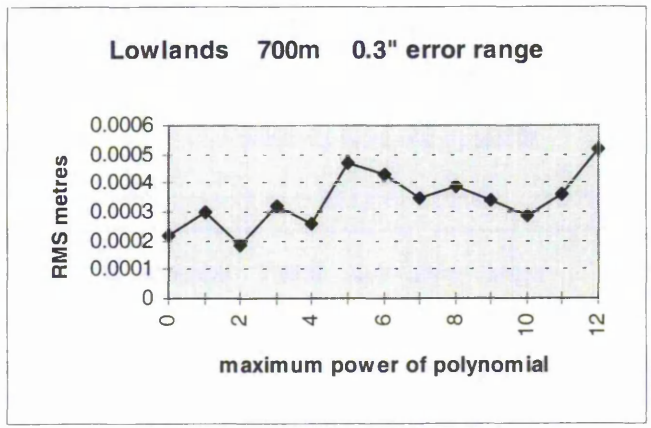
Lowlands 700m 0.3" error range
RMS metres
0.0006
0.0005
0.0004
0.0003
0.0002
0.0001
0
0 2 4 6 8 10 12
maximum power of polynomial

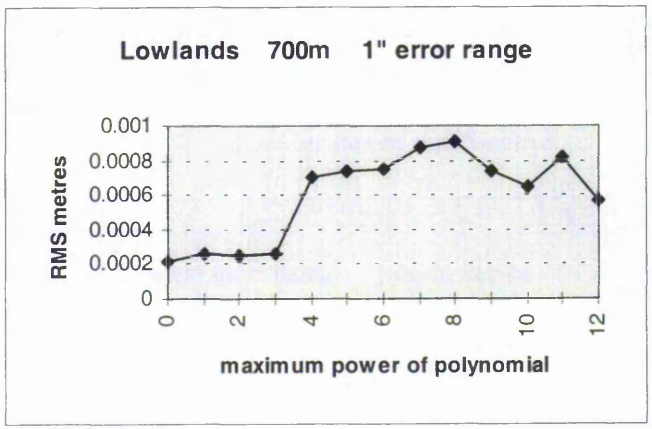
Lowlands 700m 1" error range
RMS metres
0.001
0.0008
0.0006
0.0004
0.0002
0
0 2 4 6 8 10 12
maximum power of polynomial

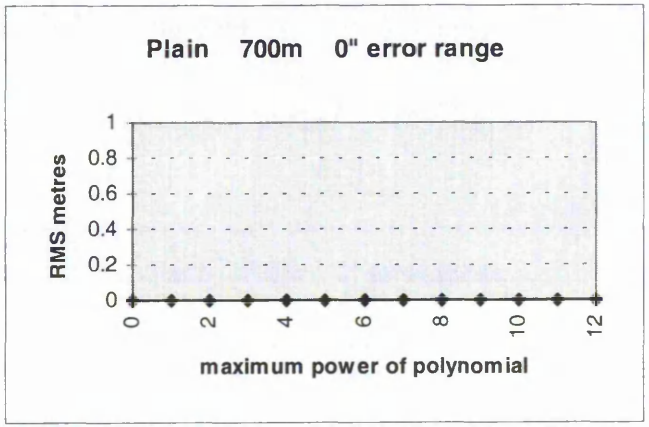
Plain 700m 0" error range
RMS metres
1
0.8
0.6
0.4
0.2
0
0 2 4 6 8 10 12
maximum power of polynomial

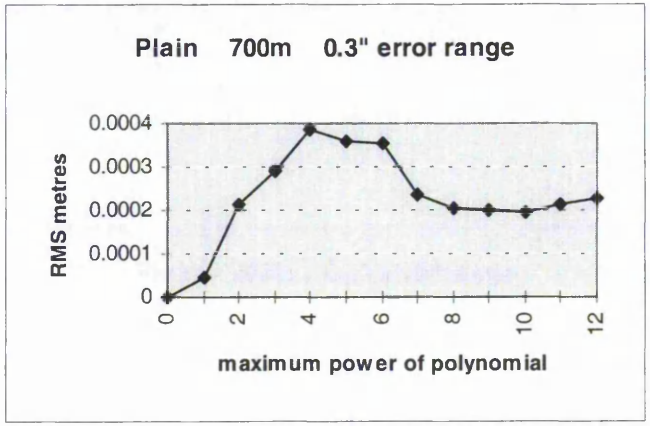
Plain 700m 0.3" error range
RMS metres
0.0004
0.0003
0.0002
0.0001
0
0 2 4 6 8 10 12
maximum power of polynomial

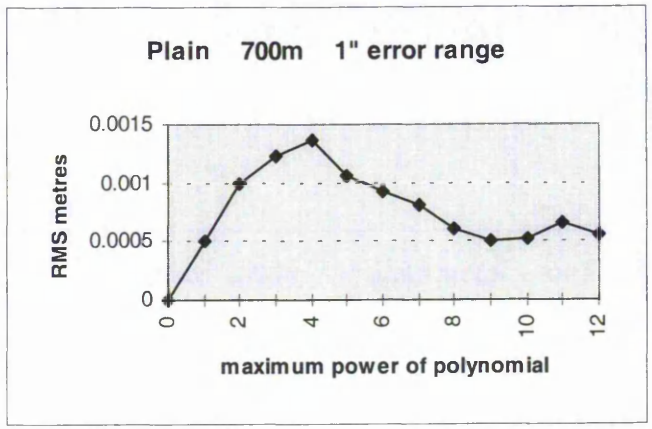
Plain 700m 1" error range
RMS metres
0.0015
0.001
0.0005
0
0 2 4 6 8 10 12
maximum power of polynomial

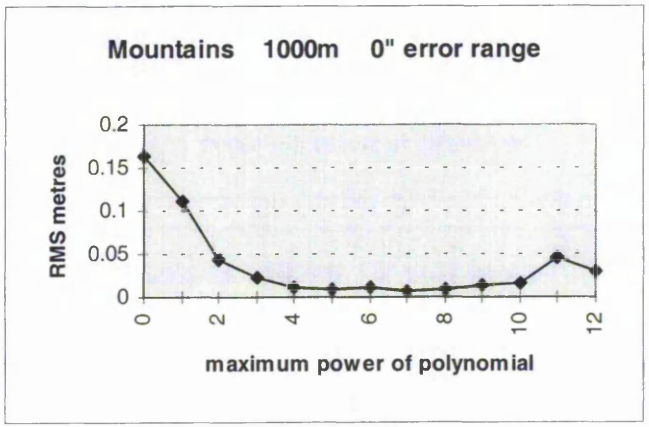
Mountains 1000m 0" error range
RMS metres
0.2
0.15
0.1
0.05
0
0 2 4 6 8 10 12
maximum power of polynomial

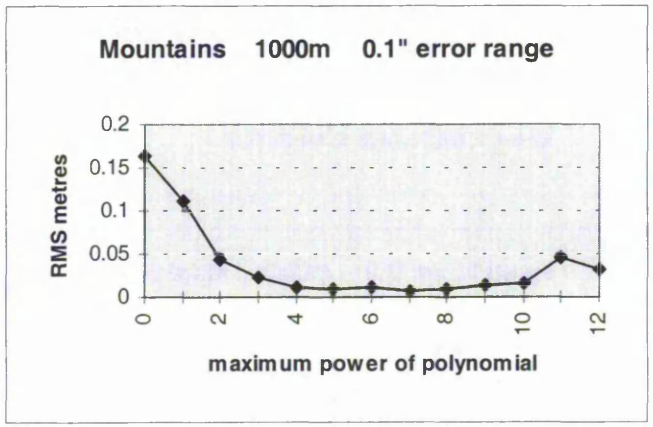
Mountains 1000m 0.1" error range
RMS metres
0.2
0.15
0.1
0.05
0
0 2 4 6 8 10 12
maximum power of polynomial

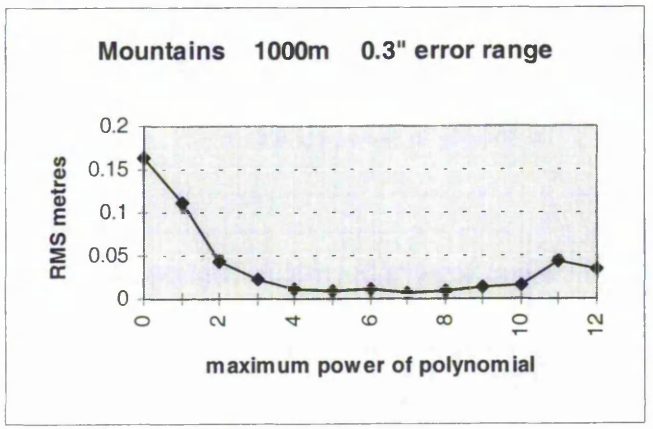
Mountains 1000m 0.3" error range
RMS metres
0.2
0.15
0.1
0.05
0
0 2 4 6 8 10 12
maximum power of polynomial

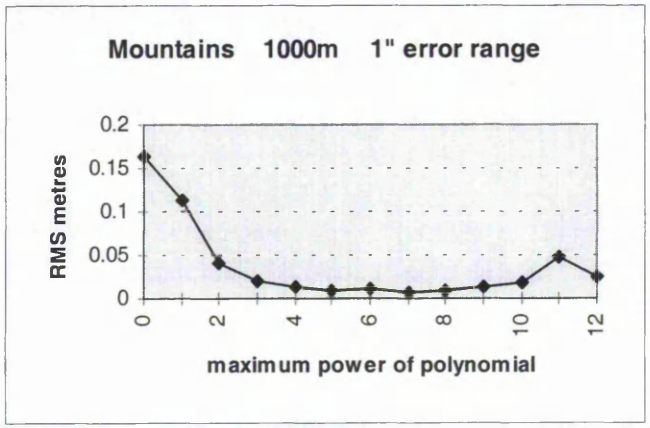
Mountains 1000m 1" error range
RMS metres
0.2
0.15
0.1
0.05
0
0 2 4 6 8 10 12
maximum power of polynomial

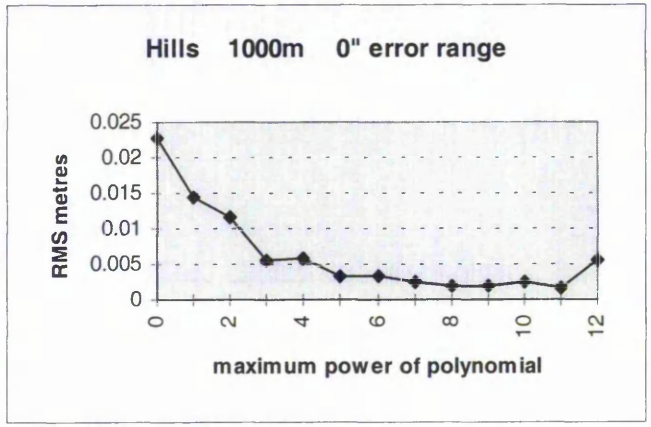
Hills 1000m 0" error range
RMS metres
0.025
0.02
0.015
0.01
0.005
0
0 2 4 6 8 10 12
maximum power of polynomial

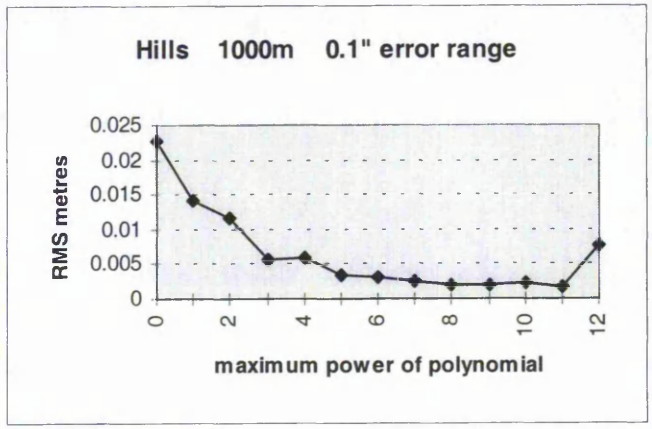
Hills 1000m 0.1" error range
RMS metres
0.025
0.02
0.015
0.01
0.005
0
0 2 4 6 8 10 12
maximum power of polynomial

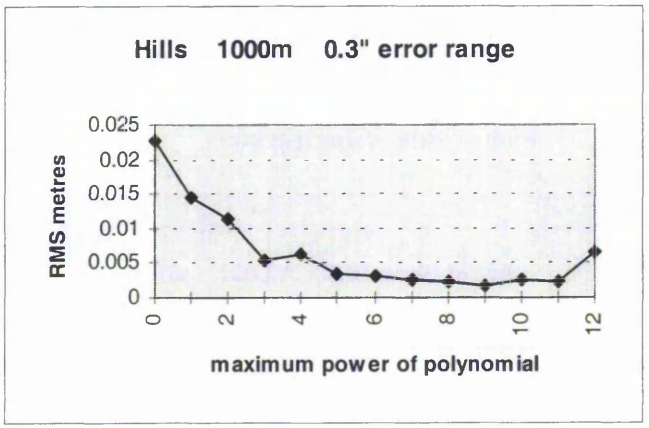
Hills 1000m 0.3" error range
RMS metres
0.025
0.02
0.015
0.01
0.005
0
0 2 4 6 8 10 12
maximum power of polynomial

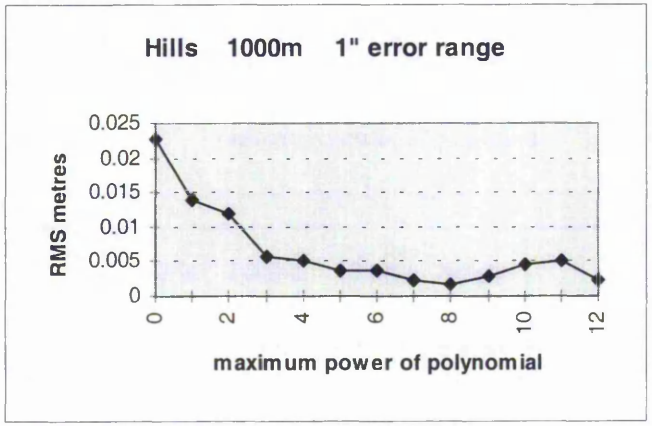
Hills 1000m 1" error range
RMS metres
0.025
0.02
0.015
0.01
0.005
0
0 2 4 6 8 10 12
maximum power of polynomial

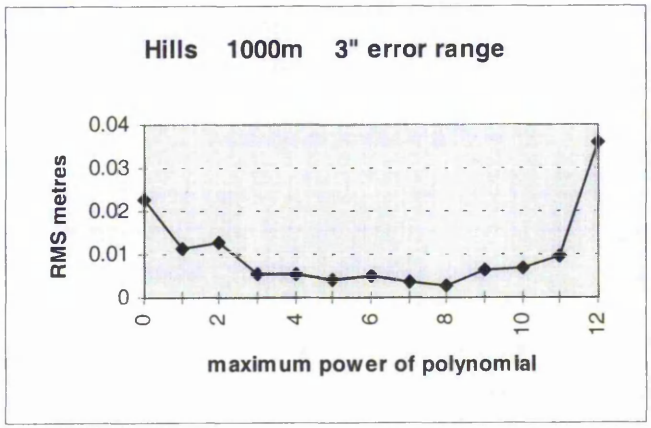
Hills 1000m 3" error range
RMS metres
0.04
0.03
0.02
0.01
0
0 2 4 6 8 10 12
maximum power of polynomial

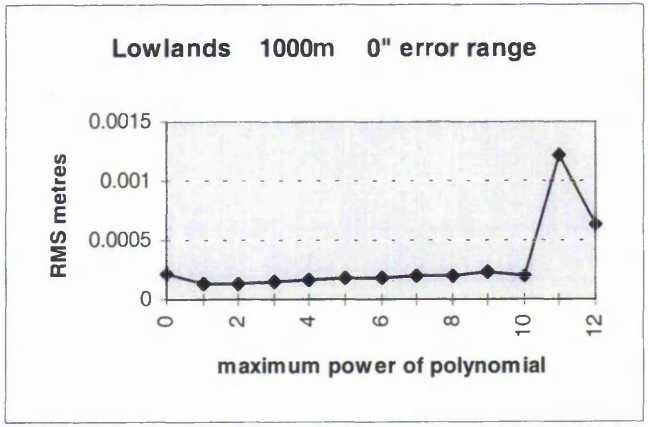
Lowlands 1000m 0" error range
RMS metres
0.0015
0.001
0.0005
0
0 2 4 6 8 10 12
maximum power of polynomial

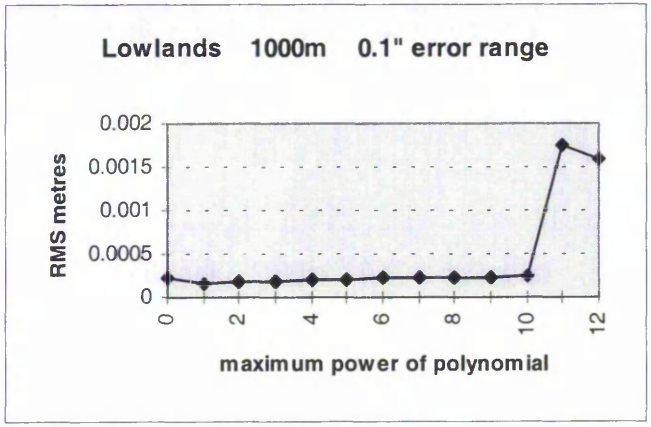
Lowlands 1000m 0.1" error range
RMS metres
0.002
0.0015
0.001
0.0005
0
0 2 4 6 8 10 12
maximum power of polynomial

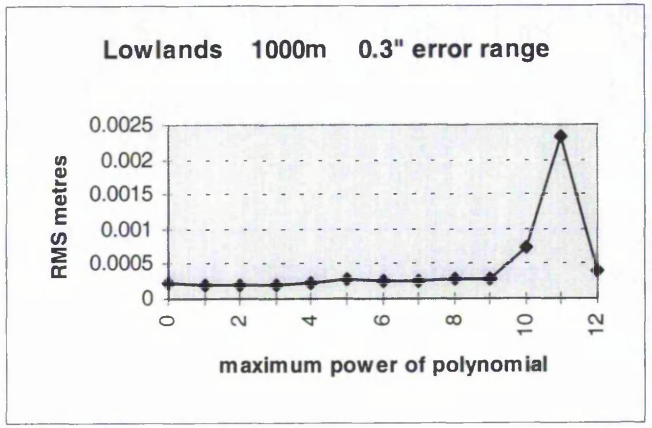
Lowlands 1000m 0.3" error range
RMS metres
0.0025
0.002
0.0015
0.001
0.0005
0
0 2 4 6 8 10 12
maximum power of polynomial

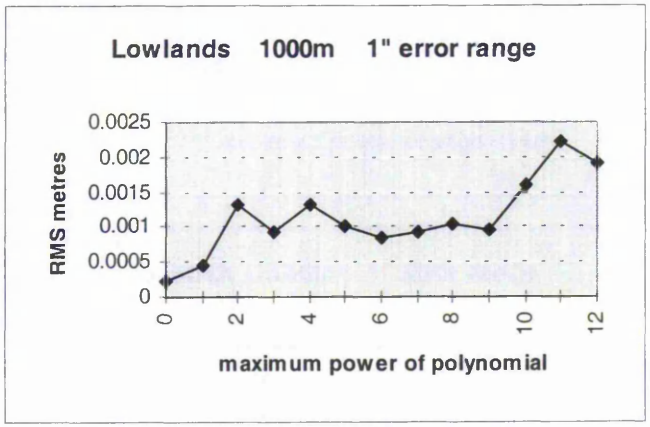
Lowlands 1000m 1" error range
RMS metres
0.0025
0.002
0.0015
0.001
0.0005
0
0 2 4 6 8 10 12
maximum power of polynomial

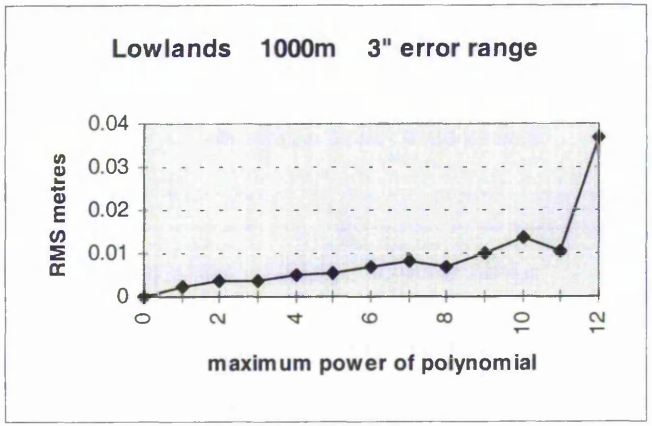
Lowlands 1000m 3" error range
RMS metres
0.04
0.03
0.02
0.01
0
0 2 4 6 8 10 12
maximum power of polynomial

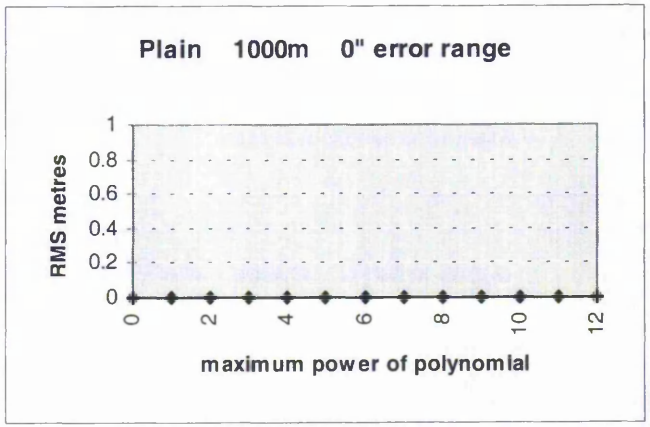
Plain 1000m 0" error range
RMS metres
1
0.8
0.6
0.4
0.2
0
0 2 4 6 8 10 12
maximum power of polynomial

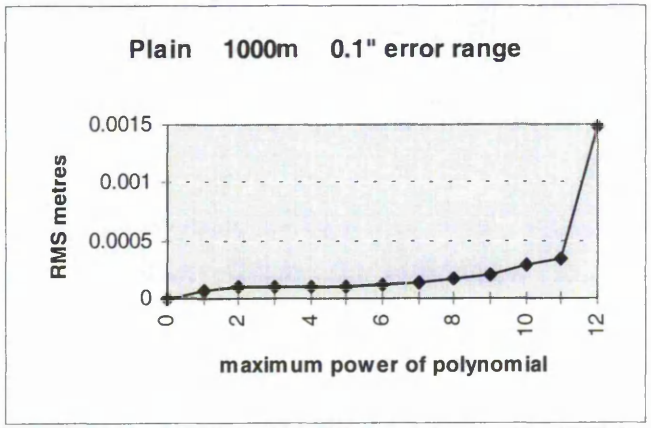
Plain 1000m 0.1" error range
RMS metres
0.0015
0.001
0.0005
0
0 2 4 6 8 10 12
maximum power of polynomial

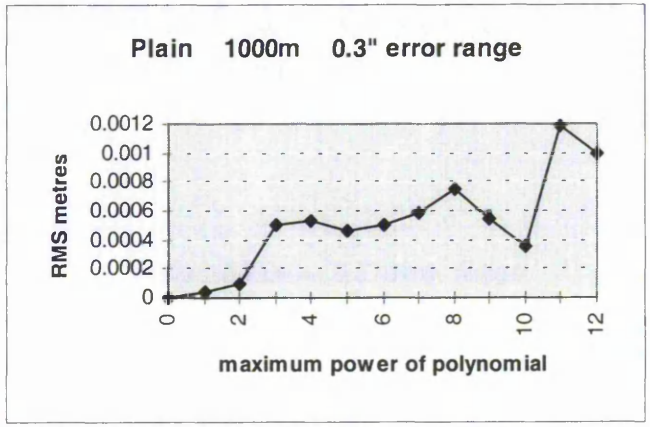
Plain 1000m 0.3" error range
RMS metres
0.0012
0.001
0.0008
0.0006
0.0004
0.0002
0
0 2 4 6 8 10 12
maximum power of polynomial

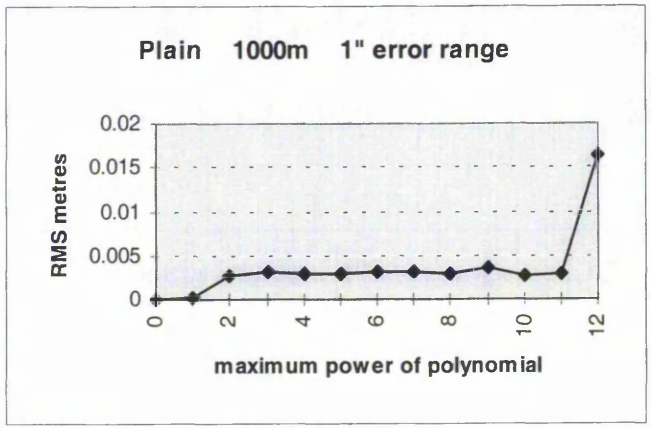
Plain 1000m 1" error range
RMS metres
0.02
0.015
0.01
0.005
0
0 2 4 6 8 10 12
maximum power of polynomial

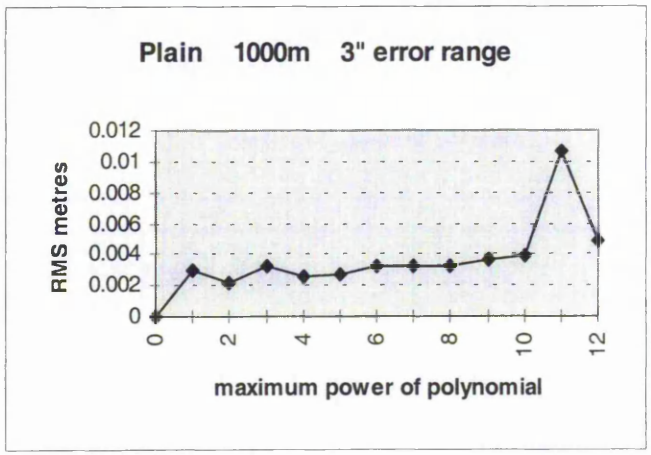
Plain 1000m 3" error range
RMS metres
0.012
0.01
0.008
0.006
0.004
0.002
0
0 2 4 6 8 10 12
maximum power of polynomial

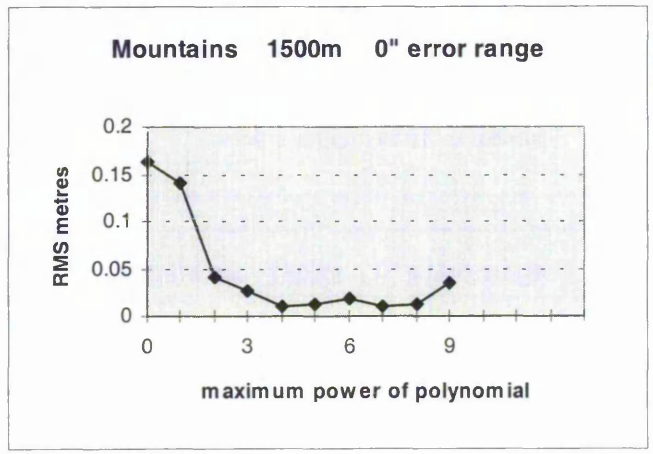
Mountains 1500m 0" error range
RMS metres
0.2
0.15
0.1
0.05
0
0 3 6 9
maximum power of polynomial

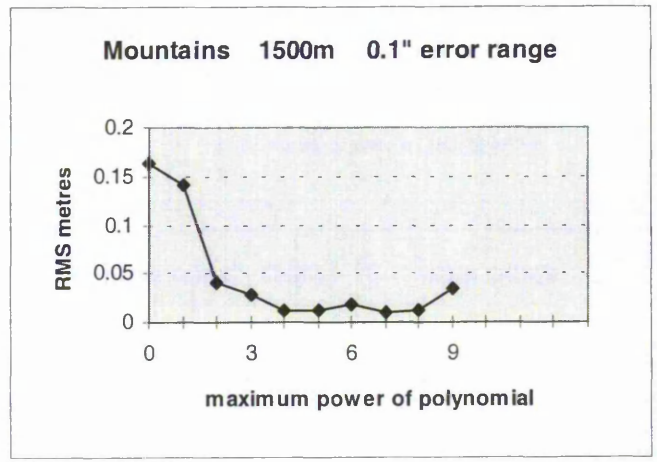
Mountains 1500m 0.1" error range
RMS metres
0.2
0.15
0.1
0.05
0
0 3 6 9
maximum power of polynomial

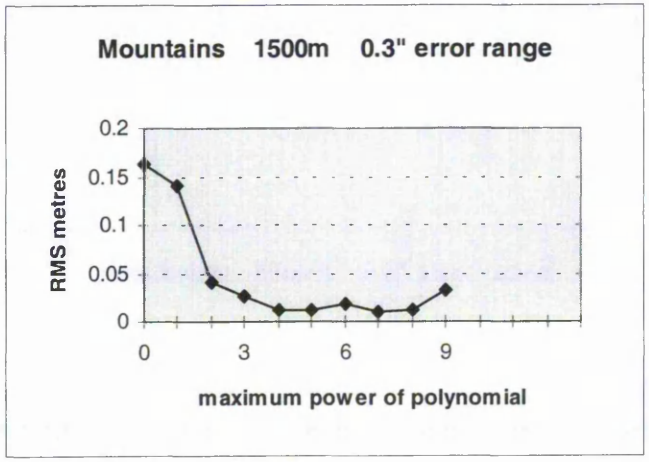
Mountains 1500m 0.3" error range
RMS metres
0.2
0.15
0.1
0.05
0
0
3
6
9
maximum power of polynomial

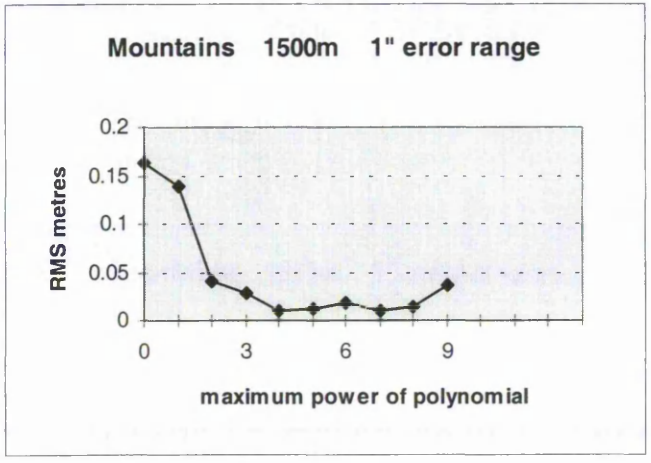
Mountains 1500m 1" error range
RMS metres
0.2
0.15
0.1
0.05
0
0
3
6
9
maximum power of polynomial

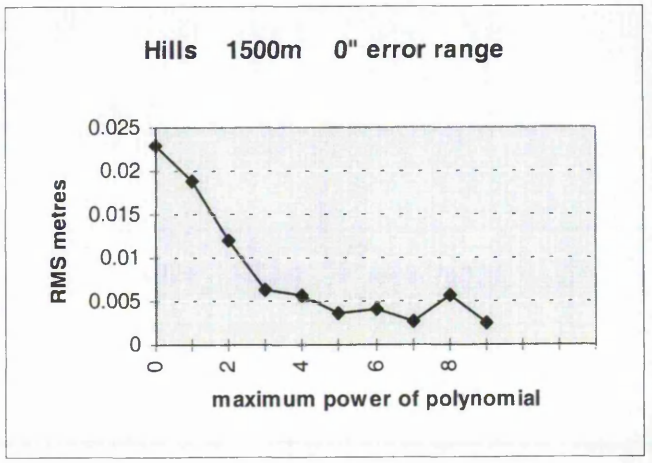
Hills 1500m 0" error range
RMS metres
0.025
0.02
0.015
0.01
0.005
0
0
2
4
6
8
maximum power of polynomial

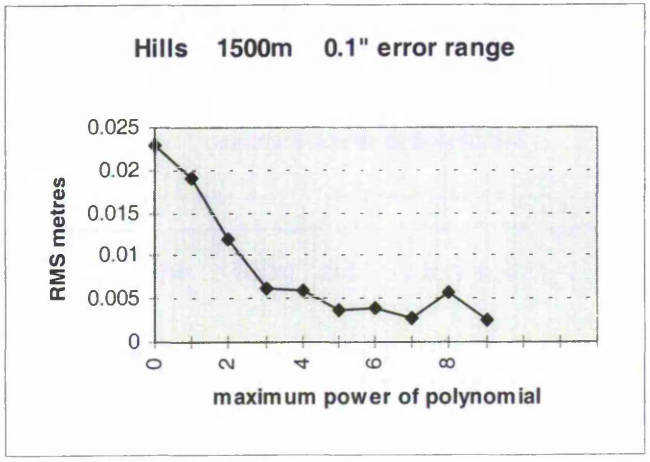
Hills 1500m 0.1" error range
RMS metres
0.025
0.02
0.015
0.01
0.005
0
0
2
4
6
8
maximum power of polynomial

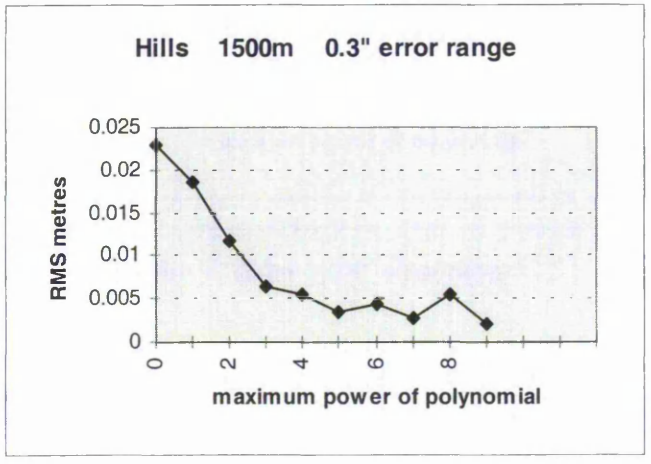
Hills 1500m 0.3" error range
RMS metres
0.025
0.02
0.015
0.01
0.005
0
0
2
4
6
8
maximum power of polynomial

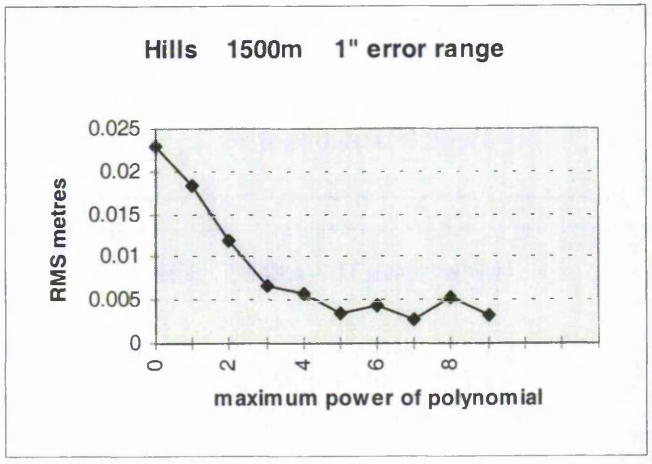
Hills 1500m 1" error range
RMS metres
0.025
0.02
0.015
0.01
0.005
0
0
2
4
6
8
maximum power of polynomial

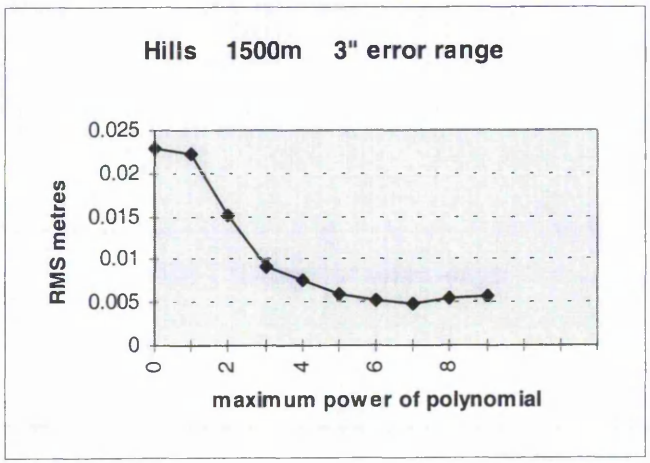
Hills 1500m 3" error range
RMS metres
0.025
0.02
0.015
0.01
0.005
0
0 2 4 6 8
maximum power of polynomial

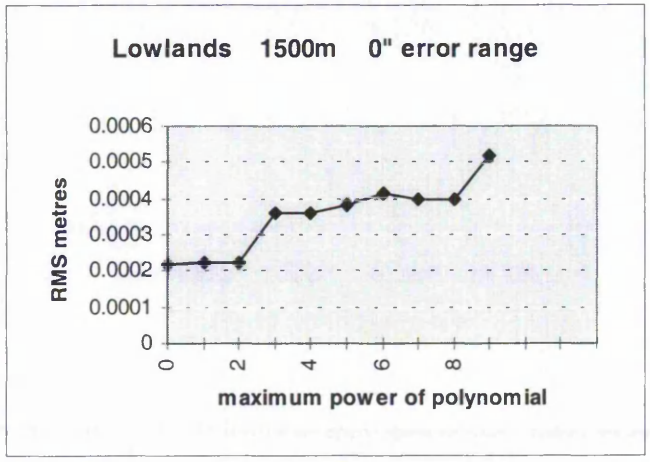
Lowlands 1500m 0" error range
RMS metres
0.0006
0.0005
0.0004
0.0003
0.0002
0.0001
0
0 2 4 6 8
maximum power of polynomial

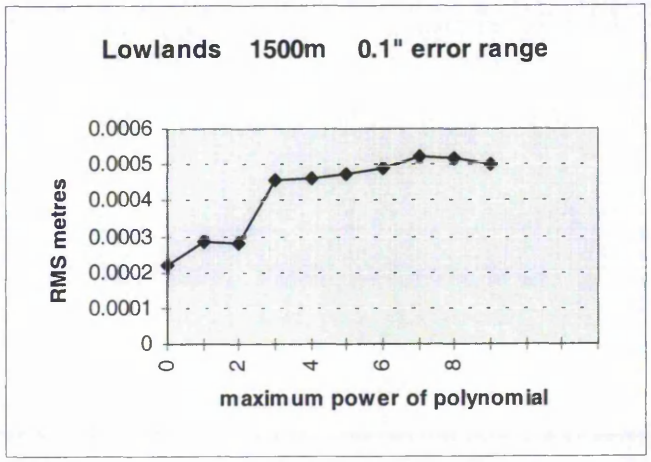
Lowlands 1500m 0.1" error range
RMS metres
0.0006
0.0005
0.0004
0.0003
0.0002
0.0001
0
0 2 4 6 8
maximum power of polynomial

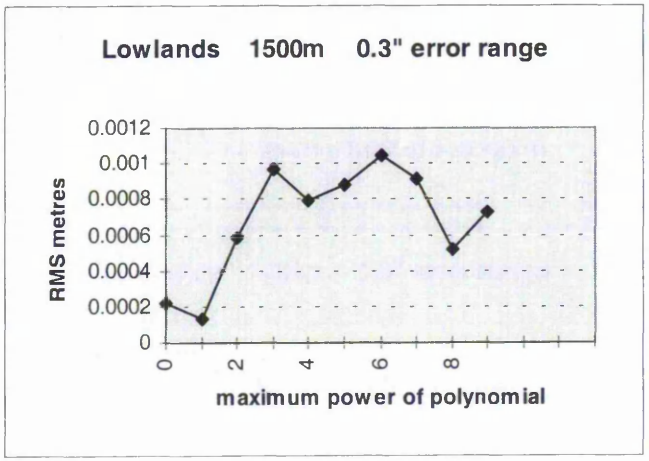
Lowlands 1500m 0.3" error range
RMS metres
0.0012
0.001
0.0008
0.0006
0.0004
0.0002
0
0 2 4 6 8
maximum power of polynomial

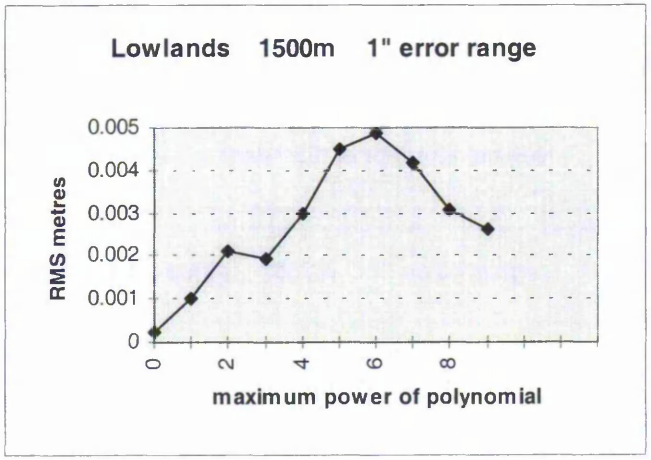
Lowlands 1500m 1" error range
RMS metres
0.005
0.004
0.003
0.002
0.001
0
0 2 4 6 8
maximum power of polynomial

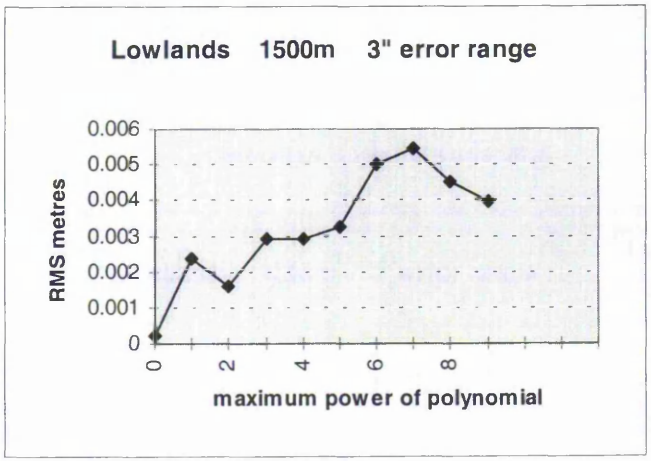
Lowlands 1500m 3" error range
RMS metres
0.006
0.005
0.004
0.003
0.002
0.001
0
0 2 4 6 8
maximum power of polynomial

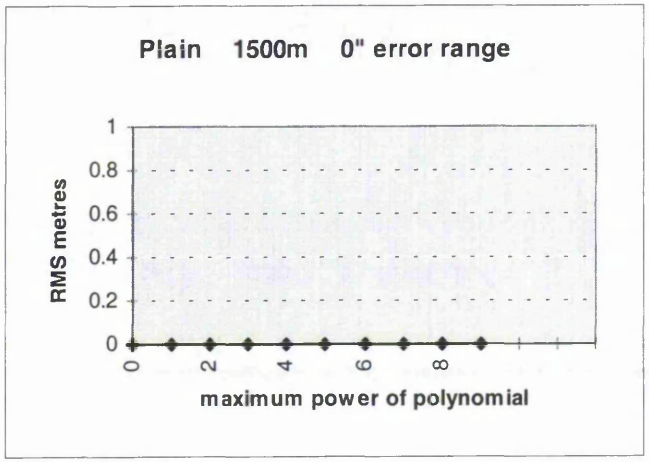
Plain 1500m 0" error range
RMS metres
1
0.8
0.6
0.4
0.2
0
0 2 4 6 8
maximum power of polynomial

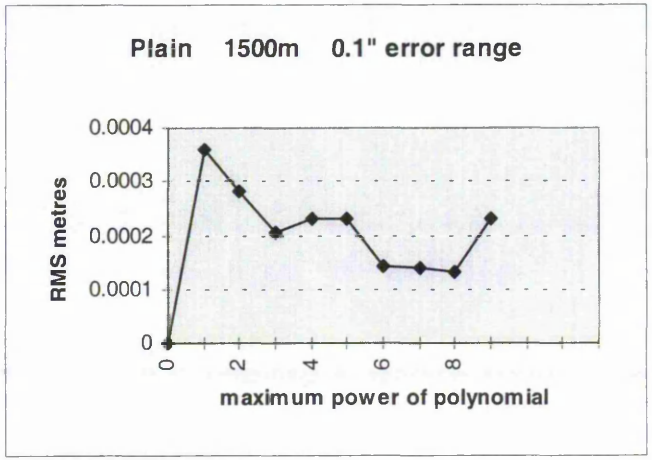
Plain 1500m 0.1" error range
RMS metres
0.0004
0.0003
0.0002
0.0001
0
0 2 4 6 8
maximum power of polynomial

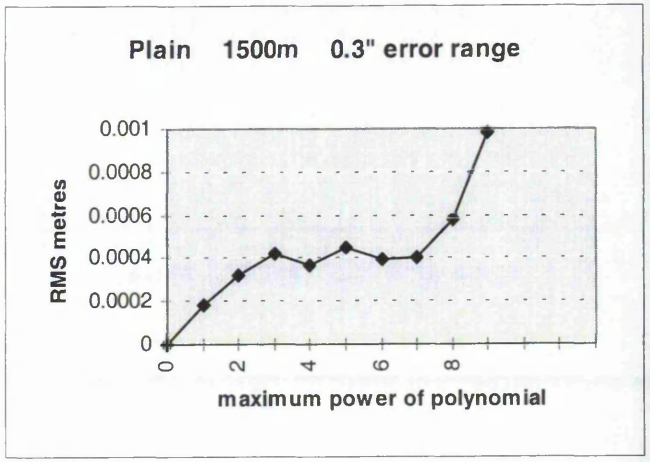
Plain 1500m 0.3" error range
RMS metres
0.001
0.0008
0.0006
0.0004
0.0002
0
0 2 4 6 8
maximum power of polynomial

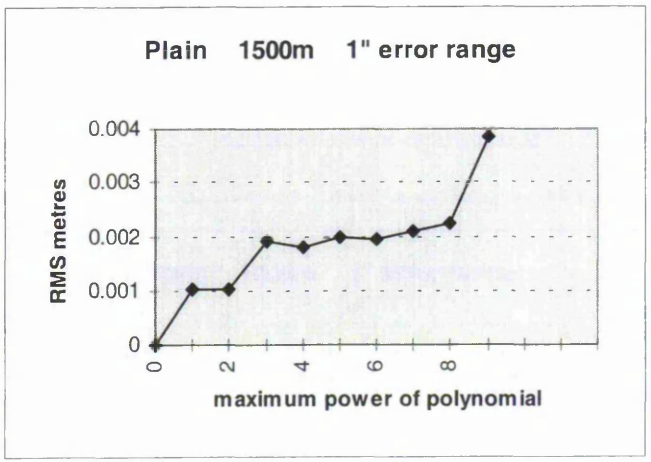
Plain 1500m 1" error range
RMS metres
0.004
0.003
0.002
0.001
0
0 2 4 6 8
maximum power of polynomial

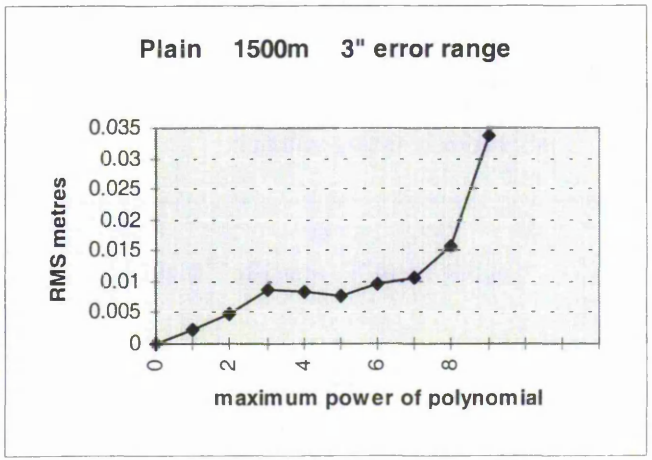
Plain 1500m 3" error range
RMS metres
0.035
0.03
0.025
0.02
0.015
0.01
0.005
0
0 2 4 6 8
maximum power of polynomial

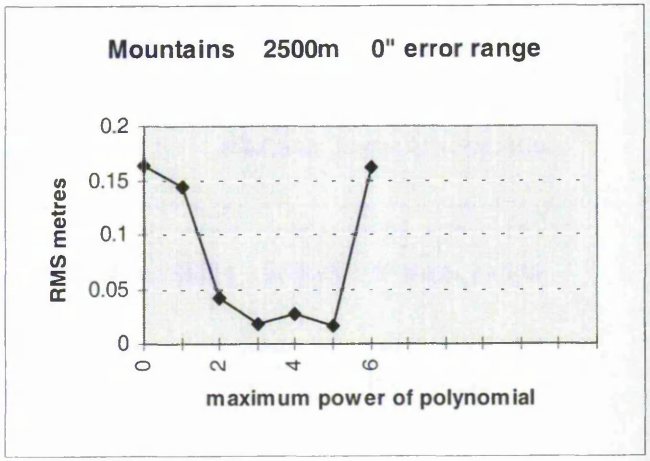
Mountains 2500m 0" error range
RMS metres
0.2
0.15
0.1
0.05
0
0 2 4 6
maximum power of polynomial

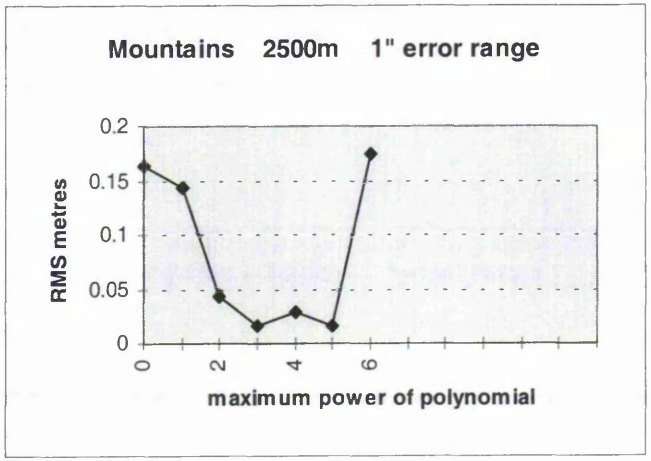
Mountains 2500m 1" error range
RMS metres
0.2
0.15
0.1
0.05
0
0
2
4
6
maximum power of polynomial

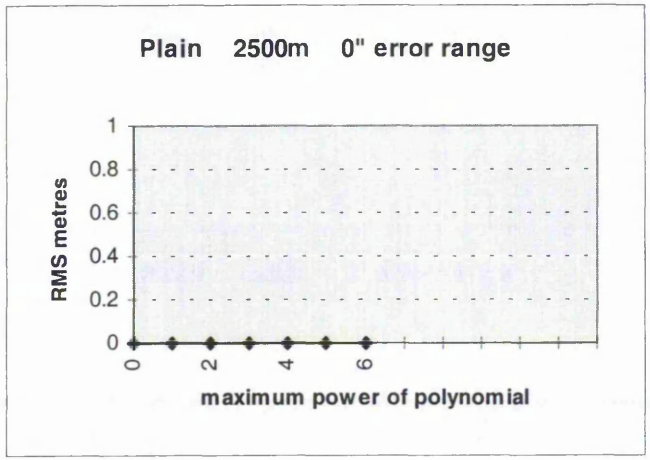
Plain 2500m 0" error range
RMS metres
1
0.8
0.6
0.4
0.2
0
0
2
4
6
maximum power of polynomial

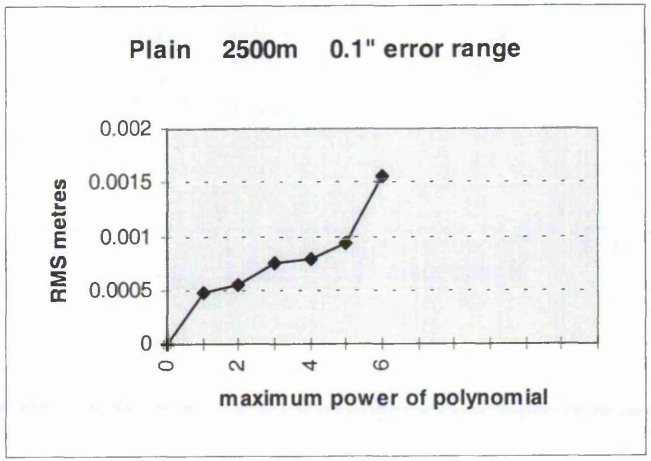
Plain 2500m 0.1" error range
RMS metres
0.002
0.0015
0.001
0.0005
0
0
2
4
6
maximum power of polynomial

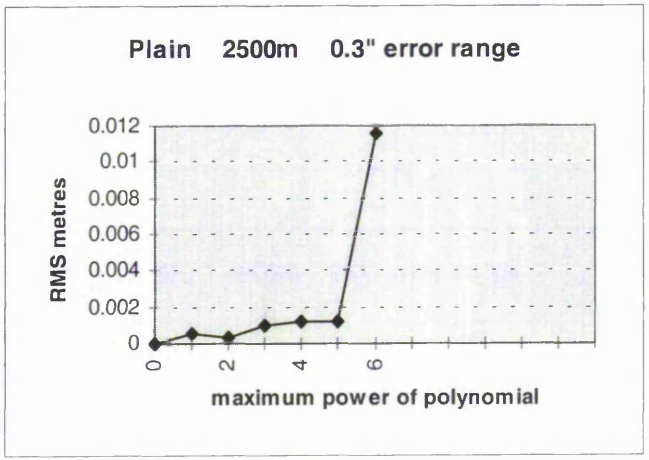
Plain 2500m 0.3" error range
RMS metres
0.012
0.01
0.008
0.006
0.004
0.002
0
0
2
4
6
maximum power of polynomial

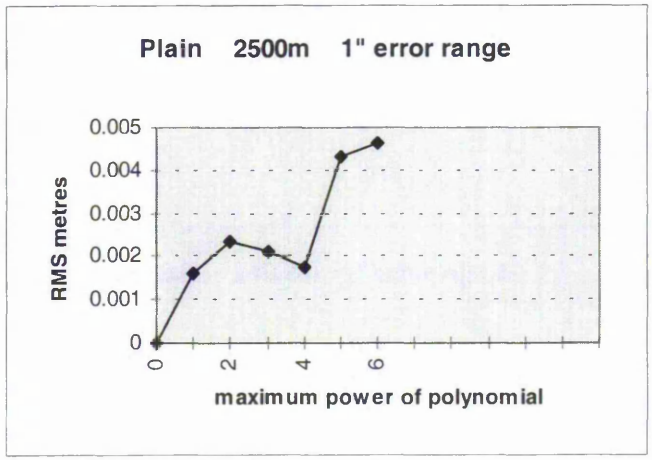
Plain 2500m 1" error range
RMS metres
0.005
0.004
0.003
0.002
0.001
0
0
2
4
6
maximum power of polynomial